

DTIC FILE COPY

AFOSR-TR- 90-0204

2

AD-A218 394

DYNAMIC FRACTURE OF CONCRETE

PART I

Approved for public release;
distribution unlimited.

Jiaji Du
Department of Mechanical Engineering

A.S. Kobayashi
Department of Mechanical Engineering

Neil M. Hawkins
Department of Civil Engineering

University of Washington
Seattle, WA 98195

DTIC
ELECTE
FEB 23 1990
S D

AIR FORCE OFFICE OF SCIENTIFIC RESEARCH (AFOSR)
BOLLING AIR FORCE BASE
WASHINGTON, DC 20332-6448
Chief Technical Officer

Prepared for

Air Force Office of Scientific Research
Bolling Air Force Base
Washington, DC 20332-6448

Final Report on AFOSR Contract 86-0204

February 14, 1990

Distribution Unlimited:

90 02 23 031

Unclassified

SECURITY CLASSIFICATION OF THIS PAGE

REPORT DOCUMENTATION PAGE

Form Approved
OMB No. 0704-0188

| | | | | | |
|--|-------|--|---|--|--------------------------------|
| 1a. REPORT SECURITY CLASSIFICATION Unclassified | | | 1b. RESTRICTIVE MARKINGS None | | |
| 2a. SECURITY CLASSIFICATION AUTHORITY | | | 3. DISTRIBUTION / AVAILABILITY OF REPORT Unlimited | | |
| 2b. DECLASSIFICATION / DOWNGRADING SCHEDULE | | | | | |
| 4. PERFORMING ORGANIZATION REPORT NUMBER(S) UWAF/DCE/TR-90/1 | | | 5. MONITORING ORGANIZATION REPORT NUMBER(S) AFOSR-TR-90-0209 | | |
| 6a. NAME OF PERFORMING ORGANIZATION University of Washington | | 6b. OFFICE SYMBOL (if applicable) UWCE | | 7a. NAME OF MONITORING ORGANIZATION Air Force Office of Scientific Research | |
| 6c. ADDRESS (City, State, and ZIP Code) Seattle, WA 98195 | | | 7b. ADDRESS (City, State, and ZIP Code) Bolling Air Force Base Washington, D.C. 20332 | | |
| 8a. NAME OF FUNDING / SPONSORING ORGANIZATION Air Force Office of Sci. Res. | | 8b. OFFICE SYMBOL (if applicable) AFOSR/NA | | 9. PROCUREMENT INSTRUMENT IDENTIFICATION NUMBER AFOSR-86-0204 | |
| 8c. ADDRESS (City, State, and ZIP Code) Bolling Air Force Base Washington, D.C. 20332 | | | 10. SOURCE OF FUNDING NUMBERS | | |
| | | | PROGRAM ELEMENT NO. 61102F | PROJECT NO. 2302 | TASK NO. C2 |
| 11. TITLE (Include Security Classification) Dynamic Fracture of Concrete, Part I | | | | | |
| 12. PERSONAL AUTHOR(S) J. Du, N.M. Hawkins, A.S. Kobayashi | | | | | |
| 13a. TYPE OF REPORT Final | | 13b. TIME COVERED FROM 15/06/86 TO 14/12/89 | | 14. DATE OF REPORT (Year, Month, Day) 1990 February 14 | |
| 15. PAGE COUNT 275 | | | | | |
| 16. SUPPLEMENTARY NOTATION | | | | | |
| 17. COSATI CODES | | | 18. SUBJECT TERMS (Continue on reverse if necessary and identify by block number) | | |
| FIELD | GROUP | SUB-GROUP | Concrete fracture, fracture process zone, moire interferometry, static finite element analysis, dynamic finite element analysis | | |
| | | | | | |
| 19. ABSTRACT (Continue on reverse if necessary and identify by block number) | | | | | |
| <p>Static and dynamic analyses of concrete failure based on fracture mechanics were conducted using crack-line wedge-loaded, double cantilever beam (CLWL-DCB) and edge-cracked, three point bend specimens under Mode I loading conditions, aimed at developing a mathematical model which describes the tensile failure process of concrete materials at the macro-level. The fracture process zone associated with a stably growing crack in concrete was determined by a hybrid experimental-numerical technique where a crack closure stress versus crack opening displacement (COD) relation of a finite element model of the specimen was optimized to fit the COD data, obtained by Moire interferometry with real reference grating, and other experimental measurements. For the first time, the crack closure stress versus COD relation of a fracture process zone in concrete was determined directly and was found to be similar to those obtained by others using inverse procedures. The crack closure stress versus COD relation for the two CLWL-DCB and edge-cracked, three point bend specimens were identical thus implying that this relation is a specimen-independent but material-dependent constitutive relation. The above static constitutive relation, with modifications to account for the differences in tensile strengths and aggregate sizes, were used to simulate the recorded dynamic crack propagation in large scale, impacted three point bend specimens (unnotched) by Mindess and the Charpy type impact tests by Shah. In both cases, dynamic finite element modeling with the adjusted constitutive equations for the fracture process zones simulated the measured crack propagation histories within the experimental accuracies. (K.P.)</p> | | | | | |
| 20. DISTRIBUTION / AVAILABILITY OF ABSTRACT <input checked="" type="checkbox"/> UNCLASSIFIED/UNLIMITED <input type="checkbox"/> SAME AS RPT. <input type="checkbox"/> DTIC USERS | | | 21. ABSTRACT SECURITY CLASSIFICATION Unclassified | | |
| 22a. NAME OF RESPONSIBLE INDIVIDUAL Dr. Spencer Wu | | | 22b. TELEPHONE (Include Area Code) (202) 767-6962 | | 22c. OFFICE SYMBOL AFOSR/NA |

405 0-06 100-1000

Research sponsored by the Air Force Office of Scientific Research, Air Force Systems Command, USAF, under grant or cooperative agreement number, AFOSR XX-XXXX. The US Government is authorized to reproduce and distribute reprints for Governmental purposes notwithstanding any copyright notation thereon.

This manuscript is submitted for publication with the understanding that the US Government is authorized to reproduce and distribute reprints for Governmental purposes.

Abstract

Static and dynamic analyses of concrete failure based on fracture mechanics were conducted using crack-line wedge-loaded, double cantilever beam (CLWL-DCB) and edge-cracked, three point bend specimens under Mode I loading conditions, aimed at developing a mathematical model which describes the tensile failure process of concrete materials at the macro-level.

The fracture process zone associated with a stably growing crack in concrete was determined by a hybrid experimental-numerical technique where a crack closure stress versus crack opening displacement (COD) relation of a finite element model of the specimen was optimized to fit the COD data, obtained by Moire interferometry with real reference grating, and other experimental measurements.

For the first time, the crack closure stress versus COD relation of a fracture process zone in concrete was determined directly and was found to be similar to those obtained by others using inverse procedures. The crack closure stress versus COD relation for the two CLWL-DCB and edge-cracked, three point bend specimens were identical thus implying that this relation is a specimen-

independent but material-dependent constitutive relation.

The above static constitutive relation, with modifications to account for the differences in tensile strengths and aggregate sizes, were used to simulate the recorded dynamic crack propagation in large scale, impacted three point bend specimens (unnotched) by Mindess and the Charpy type impact tests by Shah. In both cases, dynamic finite element modeling with the adjusted constitutive equations for the fracture process zones simulated the measured crack propagation histories within the experimental accuracies.

| | |
|--------------------|--|
| Accession For | |
| NTIS CRASH | <input checked="checked" type="checkbox"/> |
| DTIC TAB | <input type="checkbox"/> |
| Unannounced | <input type="checkbox"/> |
| Justification | |
| By | |
| Distribution | |
| Availability Codes | |
| Dist | Avail and/or |
| A-1 | |



TABLE OF CONTENTS

| | page |
|---|--------|
| | ---- |
| LIST OF FIGURES | vii |
| LIST OF TABLES | xiv |
| NOMENCLATURE | xv |
| CHAPTER 1 INTRODUCTION AND OBJECTIVES | 1 |
| 1.1 General Aspect of Research on Concrete Fracture | 1 |
| 1.2 Objectives | 7 |
| CHAPTER 2 LITERATURE REVIEW | 9 |
| 2.1 Linear Fracture Mechanics Applied to Concrete Fracture | 11 |
| 2.1.1 Notch Sensitivity | 12 |
| 2.1.2 Size Effect | 12 |
| 2.2 Nonlinear Fracture Analysis Applied to Concrete Fracture | 13 |
| 2.2.1 J Integral Approach | 13 |
| 2.2.2 R-Curve Approach | 14 |
| 2.2.3 Tied Crack Model | 15 |
| 2.2.4 Smeared Crack Model | 20 |
| 2.2.5 Two-Parameter Model | 25 |
| 2.3 Test Methods for Fracture Process Zone Determination | 25 |
| 2.3.1 Acoustic Emission | 26 |

| | | |
|-----------|--|----|
| 2.3.2 | Replica Technique | 27 |
| 2.3.3 | Optical Interferometry | 28 |
| 2.4 | Dynamic Fracture of Concrete | 30 |
| 2.4.1 | Impact Tests | 31 |
| 2.4.2 | Fracture Mechanics Modeling | 32 |
| 2.4.3 | Damage Mechanics Modeling | 33 |
| 2.4.4 | Statistics Modeling | 34 |
| 2.5 | Discussions and Conclusions | 35 |
| CHAPTER 3 | FRACTURE PROCESS ZONE OF CONCRETE | 38 |
| 3.1 | General Concept of Fracture Process Zone | 38 |
| 3.1.1 | Tensile Behavior of Materials Failure . | 38 |
| 3.1.2 | Definition of Fracture Process Zone ... | 40 |
| 3.1.3 | Role of Fracture Process Zone in Fracture | 41 |
| 3.2 | Fracture Process Zone in Concrete | 42 |
| 3.2.1 | Observed Fracture Process Zone in Concrete | 42 |
| 3.2.2 | Features of Fracture Process Zone in Concrete | 43 |
| 3.2.3 | Significance of Fracture Process Zone in Concrete | 45 |
| 3.3 | Method of Research | 46 |
| 3.3.1 | Scope of Research | 46 |
| 3.3.2 | Mathematical Representation - Assumptions | 47 |
| 3.3.3 | Hybrid Experimental - Numerical Approach | 49 |

| | | |
|-----------|--|----|
| CHAPTER 4 | EXPERIMENTAL APPROACH | 51 |
| 4.1 | Test Program | 51 |
| 4.1.1 | Objectives of the Experiments | 51 |
| 4.1.2 | Test Groups and Test Variables | 52 |
| 4.1.3 | Loading and Data Recording Devices | 56 |
| 4.2 | Specimen Preparation | 58 |
| 4.2.1 | Fabrication of Specimens | 58 |
| 4.2.2 | Material Properties Determination | 60 |
| 4.2.3 | Specimen Surface Treatment for Moire Testing | 62 |
| 4.3 | Moire Interferometry Test Method | 63 |
| 4.3.1 | Introduction to Moire Interferometry Method | 63 |
| 4.3.2 | Moire Interferometry with Real Reference Grating | 68 |
| 4.3.3 | Moire Interferometry with White Light | 71 |
| 4.4 | Optical Instrumentation and Test Procedures | 73 |
| 4.4.1 | White Light Moire Set-Up | 73 |
| 4.4.2 | Laser Moire Set-Up | 74 |
| 4.4.3 | Test Procedures | 77 |
| CHAPTER 5 | NUMERICAL PROCEDURES | 81 |
| 5.1 | Finite Element Analysis | 81 |
| 5.1.1 | Special Features in Finite Element Analysis | 81 |
| 5.1.2 | Superposition Principle and Fundamental Solutions | 85 |

| | | |
|-----------|---|-----|
| 5.1.3 | Formulation Using Fundamental Solutions | 86 |
| 5.2 | Indirect Method | 89 |
| 5.2.1 | Three - Line Model | 89 |
| 5.2.2 | Iteration Simulation Scheme | 92 |
| 5.2.3 | Trial and Error Procedure | 93 |
| 5.3 | Direct Method | 93 |
| 5.3.1 | Motivations | 93 |
| 5.3.2 | One - Curve Model | 96 |
| 5.3.3 | Optimization Procedure | 99 |
| 5.4 | Discussion on Numerical Procedure | 101 |
| 5.4.1 | Prediction of Crack Propagation | 101 |
| 5.4.2 | Relation between Indirect and Direct Methods | 102 |
| 5.4.3 | Finite Element Size | 103 |
| CHAPTER 6 | STATIC FRACTURE OF CONCRETE SPECIMENS | 104 |
| 6.1 | Small Three Point Bend Specimens | 104 |
| 6.1.1 | Experimental Results | 104 |
| 6.1.2 | Numerical Results | 113 |
| 6.2 | Large Double Cantilever Beam Specimens | 116 |
| 6.2.1 | Experimental Results | 118 |
| 6.2.2 | Numerical Results | 127 |
| 6.3 | Specimens of Adequate Size | 127 |
| 6.3.1 | Experimental Results | 131 |
| 6.3.2 | Numerical Results | 145 |

| | |
|---|-----|
| 6.3.3 Discussions | 155 |
| CHAPTER 7 DYNAMIC FRACTURE OF CONCRETE SPECIMENS | 163 |
| 7.1 Dynamic Fracture Process Zone Model | 163 |
| 7.1.1 General | 162 |
| 7.1.2 Formulation Considerations | 164 |
| 7.2 Preliminary Results | 165 |
| 7.2.1 Simulation of Mindess' Impact Tests .. | 165 |
| 7.3 Refined Results | 187 |
| 7.3.1 Simulation of Shah' Impact Tests | 187 |
| CHAPTER 8 SUMMARY | 211 |
| CHAPTER 9 CONCLUSIONS | 218 |
| CHAPTER 10 RECOMMENDATIONS | 220 |
| REFERENCES | 223 |
| APPENDIX A DETAILS OF SPECIMEN PREPARATION | 236 |
| APPENDIX B FABRICATION AND TRANSFER DIFFRACTION GRATING | 239 |
| APPENDIX C SOLUTION OF OVERDETERMINISTIC EQUATIONS | 243 |
| APPENDIX D SOME DYNAMIC FINITE ELEMENT COMPUTATION DETAILS | 245 |
| APPENDIX E A MODEL FOR FATIGUE OF A SIMILAR MATERIAL | 251 |
| APPENDIX F K_R CURVE RE-EVALUATION BASED ON TEST RESULTS | 267 |

LIST OF FIGURES

| | page ---- |
|--|--------------|
| Figure 3.1 Comparison of Tensile Behavior of Metal and Concrete | 39 |
| Figure 3.2 Normal Stress Distribution Around Fracture Process Zone | 44 |
| Figure 3.3 Published Direct Tension Test Results | 48 |
| Figure 4.1 Small Beam and Large CLWL-DCB Specimens (a) Group 1, (b) Group 2,3 | 54 |
| Figure 4.2 Specimens of Appropriate Sizes (a) Group 4, (b) Group 5 | 55 |
| Figure 4.3 Wedge Load and Specimen Holding Assembly for CLWL-DCB Specimen Tests Group 2,3,4 | 57 |
| Figure 4.4 Principle of Moire Interferometry | 65 |
| Figure 4.5 Generation of Virtual Grating with Real Reference Grating | 70 |
| Figure 4.6 Optical Set-Up for White Light Moire Interferometry ($f=1200$ lines/mm) | 72 |
| Figure 4.7 Optical Set-UP for Laser Moire Interferometry ($f=1200$ lines/mm) | 75 |
| Figure 4.8 Staging for Real Reference Grating | 78 |
| Figure 5.1 Boundary Conditions and Loading Systems | 83 |
| Figure 5.2 Fracture Process Zone Model with Three Line Segments | 91 |
| Figure 5.3 Assumed Functional Form for Crack Closure Stress Versus COD Relation | 98 |
| Figure 6.1 Experimental Set-Up for Test Group 1. | 105 |
| Figure 6.2 Moire Interferometric Pattern at Crack Tip Three Point Bend Specimen No. SB-1 at Load 624 N | 107 |

| | | |
|-------------|--|-----|
| Figure 6.3 | Moire Interferometric Pattern at Crack Tip Three Point Bend Specimen No. SB-4 at Load 557 N | 108 |
| Figure 6.4 | COD Variations along Fracture Process Zone Specimen No. SB-1 | 109 |
| Figure 6.5 | COD Variations along Fracture Process Zone Specimen No. SB-4 | 110 |
| Figure 6.6 | COD at Prenotch End Versus Microcrack Extension Small Three Point Bend Specimen | 112 |
| Figure 6.7 | Finite Element Model of the Concrete Small Three Point Bend Specimen | 114 |
| Figure 6.8 | Crack Closure Stress Versus COD Relation for Concrete Fracture Process Zone Group 1. Small Beams | 115 |
| Figure 6.9 | Load Versus Crack Mouth Opening Displacement for Small Three Point Bend Specimens | 117 |
| Figure 6.10 | Experimental Set-Up for Test Group 2,3. .. | 119 |
| Figure 6.11 | Wedge Load Versus $2V_1$ for Large CLWL-DCB Specimens No. LD-1 and No. LD-2 | 120 |
| Figure 6.12 | Wedge Load Versus $2V_1$ for Large CLWL-DCB Specimens No. LD-3 and No. LD-4 | 121 |
| Figure 6.13 | $2V_2$ Versus $2V_1$ for Large CLWL-DCB Specimens No. LD-1 and No. LD-2 | 122 |
| Figure 6.14 | $2V_2$ Versus $2V_1$ for Large CLWL-DCB Specimens No. LD-3 and No. LD-4 | 123 |
| Figure 6.15 | COD Variations along Fracture Process Zone Specimen No. LD-1 | 125 |
| Figure 6.16 | COD Variations along Fracture Process Zone Specimen No. LD-3 | 126 |
| Figure 6.17 | Finite Element Mesh for Group 2,3. Large CLWL-DCB Specimens | 128 |

| | | |
|-------------|---|-----|
| Figure 6.18 | Crack Closure Stress Versus COD Relation for Group 2 Specimens | 129 |
| Figure 6.19 | Crack Closure Stress Versus COD Relation for Group 3 Specimens | 130 |
| Figure 6.20 | Experimental Set-Up for Test Group 4. | 132 |
| Figure 6.21 | Optical Set-Up for Laser Beam | 133 |
| Figure 6.22 | Experimental Set-Up for Test Group 5. | 134 |
| Figure 6.23 | Wedge Load Versus $2V_1$ for Small CLWL-DCB Specimens, Group 4. | 135 |
| Figure 6.24 | $2V_2$ Versus $2V_1$ for Small CLWL-DCB Specimens, Group 4. | 136 |
| Figure 6.25 | Load Versus Deflection Curves for Three Point Bend Specimens, Group 5. | 137 |
| Figure 6.26 | Sequential Moire Fringe Patterns of CLWL-DCB Specimen, Specimen No. SD-2 | 139 |
| Figure 6.27 | Sequential Moire Fringe Patterns of Three Point Bend Specimen, Specimen No. LB-1 ... | 140 |
| Figure 6.28 | COD Variations along Fracture Process Zone CLWL-DCB Specimen No. SD-2 | 141 |
| Figure 6.29 | COD Variations along Fracture Process Zone CLWL-DCB Specimen No. SD-4 | 142 |
| Figure 6.30 | COD Variations along Fracture Process Zone Three Point Bend Specimen No. LB-4 | 143 |
| Figure 6.31 | COD Variations along Fracture Process Zone Three Point Bend Specimen No. LB-1 | 144 |
| Figure 6.32 | Finite Element Mesh for Group 4 Small CLWL-DCB Specimens | 146 |
| Figure 6.33 | Finite Element Mesh for Group 5 Large Three Point Bend Specimens | 147 |
| Figure 6.34 | Crack Closure Stress Versus COD Relation for One Continuous Curve Model | 149 |

| | | |
|-------------|---|-----|
| Figure 6.35 | Comparison of Crack Closure Stress Versus COD Relationship with Published Direct Tension Test Results | 150 |
| Figure 6.36 | Comparison of Three - Line Model with One - Curve Model for Group 4,5 specimens | 151 |
| Figure 6.37 | Comparison of Test and Numerically Generated Moire Fringe Patterns. CLWL-DCB Specimen No. SD-4 | 153 |
| Figure 6.38 | Comparison of Test and Numerically Generated Moire Fringe Patterns. Three Point Bend Specimen No. LB-1 | 154 |
| Figure 6.39 | Computed Sequential Normal Stress Distributions along the Crack Path in Group 4 CLWL-DCB Specimens | 156 |
| Figure 6.40 | Computed Sequential Normal Stress Distributions along the Crack Path in Group 5 Three Point Bend Specimens | 157 |
| Figure 6.41 | Energy Partition for Small CLWL-DCB Specimen, Group 4 | 158 |
| Figure 6.42 | Energy Partition for Large Three Point Bend Specimen, Group 5 | 159 |
| Figure 6.43 | Crack closure stress, Crack Opening Displacement Distributions along Fracture Process Zone and Asociated Computed Moire Fringe Pattern for CLWL-DCB Specimen No. SD-4 | 162 |
| Figure 7.1 | Fracture Process Zone of Concrete for Dynamic Fracture Modelling | 166 |
| Figure 7.2 | Crack Closure Stress Versus COD for Modeling Fracture Process Zone in Impacted Beams. Simulation of Mindess' Impact Tests | 167 |
| Figure 7.3 | Crack Tip Nodal Force Released Mechanism Dynamic Finite Element Simulation | 169 |
| Figure 7.4 | Mindess' Impacted Concrete Beam Test Specimen No. 1, Ref. [88] | 172 |

| | | |
|-------------|--|-----|
| Figure 7.5 | Prescribed Load-Histroy for Concrete Beam Specimen No. 1, Ref. [88] | 173 |
| Figure 7.6 | Finite Element Model for Impacted Beam Specimen No. 1, Ref. [88] | 174 |
| Figure 7.7 | Computed Crack Length Versus Time Specimen No. 1, Ref. [88] Assumed Crack Velocity 1847 mps | 175 |
| Figure 7.8 | Computed Crack Length Versus Time Specimen No. 1, Ref. [88] Assumed Crack Velocity 319 mps | 176 |
| Figure 7.9 | Deflection Velocity Versus Time Curves at 75 mm from Beam Center Specimen No. 1, Ref. [88] | 178 |
| Figure 7.10 | Deflection Velocity Versus Time Curves at 250 mm from Beam Center Specimen No. 1, Ref. [88] | 179 |
| Figure 7.11 | Load Point Deflection Versus Time Specimen No. 1, Ref. [88] | 180 |
| Figure 7.12 | Mindess' Impacted Concrete Beam Test Specimen No. 2, Ref. [89] | 182 |
| Figure 7.13 | Prescribed Load-Histroy for Concrete Beam Specimen No. 2, Ref. [89] | 183 |
| Figure 7.14 | Finite Element Model for Impacted Beam Specimen No. 2, Ref. [89] | 184 |
| Figure 7.15 | Computed Crack Length Versus Time Specimen No. 2, Ref. [89] Assumed Crack Velocity 1847 mps | 185 |
| Figure 7.16 | Computed Crack Length Versus Time Specimen No. 2, Ref. [89] Assumed Crack Velocity 319 mps | 186 |
| Figure 7.17 | Energy Partition for Impacted Beam Specimen No. 1, Ref. [88] Assumed Crack Velocity 1847 mps | 188 |
| Figure 7.18 | Energy Partition for Impacted Beam Specimen No. 1, Ref. [88] Assumed Crack Velocity 319 mps | 189 |

| | | |
|-------------|---|-----|
| Figure 7.19 | Fracture Process Zone Used in Modeling Shah's Charpy Impact Tests | 190 |
| Figure 7.20 | Specimen Configuration and Finite Element Model for Concrete and Mortar Beam Impact Tests, Ref. [91] | 193 |
| Figure 7.21 | Applied Load and Reaction Force History Concrete Specimen No. 1, Ref. [91] | 194 |
| Figure 7.22 | Applied Load and Reaction Force History Mortar Specimen, Ref. [92] | 195 |
| Figure 7.23 | Crack Closure Stress Versus COD for Modeling Fracture Process Zone in Impacted Beams. Simulation of Shah's Impact Tests | 196 |
| Figure 7.24 | Crack Extension History for Concrete Beam Specimen No. 1, Ref. [91] | 198 |
| Figure 7.25 | Crack Extension History for Mortar Beam Ref. [92] | 199 |
| Figure 7.26 | Strain History at Prenotch Tip of Impacted Concrete Beam, Specimen No. 1, Ref. [91] . | 201 |
| Figure 7.27 | Strain History at Quarter-Span of Impacted Mortar Beam, Ref. [92] | 202 |
| Figure 7.28 | Load-Point Deflection History of Concrete Specimens, Ref. [91] | 203 |
| Figure 7.29 | Load-Point Deflection History of Mortar Specimen, Ref. [92] | 204 |
| Figure 7.30 | Energy Partition for Concrete Impact Test Specimen No. 1, Ref. [91] | 206 |
| Figure 7.31 | Energy Partition for Mortar Impact Test Ref. [92] | 207 |
| Figure 7.32 | Fracture Resistance Curves for Concrete Specimens, Ref. [91] | 208 |
| Figure 7.33 | Crack Velocity Versus Fracture Energy Dissipation Rate for Concrete Specimens Ref. [91] | 209 |
| Figure E.1 | Fracture Process Zone in Ceramic Composite | 253 |

| | | |
|-------------|---|-----|
| Figure E.2 | Crack Closure Stress Versus COD Relation SiC/Mullite Composite Flexural Specimen ... | 254 |
| Figure E.3 | SiC/Mullite Composite Flexural Specimen ... | 255 |
| Figure E.4 | Finite Element Model for Ceramic Composite Flexural Specimen | 256 |
| Figure E.5 | Reaction Force Versus Applied Displacement SiC/Mullite Composite Flexural Specimen ... | 257 |
| Figure E.6 | Failure Process Under Cyclic Loading A Model for Ceramic Composite | 260 |
| Figure E.7 | Generation of Cyclic Loading Curves A Model for Ceramic Composite | 261 |
| Figure E.8 | Cyclic Flexural Load - Deflection Curves SiC/Mullite Composite Flexural Specimen ... | 263 |
| Figure E.9 | Reaction Force Versus Applied Displacement of Cracked Ceramic Composite Beams | 265 |
| Figure E.10 | Crack Profile at Maximum Load for Each Loading Cycle in Flexural Specimens of Ceramic Composite, Finite Element Results | 266 |
| Figure F.1 | Crack Growth Resistance Curve For CLWL-DCB Specimen, Group 1, Ref. [9] | 269 |
| Figure F.2 | Crack Growth Resistance Curve For CLWL-DCB Specimen, Group 2, Ref. [9] | 270 |
| Figure F.3 | Crack Growth Resistance Curve For CLWL-DCB Specimen, Group 3, Ref. [9] | 271 |
| Figure F.4 | Crack Growth Resistance Curve For CLWL-DCB Specimen, Group 4, Ref. [9] | 272 |
| Figure F.5 | Crack Growth Resistance Curve For CLWL-DCB Specimen, Group 5, Ref. [9] | 273 |

LIST OF TABLES

| | | page ---- |
|-----------|--|--------------|
| Table 4.1 | Aggregate Gradation (Cumulative Percent Retained) | 58 |
| Table 4.2 | Concrete Mix Proportion by Weight | 59 |
| Table 4.3 | Test Groups | 60 |
| Table 4.4 | Tensile Strength and Elastic Modulus | 62 |
| Table 6.1 | Measured Peak Load List Small Beam Specimens | 113 |
| Table 6.2 | Estimated Average Values of Fracture Process Zone Width | 145 |
| Table 6.3 | Material Properties for Computation Specimens of Adequate Size | 161 |
| Table 7.1 | Material Properties of Concrete for Simulation of Mindess' Test | 170 |
| Table 7.2 | Estimated Average Crack Velocities for Mindess' Impact Tests | 181 |
| Table 7.3 | Material Properties of Shah's Specimens | 191 |

NOMENCLATURE

| | |
|-------------------|---|
| A | laser beam |
| B | laser beam, empirical constant in size effect law |
| C | laser beam |
| CLWL -DCB | crack-line-wedge-loaded double cantilever beam |
| COD | crack opening displacement |
| CTOD | crack tip opening displacement |
| CTOD _c | critical crack tip opening displacement |
| D | load point displacement |
| D _P | D due to unit P load at its node |
| D _F | D due to unit F load at its node |
| D _j | D due to unit R _j load at node j |
| E | modulus of elasticity |
| F | frequency of the optical grating, external load |
| F _c | frequency of compensator |
| FCM | fictitious crack model |
| G _c | critical strain energy release rate |
| G _{Ic} | mode I critical strain energy release rate |
| G _F | work of fracture or fracture energy |
| J | Rice's path independent contour integral |
| K | stress intensity factor |
| K _R | crack growth resistance |

| | |
|----------|---|
| K_{Ic} | mode I fracture toughness |
| LEFM | linear elastic fracture mechanics |
| N | fringe order, number of node along crack path |
| P | failure load, unknown external load |
| R | fracture resistance |
| R_j | equivalent load at node j |
| U | displacement component |
| V_{1P} | $2V_1$ due to unit P load at its node |
| V_{1F} | $2V_1$ due to unit F load at its node |
| V_{1j} | $2V_1$ due to unit R_j load at node j |
| V_{2P} | $2V_2$ due to unit P load at its node |
| V_{2F} | $2V_2$ due to unit F load at its node |
| V_{2j} | $2V_2$ due to unit R_j load at node j |
| a | size of element along fracture process zone |
| b | thickness |
| d | characteristic dimension of the specimen |
| d_a | maximum size of the inhomogeneities |
| d_o | empirical constant in size effect law |
| f | frequency of interference fringes |
| f_e | frequency of moire fringes |
| f_s | frequency of specimen grating |
| f_t | tensile strength of concrete |
| f_v | frequency of virtual grating |
| l_{ch} | characteristic length |
| s_E | brittleness number |

| | |
|---------------|--|
| w | crack opening displacement |
| w_1 | the first critical COD |
| w_2 | the second critical COD |
| w_3 | the third critical COD |
| w_c | critical COD |
| w_j | COD at node j |
| w_k | COD at node k |
| w_{kP} | COD at node k due to unit P load at its node |
| w_{kF} | COD at node k due to unit F load at its node |
| w_{kj} | COD at node k due to unit R_j load at node j |
| α | parameter for COD scaling |
| β | parameter for the shape of the curve |
| γ | angle of incident beam |
| θ_m | angle of the diffraction beam of order m |
| λ | wavelength of the light |
| ϕ | half mutual angle of two beams |
| ν | Poisson's ratio |
| ϵ | strain component |
| σ | normal stress component, crack closure stress |
| σ_N | nominal stress at failure |
| σ_{TP} | stress at crack tip due to unit P load at its node |
| σ_{TF} | stress at crack tip due to unit F load at its node |
| σ_{Tj} | stress at crack tip due to unit R_j load at node j |
| $2V_1$ | crack tip opening displacement |
| $2V_2$ | crack mouth opening displacement |

CHAPTER ONE

INTRODUCTION AND OBJECTIVES

1.1 General Aspect of Research on Concrete Fracture

Concrete is a building material consisting of a mixture in which a paste of portland cement and water molds inserted aggregates into a rock-like mass as the paste hardens through the chemical reaction of cement with water. Thus concrete is a composite material, that is, heterogeneous, at both microscopic and macroscopic levels.

There is no doubt that concrete is by far the most widely used structural material. In addition to its tolerance, the versatility of concrete has contributed to this popularity. Concrete can be molded readily to any size or shape. If the composition and method of construction are selected appropriately, concrete can be used for dams, foundations, highway and airport pavements, water and sewer pipes, shielding harmful radiations, heat insulation of buildings. Lightweight concrete is used for blocks and panels, and architectural concrete is used for decorative purposes. In combination with reinforcing steel, it can be used for bridges, building constructions, water reservoirs, maritime structures, highly impact resistant military installations, precast and prestressed elements, rocket launching pads, thin shells, ships, and

other purposes. The other factor contributing to the general acceptance of concrete is its low cost. This is so partly because the ingredients of concrete are inexpensive and in most cases they are locally available.

Concrete has been used for more than two thousand years [1]. Ancient concrete structures can still be found in various sites of the Roman Empire in Europe, Middle East, and elsewhere. This fact underlines not only the utility but also the durability of concrete.

Portland cement concrete is a relatively brittle material. Cracks are commonly observed on the surface of concrete members. Earliest tests of plain concrete cylinders at Cornell University [2], in 1928, indicated that the various mechanical behaviors are related to the development of microcracks within concrete. Using sensitive microphones, Jone [3] detected cracking noises beginning at 25% to 50% of the ultimate load. It is now well known that the failure mechanism of concrete is cracking, while that of metals is yielding. Consequently, the mechanical behavior of concrete, conventionally reinforced concrete and prestressed concrete is critically influenced by crack propagation. It is not surprising that many attempts are being made to apply the concepts of fracture mechanics to quantify the resistance to cracking in cementitious composites.

Although Griffith's original work [4] on fracture mechanics, in 1920, was for the fracture of brittle materials such as glass, its most significant application, has been for controlling brittle fracture and fatigue failure of metallic structures such as pressure vessels, airplanes, ships and pipelines. During the last twenty years, considerable advances have been made in modifying Griffith's idea or in proposing new concepts to account for the ductility typical of metals. As a result of these efforts, standard testing techniques are now available for obtaining fracture parameters for metals and design based on these parameters are routinely incorporated in relevant design specifications.

In contrast to metals, which are relatively uniform and isotropic, concrete is more complicated due to its nonhomogeneity and nonisotropy. Obviously, the fracture process in concrete is more complicated than that in metals. Since the pioneer experimental work by Kaplan in 1961 [5], many efforts have been made to apply the fracture mechanics concepts to cement, mortar, concrete and reinforced concrete. So far, these attempts have not led to a unique set of material parameters which can quantify the resistance of these cementitious composites to fracture. No standard testing methods nor a generally accepted theoretical analysis similar to those for metals

have been established for concrete. Indeed, this is a challenging task which confronted researchers in the field of civil engineering, material science, and applied mechanics.

One of the primary reason for this lack of success is that most past work is based on the application of fracture mechanics developed for other materials to concrete. Because of the large-scale heterogeneity inherent in the microstructure of concrete, as well as the strain softening, microcracking and large scale process zone, the classical linear elastic (or the classical elastic-plastic) fracture mechanics concepts must be significantly modified in order to predict crack propagation in concrete. More recently, research in many countries are exploring, theoretically, numerically and experimentally these unexplored aspects of nonlinearity associated with crack growth in cementitious composites as well as in ceramics and rocks.

The recent increased understanding and awareness of the unusual aspects of crack growth in concrete has resulted, for example, by: optically observing crack growth in double torsion and double cantilever beam specimens; use of infrared spectroscopy and optical interference microscopy to study process zone; development of finite element programs which incorporate the nonlinear process

zone in the structural modeling; theoretical analysis which includes the tensile strain softening in the process zone in front of the crack tip; application and extension of continuum damage theory; analysis of stochastic aspects of crack growth; and a better understanding of the mixed mode fracture criteria.

In March 1982, an investigation of the diagonal tension fracture strength of concrete was initiated at the University of Washington under a National Science Foundation funding. That investigation [6-10] involved a systematic series of experiments on crack-line wedge-loaded double cantilever beam specimens (CLWL-DCB specimens) subjected to both mode I and mixed mode I and II loadings. Those experiments were backed by an analytical program aimed at developing a two-dimensional finite element code capable of predicting the CLWL-DCB results and therefore capable of predicting discrete crack propagation in concrete members.

This prior investigation [6-8] showed that a consistent nonlinear fracture mechanics concept can be developed for both mode I and mixed mode loadings of concrete. However, the analysis and subsequent interpretation of the test data also raised questions, both as to the limitations inherent in the data base used to develop the fracture parameters [9-10], and in the factors

that must be represented in the numerical model. In particular, the effects of the overall stress state in a specimen, its geometry, and its size were identified as topics for further studies in mode I loading of concrete. The existence or non-existence of a mode II crack propagation was identified as a topic for further studies in mixed mode loadings. In numerical modeling the issues which were identified for further studies are the appropriate distribution of crack closure forces in the process zone along the crack path for increasing crack widths, the existence or non-existence of a stress singularity at the crack tip, the factors affecting shear transfer across the process zone and the interrelation between the crack width, crack closure forces and aggregate interlocking forces, and the factors determining the direction of crack propagation under mixed mode loading. The need for information on those topical problems has also been identified by other investigators [11-16].

The common practice for evaluating the resistance of concrete structure to dynamic loading is to: a) estimate the transient state of stress due to elasto-dynamic analysis; and to b) evaluate the material resistance using strength properties which are enhanced by strain rate dependent factors. For those modes of concrete failure controlled by yielding of the reinforcement or crushing of

the concrete, common practice provides reliable design information. However, for those failure modes controlled by crack propagation, such as concrete fracture, diagonal tension failure, and splitting failure, and where resistance to fracture is of fundamental importance for computations of energy absorption and energy dissipation, common practice does not yield reliable information. This inadequacy of common practice is due primarily to the fact that dynamic failure of concrete structures involves not instantaneous fracture but a continuous dynamic crack propagation history under dynamic loading. Therefore, reliable dynamic fracture analyses of concrete structures require knowledge of the dynamic fracture properties of the material.

1.2 Objectives

The main goal of this thesis is to advance the understanding of the mathematical modeling of the fracture process zone in concrete and to develop appropriate experimental and numerical procedures to study fracture process zone in concrete.

There are four objectives:

- 1) Develop a moire interferometry test procedure to observe the fracture process zone in concrete and measure

crack opening displacement along this zone.

2) Develop a finite element numerical procedure to establish an analytical model which characterizes the material behavior inside the fracture process zone and to extract the fracture parameters for the model from test data.

3) Using the procedures developed in 1) and 2), identify specimen geometry effect, overall stress state effect, and strain rate effect on the fracture process zone model.

4) Using the knowledge gained in 1), 2), and 3), develop finite element programs which predict static and dynamic crack propagation in concrete structures.

A literature survey on previous fracture mechanics studies of concrete is presented in Chapter 2. Chapter 3 proposes a new concept of fracture mechanics for concrete and similar materials. Chapter 4 and 5 describe the developed experimental techniques and numerical methods, respectively. Chapter 6 reports the results on static fracture of concrete specimens and Chapter 7 reports the results on dynamic fracture of concrete specimens. Chapter 8 is a summary of the work. Chapter 9 gives conclusions. Finally, recommendations for future study are presented in Chapter 10.

CHAPTER TWO

LITERATURE REVIEW ON FRACTURE MECHANICS OF CONCRETE

The Griffith's theory [4] states that unstable crack growth occurs if the energy delivered by the system exceeds the energy necessary to form an additional new crack surface in brittle material. Irwin [16,17] and Orowan [18] modified, independently, Griffith's criterion by incorporating the energy dissipated within the plastic process zone due to plastic deformation during crack propagation in metals. Concrete, like a brittle material, is neither homogeneous nor elastic and thus Griffith's theory may not be applicable to concrete. Whether a possible modification, similar to Irwin's modification to Griffith's theory, for concrete can be made has attracted attentions of many researchers [5,19-28].

Kaplan [5] conducted the first experimental study on the applicability of fracture mechanics to concrete. Flexural beams notched on the tension face and subjected to either three or four point loading were used to determine the crack extension force, G_c . With the assumption of no crack growth before fracture, Kaplan found that G_c was somewhat related to the specimen configuration and dimension and G_c was 12 times as large as that estimated from the surface energy. Kaplan attributed the variance of

G_c to slow crack growth before fracture, and then he concluded that the Griffith's concept of a critical strain energy release rate as a condition for rapid crack propagation was applicable to concrete.

Following Kaplan's work, Glucklich [19] developed the Griffith's theory for concrete in much greater detail. He reasoned that G_c was much larger than the surface energy because fracture of concrete was not limited to the propagation of a single crack. Instead, a multitude of microcracks formed in the highly stressed zone and therefore the true fracture surface area was much greater than the apparent one. He also showed that "high strength" areas in concrete, such as aggregates, act as crack arrestors because they increased the energy demand or diverted the crack under higher energy. Glucklich found that, in tension, the slope of the curve representing the relationship of fracture energy versus crack length increased with crack extension until a critical crack length was reached. At that point, the slope of the energy requirement curve ceased to increase and the crack grew spontaneously. This phenomenon suggests that the microcracking process zone has to be fully developed before unstable crack propagation occurs. For concrete, the final slope may be regarded as a material constant with respect to a specific kind and size of aggregates, mixture

proportion, age and curing conditions.

2.1 Linear Elastic Fracture Mechanics Applied to Concrete

Many attempts have been made to apply linear elastic fracture mechanics (LEFM) to the fracture of concrete in spite of its nonhomogeneity and nonlinearity. However, when the dimensions of the structure exceed the largest irregularities in the material by several orders of magnitude, common practice is to treat this material as homogeneous and isotropic with bulk constants, such as the modulus of elasticity.

The basic concept of LEFM is that the state of stress at crack tip is highly concentrated so that a small crack would greatly reduce the loading capacity of the body. The LEFM derived fracture toughness or critical stress intensity factor, which is assumed to be a material property, is independent of the dimension of the specimen. For concrete, this is not guaranteed to be true because there are many pre-existing defects in concrete before load is applied, and the aggregate bridging effect in fracture process zone violates the postulate that the crack surfaces are traction free. These observations led to the results [20-28] on notch sensitivity or critical length for concrete and specimen size effect for concrete.

2.1.1 Notch Sensitivity

Based on the previous work by Huang [20], Naus and Lott [21], Imbert [22] and Kaplan [5], and their own work, Shah and McGarry [23] concluded that cement paste was a notch sensitive material while both mortar and concrete were relatively notch insensitive at least for notch depth of 25.4 mm (1 inch) for specimen dimension of 304.8 x 76.2 x 12.7 mm (12 x 3 x 0.5 inches). And they also found that the toughness of the concrete increased with increasing aggregate size, and was independent of the size of the cracked body.

The same conclusion was obtained by Gjorve, Sorensen and Arensen [24] who found that the failure loads for their specimens were not consistent with a modulus of rupture based on the net cross section and only be explained by nonlinear effects of the microcracks ahead of the macrocrack. Thus, the crack in a concrete specimen can not be adequately simulated by a saw cut, no matter how sharp it is, due to the lack of aggregate bridging force which acts on the natural crack surfaces.

2.1.2 Size Effect

Another important effect is the specimen size effect. Walsh [25-27] concluded, through his tests, that LEFM is

applicable for large pre-cracked concrete specimens. The minimum depth used for fracture tests of concrete should be 228.6 mm (9 inches) and that a depth of 914.4 mm (36 inches), was needed for LEFM to be applicable. Walsh's findings were also confirmed by later studies [23-24,28]. It has been widely accepted that fracture of plain concrete in tension (or in flexure) is preceded by slow crack growth. Unless the size of the specimen is such that the length of the uncracked ligament is substantially larger than the size of the highly stressed fracture process zone, the specimens are sensitive to the effects of nonlinear deformation in the process zone. However, much of the fracture test specimens reported in the early literature were too small to be valid according to Walsh's criterion.

It might be concluded here that LEFM is almost inapplicable to concrete because of the large specimen size requirement and low notch sensitivity. Hence, nonlinear fracture analysis is necessary.

2.2 Nonlinear Fracture Analysis

2.2.1 J Integral Approach

In response to the above difficulties in applying LEFM, a number of nonlinear fracture criteria have been tried. Mindess et al [29] and Halvorsen [30-31] suggested

that the J integral [32] might be an appropriate fracture criterion for concrete. Carrato [33] showed that the J integral was independent of the notch geometry and that in notched beam tests the notch depth became important only when the maximum aggregate size approached the size of the uncracked ligament. However, all investigators pointed out that the large variability of the J integral values did not justify the adoption of the J integral as a fracture criterion.

Hillerborg [34] indicated that if the crack tip was well defined, it was possible to determine J by the change in the load-deflection curve with crack growth. However, reliable J integral values could not be obtained since the crack tip was never well defined for concrete. He thus concluded that the J integral approach did not offer any advantages with regard to the practical application of fracture mechanics to concrete structures.

2.2.2 R-curve Approach

In a review of the application of fracture mechanics to cement and concrete, Shah [35] suggested that an R-curve [36] analysis might provide a unique fracture mechanics parameter for such systems. Wecharatana and Shah [37] studied the crack growth resistance in mortar, concrete and fiber reinforced concrete. They modified the definition of

G_c , energy release rate, to include both the elastic and the inelastic strain energy absorbed during crack extension. After testing, they concluded that the R-curve could be useful in characterizing the resistance of cementitious materials during slow crack growth provided that the ordinate of the R-curve was modified to include the effect of the process zone on specimen size. In the author's point of view, this statement is very doubtful because the effect of the fracture process zone is of strongly geometrical dependence.

2.2.3 Tied Crack Models

A method for modeling discrete concrete cracking is to represent the large microcracking region or fracture process zone preceding the advancing crack tip by a Dugdale-Barenblatt [38-39] model so that the otherwise nonlinear problem is reduced to a linear elastic problem.

The models proposed by Hillerborg [40] and modified by Modeer [41] and Petersson [42], by Wecharatana and Shah [11], by Visalvanich and Naanman [43], by Ingraffea and Gerstle [14], and by Reinhardt [12], are all variations of the Dugdale-Barenblatt model. For the resultant equilibrium-type cracks, Griffith's criterion is no longer applicable. Therefore, these models differ in three ways:

- 1) in the postulated fracture criterion which replaces the

Griffith's criterion; 2) in their assumptions for determining the crack length and the prescribed crack opening resistance for the fracture process zone; and 3) in the experimental procedures used to determine the crack lengths perceived in concrete fracture specimens.

Hillerborg and his students, Modeer and Petersson, proposed a tied crack model, which was associated with a two dimensional finite element analysis, for fracture of concrete. In that model, it is assumed that the stress does not fall to zero at once as the crack opens, but decreases with increasing crack width. That region of decreasing stress corresponds to a fracture process zone with some remaining ligaments for load transfer. Thus those ligaments absorb energy as the crack grows. Since the fracture zone is still capable of carrying some load, the model is called fictitious crack model (FCM). It is assumed that the constitutive equations of linear elasticity are still valid in the region outside the fracture process zone. Inside the process zone, another constitutive relation, which governs the deformation of the material associated with crack bridging stress, exists. That is the relation between, the closure stress, σ , and the crack opening displacement, w , along the fracture process zone:

$$\sigma = f(w). \quad (2-1)$$

When a very stiff tensile testing machine and small specimens were used, Hillerborg et al. found it was possible to determine the complete tensile stress-strain curve of concrete. Using this curve and through some manipulation, the crack closure stress versus crack opening displacement curve was determined. It is easy to see that the area under the curve of Equation (2-1) is the amount of energy necessary to create a unit area of a traction free crack. It is defined as:

$$G_F = \int_0^{\infty} \sigma(w) dw \quad (2-2)$$

and a standard testing procedure for the determination of this energy value was recommended and discussed [44-47].

Modeer implemented the FCM in a finite element analysis of a three point bend problem. Crack extension was modeled by node separations and a maximum tensile stress criterion was used as a fracture criterion. In order to characterize the brittleness of the materials, a characteristic length, L_{ch} , was defined. That is

$$L_{ch} = G_F E / f_t'^2 \quad (2-3)$$

in which E is the elastic modulus and f_t' is the tensile

strength of the concrete.

It was further found that the ratio of beam depth to characteristic length had to be greater than ten before LEFM was applicable. Petersson analyzed the development of the fracture process zone of concrete using FCM. He concluded that FCM described the crack propagation properties if the nodal distance between the two adjacent nodes along the crack propagation path was less than $0.2 L_{ch}$. Recently, Gustafsson and Hillerborg [48] reported on the application of FCM to the design of concrete pipes and beams.

The models proposed by Visalvanich and Naanman [43], by Ingraffea and Gerstle [14] are essentially the same as FCM except that the former used the model for fiber reinforced concrete while the latter for mixed mode fracture problems. Wecharatana and Shah's [11] approach is slightly different from FCM. They replaced the maximum tensile stress criterion by fitting computational results to the measured crack mouth opening displacement (CMOD), which is not a material constant, at each loading stage. In Reinhardt's model, the crack closure stress is described by a assumed power function without relating the closure stress to opening displacement in the fracture process zone.

Similar work was done by Kobayashi, Hawkins and their colleagues [6-10,49] on Crack-Line Wedge-Loaded Double-Cantilever beam specimens at the University of Washington. Both mode I and mixed mode fracture were investigated. The fracture process zone model developed had three straight line segments and the finite element procedure involved an iteration and a trial and error scheme. For mixed mode study, diagonal compressive load was applied with the wedge load. The test variables included specimen size, aggregate size, concrete strength, and loading history for mode I cracking and concrete strength, aggregate size, diagonal loading force and the ratio of the diagonal force to the wedge force for mixed mode I and II cracking.

Carpinteri and his co-workers [50] numerically analyzed the effect of the parameters involved in FCM. They explored, over a wide range, the influence of elastic modulus, tensile strength, fracture energy, specimen depth and initial crack length. Based on this analysis, they defined a dimensionless number to describe the brittleness of the system in which a straight line $\sigma - w$ relation was assumed and finite element method was employed. This number is

$$S_E = G_F / (f_t' d). \quad (2-4)$$

in which d is the depth of the beam specimen. According to this analysis, Capinteri et al. [51] determined an upper bound of the finite element size of 625 times w_c , the critical crack opening displacement or the maximum crack opening displacement at which stress can be transferred between the two crack faces.

This kind of model was also used by Victor Li and his co-workers at the M.I.T. [52-54] and an indirect crack closure stress versus crack opening displacement determination procedure seems to have been developed. This procedure utilized the crack closure stress and the J integral relation, which was given by Rice [32], and the energy release rate based J integral determination method. Although the former is valid for concrete the latter is still uncertain. Besides this theoretical difficulties, this method is not suitable for concrete because of the inherent material property variation of concrete. Perhaps, this is why only mortar specimens were tested in developing this procedure.

2.2.4 Smeared Crack Band Model

A somewhat different modeling procedure for discrete cracking, which is based on finite element methods, is that developed by Bazant and his co-workers [55-61]. Their approach utilizes a smeared crack concept. Fracture is

related to propagation of a crack band which has a cell width determined by the aggregate size at its front. That band causes a zone of stress relief in the surrounding concrete, which was first recognized by Hawkins et al. [62], as well as at the crack front. To date, this theory is restricted to mode I problems.

Bazant stated that the crack band theory was a fracture theory for a heterogeneous aggregate material, which exhibits a gradual strain softening due to microcracking, and contains aggregate pieces that are not necessarily small compared to the structural dimensions. The crack is modeled as a blunt smeared crack band, which is justified by random cracking in the microstructure. Simple triaxial stress-strain relations, which model the strain-softening effect and describe the gradual microcracking in the crack band, were derived. The stress-strain relation of uniaxial tension had a linear ascending portion as well as a post peak-load descending portion. The shear resistance was assumed to be zero after peak-load, and energy balance was used as a fracture criterion.

Crack initiation in a body without pre-existing cracks and stress concentration, can be prescribed by the tensile strength criterion. Bazant claimed that this criterion cannot be used in the presence of a sharp crack. The

elastic analysis yields an infinite stress at the crack front and the tensile strength criterion will incorrectly predict crack extension at an infinitely small load. When a finite element mesh is refined, the load needed to reach the tensile strength strongly depends on the choice of the element size and incorrectly converges to zero. Thus, the elastic finite element analysis of cracking based on the strength criterion, as currently used in the computer code, is unobjective in that it strongly depends on the analyst's choice of mesh if the specimen has a sharp pre-notch. This difficulty was overcome by fracture mechanics, in which the basic criterion is that of the energy release needed to create the crack surface.

In the finite element programming, it was shown by Bazant and Oh [60] that the compliance matrix is easier to use than the stiffness matrix because it is sufficient to adjust a single diagonal term in the compliance matrix to reduce the stiffness of the material in the fracture process zone. The limiting case of this matrix for complete (continuous) cracking is shown to be identical to the inverse of the well-known stiffness matrix for a perfectly cracked material. Since a straight line was assumed for the descending part of stress-strain curve, the material properties were characterized by only three parameters i.e. the fracture energy, the uniaxial strength

limit and the width of the crack band. The strain-softening modulus was a function of these parameters. A method for determining the fracture energy from the measured complete stress-strain relations was also given and triaxial stress effects on fracture had been accounted for.

This theory was verified by analyzing the numerous experimental data in literature. Satisfactory fits of the maximum load data as well as the resistance curve were achieved and values of the three material parameters involved, namely, the fracture energy, the strength, and the width of crack band front, were determined from test data. The optimum value of the latter width was found to be three aggregate size, which is also justified as the minimum acceptable width for a homogeneous continuum modeling. Finally, a simple formula was derived to predict, from the tensile strength and the aggregate size, the fracture energy as well as the strain softening modulus. A statistical analysis of the errors reveals a drastic improvement compared to the LEFM as well as the strain theory. Bazant then concluded that the applicability of fracture mechanics to concrete is thus solidly established.

In conjunction with the crack band theory, Bazant [63] proposed a size effect law which provided a smooth transition from the tensile strength criterion for small specimens to LEFM criterion for large specimens. This law says:

$$\sigma_N = B f_t' (1 + d/d_0)^{-1/2} \quad (2-5)$$

in which $\sigma_N = P/bd$ is the nominal stress at failure; P is the failure load; b is the thickness; d is the characteristic dimension of the specimen or structure; B and d_0 are empirical constants, d_0 being a certain multiple of the maximum size of the inhomogeneities in the material, d_a . B and the ratio of d_0 to d_a depend only on the geometrical shape of the structure, and not on its size. This law was also used to evaluate parameters in the R-curve approach [61].

Essentially the same models to the Bazant's crack band approach were presented recently by Riot et al. [64,65] and by Borst [66], respectively. The difference is that their models are more general and incorporated allow dissipative bulk behavior and triaxial effects.

Although crack band models have been successfully used to fit some global responses of certain concrete specimens, they lack theoretical foundation. For instance, the equilibrium and compatible conditions can only be satisfied

on average bases, and convergency is still an open question.

2.2.5 Two-Parameter Model

A two-parameter model was proposed by Jenq and Shah [67,68], The first parameter is the critical stress intensity factor and the second parameter is the critical crack tip opening displacement. This model postulates that the maximum load is reached when the crack opening at the initial crack tip reaches its critical value and the crack starts to extend when the critical stress intensity factor is reached at an effective crack tip. The effective crack is defined as an elastically equivalent crack length according to the initial crack opening displacement. This model seems can only be used for bend specimens due to the geometry dependency in determining the parameters.

2.3 Test Methods for Fracture Process Zone Determination

In resent years, a number of experimental studies have been carried out, using a variety of experimental techniques, to measure the extent of the fracture process zone. Although there is a general agreement by now that such a zone exists, there is still no agreement on the extent of this zone: estimates range from several

millimeters to more than half meter. As with other fracture mechanics measurements in cementitious materials, the values obtained seem to depend upon specimen size and geometry and on the technique used to identify the process zone.

2.3.1 Acoustic Emission

Acoustic emission measurements have increasingly been used to detect and monitor the formation and propagation of cracks in concrete. An early review on this topic has been given by Diederichs et al. [69]. The measured extent of fracture process zone appear to depend on the specimen geometry, the type of instrumentation used and the method of analysis.

Maji and Shah conducted a very extensive series of tests to study the formation and propagation of cracks in concrete using this technique [70,71]. They found [71] that, in the initial stages of loading, acoustic signals were emitted at various parts of the specimen. However, most of the signals came from the crack area when the peak load was approached and thereafter. They also found that some acoustic emission events occurred ahead of the crack tip, while others continued to occur behind the crack tip. A 25 mm fracture process zone extending ahead of the visible crack tip was observed in their tests.

Izumi et al. [72], Chhuy et al. [73], and Berthelot [74] have also used acoustic emission to study the fracture process zone and the evolution of damage in concrete. They found that the fracture process zone in concrete was about 100 mm long. However, in earlier work, Chhuy et al. [75] estimated a 500 mm long damage zone ahead of the crack tip.

2.3.2 Replica Technique

Kobayashi et al. [6-9] used a replica technique to estimate the size of the fracture process zone. A replica of the surface of the specimen obtained for determining the extent of cracking by forming a small puddle of methyl acetate on the specimen surface in which a thin sheet of acetycellulose replicating film placed. Methyl acetate is a solvent of acetycellulose. As the solvent slowly evaporates, a replica of the specimen surface is created. The solvent evaporates along the entire crack-line a little faster than where there is no cracking. Any cracking is immediately visible with the naked eye by carefully viewing the reflection of the surface of the smooth replicating film. This technique reveals cracks that are very difficult to almost impossible to see even with the aid of a 10X magnifying glass.

Because this method can only detect surface cracking, the consistency of the cracking through the thickness of the specimen must be checked to validate that the replica measurement is a representation of cracking in the concrete specimens. Sectioned specimens have been found to have the same crack lengths inside and outside the specimen.

2.3.3 Optical Interferometry

The most sensitive and accurate techniques for determining the fracture process zone in concrete are optical interferometry techniques, i.e. holographic interferometry, moire interferometry and speckle interferometry. With speckle interferometry, a sensitive of 1-5 μm can be achieved. With holographic interferometry, the theoretical sensitivity is about 0.5 μm , the wavelength of the light used. And the maximum sensitivity of moire interferometry is about 0.25 μm , one half of the wavelength of the light used.

Maji and Shah [70] used holographic interferometry to study the whole field deformation pattern in real time. They found cracks could be detected as discontinuities in the fringe pattern corresponding to the discontinuities in the displacement field and the progress of the cracking between two stages of loading could be determined by double-exposure holographic interferometry. They also used

speckle interferometry to quantitatively measure the displacement discontinuities at bond cracks at various stages of loading.

Iori et al. [76] used moire interferometry techniques to measure strains and displacements in concrete, with a sensitivity of about 1 μm . Later, Cedolin et al. [77,78] carried out several fracture tests on concrete direct tension specimens aimed at determining the fracture process zone. With this technique, a virtual reference grating of 1000 lines/mm is generated on the surface of the specimen by interference of two laser beams. The same grating is also recorded on a layer of photoresist placed on the specimen surface, so that it will follow the deformation of the specimen, while the virtual reference grating remains undeformed. The light emerging from the deformed grating produces a moire fringe pattern, from which the strain components in the direction normal to the grating lines can be determined.

With their small tension specimens they found that the extent of the fracture zone is large with respect to the dimensions of the concrete specimens and the stress-strain curves obtained with strain gage readings of the deformation represent only an average behavior.

In their later work [78], they found that concrete in tension could reach high level of strain, up to 700 microstrains, before a localized fracture. However, this strain measurement is difficult to define, because the "gage length", which must be smaller than the width of the strain concentration area, is far smaller than the representative length of the heterogenous material, such as concrete.

One drawback of the test technique is that the high density of an optical grating can be obtained only by isolating the testing apparatus from vibrations. This limits the weight and the type of loading device which can be used. Variations of the same technique are less sensitive to these effects, and may be used for specimen of larger dimensions. Another drawback is that the fringe image they photographed is only formed by the scattered light rather than the diffraction beams, which could be used by other arrangements, so that hazy fringe patterns were obtained which was not good for detailed analysis.

2.4 Concrete Members Subjected to Impact Loading

In the area of dynamic fracture of concrete, there is increasing interest in studying the effects of the strain or loading rate on the strength and fracture of concrete.

Most of these studies have been reviewed by Mindess [79], Wittmann [80], Suaris and Shah [81], and Reinhardt [82]. Those studies are in general qualitative agreement in that almost all results show that the apparent strengths of cement, mortar and concrete increase as the rate of loading increases. It is clear that strain rate effects are associated with the phenomenon of subcritical crack growth, and this has led to many attempts to interpret the strain rate effects by fracture mechanics. However, a satisfactory theoretical model for these effects has not been formulated.

2.4.1 Impact Tests

Through direct tension tests under impact loading [83-87], the stress-deformation curves obtained exhibited considerable large strain softening effect and strain rate dependency. Three point bend tests of concrete and mortar beams have also been carried out by Mindess et al. [88,89] and Shah et al. [90-92] using a drop weight machine and a Charpy impact machine, respectively. There were also many compression impact test reported in the literature. The available results indicate that the rate sensitivity of the tensile strength is higher than the compressive strength and that the rate sensitivity of flexural strength is in between that of the tensile strength and the compressive

strength [93,94].

One topic, which commanded a lot of attention, was the inertial effect involved in an impact test [95]. Many efforts have been devoted to reduce this effect such that dynamic test data can be used to evaluate the dynamic strength of concrete by static analysis. Inertial effect, however, is inherent in a dynamic event of material deformation or fracture consisting of major differences between static and dynamic analyses. In reality, the inertial effect of a large mass of concrete considerably increases the impact resistance of the structure. This is due to the fact that a portion of the input energy must transform to kinetic energy, which is directly proportional to the mass, for moving the material, which is necessary for crack formation and propagation. Therefore, the developed theory must incorporate inertial effect rather than avoiding it. In fact, dynamic finite element analysis can handle this problem very easily.

2.4.2 Fracture Mechanics Modeling

The two-parameter approach developed by Jenq and Shah was later extended to model the dynamic flexural tests with modification [96]. One of the parameters, K_{IC} , was assumed to be strain rate invariant while the other parameter, $CTOD_c$, was assumed to decrease exponentially with the

logarithm of the relative strain rate. They claimed that their model predicted values correlated well with the experimentally observed trends in the strain rate effects on mode I fracture of concrete.

Although the Dugdale type model has been successfully applied to static fracture of concrete by many investigators, its dynamic extension was developed for the first time by the author and is one of the subjects of this study.

2.4.3 Damage Mechanics Modeling

Fracture mechanics deals with only a single crack or separated discrete cracks. For concrete fracture, especially under dynamic loading conditions, distributed multiple cracks are also commonly observed, thus leading to the use of damage mechanics [97] in concrete fracture research. Damage mechanics describes the continuous distributed and progressive damage in the material by "internal variables." These internal variables can be scalar, vector or tensor depending on the materials and the loading configurations. The corresponding kinetic equations or evolution equations for these variables are determined from experimental data and the principles of the thermodynamics.

Damage mechanics was first developed by Kachanov [98] for modeling creep rupture of metallic materials. During the last two decades, the basic principles were formulated and some special problems were solved. The simplest damage mechanics model for concrete, as an example, is the scalar damage model developed by Mazars [99], in which only one scalar internal variable is introduced to characterize the stiffness degradation. Chen [100] as well as Surris and Shah [93,94] explicitly included the strain rate effect in their damage mechanics models for studying impact damage of concrete. Although various complicated damage models have been developed, no accepted damage mechanics theory has been established for dynamic fracture of concrete due to the great difficulties involved in both the mathematical formulation and the numerical implementation.

2.4.4 Statistics Modeling

Lacking a physical understanding of damage in concrete, a stochastic model of damage was developed by Mihashi and Izumi [101]. In this theory, it was assumed that the distribution of the local tensile stress depended on the microstructure and was governed by the probability density function of a Gamma distribution. Transition from one state to another was modeled as a Markovian process. The stochastic model seems to be able to explain the

variance of the fracture strength, which is dependent on several factors such as the kind of stress, stress concentration by heterogeneity, loading rate, temperature, and the scaling effects. However, it is a purely stochastic theory that does not attempt to describe the fracture mechanism.

Zech and Wittmann [102] found that this theory could provide a reasonable prediction of the ultimate strength of their impacted mortar beams.

2.5 Discussion and Conclusion

Earlier work has indicated that LEFM is not a appropriate tool for investigating cracking in practical concrete members. In the area of nonlinear analysis, J integral and R-curve approaches are basically used for fracture problems in the presence of a small fracture process zone. One-parameter approaches are generally invalid for concrete due to the large fracture process zone involved.

Also as an nonlinear analysis, the concept of fracture process zone associated with the Dugdale type constitutive modeling has proved most reasonable and most successful. In such modeling, two crack representations, i.e. the tied crack and the smeared crack, and two criteria for crack

propagation, i.e. the tensile strength and the energy release rate, have been introduced. Any combination of these is possible to construct a model.

Finite element methods have played a very important role in putting the above ideas to practice. The computational efficiency is a dominant factor in evaluating these models. For the tied crack model, the crack propagation path must be known prior to the computation. Otherwise, the finite element mesh must be changed as crack tip advances. A change in the mesh requires re-computation of the stiffness matrix and some times another minimization of the matrix band-width. For the smeared crack model, no such computations are needed. The tied crack model can be used in combined opening and shearing mode cracking [9]. Mixed mode cracking, for the smeared crack model is, however, still to be resolved.

An advantage of FCM is that it can be used for both notched and unnotched specimens. For a sharply notched specimen, the tensile strength criterion of FCM makes the finite element computation result prior to the crack extension, unobjective due to the existence of the stress singularity at crack tip. However, once the first pair of nodes are released associated with crack tip advancing, crack closure stress is applied on these nodes so that the singular stress created by the external loads can be

cancelled by the negative singular stress created by the crack closure stress. Therefore, as long as the first element ahead of the notch tip is small enough, the effect of the unobjectivity problem can be reduced to any desired level.

Due to the difficulties [103-107] in conducting direct tension tests, using other specimens may be necessary in certain circumstances. Using the test data from such specimens, a numerically more convenient procedure, which replaces the trial and error inverse routine developed at the University of Washington, must be developed to determine the crack closure stress versus COD relation. A better test procedure must also be developed for studying the fracture process zone in concrete. As mentioned previously, optical interferometric methods are most accurate and accessible. Among the various optical interferometric methods, holographic interferometry requires strict vibration control and in-plane deformation is not easily measured; and speckle interferometry can be used only for small deformation measurement because of a decoding problem involved in this method. Moire interferometry technique has been proved to be the best candidate for this purpose. Finally, the basic theory as well as the related experimental-numerical techniques for dynamic fracture of concrete need also to be developed.

CHAPTER THREE

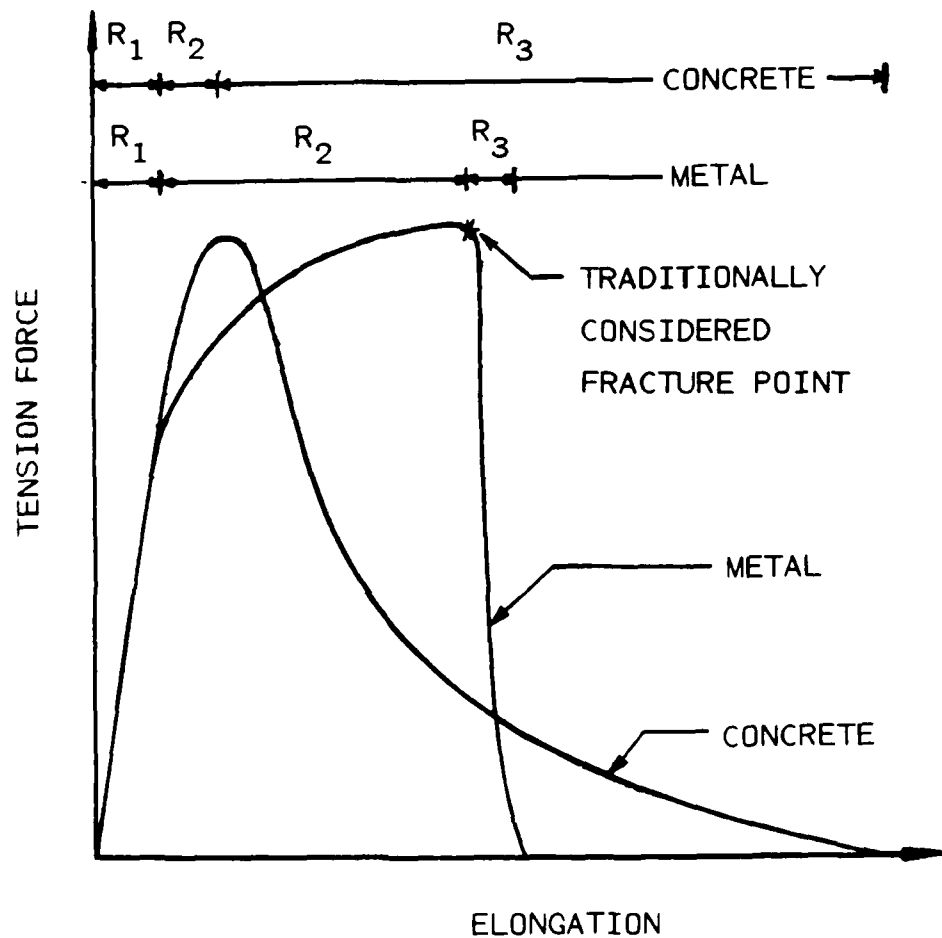
FRACTURE PROCESS ZONE OF CONCRETE

The major goal of this study is to investigate the effect of fracture process zone on concrete fracture. The fracture process zone is being modeled at a macroscopic level. No attempt will be made to study the micro-structure of the fracture process zone. In the following, a physical and a mathematical explanations of the fracture process zone in terms of fracture mechanics is presented.

3.1 General Concept of Fracture Process Zone

3.1.1 Tensile Behaviour of Material Failure

For the most useful engineering material, metal, tensile behavior seems to be a classical and well studied topic since a tension curve can be found in any strength of material text book. In fact, the tension curve is never completed since the tension force (or stress) versus elongation (or strain) relation always terminated at so called "fracture point", as shown in Figure 3.1. The tensile behavior of the material beyond the fracture point is seldom studied. This lack of knowledge is not only due to the difficulties involved in the tension test but also the ignorance of an important fact --- any material must



- R_1 --- LINEAR ELASTIC REGION
 R_2 --- STRAIN HARDENING REGION
 R_3 --- STRAIN SOFTENING REGION

Figure 3.1 Comparison of Tensile Behavior of Metal and Concrete

undergo a process in which the stress carrying ability decreases from certain level to zero. Even in the fracture mechanics books, the post-fracture material behavior is not carefully considered. Generally, for any kind of material, the tension curve can be divided into three regions, as schematically illustrated in Figure 3.1, linear elastic region, strain hardening region, and strain softening region.

For homogeneous materials, such as metals, the strain softening region is so small compared to the strain hardening region, that the traditional fracture mechanics does not need to study the tensile behavior in that region. However, for nonhomogenous materials, such as concrete, the strain softening region is much larger than the strain hardening region. This large size of strain softening region is due to microcrack coalescing and aggregate bridging in the materials.

3.1.2 Definition of fracture Process Zone

As a matter of fact, fracture is not a state but a process which occurs between two different states. One state is associated with perfect connection and the other associated with completely separation of the material. Thus, there must be an infinite number of intermediate states associated with the partial connection. The

material which is undergoing this process constitutes the fracture process zone.

In this dissertation, the fracture process zone is defined as the region in which the tensile stress in the material is decreasing from its maximum value to zero when displacement controlled loads are applied.

On the other hand, fracture process zone can be defined as the region of discontinuous microcracking ahead of the continuous crack or as the partially damaged area with some remaining stress transfer ability. Since in this study, with only the mathematical models on macro-level is concerned, the physical phenomena on either micro-level or meso-level will not be studied.

3.1.3 The Role of Fracture Process Zone in Fracture

The material within the fracture process zone provides a monotonically decreasing resistance to fracture with fracture in progress. It is an energy absorber which makes the material tougher or less brittle. The energy dissipated to overcome the resistance is called work of fracture, or customarily the fracture energy. Although for some material, such as glass, the fracture energy is mainly the surface energy, for most other materials the surface energy is much smaller than the energy which is absorbed in the fracture process zone. For instance, the

surface energy is negligible compared to the energy required for plastic deformation in metals or the energy required to create microcracking and to overcome aggregate bridging in cementitious materials.

3.2 Fracture Process Zone in Concrete

3.2.1 Observed Fracture Process Zone in Concrete

Fracture process zone in concrete was first measured by Heilmann et al [107], using strain gages. A strain value which is much larger than the maximum tensile strain of the material was measured in a small region of a direct tension specimens. As the strains in other regions decrease beyond the peak load, the strains in this small region still increase. The strain softening behavior, i.e. the smaller the load the larger the strain was clearly observed in that small region. Despite of the fact that the strain gages gave only the average strain over its gage length, this observation still proved the existence of fracture process zone.

The fracture process zone were also revealed by many test method. Using Scanning Electron Microscopy technique, Dimond and Bentur [108] found that a system of very fine multiple cracks appear in the vicinity of the crack. They reported: "While the subdivision and branching seen to

occur near the tip zone in the concretes examined, is in some respects reminiscent of what is expected in a 'process zone', there is no physical distinction corresponding to separate lengths of 'straight, open crack' behind a crack tip and 'process zone microcracking' ahead of a crack tip." Also using in-situ SEM observations, Tait and Garret [109] did find a process zone of microcracking in the vicinity of the crack tip of mortar or cement paste specimen.

3.2.2 Features of Fracture Process Zone in Concrete

Concrete is a heterogeneous material and its fracture mechanism is much more complicated than that of homogeneous materials. Despite its microscopic mechanism, the whole fracture process can be divided into three subprocesses: microcracking process, transition process, and aggregate bridging process, as shown in Figure 3.2.

When a crack is extending in a concrete member, a portion of the process zone adjacent to the microcrack tip is in the microcracking process, while another portion of the process zone closest to the crack mouth is in an aggregate bridging process. The former is referred to the microcracking zone, the latter the aggregate bridging zone, and the middle portion the transition zone. As shown in Figure 3.2, the transition zone can be recognized by a relatively sharp drop of stress along the crack even though

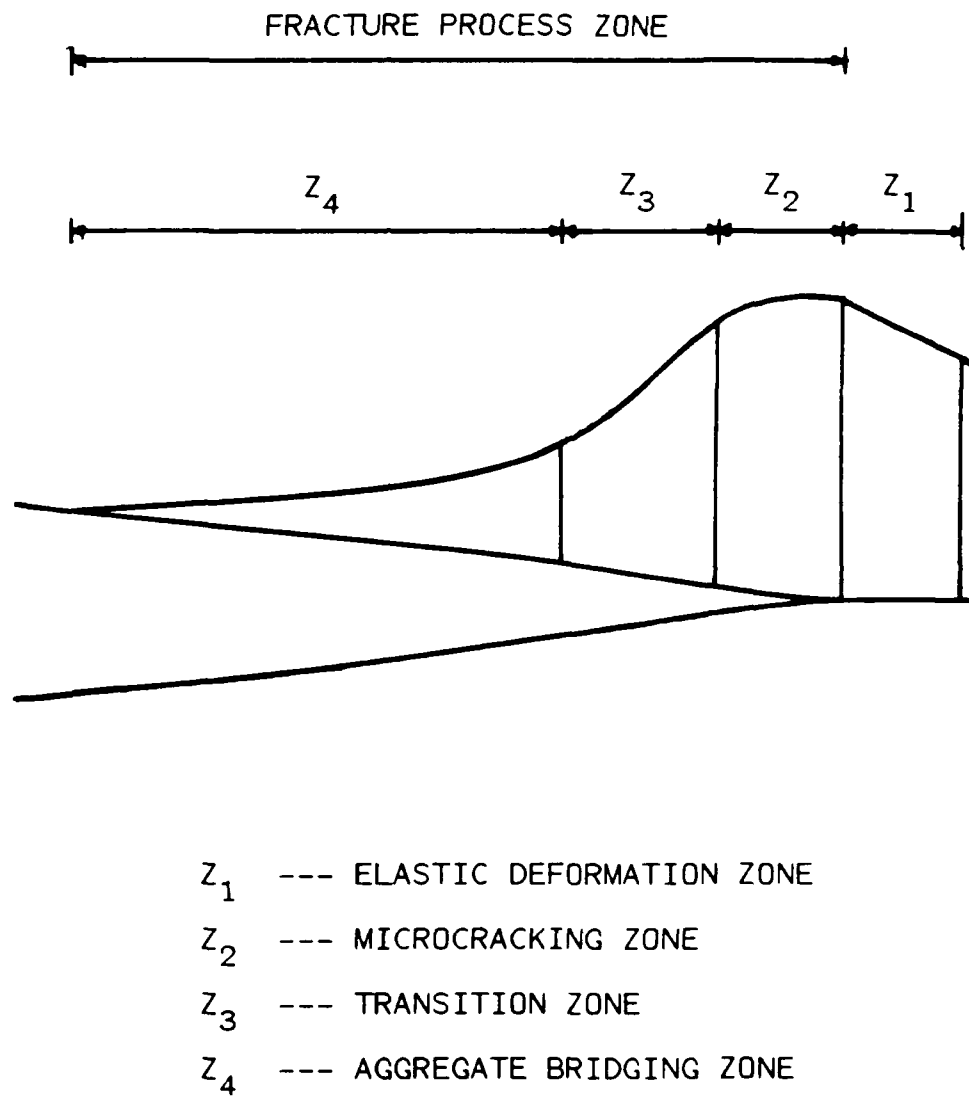


Figure 3.2 Normal Stress Distribution Around Fracture Process Zone

the boundaries are not well defined:

Another important feature of the fracture process zone for concrete is the large size of that zone which brought about new research topics to traditional fracture mechanics. It is easy to see from Figure 3.1, that concrete has a much different tension curve than metals. Its strain hardening zone is very small but its strain softening zone is very large. For metals, only the strain hardening zone is of major concern in fracture mechanics because it is much larger than the softening part. Logically, for concrete the strain softening zone ought to be of major concern.

3.2.3 Significance of Fracture Process Zone in Concrete

For those materials having small fracture process zone (relative to the specimen size), the fracture resistance stress is highly concentrated in that small region so that it can be treated as a concentrate force. In this situation, a single parameter, such as K_{Ic} , G_{Ic} , and J_{Ic} , can be used to represent the magnitude of the fracture resistance of the material.

In contrast, concrete and also other cementitious materials usually have large fracture process zone (of the same order of the specimen size), the fracture resistance stress is distributed along the process zone and can no

longer be treated as a concentrate force. Obviously, a single parameter model is not applicable. Moreover, the distribution of the crack opening resistance stress is specimen geometry and loading configuration dependent rather than a material property.

An appropriate representation of the fracture resistance of this kind of materials and the theory which is able to predict both magnitude and distribution of resistance stress along the fracture process zone in any circumstances must be developed. This is the aim of this study.

3.3 Method of Approach

3.3.1 Scope of Research

The structure of concrete has been subdivided into three different levels [110]: micro, meso and macro. The models on the different levels are interrelated in a systematic way, or more precisely, models on a given level are based on the results of the previous level.

At the micro-level, the structure of hardened cement paste is treated. At the meso-level, the main characteristics are big pores, pre-existing cracks and inclusions. And at the macro-level, concrete is treated as a continuum and homogeneous medium.

This study investigates and models the fracture of concrete material only at the macro-level.

For simplicity, the strain hardening effect is not considered since the strain hardening region is much smaller than the strain softening region in concrete.

Finally, only Mode I fracture is studied in this dissertation.

3.3.1 Mathematical Representation - Assumptions

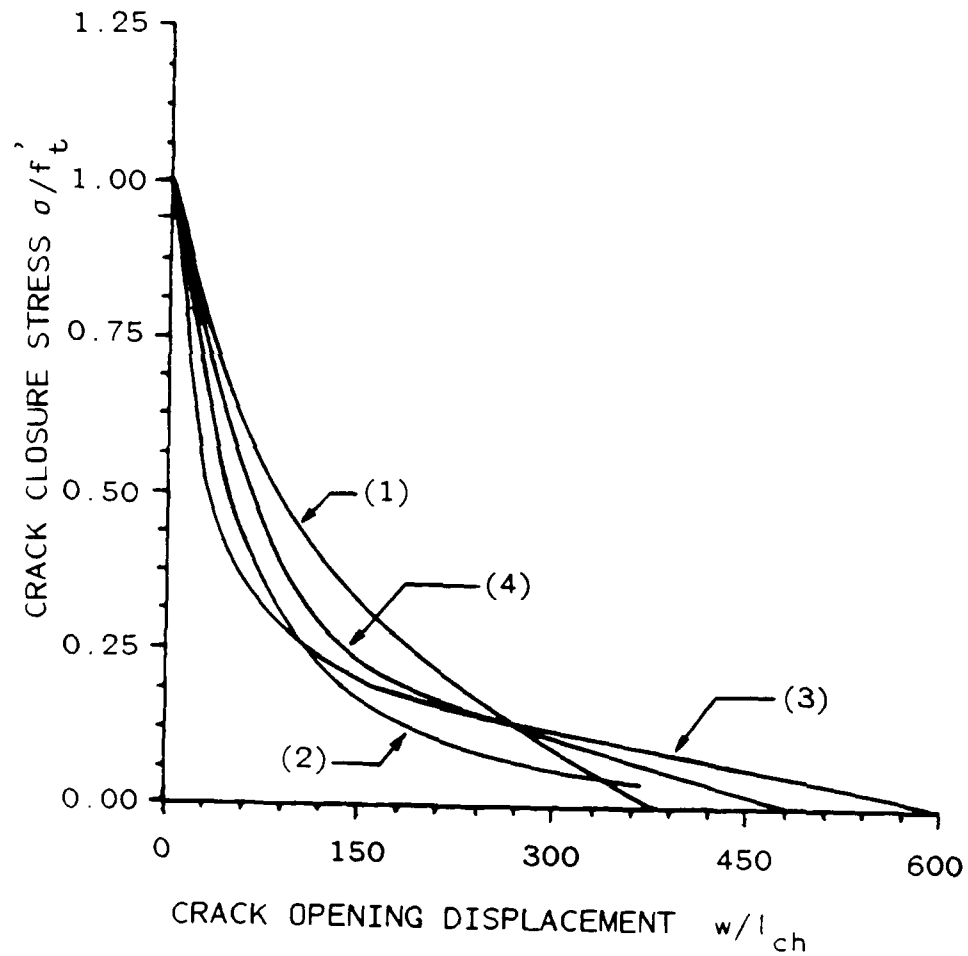
Figure 3.3 shows the published direct tension test results. These results suggest that a strain softening representation should be included in the mathematical model.

Three following basic assumptions are made to construct a mathematical model for the tensile fracture behavior of concrete:

- 1) The fracture process zone is represented by a crack or a material discontinuity along a line with a closure stress acting on the opposing crack surfaces.

- 2) The material outside the fracture process zone is linearly elastic, homogeneous, and isotropic such that the classical elasticity theory can be applied.

- 3) Inside the fracture process zone, the closure stress is uniquely related to the crack opening displacement by a non-increasing function of



- (1) Evans, R. H. [103]
- (2) Petersson, P. E. [42]
- (3) Reinhardt, H. W. [12]
- (4) Gopalarathan, V. S. and Shah, S. P. [104]

Figure 3.3 Published Direct Tension Test Results

$$\sigma = f(w) \quad (3-1)$$

in which, σ is the closure stress and w is the crack opening displacement at the same position.

These basic assumptions will be justified by a series of experimental and numerical investigations in the subsequent chapters.

3.3.3 Hybrid Experimental - Numerical Approach

Following the hybrid experimental - numerical technique by Kobayashi [111,112], this research consists of two components. First, the laboratory tests are conducted on concrete CLWL-DCB and three point bend specimens in order to physically observe and measure the fracture process zone and the deformation of the specimens. Second, the test data are used as input to the finite element analysis for determining the fracture parameters involved in the fracture process zone model. The experimental method used in this study is moire interferometry. The numerical method is finite element analysis.

This investigation uses a two phase analyses [111], the generation phase and the application phase. In the generation phase, test data are used, through finite element analysis, to generate the fracture parameter, which, in this case, is the crack closure stress versus

crack opening displacement relation. In the application phase, the fracture parameter is used as input to the finite element analysis to predict the test results, which is the crack propagation, COD, and all other specimen behaviors.

CHAPTER FOUR

EXPERIMENTAL APPROACH

Experimental observation and measurements are essential sources of information for a correct development of the mathematical models of real materials. In this chapter, a series of fracture tests of concrete specimens are reported and a moire interferometry technique applied to concrete fracture process zone measurement is presented.

4.1 Test Program

4.1.1 Objectives of the Experiments

In general, the objectives of the tests are to physically observe the fracture process zone, to measure its size and the crack opening displacement along its extent, as well as the specimen response to the external load. A replica film technique was used for detecting the microcracking zone on the concrete specimen surface. However, the use of the replica film technique can only provide the information of crack length, and not the crack opening displacement. Two clip-on gages (clip shape extensometer) were used to measure the crack openings at two locations, one was near the prenotch mouth, the other was close to the prenotch tip. The former measured the

crack mouth opening displacement called $2V_1$, the latter measured the crack tip opening displacement called $2V_2$. Both crack opening displacement measurements are on the prenotch. It is not possible to mount any mechanical or electrical displacement transducer into the fracture process zone region since the crack extension path is unknown, and it is never straight. Apparently, the information obtained in this stage did not include the width of the fracture process zone nor the crack opening along the process zone. The resultant theoretical model thus was only relaying integrated and smeared information of the process zone.

An advanced test method must be developed for furthering the physical knowledge and also for improving the theoretical model. The best candidate chosen is the moire interferometry method since it provides a full - field information. Moire interferometry is a new displacement measuring technique which combines moire effect with holographic interferometry. To develop a application procedure for fracture of concrete research will solve the above problems.

4.1.2 Test Groups and Test Variables

Five groups of specimens were tested using moire interferometry. Three of them are CLWL-DCB specimens with

different sizes and different materials. The other two groups are three point bend specimens of different sizes and materials. The specimen dimensions are shown in Figures 4.1 and 4.2.

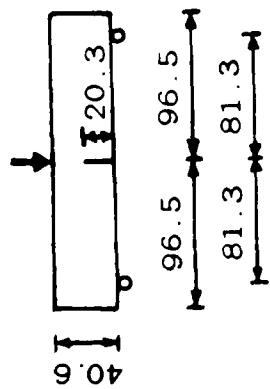
The first group of investigation used small scale three point bend specimens, as shown in Figure 4.1 (a), because this is an exploratory and equipment limited investigation.

In the second group an attempt was made to apply moire interferometry method to the previously used CLWL-DCB specimens [9], as shown in Figure 4.1 (b).

The third group had the same purpose as the second group but used different material to check the aggregate size dependency of the developed model. Specimens of the same size and geometry as the third group were used.

The fourth group was used to generate fully developed fracture process zone in the smaller CLWL-DCB specimens, shown in Figure 4.2 (a). Fully developed fracture process zone could not be obtained in 102 mm x 102 mm (4 in. x 4 in.) area of these specimens.

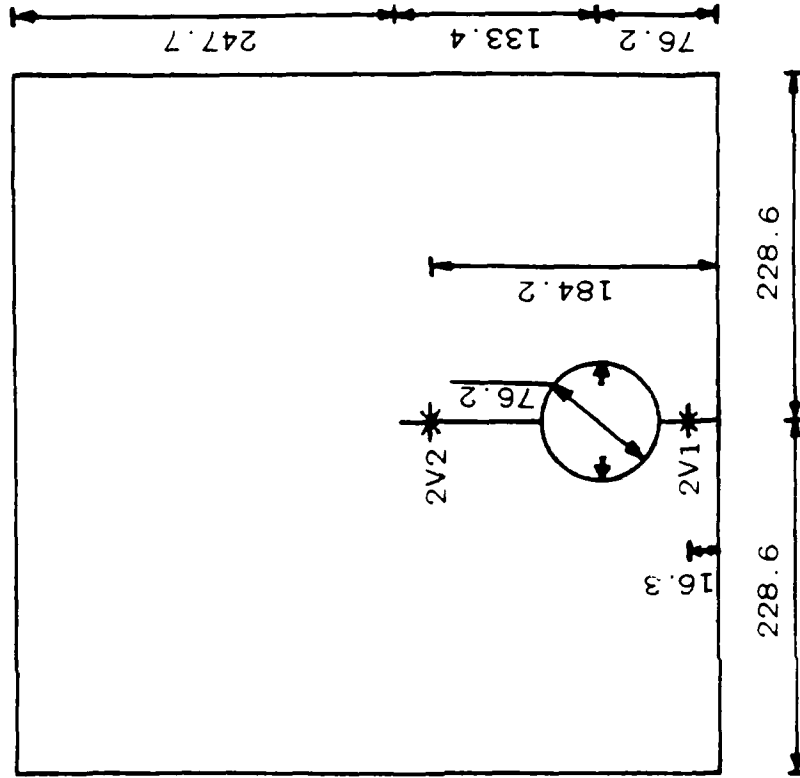
The fifth group specimens were similar in size, and the same material as the fourth group, but different geometry, as shown in Figure 4.2 (b), to check the geometry effect on the fracture process zone model.



(a) SMALL BEAM

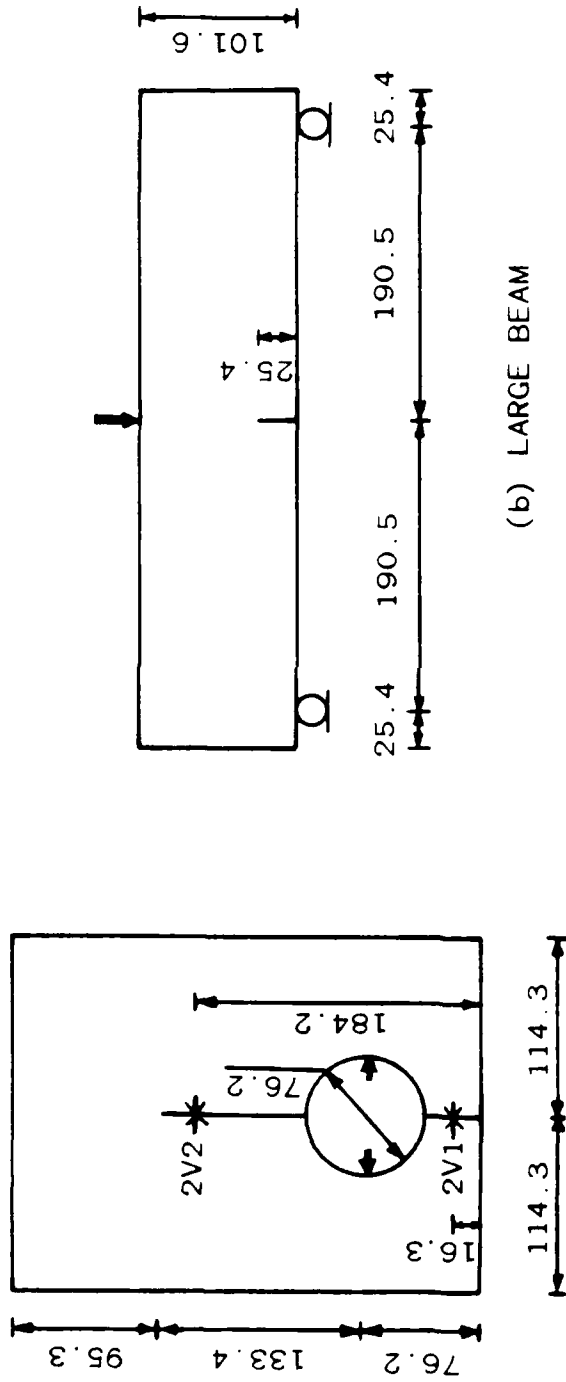
UNIT: mm

THICKNESS = 50.8 mm



(b) LARGE CLWL-DCB

Figure 4.1 Small Beam and Large CLWL-DCB Specimens
(a) Group 1, (b) Group 2,3



(a) SMALL CLWL-DCB

UNIT: mm THICKNESS = 50.8 mm

Figure 4.2 Specimens of Appropriate Sizes
(a) Group 4, (b) Group 5

4.1.3 Loading and Data Recording Devices

Three different loading devices were used in this investigation. A small screw drive loading fixture was used for the first group. This fixture is made of C-channel steel. It is much more rigid than the small concrete three point bend specimens so that a displacement controlled loading condition was achieved. Starting from the second group, larger specimens were tested. To accomodate large specimens, a testing machine was needed. Only a simple shop press was available when Groups 2 - 4 tests were conducted. Fortunately, these CLWL-DCB specimens were inherently rigid, and thus stable crack growth was obtained with this simple machine in Groups 2 - 4. The previously developed wedge load assembly and the adjustable specimen holder, shown in Figure 4.3, were mounted on this shop press. And the wedge load was applied manually. The shop press was not suitable for these three point bend specimens of fifth group because these specimens were less rigid than double cantilever beam specimens. The third machine is a screw-drive universal testing machine which induced stable crack growth in these three point bend specimens.

In the CLWL-DCB specimen testing, an HP computer was used to record the wedge load and the crack opening displacements $2V_1$ and $2V_2$. For these three point bend

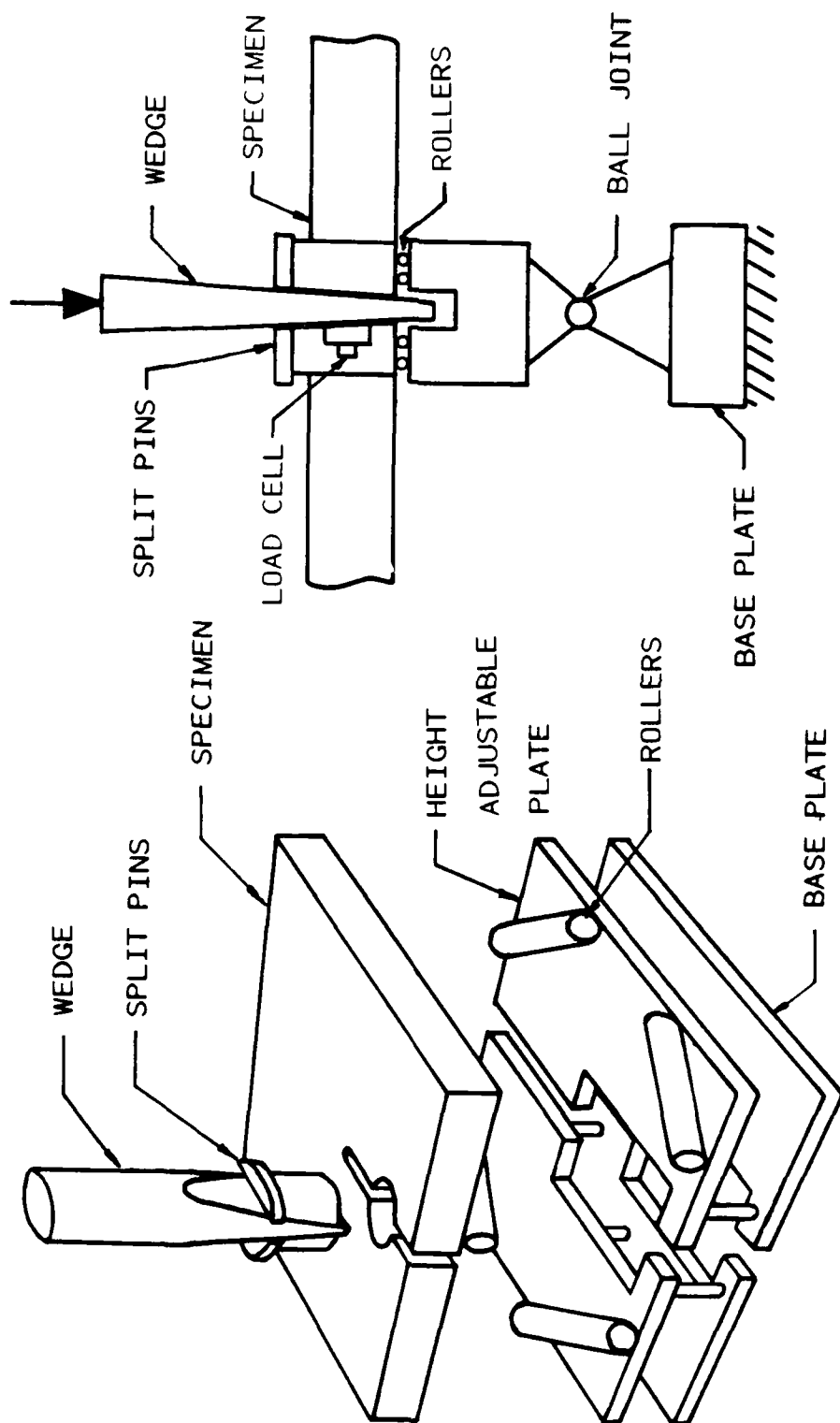


Figure 4.3 Wedge Load and Specimen Holding Assembly
For CLWL-DCB Specimen Tests Group 2,3,4

specimen tests, the load and the load point deflection were recorded manually.

4.2 Specimen Preparation

4.2.1 Fabrication of Specimens

Sand, aggregate, and portland cement were all purchased from local commercial sources and then stored in plastic bags within metal drums in the laboratory. The cement was a type III, high early strength portland cement. The sand and aggregate were carefully sieved and then recombined to provide the gradations shown in Table 4.1. The mix proportions for each test group are shown in Table 4.2.

Table 4.1 Aggregate Gradation (Cumulative Percent Retained)

| Gravel | | | | |
|-----------|---------|---------|---------|-------|
| Group | 12.7 mm | 9.53 mm | 6.35 mm | No. 8 |
| 1, 2, 4-5 | 0 | 0 | 0 | 100 |
| 3 | 0 | 30 | 90 | 100 |

Sand
(For All Groups)

| | |
|---------------|-------------------------|
| No. 4 -- 1 | No. 8 -- 12 |
| No. 16 -- 29 | No. 30 -- 50 |
| No. 50 -- 100 | No. 100 -- 96 |
| Pan -- 100 | Fineness Modulus = 2.61 |

Table 4.2 Concrete Mix Proportion by Weight

| Group | Cement | Sand | Gravel | Water |
|-------|--------|------|--------|-------|
| 1 | 1.00 | 1.83 | 0.94 | 0.36 |
| 2 | 1.00 | 3.70 | 3.16 | 0.71 |
| 3 | 1.00 | 3.70 | 3.13 | 0.72 |
| 4 | 1.00 | 3.42 | 2.88 | 0.58 |
| 5 | 1.00 | 3.42 | 2.88 | 0.58 |

All specimens and their companion 152.4 x 304.8 mm (6 x 12 in.) cylinders were cast in steel molds and cured in the same manner following the same procedure of the previous work [9], which is also given in Appendix A.

The average cylinder compressive strength and the average age of the specimens for each group except for the first group at the time of testing are listed in Table 4.3. The age of the first group is unknown because these specimens were made by cutting the previously cast concrete plates at the age of about two years.

Table 4.3 Test Groups

| Group | No. of Specimens | Specimen Type | Max. Aggr. Size mm | Compre. Strength psi | Strength MPa | Age day |
|-------|------------------|---------------|--------------------|----------------------|--------------|---------|
| 1 | 5 | Beam | 6.35 | N/A | N/A | N/A |
| 2 | 2 | CLWL-DCB | 6.35 | 4320 | 29.8 | 41 |
| 3 | 3 | CLWI-DCB | 9.53 | 4480 | 30.9 | 52 |
| 4 | 5 | CLWL-DCB | 6.35 | 5142 | 35.4 | 64 |
| 5 | 5 | Beam | 6.35 | 5142 | 35.4 | 89 |

4.2.2 Material Properties Determination

Compressive strength was measured using cylinders which were cast with the specimens of each group. The rough end of each cylinder was capped with waterstone, and pressed in a 1335 kN (300 kip) hydraulic testing machine. The load was applied at a constant rate of 241 kPa/sec

(35 psi/sec). The average of measured value from five cylinders of each cast batch of concrete was taken as the material strength. The modulus of elasticity, E , and the tensile strength f'_t was measured using 50.8 x 50.8 x 203.2 mm (2 x 2 x 8 in.) rectangular specimens. These specimens were cut from broken CLWL-DCB and three point bend specimens by a water cooled saw machine after these specimens had been tested to failure. The ends of the specimens then were glued with concrete epoxy to steel blocks which in turn were connected to screw bars. The other two sawed surfaces of the specimens were sanded and cleaned and concrete strain gages of 50.8 mm (2 in.) gage length were applied. After the epoxy was cured, the specimens were mounted on a testing machine by connecting universal joints to the screw bars. The loading speeds were controlled at the same rate as that in the CLWL-DCB or the beam tests. The load was applied three times to approximately 30 % of the maximum load and the average slope was used to evaluate tangential stiffness of the specimen. The modulus of elasticity and tensile strength were then calculated from the average of the recorded data of two identical specimens for each batch. These results are listed in Table 4.4.

Table 4.4 Tensile Strength and Elastic Modulus

| Group | No. of Specimens | Tensile Strength psi | Tensile Strength MPa | Elastic Modulus ksi | Elastic Modulus GPa | Age day |
|-------|------------------|-------------------------|-------------------------|------------------------|------------------------|------------|
| 1 | 2 | 550 | 3.79 | 4500 | 31.0 | N/A |
| 2 | 2 | 471 | 3.25 | 4900 | 3.38 | 151 |
| 3 | 2 | 397 | 2.74 | 3890 | 2.68 | 152 |
| 4,5 | 2 | 500 | 3.45 | 4300 | 2.96 | 124 |

4.2.3 Specimen Surface Treatment for Moire Testing

For moire interferometry testing, a optical diffraction grating frequency must be replicated on to the observation area of the specimen surface. The diffraction grating used in this study has 600 lines per millimeter and can only be transferred to a very flat and smooth surface. One side of each specimen requires be carefully polished with a carborundum stone when the concrete is still young but strong enough that the polishing did not dislodge the sand particles. Generally sufficient strength for polishing was reached within three days of curing. Unlike using replica film, the specimen surface flatness is more important than the smoothness because the optical grating is on a optically flat glass plate.

4.3 Moire Interferometry Test Method

4.3.1 Introduction to Moire Interferometry Method

The fracture process zone in concrete is difficult to determine experimentally, since the resulting deformation is strongly localized and can not be measured adequately by strain gages which provide only the average strain values over the gage length. The sensitivity of the conventional moire technique, on the other hand, is not adequate for measuring the small tensile deformation in concrete prior to its failure. The solution is to use moire interferometry.

Moire interferometry is a full-field method of measuring deformations of the surface of the specimen. The result of a moire experiment is a fringe pattern, which is a contour map of in-plane displacements in the direction perpendicular to the lines of the diffraction grating replicated on the specimen surface.

There are various methods for moire interferometry. As mentioned in Chapter 2, the method Cedolin et al. [77] used can only photograph images by collecting the scattered light coming from the specimen grating so that the resultant fringe patterns were not distinct. In order to overcome this difficulty, a different method which was

originally proposed by Post [113] was used in this study..

Post's moire interferometry is based on the interference of two symmetrically diffracted beams of light. These beams are the first diffraction orders of two mutually coherent, collimated beams of light that are used to illuminate a specimen grating. Their interference creates a fringe pattern. Figure 4.4 shows the basic configuration of an optical system in which monochromatic laser light is used. The mutual coherence of beams A and B is achieved by a beamsplitter, or a plane mirror placed near the specimen grating.

Two basic equations in optics are involved: first is the interference of two intersecting beams, and second is the diffraction of a beam on an optical grating. These equations are:

$$f = (2/\lambda) \sin\phi \quad (4-1)$$

and

$$\sin\theta_m = \lambda Fm + \sin\gamma, \quad (4-2)$$

respectively, where:

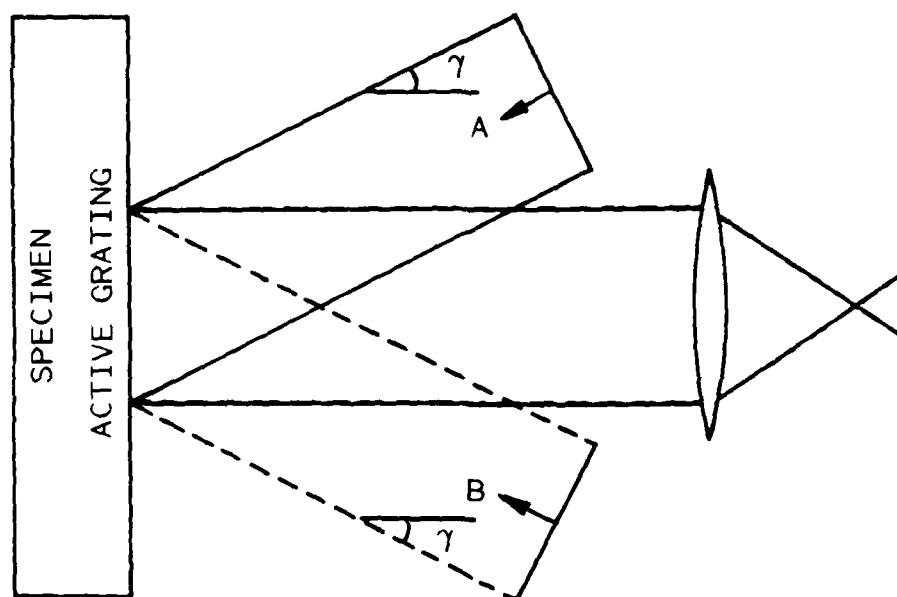
f : frequency of the interference fringes

λ : wavelength of the light

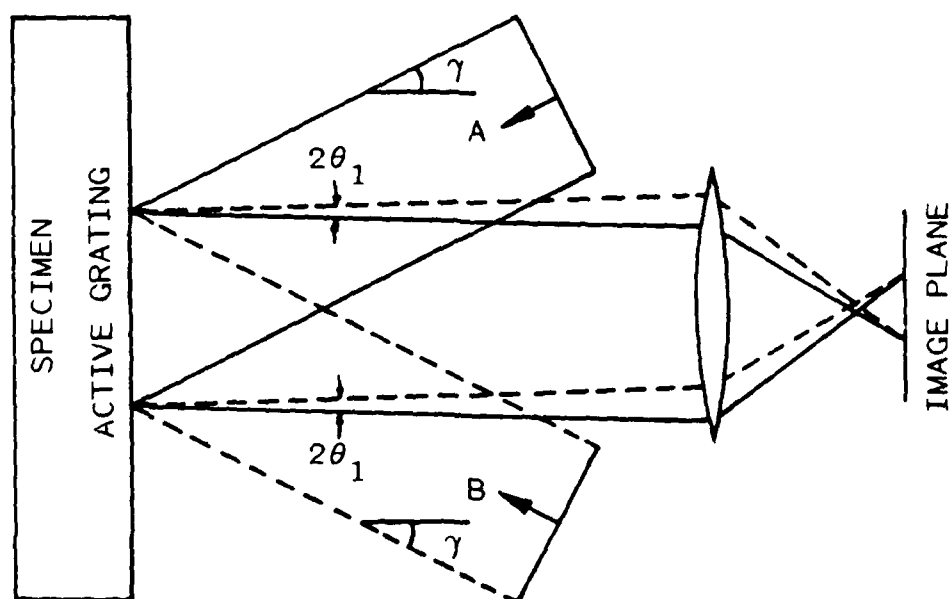
ϕ : half mutual angle of the two beams

F : frequency of the optical grating

m : order of diffraction



(a) SPECIMEN UNDEFORMED



(b) SPECIMEN DEFORMED

Figure 4.4 Principle of Moiré Interferometry

θ_m : angle of the diffraction beam of order m

γ : angle of incident beam to the grating

as shown in Figure 4.4.

The specimen gratings used in this study were made by holographically recording interference pattern of two monochronic coherent laser beams. The half mutual angle ϕ was determined by Equation (4-1) for the required frequency, then, transferred to specimen surfaces so that the deformation of the specimen was identical to the deformation of the grating. Whenever the grating deformed, the frequency of the grating changed.

As shown in Figure 4.4, the incident angles for beam A and beam B are chosen in such a way that the plus first order diffraction of one beam and minus first order diffraction of the other beam are in the specimen grating normal direction. These incident angles can be determined by Equation (4-2) as

$$\gamma = \mp \arcsin(f_s \lambda), \quad \text{when } m = \pm 1 \quad (4-3)$$

or

$$f_s = \mp (1/\lambda) \sin \gamma, \quad \text{when } m = \pm 1 \quad (4-4)$$

where, f_s represents the frequency of the specimen grating.

These two diffraction beams also create a interference fringe pattern on the specimen grating plane as well as in the surrounding space. This is called "virtual grating"

because it is analogous to the reference grating in geometrical moire and it is not real. Comparing (4-4) and (4-1), it is easy to see that the interference fringe pattern produced by these two diffraction beams has twice frequency of the specimen grating has. This is the difference between moire interferometry and geometrical moire.

When the specimen grating deforms, as shown in Figure 4.4, the two first order diffraction beams become slightly offset to the normal of the specimen grating. Using Equation (4-2), replacing F by $f_s/(1+\epsilon)$ and eliminating γ by (4-3), one obtains

$$\sin\theta_1 = \pm f_s \lambda \epsilon, \quad \text{when } m = \mp 1. \quad (4-5)$$

According to Equation (4-1), the frequency of the interference fringes of these two diffraction beams is

$$f_\epsilon = 2f_s \epsilon. \quad (4-6)$$

Since $2f_s$ equals the virtual grating frequency f_v , the resultant fringe gradient is proportional to the virtual grating frequency and strain.

After integration, Equation (4-6) becomes

$$U = N / f_v \quad (4-7)$$

where, U is the displacement component in the direction

perpendicular to the lines of specimen grating. We might note that this governing equation is common for geometrical moire and moire interferometry, though the two differ in the optical principles from which they were generated.

4.3.2 Moire interferometry with real reference grating

Moire interferometry measures small displacement by comparing the phases of light waves. Any distance change of a fraction of the light wave length in the optical path before the interference pattern is formed can blur the whole fringe pattern. Usually, all the optical devices, the test specimen and the loading fixture must be fixed on an isolation bench to prevent them from any vibration. Such an arrangement requires that the test be conducted in special equipped laboratory and the specimen as well as the loading fixture must be small.

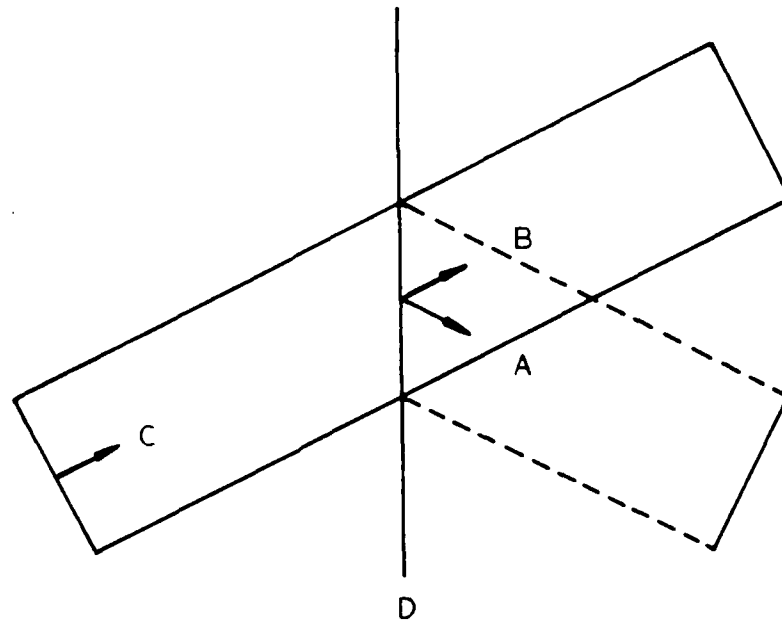
Traditionally, moire interferometry test is only conducted on small specimens made of materials of small grain size, such as metals or polymers. For concrete, however, large size specimens must be used because of the large aggregate size and big strong loading fixtures must be used for big specimens to which the displacement controlled load must be applied. The loading fixtures for concrete testing usually are standard universal testing

machines, which are too heavy to be mounted on any vibration isolation bench.

This problem is solved by using a real reference grating, which is mounted directly on the specimen or on the testing machine, to create these two incident beams. As shown in Figure 4.5, the zero's order and first order diffraction beams of the beam C can be used as the incident beam A and beam B for the moire interferometry optical system of Figure 4.4. According to Equation (4-2), the emergence angle of the first order diffraction is the same as the incident angle of the input beam when the frequency of the grating is the same as that of the virtual grating. Therefore, if the incident angle of beam C is chosen as the same as the angle of the beam A or B, the same virtual grating is created around the specimen grating.

Because the real reference grating can only move with the specimen or the testing machine, the distance of the optical path is kept constant in any vibration event. The vibration sensitivity of the moire interferometry system is significantly reduced and an off-bench test becomes possible.

Real reference grating method was used in all the tests conducted in this study. The stable fringe patterns obtained have shown that with real reference grating isolation benches are no longer needed and large specimens



- A --- INCIDENT LASER BEAM
- B --- ZERO'S ORDER DIFFRACTION BEAM
- C --- FIRST ORDER DIFFRACTION BEAM
- D --- REAL REFERENCE GRATING

Figure 4.5 Generation of Virtual Grating with Real Reference Grating

can be tested by moire interferometry technique even outside the optical laboratory.

4.3.3 Moire Interferometry With White Light

Due to the high cost of laser, monochronical light source is not always available. In the first test group of this study, a white light moire set-up constructed by Kang [114] was used. The principle of white light moire is the same as the laser moire with real reference grating except that another optical grating called compensator is added to the system to direct the incident beams of different wavelength in correct angles, as shown in Figure 4.6.

From diffraction Equation (4-2), when the incident angle is zero, the emergence angle of the first order diffraction θ_1 is

$$\theta_1 = - \arcsin (F_c \lambda) \quad (4-8)$$

where, F_c is the frequency of the compensator. Comparing (4-8) and (4-3), it is obvious that correct incident angles for all the wavelength can be achieved by letting F_c equal to f_s , which is the frequency of the specimen grating.

Furthermore, since the resulting fringe pattern is independent of wavelength (4-7), the fringe pattern produced by the light of each wavelength is identical and superimposed on each other.

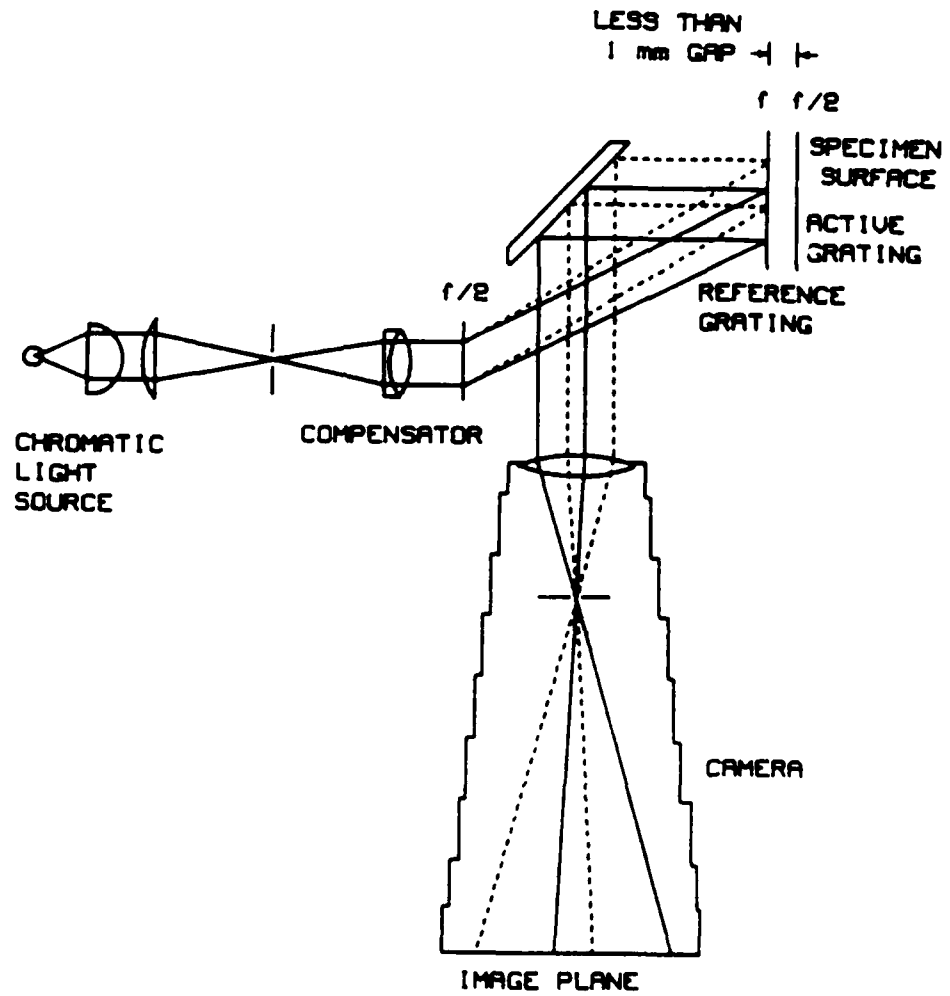


Figure 4.6 Optical Set-Up for White Light Moire Interferometry ($f=1200$ lines/mm)

4.4 Optical Instrumentation and Test Procedures

4.4.1 White Light Moire Set-Up

The optical arrangement of white light moire interferometry is depicted in Figure 4.6. Here a mercury light source is used in order to obtain higher light intensity with smaller light source size. This is important because the short coherence length problem of white light source is compounded with a spatial coherence problem. Each point in the finite light source generates its own moire fringe pattern and all of these patterns will be superimposed to form a blurred picture. Also the gap between the real reference grating and the active grating must be smaller than 1 mm to cope with the finite size of the light source although it is smaller than 0.1 mm.

As shown schematically in Figure 4.6, the light from the mercury lamp, which passes through a condenser assembly, forms a collimated light beam. This light beam then passes through the compensator grating with a wave front of the diffraction order one. Although the zero's order diffraction energy is wasted, about half of the total energy is still taken with the first diffraction by having chosen the first order preferred unsymmetrically ruled grating as the compensator. The same consideration have

also been given to the design of the real reference grating to make the intensities of the first order and zero's order diffraction beams approximately equal.

Because of the extremely short coherence length of the white light, less than 1 mm, a very careful alignment must be done before moire fringe pattern can be obtained. Thus, the light source, the compensator grating and the real reference grating all require provisions for minute adjustments. Customer made stagings, using many micrometers, have met this requirement.

The final image of the moire fringe pattern is recorded by a 35 mm camera which is operated either manually or automatically. Black and white ASA 400 films are used as recording medium and a zoom lens is used to obtain the desired image size on the film plane.

4.4.2 Laser Moire Set-up

The optical arrangement of the laser moire interferometry tests are given in Figure 4.7. A 5 watt water-cool argon laser was used as the light source. The real reference grating and specimen gratings were also made with this laser on an isolation bench.

The output laser light beam of intensity about 100 mw is expanded after "cleaned" by a spatial filter and then collimated by a 152.4 mm (6 in.) diameter parabolic mirror

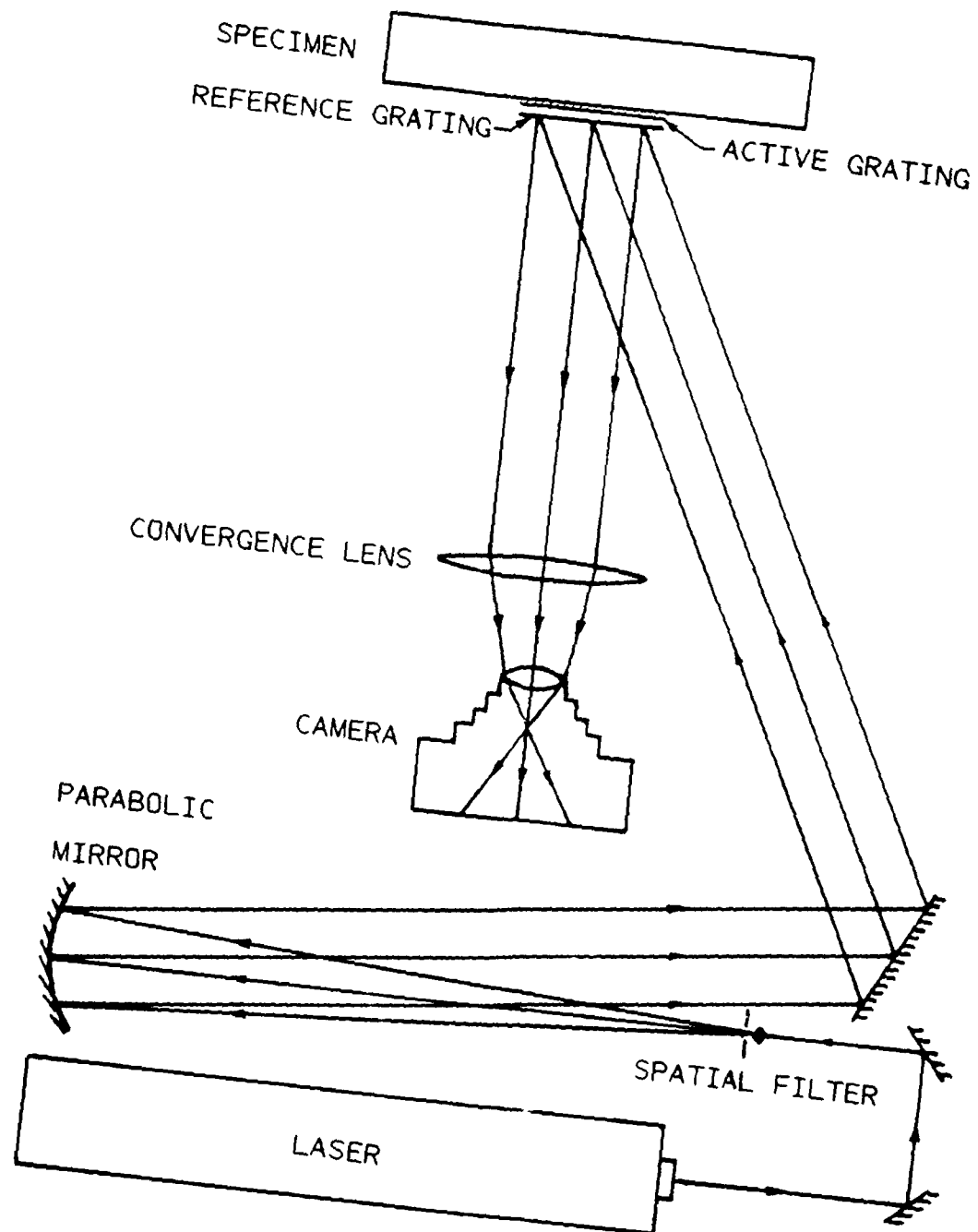


Figure 4.7 Optical Set-UP for Laser Moire Interferometry ($f=1200$ lines/mm)

to provide a square field of 102 x 102 mm (4 x 4 in.). This expanded laser beam was projected onto a flat mirror mounted on the loading machine for double cantilever beam test or mounted near the loading machine for three point bend specimen test. These two machines were all located in another room next to the laser lab.

Real reference grating technique was used in these tests for vibration control. The frequency of the real reference grating was 1200 line per millimeter. When the laser beam was directed by that flat mirror onto the real reference grating which sat right on the specimen upper surface, the transmitted light through the real reference grating and the first order diffraction light generated a virtual grating field around the specimen grating. The specimen grating had only one half density of lines, 600 line per millimeter, as virtual grating had.

All lenses and mirrors must be of high quality. The surface flatness or smoothness must be in the order of a fraction of light wavelength to ensure a perfect wave front before the laser reaches the specimen grating. For this kind of optical devices, if large sizes are required, they are not easy to make and rarely commercially available.

When the deformation event occurs, an interference fringe pattern, which can clearly be seen by naked eyes, appears on the specimen grating surface. This output light

image is first collected by a large diameter objective lens with the help of a simple flat mirror. It, then, passes through a image lens to form a real image for further recording. Finally, this fringe image is recorded on a 35 millimeter film through an ordinary camera without camera lens.

The optical devices which record the formed fringe pattern need not be of special high quality. And the optical design of this recording system is based only on elementary geometrical optics. Stagings and all other adjustment devices were purchased except that for real reference grating was home-made.

Experience and error analysis [114] have shown that for real reference grating, only in-plane rotation is sensitive to adjustment. Thus, a very simple, economical staging for the real reference grating was made. With a micrometer quality screw, 40 threads per inch, a fine and smooth in-plane angle change was accomplished. This device is shown in Figure 4.8.

4.4.3 Test Procedures

The major steps in running a test are listed in the following.

- 1) Transfer a grating to specimen. Due to the porosity of the concrete, precoating is preferred for

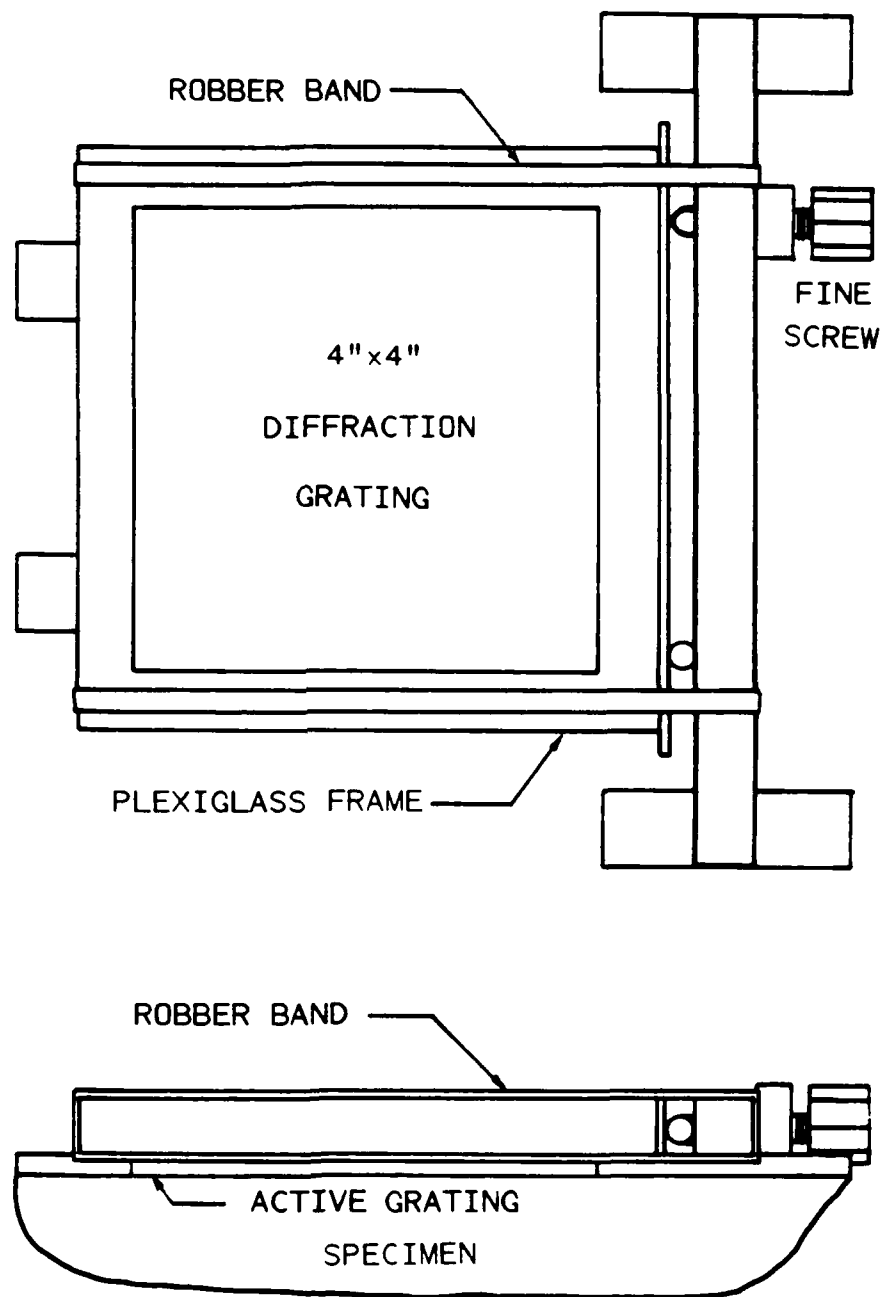


Figure 4.8 Staging for Real Reference Grating

reducing the absorption which may cause roughness of the transferred result or even failure. Details of this technique is given in Appendix B.

2) Mount the specimen to the testing machine. For Wedge Loaded Double Cantilever Beam specimens, the out-plane bending effect has to be checked and eliminated before the actual test is started as described in ASTM Standard 561 [115] and Reference [9]. For beam specimens, small metal plates must be glued to the loading area of the specimen to reduce stress concentration and the statically determinate loading condition must be checked.

3) Align optical system. Using real reference grating and laser, the optical system is very easy to align. Actually, only the incident angle of the laser beam and the in-plane rotation of the real reference grating need be carefully aligned to obtain the minimum null pattern. If white light is used as light source, the alignment is much more difficult due to the short coherence length. In that case, everything must be aligned in order to obtain a clear fringe pattern. The camera must be focused with the help of another scattered light source since parallel light of the laser beam does not provide any target for focussing.

4) Apply displacement to the specimen. The displacement controlled load must be applied slowly, smoothly, and continuously. Any impact could alter the

result or even break the specimen.

5) Record moire fringe pattern, load and displacements. The initial record should be taken before load is applied and each picture should be taken at the same moment as the load and displacements are recorded. The use of a 35 mm camera is recommended because it is fast and sequential pictures can be obtained if a motor drive is used.

CHAPTER FIVE

NUMERICAL PROCEDURES

Research on numerical procedures involved in this study is based on finite element analysis and is a continuation of the finite element investigation on fracture of concrete conducted at University of Washington. The models developed in the previous study are refined and new models as well as new numerical procedures are developed. This chapter describes these developments

5.1 Finite Element Analysis

5.1.1 Special Features in Finite Element Analysis

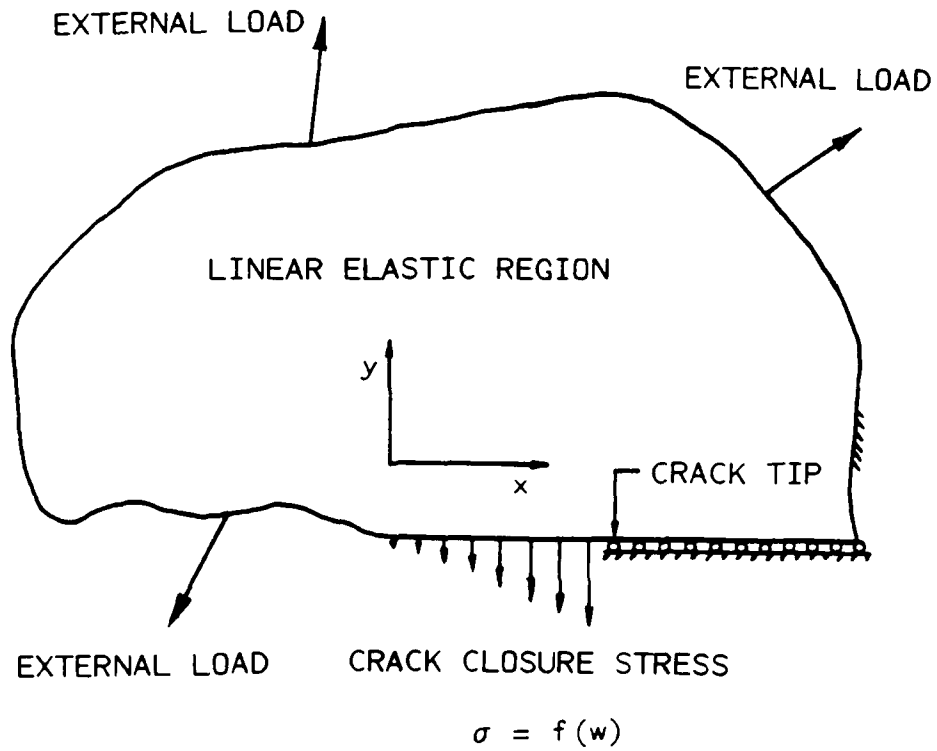
As defined in Chapter 3, the fracture process zone model treats the material outside the fracture process zone as linearly elastic and the material inside the fracture process zone and only along the crack line as nonlinear relaxed. Thus, any linearly elastic finite element code can be used for this analysis provided that the boundary condition along the fracture process zone is properly treated. In some finite element programs, linear elastic boundary condition, which prescribes springs to the boundary nodes, is available. No iteration is needed in this nonlinear analysis but the springs can not model

strain softening effect. The reason is that the springs have larger deformation with greater force. This is just opposite to the softening behavior. The essential point is that a nonlinear problem can never be solved by a linear routine no matter what kind of strategy is used.

Therefore, a linear finite element program with nonlinear boundary conditions, in which iteration is necessary for solving this nonlinear problem, must be developed. According to the assumptions in Chapter 3, the mode I fracture problem is defined as that illustrated in Figure 5.1. There are two special features in this problem. First, the boundary condition along the fracture process zone is given indirectly by relating the normal stress and displacement. Second, one of the external loads can not be given if a maximum tensile stress criterion is prescribed at the crack tip or vice versa.

Such defined problems can be solved in the following steps:

- 1) Assume a crack closure stress versus crack opening displacement relation, which is the constitutive equation.
- 2) Assume an initial stress distribution along the boundary including the entire crack surface and an initial unknown external load.



NOTE:

ONE OF THE EXTERNAL LOADS MUST BE UNKNOWN
 IF A TENSILE STRENGTH CRITERION IS USED
 AND A TENSILE STRENGTH VALUE IS GIVEN

Figure 5.1 Boundary Conditions and Loading Systems

3) Apply all the external loads including the initial stress distribution and compute the tensile stress at the crack tip element and the displacement field.

4) Correct the initial crack closure stress distribution according to the constitutive equation in 1) and using the computed displacement data in 3).

5) Correct the initial external load according to the tensile strength of the material and the computed crack tip tensile stress in 3).

6) Apply all the loads again, compute again, and correct again.

7) Compare the corrections with the corrected values of the unknown load and crack closure stress or crack opening displacement to determine if they have already converged into a acceptable limit.

8) Return to 4) if they have not converged, otherwise, advance the crack tip one element size by releasing the corresponding crack tip node.

9) Return to 2) and repeatedly follow 2) through 9) until the running crack tip reaches the specimen boundary.

10) Compare computed results with test results to make sure that the assumed constitutive equation in 1) is correct, otherwise, go back to 1) to assume a modified constitutive equation based on experiences.

This is the most normal solution method, but it is only good for explaining the principle because there are too many finite element computations involved which need too much computing time. Therefore, a more efficient solution method has been developed which takes the advantage of the superposition principle.

5.1.2 Superposition Principle and Fundamental Solutions

Superposition principle holds for any linear system. With the help of this principle, the solution of a linear system can be obtained by linearly superimposing other known solutions. For linear elasticity, the external loads are linearly related to any displacement component and also any stress component at any point inside the elastic domain. Green functions of displacement and stress of unit load at a certain point can be used as these known solutions and easily be computed using finite element method if the analytical solution can not be derived. The advantage of this method is that once the Green functions, which are called fundamental solutions in this dissertation, are known, no additional finite element computation is needed.

The fundamental solutions can be obtained simply by using finite element analysis to solve for a prescribed unit load at a certain point and compute the displacements and stresses at other points of interest.

One thing should be pointed out is that Green function for unit displacement does not exist because no displacement can be applied to a point of a elastic body exclusively without disturbing the displacement of the adjacent area. It is easy to understand that if the adjacent displacement field is changed the applied displacement can not be considered as only applied to one point. This concept is sometimes confused and it is worthwhile to clarify.

5.1.3 Formulation Using Fundamental Solutions

The basic governing equations for the linear elastic domain with nonlinear boundary conditions can be formulated using fundamental solutions. Suppose the fundamental solutions have already been computed, then, according to the superposition principle, the following equations can be established:

$$w_k = P w_{kP} + F w_{kF} + \sum_{j=1}^N w_{jk} R_j, \quad k = 1, \dots, N, \quad (5-1)$$

$$\sigma_{TP} P + \sigma_{TF} F = f'_t - \sum_{j=1}^N \sigma_{Tj} R_j, \quad (5-2)$$

$$\sigma_j = f(w_j), \quad j = 1, \dots, N, \quad (5-3)$$

$$R_j = (\sigma_{j-1}/6 + \sigma_j^2/3 + \sigma_{j+1}/6)ab, \quad j = 1, \dots, N, \quad (5-4)$$

where, constants:

a : element size along fracture process zone;

b : thickness;

F : prescribed external load;

variables:

P : unknown external load;

R_j : equivalent load at node j;

w_j : COD at node j;

w_j : COD at node k;

σ_j : surface traction at the position of node j;

and fundamental solutions:

w_{kP} : COD at node k due to unit P load at its node;

w_{kF} : COD at node k due to unit F load at its node;

w_{kj} : COD at node k due to unit R load at node j;

σ_{TP} : stress at crack tip due to unit P load at its node;

σ_{TF} : stress at crack tip due to unit F load at its node;

σ_{Tj} : stress at crack tip due to unit R load at node j.

Equations (5-1) are the relations between the CODs and all the loads, including the crack closure forces applied to

the elastic domain. Equation (5-2) is the tensile strength criterion. Equations (5-3) are the constitutive relations of COD and crack closure stress. Equations (5-4) are the equivalence relations of nodal forces and the corresponding tractions along the fracture process zone. There are N equations in (5-1), (5-3) and (5-4), respectively, and one equation in (5-2). The total number of equations is $3N+1$.

Suppose the function $y = f(x)$ in Equations (5-3) is known, the unknown variables are w_j , σ_j , R_j , $j = 1, \dots, N$ and P (note F is known applied load). The total number of unknowns is $3N+1$, the same as the number of equations. Thus, these equations are solvable. Since this is a set of nonlinear equations, an iteration method must be applied. For CLWL-DCB specimen, the crack mouth opening displacement $2V_1$ and the crack tip opening displacement $2V_2$ can be computed as:

$$2V_1 = P V_{1P} + F V_{1F} + \sum_{j=1}^N V_{1j} R_j, \quad (5-5)$$

$$2V_2 = P V_{2P} + F V_{2F} + \sum_{j=1}^N V_{2j} R_j, \quad (5-6)$$

where, fundamental solutions:

V_{1P} : $2V_1$ due to unit P load at its node;

V_{1F} : $2V_1$ due to unit F load at its node;

$$\begin{aligned}
 V_{1j} &: 2V_1 \text{ due to unit } R_j \text{ load at node } j; \\
 V_{2P} &: 2V_2 \text{ due to unit } P \text{ load at its node;} \\
 V_{2F} &: 2V_2 \text{ due to unit } F \text{ load at its node;} \\
 V_{2j} &: 2V_2 \text{ due to unit } R_j \text{ load at node } j.
 \end{aligned}$$

For three point bend beam specimen, the load point displacement D can be determined as:

$$D = D_P P + D_F F + \sum_{j=1}^N D_j R_j, \quad (5-7)$$

where, fundamental solutions:

$$\begin{aligned}
 D_P &: D \text{ due to unit } P \text{ load at its node;} \\
 D_F &: D \text{ due to unit } F \text{ load at its node;} \\
 D_j &: D \text{ due to unit } R_j \text{ load at node } j.
 \end{aligned}$$

Equations (5-1) through (5-7) are basic equations of the formulation.

5.2 Indirect Method

5.2.1 Three - Line Model

An indirect method of solving for fracture parameters was developed. This method is based on a three line model which relates crack closure stress to crack opening displacement by three straight lines segmented by three critical CODs, w_1 , w_2 , and w_3 , as shown in Figure 5.2.

For small CODs, $0 < w < w_1$, the fracture process zone consists of coalescing microcracks. That segment can sustain a closure stress equal to the maximum crack opening resistance defined here as the tensile strength, f_t' . For intermediate range CODs, $w_1 < w < w_2$, the closure stress drops sharply with increasing CODs to a closure stress that is only a fraction of f_t' . The strain-softening behavior for that segment reflects the spreading of the micro-cracks. Petersson [42] found that the closure stress at the trailing end of that segment to be equal to one-third of the maximum closure stress for his small sized specimen. For the large specimens a similar value of $0.3 f_t'$ was found to be appropriate. For CODs ranging between w_2 and w_3 , the closure stress decreases slowly from $0.3 f_t'$ to zero. The fracture process zone terminated at w_3 and the crack can no longer transmit tensile stresses.

The three-line model can also be described in mathematical form as:

$$\sigma = \begin{cases} f_t', & 0 < w < w_1, \\ f_t' [.7(w-w_2)/(w_1-w_2) + .3], & w_1 < w < w_2, \\ f_t' [.3(w-w_3)/(w_2-w_3)], & w_2 < w < w_3. \end{cases} \quad (5-8)$$

In addition, $\sigma = 0$, when $w > w_3$. These three CODs must be obtained through a trial and error procedure.

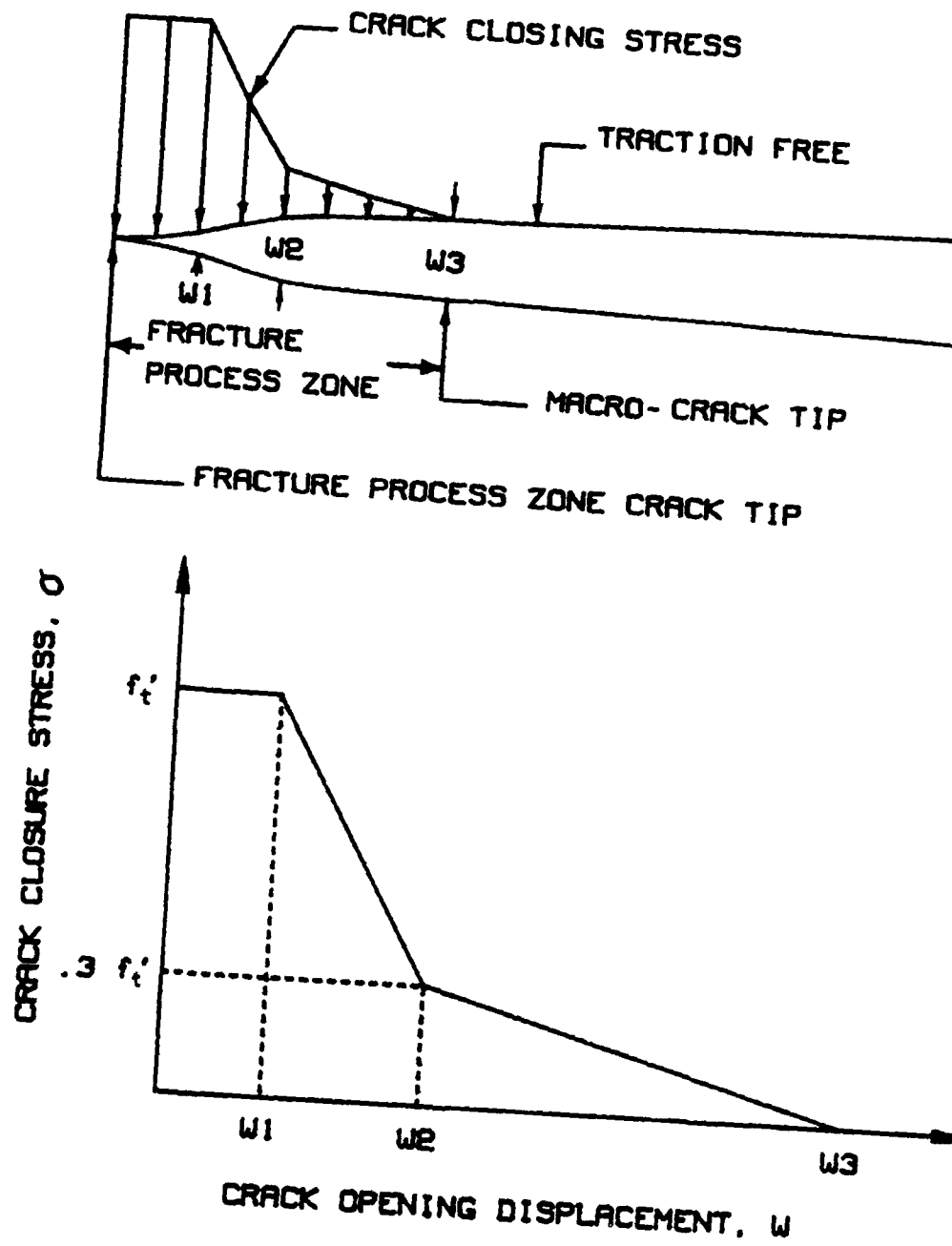


Figure 5.2 Fracture Process Zone Model with Three Line Segments

5.2.2 Iterative Solution Scheme

To solve the basic equations given in 5.1.3 using the indirect method and three-line model, a iterative scheme was established. Let $]_i$ be representing i^{th} iteration. the iterative scheme can be summarized as follows:

1. Estimate the initial CODs $w_k]_0$, $k = 1, \dots, N$. Experience showed that those initial values could be given zero values.
2. Compute the corresponding surface tractions $\sigma_k]_0$ based on a assumed closure stress versus crack opening displacement relation, Equations (5-3).
3. Evaluate the equivalent nodal forces $R_k]_0$, using Equations (5-4).
4. During the i^{th} iteration, compute unknown load P by Equation (5-2).
5. Compute the resulting CODs for the load along the fracture process zone by Equations (5-1).
6. Compute the corresponding surface traction $\sigma_k]_i$ based on the assumed $\sigma - w$ relation which is Equations (5-3).
7. Evaluate the equivalent nodal forces $R_k]_i$ by Equations (5-4).

8. Repeat steps 4 through 7 until convergence is reached as defined by:

$$w_k]_i - w_k]_{i-1} / w_k]_i < 0.01$$

9. Compute $2V_1$ and $2V_2$ for CLWL-DCB specimens or deflection at mid-span of three point bend specimens by Equations (5-5) and (5-6) or (5-7), respectively.

Once the iterative procedure for the (N+1)th node is completed, the microcrack tip is then advanced to the next node and the iterative scheme is repeated until the specimen boundary is reached.

5.2.3 Trial and Error Procedure

The computed results of load, $2V_1$ and $2V_2$ or deflections of beam specimens are compared to test results. If they do not agree with each other, changes must be made in the assumed $\sigma - w$ relation. The whole steps given in 5.2.2. must then be repeated. Usually, such a trial and error procedure is very tedious. This is the drawback of the indirect method.

5.3 Direct Method To Determine $\sigma - w$ Relation

5.3.1 Motivations

The fracture process zone model characterized by a $\sigma - w$ relation for concrete and similar materials has

been widely accepted. The question left now is how to appropriately determine this relation. Although direct tension test seems to be a solution, there are many difficulties in conducting such tests. For example, an extremely high stiffness is required for the testing machine and possible eccentric loading due to material non-homogeneities or axial misalignment are serious drawbacks for a direct tension test.

In order to study specimen geometry effects, boundary effects, and overall stress state effects on $\sigma - w$ relation, specimens other than direct tension specimen must be tested and results analyzed. An effective, convenient, reasonable and reliable procedure to determine $\sigma - w$ relation from test data is needed.

In the absence of direct tension data, measured G_F values have been used, together with measured tensile strengths, to determine the constitutive equation. The quantity G_F , the area under the $\sigma - w$ curve can, however, be used only for a model that is a straight line approximation or is an assumed function for the crack closure stress versus COD relationship. Since it has been found that model predictions of specimen response are very sensitive to the assumed function even for functions with the same G_F and tensile strength values, and accurate measurement of G_F is also difficult, this approach is

neither appropriate nor complete.

In order to determine accurately an appropriate function the measured global responses of the specimen must be used to check the assumed function by comparing them with corresponding numerical predictions and then making changes as needed in the form of the function. This is the indirect method described in the former section or called trial and error procedure. For three-line model six unknown parameters must be determined. If ten different values are tried for each parameter, a million computations must be executed for advancing the crack tip only one step. Such procedures are not only very tedious and time consuming but also suffer from uncertainty in the solution's uniqueness as well as the lack of a benchmark solution for computation.

When crack opening displacements along the fracture process zone have been measured by moire interferometry, Those displacements can be taken as input displacement boundary conditions for a finite element computation to find crack closure stresses along that boundary. As soon as crack closure stresses are determined, the relationship between the crack closure stress and crack opening displacement, which has already been measured in the test, is determined. However, that procedure has a potential problem. The solution is very sensitive to errors in the

input data resulting from boundary displacements which have been erroneously recorded due to unavoidable experimental errors.

Because of the relatively large variations in test results for geomaterials, such as concrete, raw test data should never be used directly. An optimization procedure should be used in smoothly model the test data for numerical analyses. Since the $\sigma - w$ model has been studied for more than ten years, the general shape of $\sigma - w$ curve is well known and an appropriate mathematical form can be readily incorporated in the optimization procedure.

5.3.2 One - Curve Model

The $\sigma - w$ relationship for three-line model cannot be expressed as a single function form and is not continuously differentiable. In order to set up an optimization procedure, the corners of the three line model must be rounded and an appropriate function found to replace these three lines. A smooth curve is also more logical for macro-level modeling.

An appropriate function must satisfy the following conditions:

1. It has to be a monotonically decreasing function. This means that the first derivative must always be negative except at its two boundaries.

2. When $w = 0$, $\sigma = f'_t$ and $d\sigma/dw = 0$, where f'_t is tensile strength of the material.

3. When $w = \infty$, $\sigma = 0$. (This is only a approximate modeling).

4. It must have the same general shape as the $\sigma - w$ curve already established for concrete. The shape must also be changeable by adjusting parameters.

5. The total number of the parameters must be as small as possible but the shape and size of the curve must also be sensitive to the changes in those parameters. In other words, each parameter must have a distinct influence on the shape or the size of the curve.

The function chosen is

$$\sigma = \frac{f'_t}{1 + 2(w/\alpha)^\beta} \quad (5-9)$$

in which $\alpha > 0$ and $\beta > 1$. This function satisfies all five conditions. Conditions 1 - 3 can be easily checked by taking the first order derivative. Conditions 4 and 5 can be checked by using Figure 5.3. Obviously, f'_t and α are scaling factors for the σ and w coordinates, respectively, and β controls the shape of the curve. It can be seen from Figure 5.3 that smaller β values correspond to a smaller microcracking zone and a larger aggregate bridging zone,

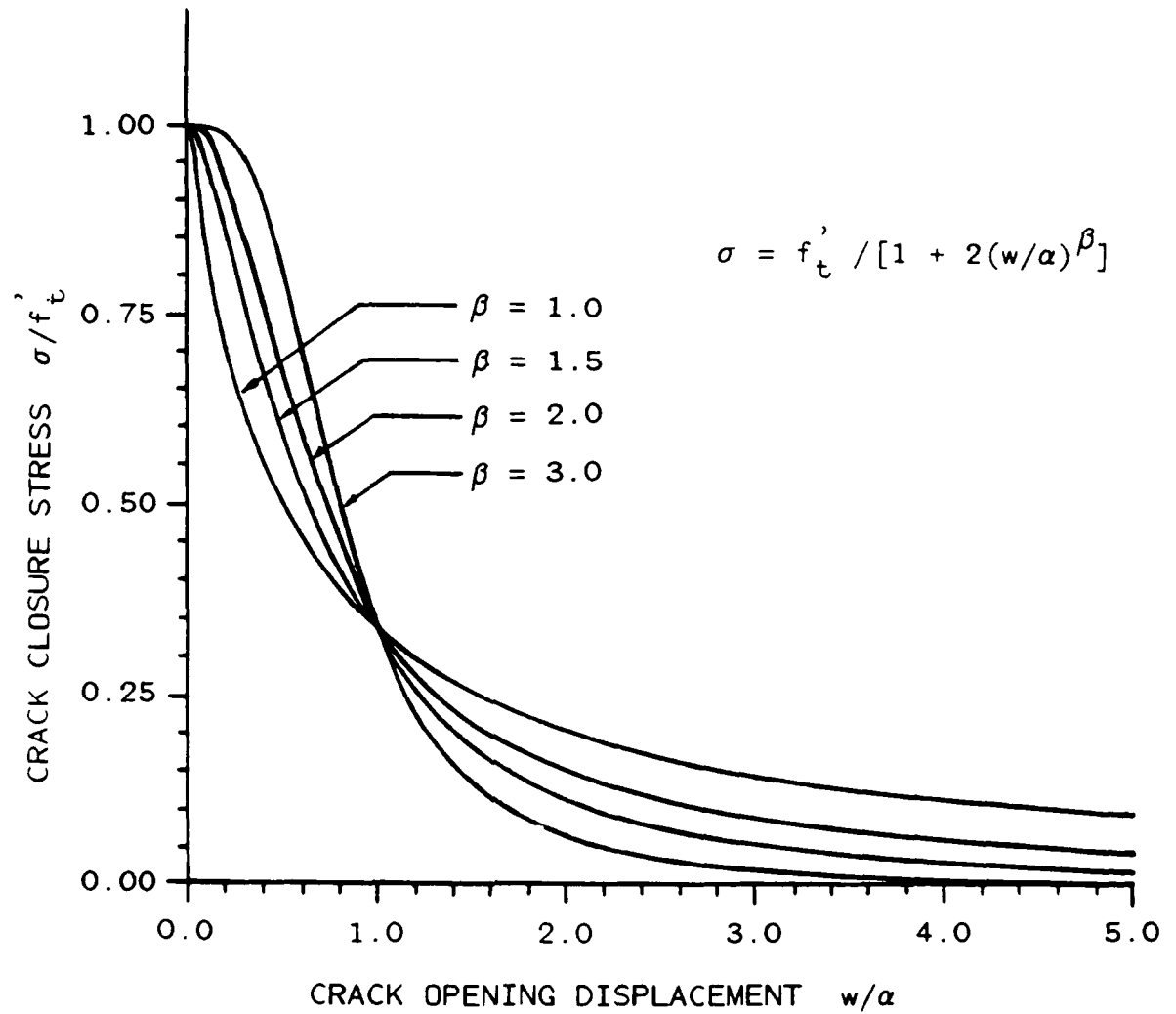


Figure 5.3 Assumed Functional Form for Crack Closure Stress Versus COD Relation

and vice versa. Also, the parameter, α , has a physical meaning. When $w = \alpha$, $\sigma = f'_t/3$ no matter what value β has. One third f'_t is the stress level at the division between microcracking and aggregate bridging. Thus α is the crack opening displacement at this division and is equal to w_2 in Three-Line model.

5.3.3 Optimization Procedure

Once the functional form is established, the parameters in the function can be determined by fitting the test data through an optimization procedure. For simplicity, the nodal force versus traction relationships, or Equations (5-4), were replaced by the expression.

$$R_j = ab \sigma_j, \quad j = 1, \dots, N \quad (5-10)$$

in this study. For the functional form of Equation (5-9), Equations (5-3) become.

$$\sigma_j = \frac{f'_t}{1 + 2(w_j/\alpha)^\beta}, \quad j = 1, \dots, N. \quad (5-11)$$

Substituting Equations (5-11) into Equations (5-10) and substituting Equations (5-10) into Equations (5-1) and (5-2), for $F = 0$, gives:

$$w_k = P w_{kP} + \sum_{j=1}^N \frac{w_{jk} f_t' ab}{1 + 2(w_j/\alpha)^\beta}, \quad k = 1, \dots, N, \quad (5-12)$$

$$\sigma_{TP} P = f_t' - \sum_{j=1}^N \frac{\sigma_{Tj} f_t' ab}{1 + 2(w_j/\alpha)^\beta}. \quad (5-13)$$

Equations (5-12) and (5-13) constitute a set of $N+1$ equations. The unknowns in these equations are fracture parameters f_t' , α and β . Since N is much larger than 2, this is an overdeterministic set of equations. In the case of CLWL-DCB specimens, two more equations can be added to fit the measured $2V_1$ and $2V_2$. Through a similar derivation, these equations can be written as:

$$2V_1 = P V_{1P} + \sum_{j=1}^N \frac{V_{1j} f_t' ab}{1 + 2(w_j/\alpha)^\beta}, \quad (5-14)$$

$$2V_2 = P V_{2P} + \sum_{j=1}^N \frac{V_{2j} f_t' ab}{1 + 2(w_j/\alpha)^\beta}. \quad (5-15)$$

For three point bend specimens, the load point deflection can be fitted with:

$$D = D_P P + \sum_{j=1}^N \frac{D_j f_t' ab}{1 + 2(w_j/\alpha)^\beta}. \quad (5-16)$$

A set of Equations (5-12), (5-13), (5-14), (5-15) are

used for the analysis of the CLWL-DCB specimen and another set of Equations (5-12), (5-13), (5-16) are used for the three point bend specimen. Each set of equations can be written using the test data measured for certain crack length. Multiple sets of such equations corresponding to the different crack growth stages were solved simultaneously to obtain an unique set of fracture parameters. The solution scheme included a Newton-Raphson routine and a Householder transformation. Additional details are given in Appendix C.

5.4 Discussion on Numerical Procedure

5.4.1 Prediction of Crack Propagation

As stated in Chapter 3, this hybrid analysis consists of two phases, i.e. The generation phase and the application phase. In the generation phase of analysis, the constitutive law, which is a fracture model for this case, for the material is established. Once the fracture model is established, all responses of the specimen can be predicted by the application phase of the analysis. Naturally, it is much easier to apply a model than to find the model. In fact, only straight forward finite element computations are needed for the prediction of specimen

behaviors. The finite element program developed for the indirect method is actually the application phase of the analysis so that it can be used directly for prediction. These predictions may include COD, crack length, crack closure stress, stress field in the specimen, deformation of the specimen and the unknown load. These predictions can be used to check the correctness of the fracture model.

5.4.2 Relation between Indirect and Direct Methods

The goals of the indirect and the direct methods are identical in that they essentially solve the same set of equations for the same unknowns which are fracture parameters in the constitutive relation of the crack closure stress versus COD. The difference is that the indirect method relies on a trial and error procedure solving the unknowns through an inverse procedure while the direct method relies on an optimization procedure by solving the unknowns.

Based on a physical reasoning, the trial-and-error procedure and the associated iterative scheme of the indirect method was given in Reference [49] without any theoretical formulation. For a complete mathematical model, such a formulation is essential. The direct method was found just after its theoretical basis was established.

The direct method can be viewed as an experimental data reduction procedure involving finite element computations. Just like the gamma curve generation for metals and polymers, the fracture process zone model parameters can also be generated without any trial and error.

5.4.3 Finite Element Size

Unlike the stress intensity factors determination, the finite element size does not have to be very small compared to the specimen size or the crack length for simulating the fracture process zone. Since a singular stress does not exist in concrete, the ordinary rule of the element size choice, that is the smaller the elements the better the results, is still valid for concrete with cracks. As long as the stress distribution can be represented by that finite element model, the element size should be considered small enough. It is not necessary to choose element size by relating it to either the maximum aggregate size or the characteristic length as suggested in Reference [42]. This is because the effect of the aggregate heterogeneity is smeared out through the depth of the specimen, which is the basic assumption for the macro-level modeling.

CHAPTER SIX

STATIC FRACTURE OF CONCRETE SPECIMENS

Stable crack growth in CLWL-DCB specimens and three point bend specimens of different sizes and different materials have been obtained. A total of five groups of specimens were cast and tested using the procedures described in Chapter 4. These concrete specimens were also analyzed by the numerical procedures and the finite element model described in Chapter 5. The results obtained are presented and discussed in this chapter.

6.1 Small Three Point Bend Specimens

This is the first group tests. As mentioned in Chapter 4, white light moire interferometry method was used for this group. In numerical analysis, the indirect method with three-line model was used to generate fracture parameters based on the moire test results.

6.1.1 Experimental Results

A total of four identical specimens were loaded near to complete penetration of microcrack tip of the fracture process zone or near the full depth of the notched beam. The test set-up and a specimen is shown in Figure 6.1.

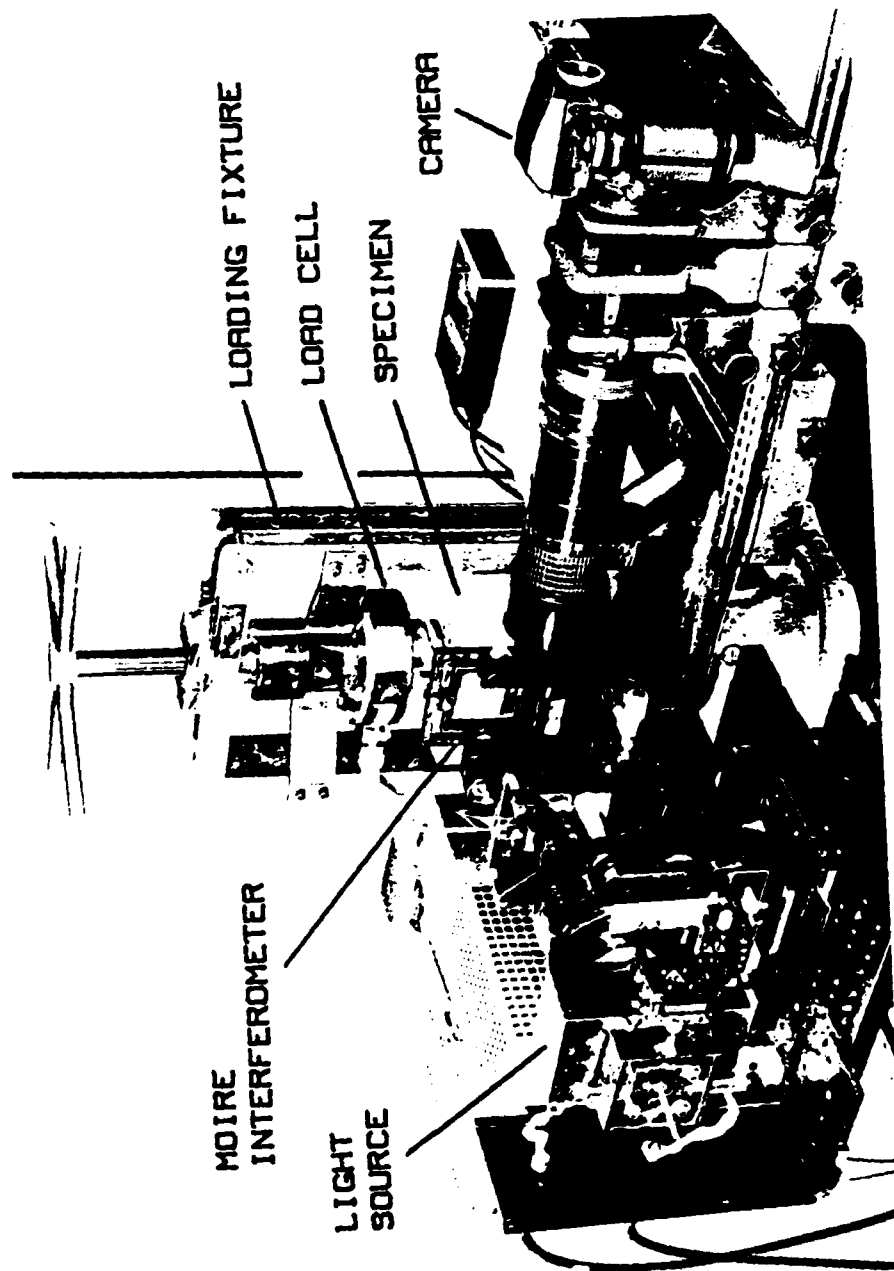


Figure 6.1 Experimental Set-Up for Test Group 1.

Figures 6.2 and 6.3 show typical moire interferometry fringe patterns for specimens No. SB-1 and No. SB-4 at different loading levels. The estimated microcrack tip of the fracture process zone is marked on each figure. The fracture process zone in those two specimens extended from the tip of the machined notches at angles of 40 and 30 degrees, respectively, to the axes of the notch. The inclined fracture process zone was caused by aggregates which were located approximately 2-3 millimeters below the surface to which the active grating, or specimen grating, was attached. The locations of those aggregates are identified by the dotted lines in Figure 6.2 and 6.3. The microcrack tip location after being projected onto the net section of the specimen, was used to determine the amount of crack extension for a given increase in load. The order of the moire fringes was used to determine the crack opening displacement (COD) variations along the fracture process zone.

The data points in Figures 6.4 and 6.5 represent the COD variation along the fracture process zone at different load levels for specimen Nos. SB-1 and SB-4, respectively. These loads are for increasing applied displacements and they occurred under decreasing applied load in the strain softening regime. The increasing COD at the relatively blunt notch tip with increasing applied displacement but



Figure 6.2 Moiré Interferometric Pattern at Crack Tip
Concrete Three Point Bend Specimen No. SB-1
at Load 624 N

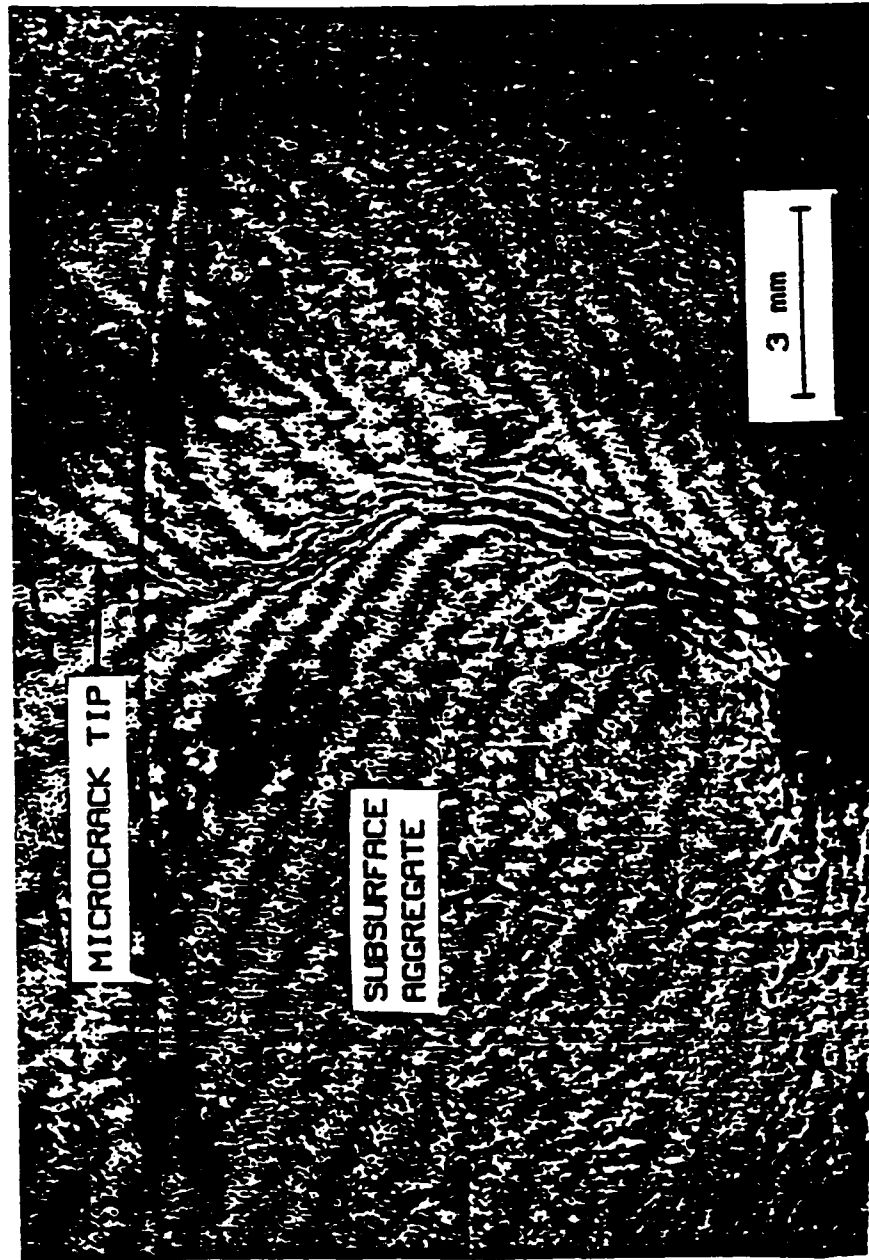


Figure 6.3 Moiré Interferometric Pattern at Crack Tip
Three Point Bend Specimen No. SB-4
at Load 557 N

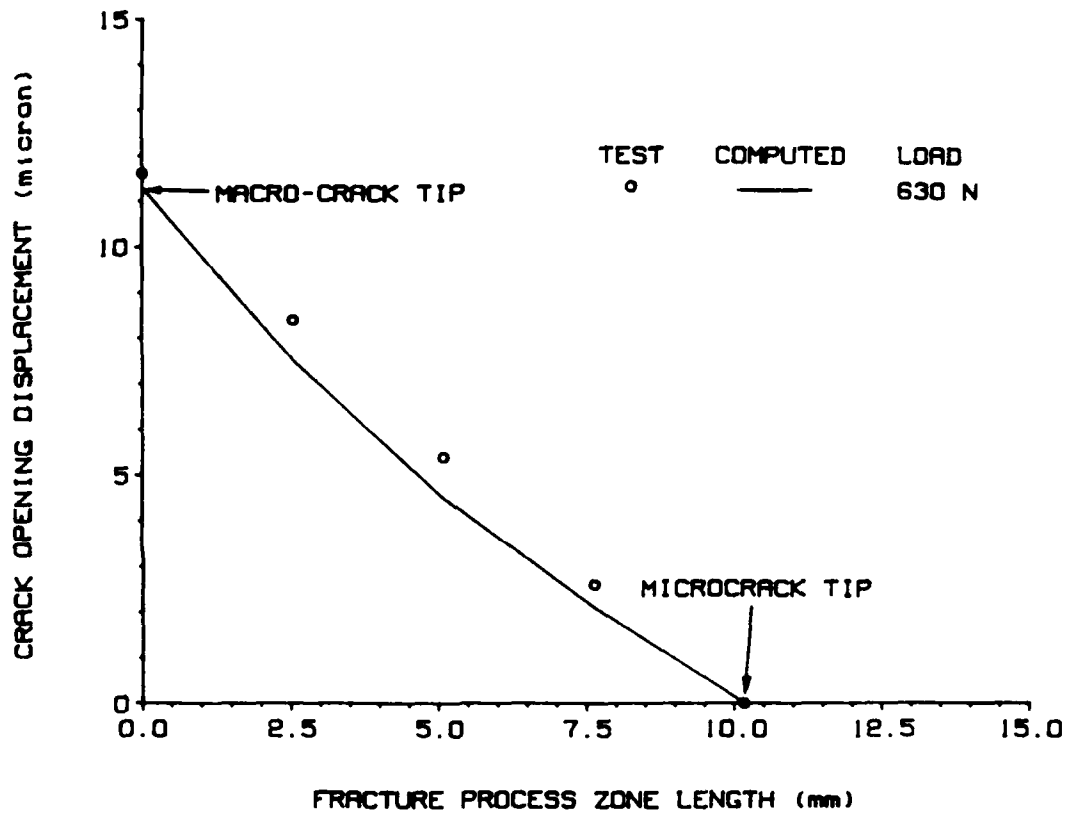


Figure 6.4 COD Variations along Fracture Process Zone
Specimen No. SB-1

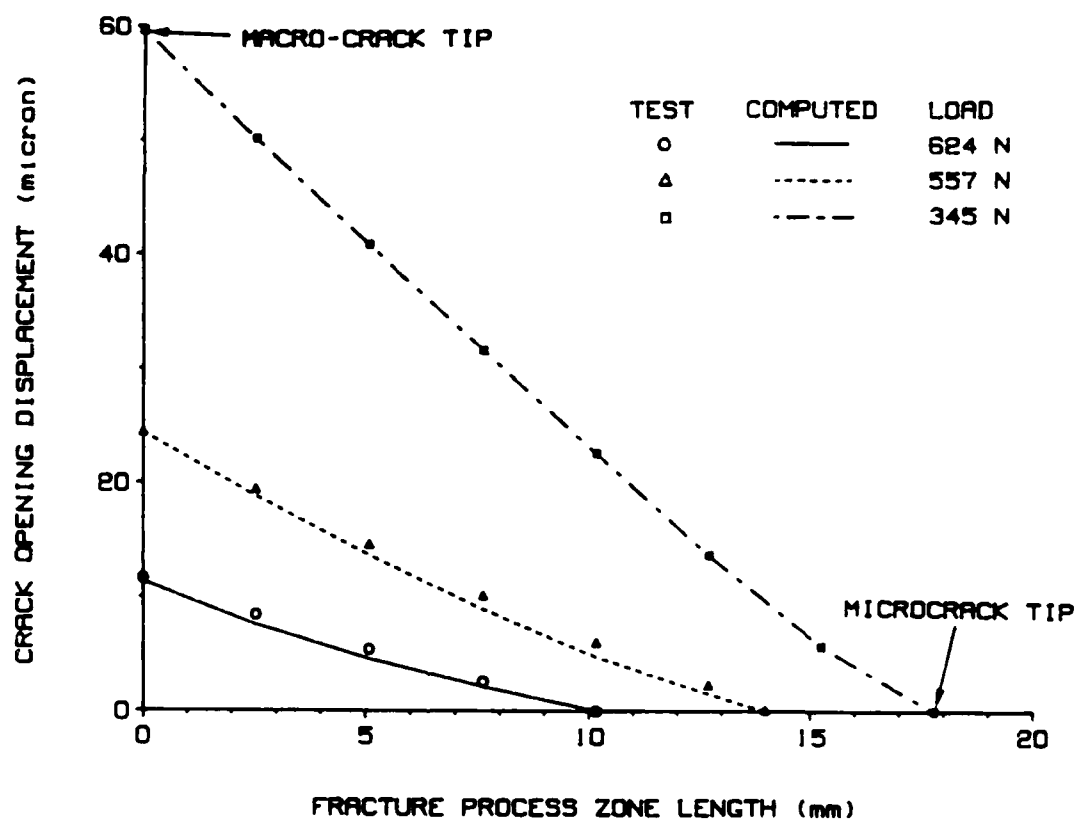


Figure 6.5 COD Variations along Fracture Process Zone Specimen No. SB-4

with decreasing load level did not reach a critical value and demonstrates that in these small specimens, the remaining ligament of 20.3 mm in length was insufficient to permit the fracture process zone to fully develop.

The increasing COD at the blunt notch tip with the extension of the microcrack length for a partially developed fracture process zone in concrete corresponds to the crack tip blunting behavior that occurs prior to stable crack growth in a ductile metal. The data points in Figure 6.6 shows the variations in COD values at the blunt notch tip with microcrack tip extension for four of the concrete bend specimens. Note that the slope of this curve increases with the development of microcrack extension while for metal the shape is always decreasing. This difference can be understood with the new concept presented in Chapter 3. For concrete, its fracture process zone develops when the material is working in its strain softening regime. That means the bigger the COD, the smaller the fracture resistance so that the easier for the crack to open. For metal, the plastic deformation zone develops when the material is working in its strain hardening regime. That means the bigger the COD, the bigger the resistance so that the more difficultly the crack to open.

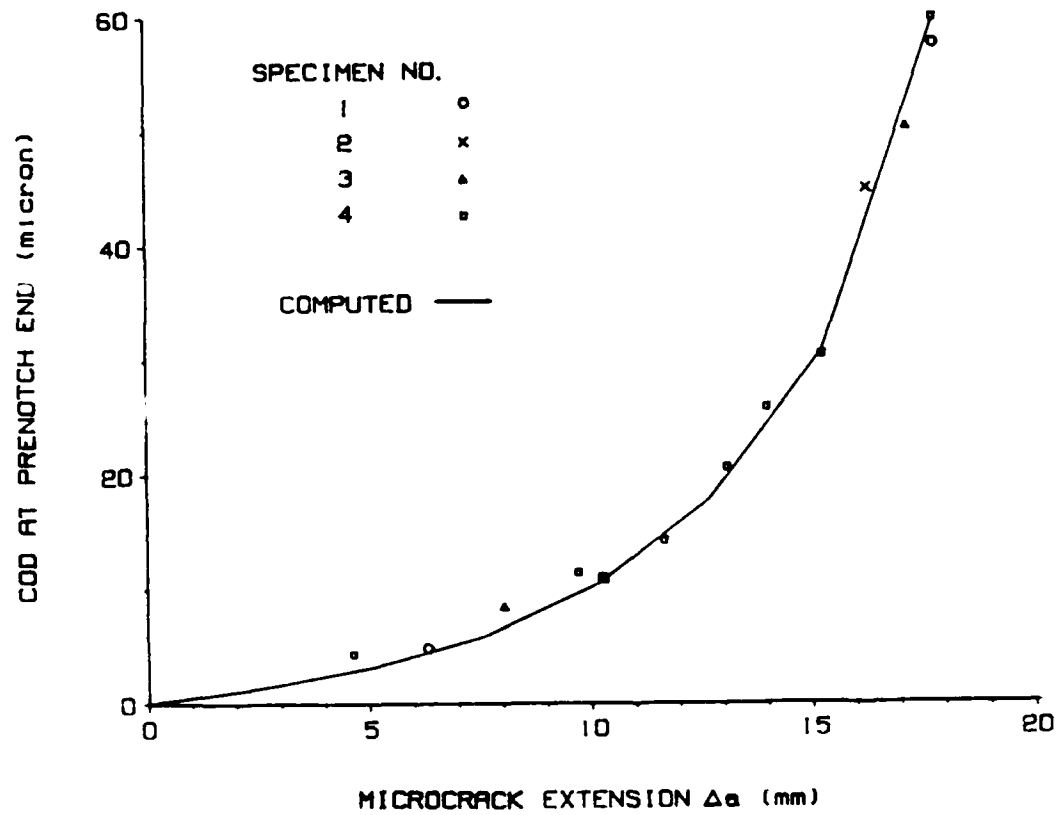


Figure 6.6 COD at Prenotch End Versus Microcrack Extension
Small Three Point Bend Specimen

Table 6.1 Measured Peak Load List
Small Beam Specimens

| SPECIMEN NO. | PEAK LOAD |
|--------------|---------------------|
| 1 | 0.669 kNs (150 lbs) |
| 2 | 0.655 kNs (147 lbs) |
| 3 | 0.678 kNs (152 lbs) |
| 4 | 0.664 kNs (149 lbs) |
| AVERAGE | 0.666 kNs (150 lbs) |

6.1.2 Numerical Results

The foregoing finite element code implemented with the three-line model and the indirect procedure was executed to determine the fracture parameters and to predict microcrack extension. The finite element mesh used for the computations is shown in Figure 6.7. The resultant crack closure stress versus COD relation shown in Figure 6.8 provided the COD variations along the fracture process zone that are indicated by the continuous curves in Figures 6.4 and 6.5. A comparison of Figure 6.8 with the corresponding constitutive relation of Reference [9] show that the two are almost identical in shape, except for the adjustment in maximum tensile strength, despite differences in the processing of the two concrete specimens. The COD's

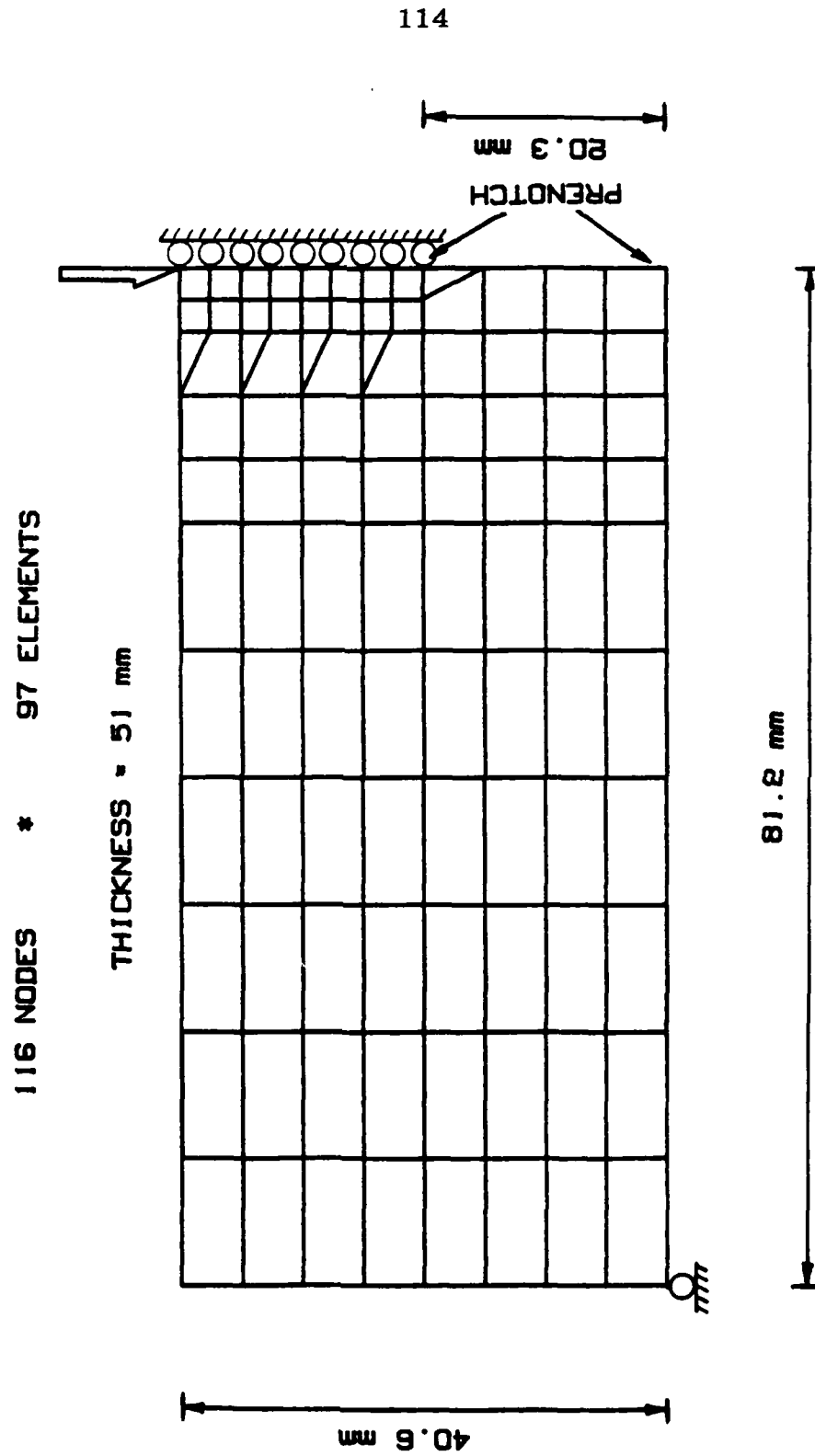


Figure 6.7 Finite Element Model of the Concrete Small Three Point Bend Specimen

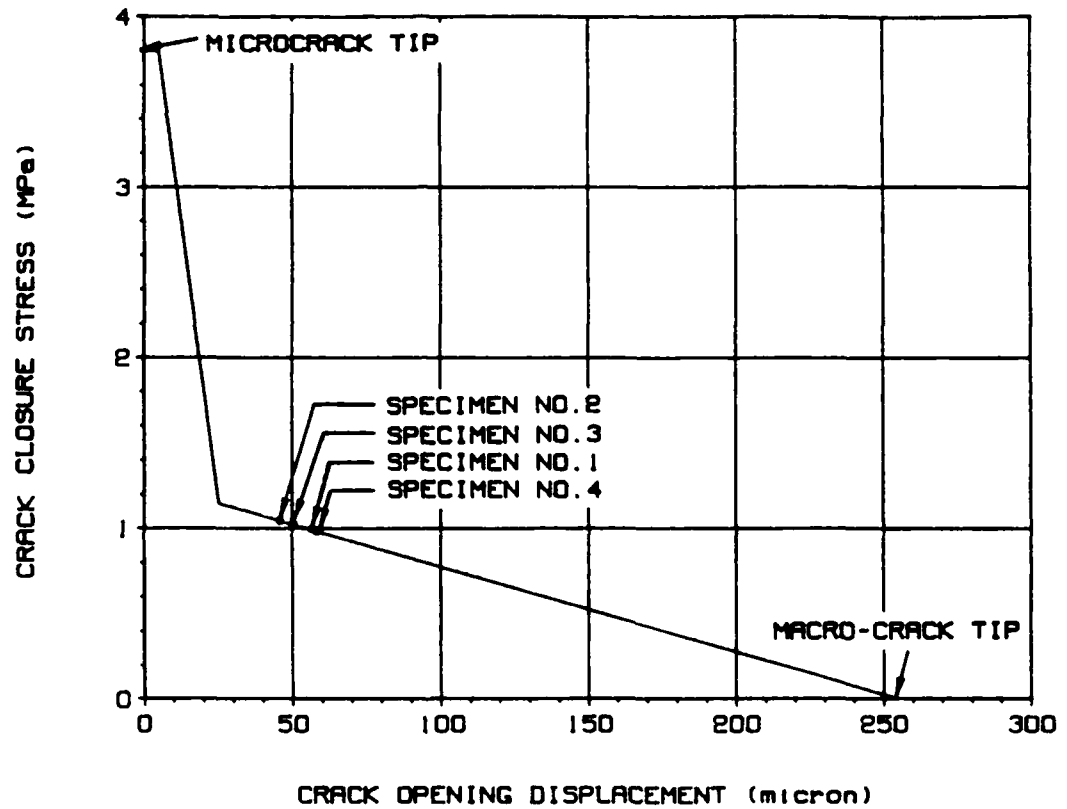


Figure 6.8 Crack Closure Stress Versus COD Relation
in Concrete Fracture Process Zone
Group 1. Small Beams

at the machined notch tip and hence the fracture process zone developments for specimen No. SB-1 through No. SB-4 are also identified in Figure 6.8. These COD's average about 50 microns and are therefore much smaller than the estimated macro-crack tip COD of 250 microns. That results indicates clearly only partial development of the fracture process zone in these subsize specimens.

The continuous curve in Figure 6.6 also, labelled "computed", shows the variations in the computed COD at the notch tip with microcrack extension. Again, the agreement between the measured and computed COD's is excellent. Figure 6.9 shows the typical applied load versus crack mouth opening displacement relation obtained using the finite element model for these concrete specimens. There is a prominent strain softening effect, typical for a concrete specimen loaded in a rigid test fixture.

6.2 Large Double Cantilever Beam Specimens

The second group and third group tests used large concrete specimens to obtain a fully developed fracture process zone. Because the portable white light moire set-up is too small for observing fracture process zone, which develops in a large area, a laser moire interferometry system was set up for the subsequent tests. This system had an observation area of 102 mm x 102 mm

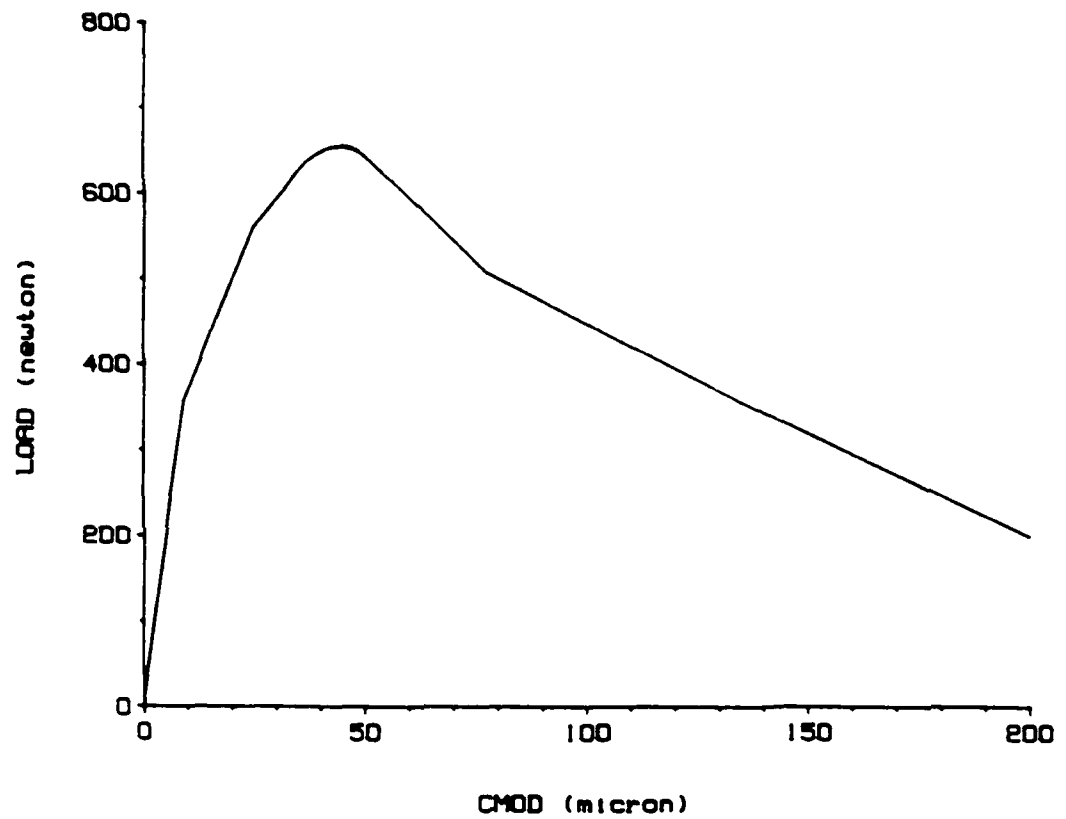


Figure 6.9 Load Versus Crack Mouth Opening Displacement for Small Three Point Bend Specimens

(4 in. x 4 in.). The numerical analysis used for these groups was also the indirect finite element method with three-line model.

6.2.1 Experimental Results

Two large identical specimens for Group 2 and two large identical specimens for Group 3 were tested using a shop press. The difference between these Groups is the maximum aggregate size. The maximum aggregate size of Group 2 is 6.3 mm and that of Group 3 is 9.5 mm. The crack opening of each specimen was detected by moire interferometry. Figure 6.10 shows the test setup and one of the specimens during the test. The specimen dimensions have already been given in Figure 4.1 in Chapter 4.

The wedge load, the crack mouth opening displacement $2V_1$ and the crack tip opening displacement $2V_2$ were recorded by a HP computer. Figures 6.11 and 6.12 show the test results of the wedge load versus $2V_1$ curves by continuous lines for Group 2 and Group 3 specimens, respectively. Considerable aggregate size effect can be seen by comparing these two figures, while the results from the same material are consistent. The peak load for Group 3 is about 25% larger than that for Group 2. Figures 6.13 and 6.14 show the measured $2V_2$ versus $2V_1$ curves also by continuous curves for Group 2 and Group 3 specimens,

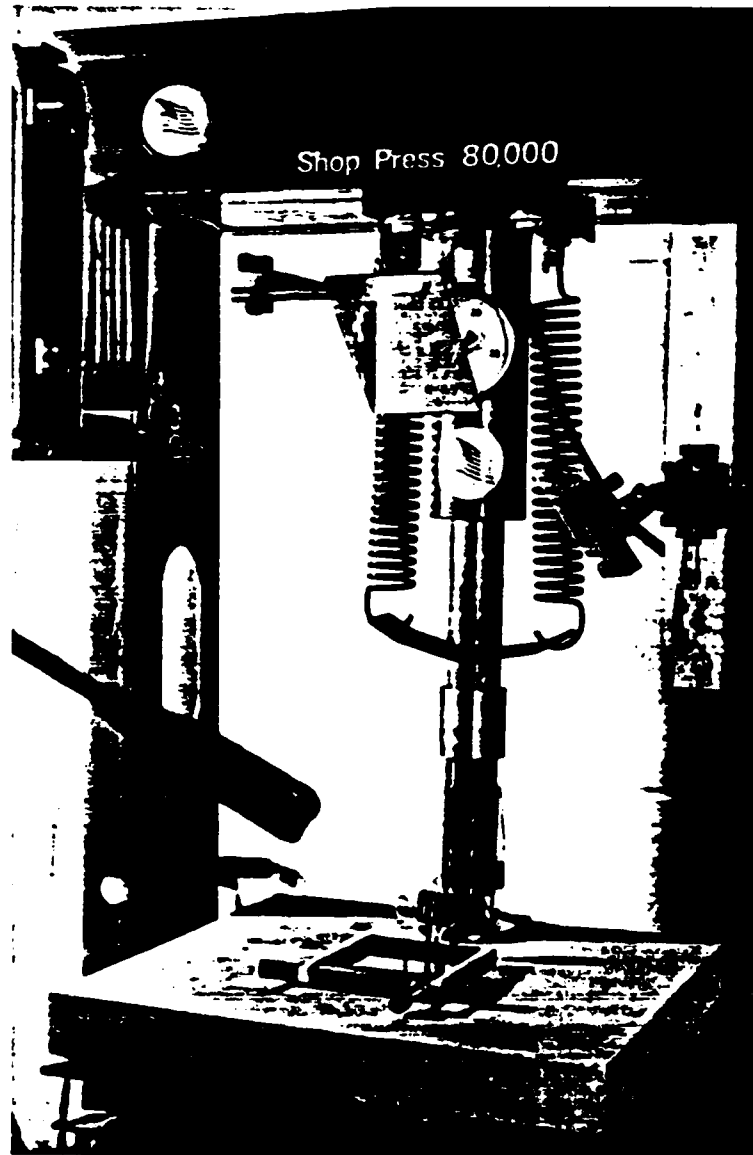


Figure 6.10 Experimental Set-Up for Test Group 2,3.

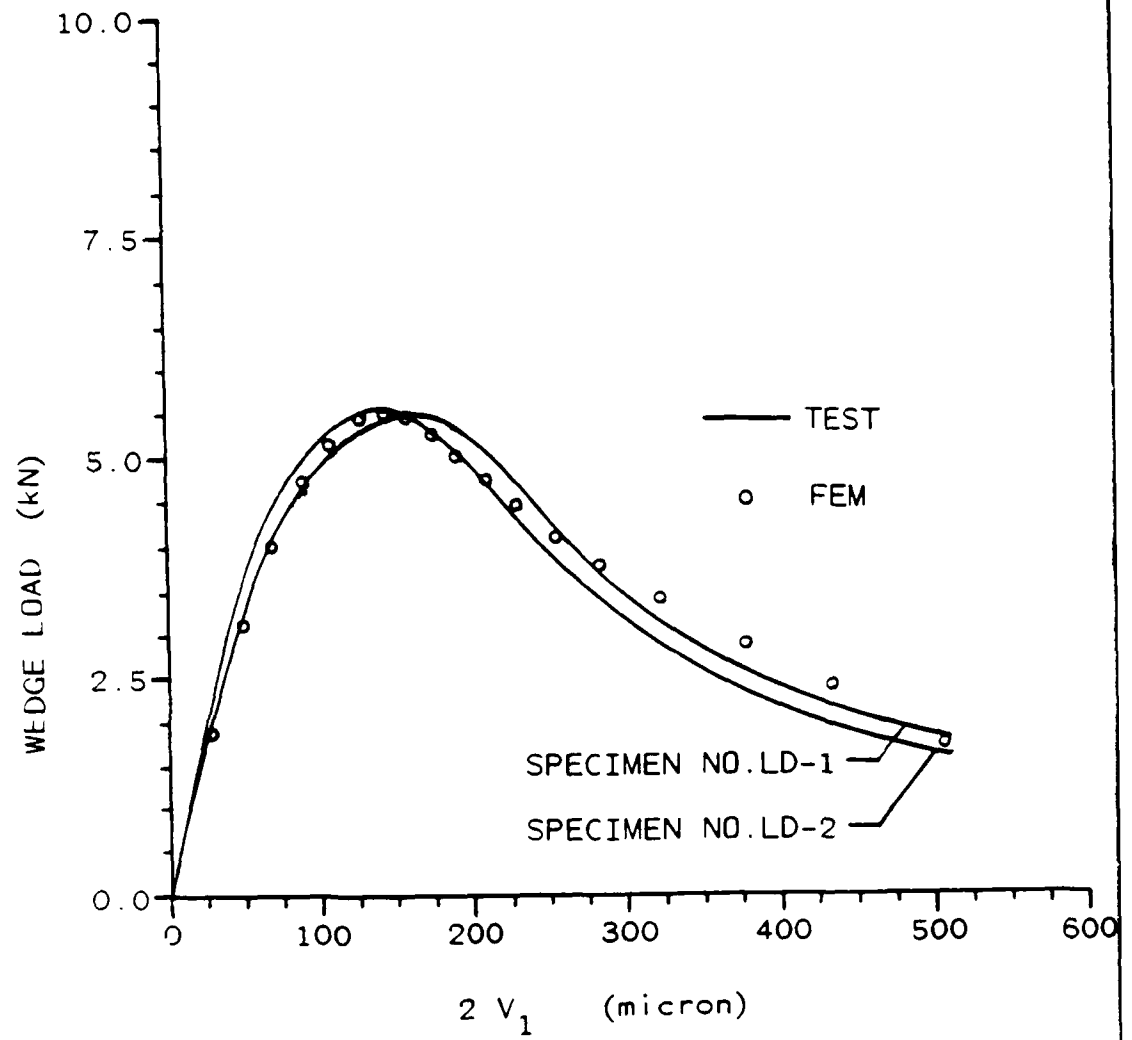


Figure 6.11 Wedge Load Versus $2V_1$ for Large CLWL-DCB Specimens No. LD-1 and No. LD-2

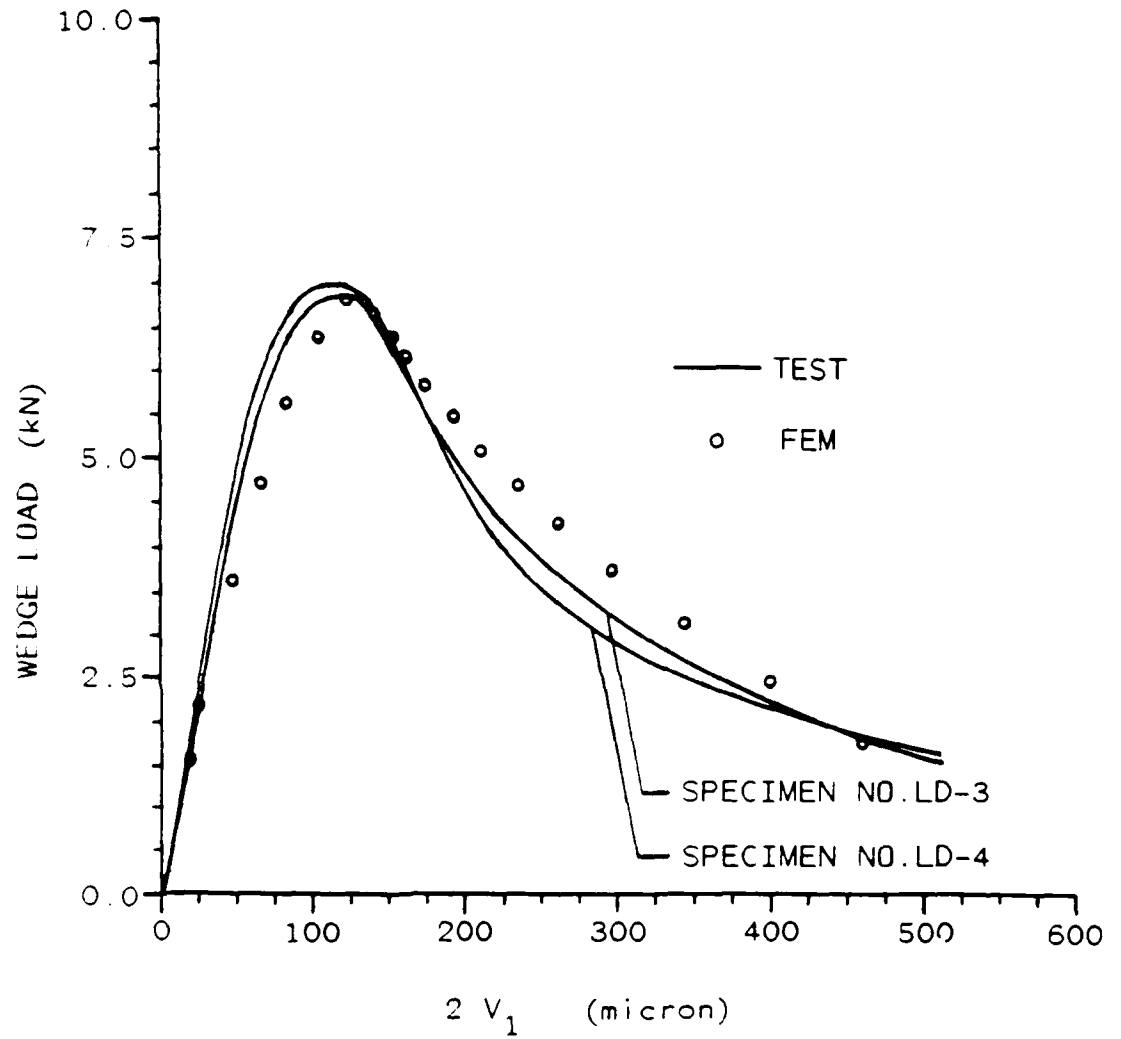


Figure 6.12 Wedge Load Versus $2V_1$ for Large CLWL-DCB
Specimens No. LD-3 and No. LD-4

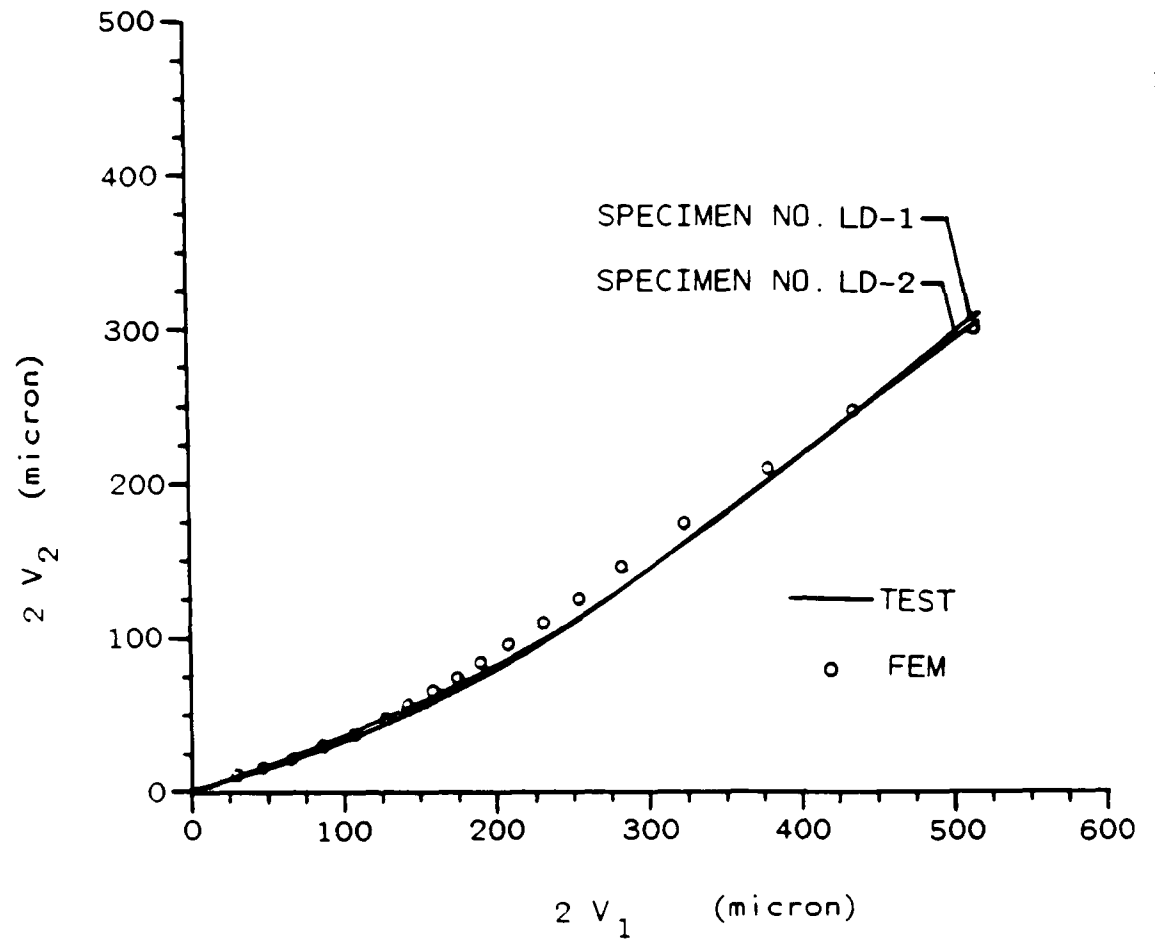


Figure 6.13 $2V_2$ Versus $2V_1$ for Large CLWL-DCB Specimens No. LD-1 and No. LD-2

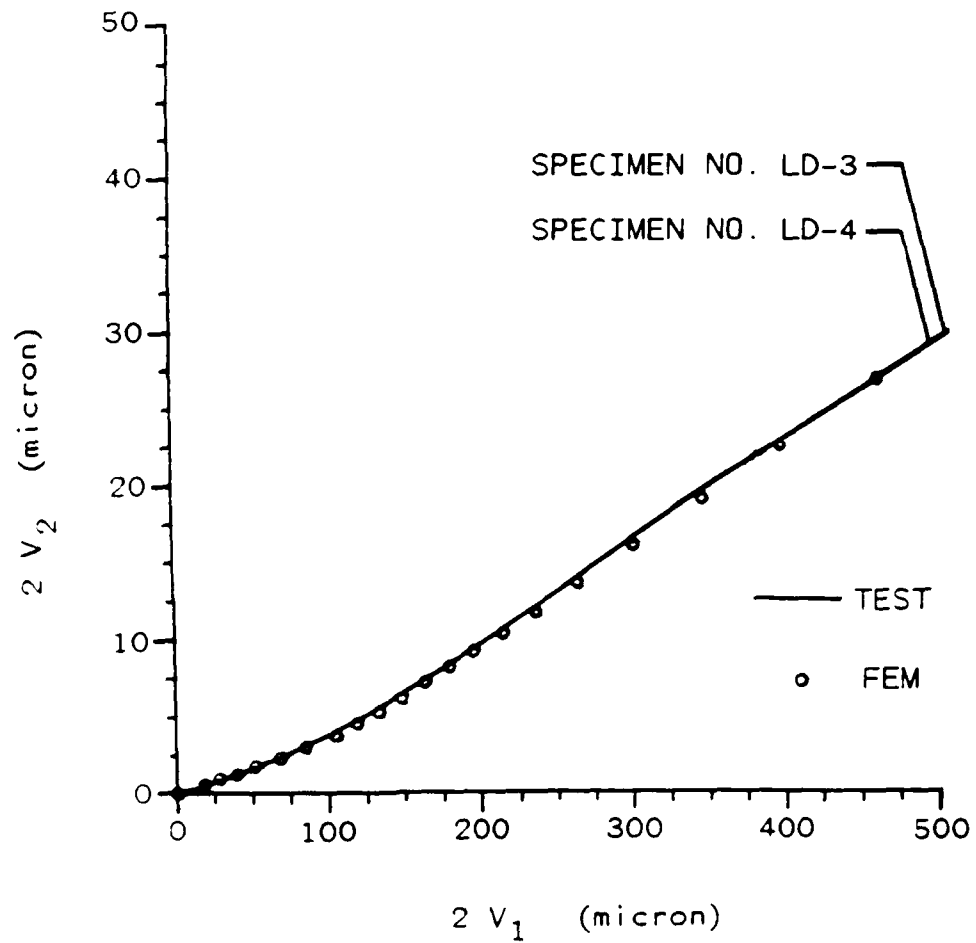


Figure 6.14 $2V_2$ Versus $2V_1$ for Large CLWL-DCB
Specimens No. LD-3 and No. LD-4

respectively. There is no big difference between the results of these COD relations of these two groups.

Moire interferometry fringe patterns were photographed and then evaluated to obtain the crack length and crack opening displacement along the fracture process zone. Difficulty was encountered when the observation area became as large as 102 mm x 102 mm. The home-made diffraction gratings of this size produced too many initial fringes in the null patterns when these groups tests were conducted. The null pattern was superimposed on the fringe patterns associated with the deformation of the specimen. Although subtraction of the null pattern was possible, the necessary software, which is a state of art in computer science, was not available.

Fortunately, the determination of the crack opening displacement does not require the absolute displacement of the entire field and only the relative displacement between the two corresponding points of the opposite crack surfaces is needed. This relative displacement is the COD and was evaluated by counting the fringes along the crack surfaces. The continuous lines in Figures 6.15 and 6.16 represent the measured crack opening displacement along the fracture process zone for Groups 2 and 3, respectively.

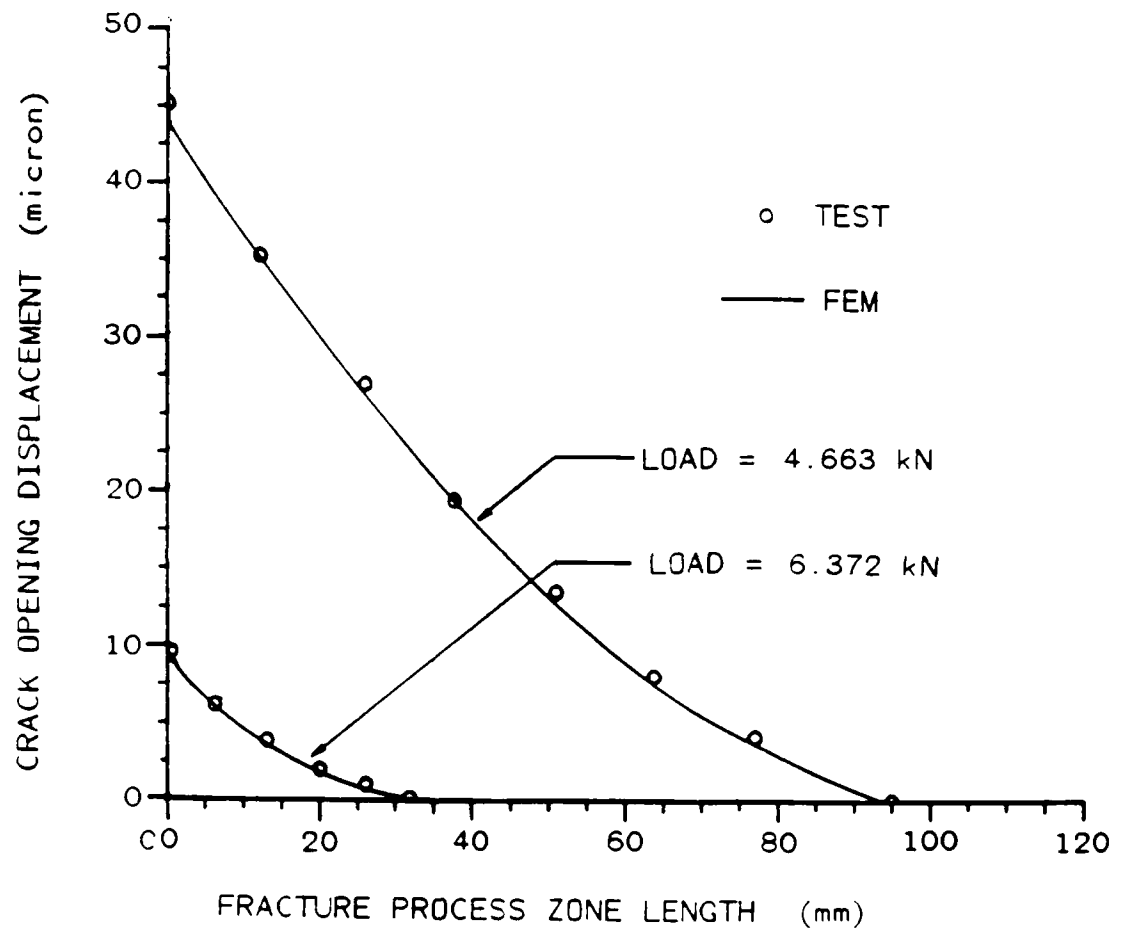


Figure 6.15 COD Variations along Fracture Process Zone
Specimen No. LD-1

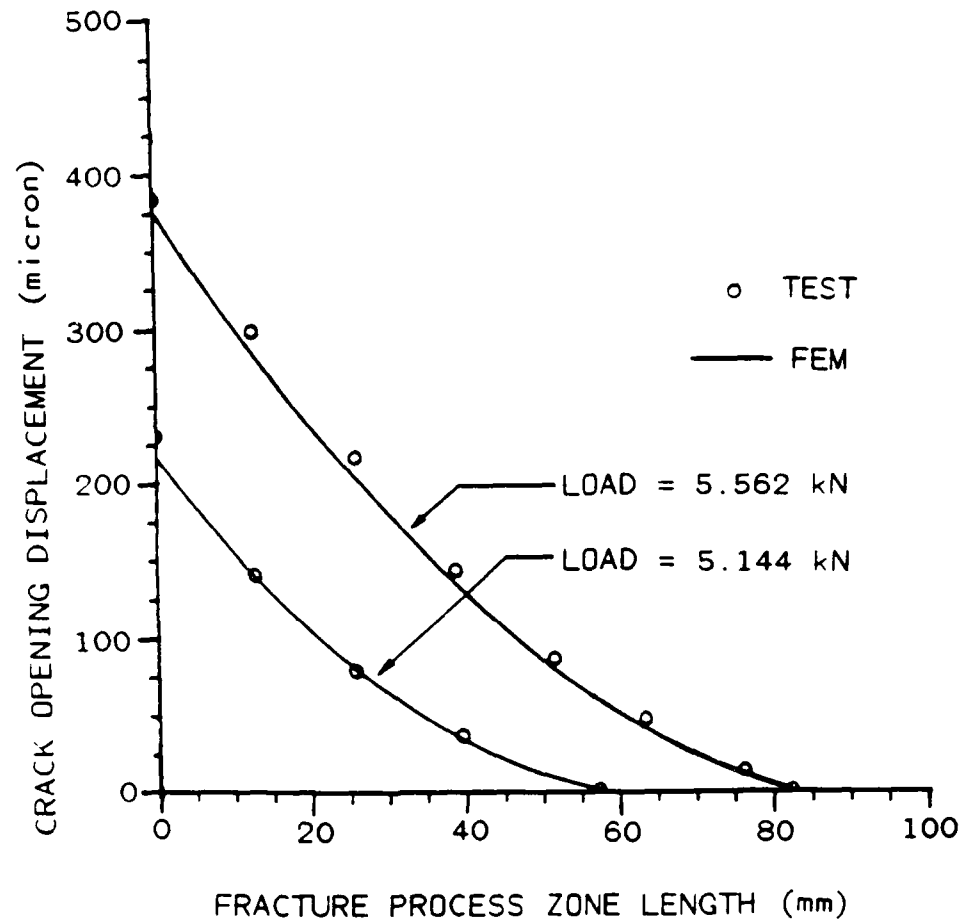


Figure 6.16 COD Variations along Fracture Process Zone
Specimen No. LD-3

6.2.2 Numerical Results

The nonlinear finite element analysis was then conducted for finding the fracture model for these specimens. The finite element model is shown in Figure 6.17. The wedge load applied to the hole surface was simplified to a concentrate force. Through extensive trial and error, fracture models of crack closure stress versus COD relation were obtained for these two groups and are shown in Figures 6.18 and 6.19. Based on these models, various specimen behaviors were predicted. The data points in Figure 6.11 through Figure 6.16 represent the numerical results of the experimental counterparts. Good agreements were obtained between the test measurements and the theoretical predictions.

6.3 Specimens of Adequate Size

It was found that even the moire interferometry measuring area had been increased to 102 mm x 102 mm it was still far from being large enough for a fully developed fracture process zone in those large CLWL-DCB specimens used in Groups 2 and 3. Larger moire set-up was not available. However, since the fracture process zone size depends on the specimen geometry and size, fully developed fracture process zones can be generated which fit the

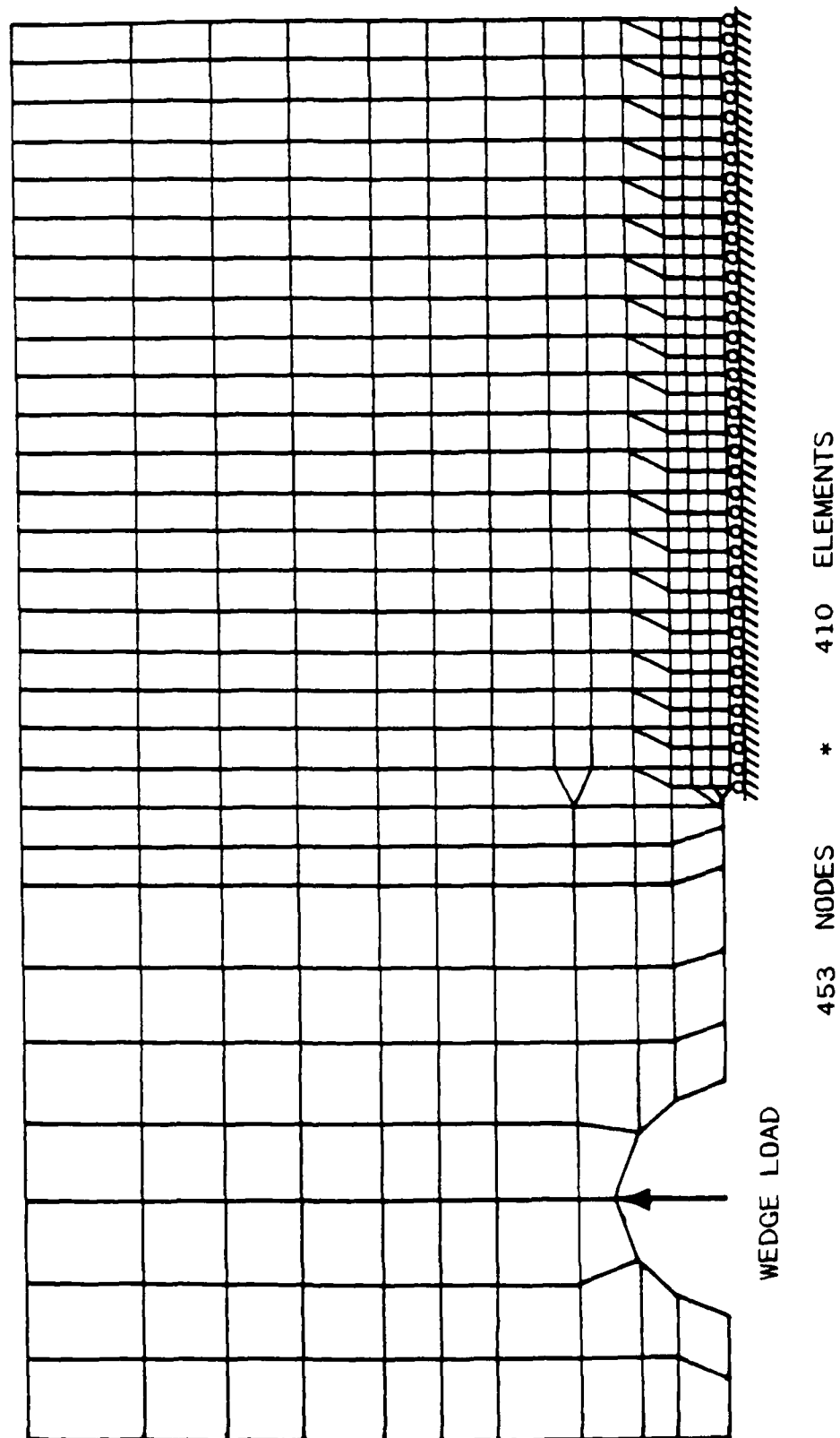


Figure 6.17 Finite Element Mesh for Group 2,3.
Large CLWL-DCB Specimens

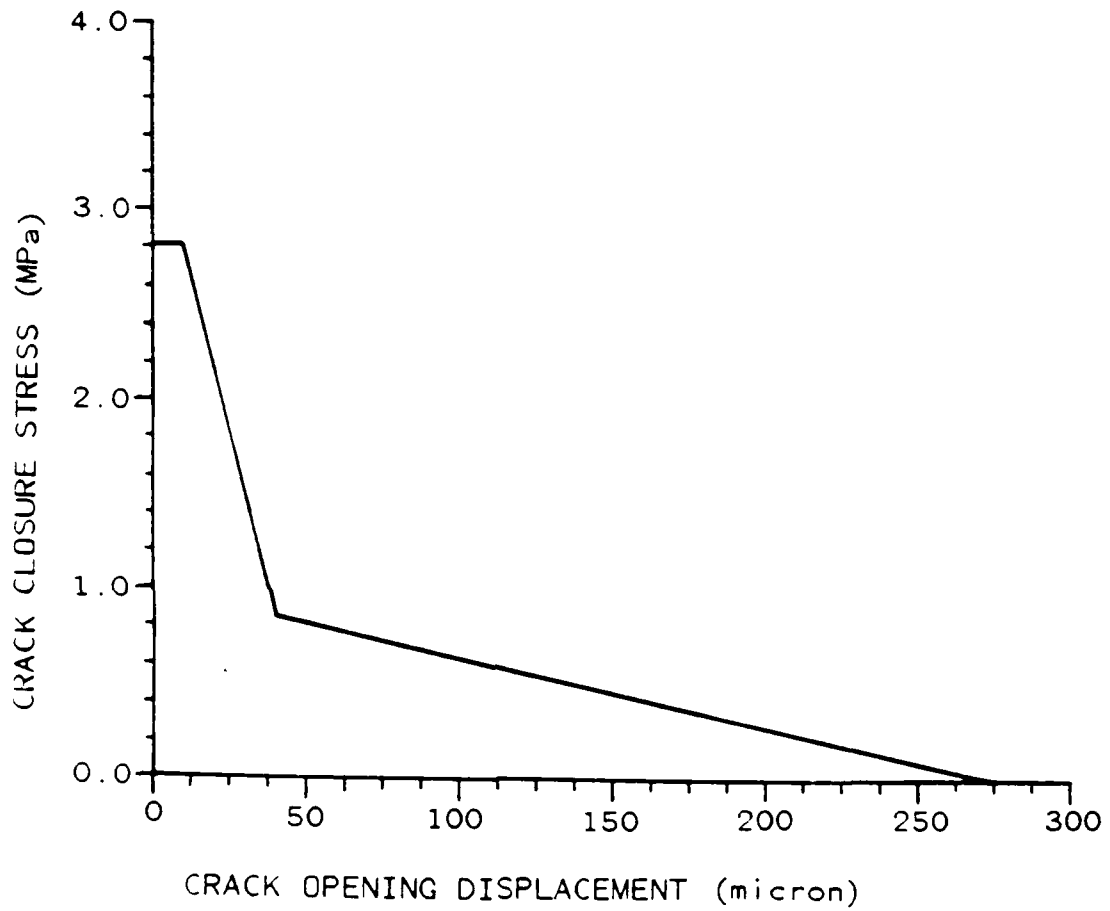


Figure 6.18 Crack Closure Stress Versus COD Relation
for Group 2 Specimens

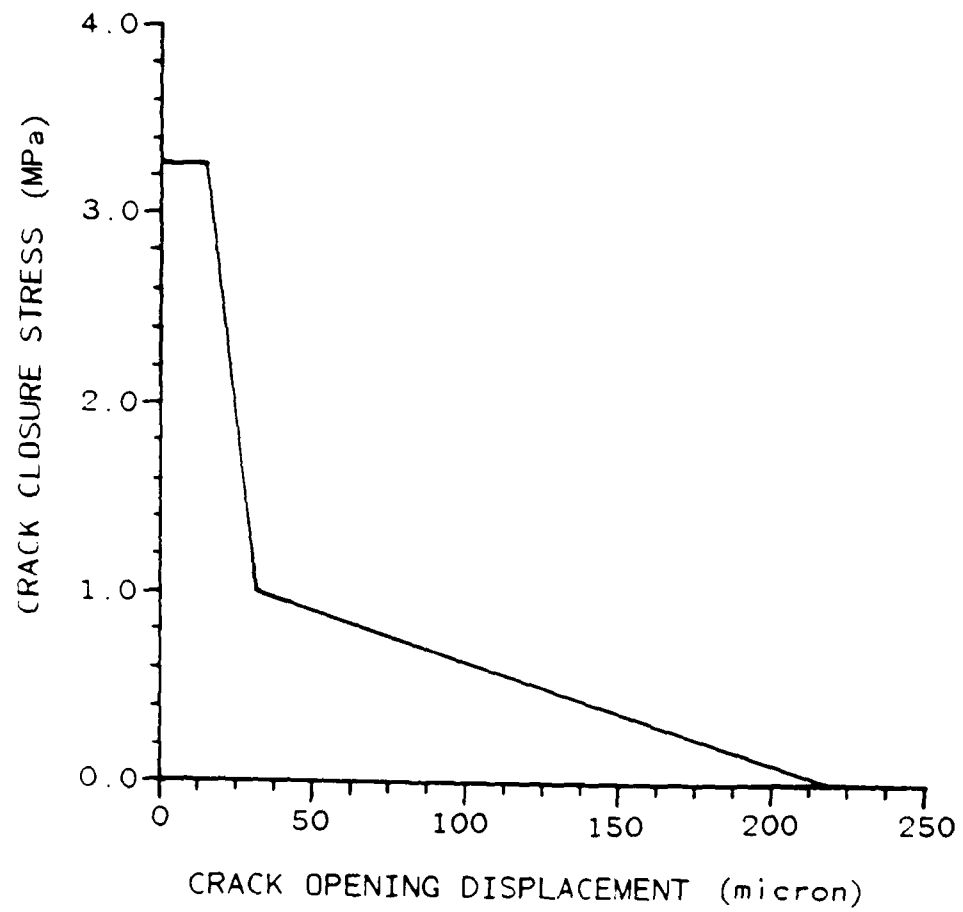


Figure 6.19 Crack Closure Stress Versus COD Relation for Group 3 Specimens

available optical set-up. Thus, finite element experiments were conducted to arrive at reasonable dimensions for CLWL-DCB specimen used for Group 4 and for three point bend specimen used for Group 5. The dimensions of these specimens are given in Figure 4.2. in Chapter 4. The laser moire interferometry with a real reference grating and the direct finite element numerical procedure with the one-curve model were used in these studies.

6.3.1 Experimental Results

A total of four CLWL-DCB specimens and four three point bend specimens were loaded nearly to complete penetration of micro-crack tip of the fracture process zone. The photographs of the test set-up and the specimens are given in Figures 6.20, 6.21 and 6.22. The measured wedge load versus $2V_1$ and $2V_2$ versus $2V_1$ curves for the four CLWL-DCB specimens are shown in Figures 6.23 and 6.24. The load versus load point deflection curve for four three point bend specimens are shown in Figure 6.25.

Moire interferometry data showed that the fracture process zone started to develop much earlier than the peak load was reached. Thus the maximum load that a concrete specimen can carry without the fracture process zone is only about 30% to 40% of the load-carrying capacity of a concrete specimen with a developed fracture process zone.

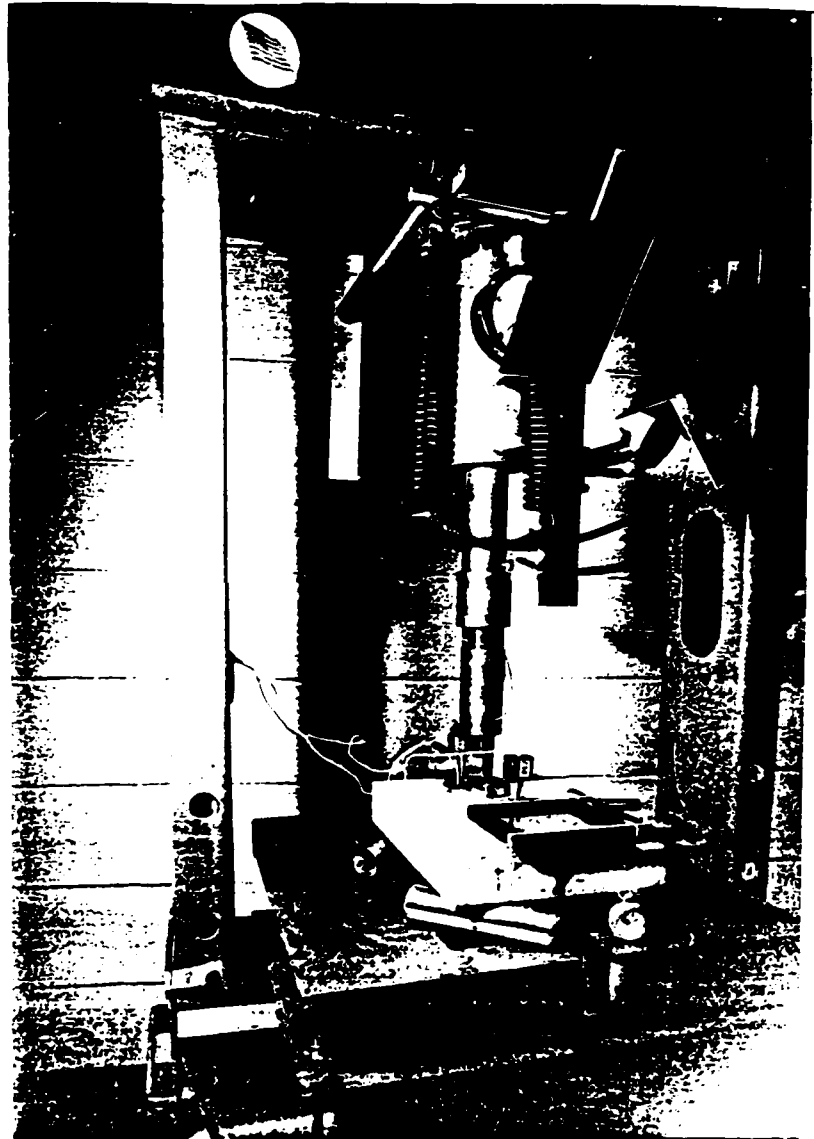


Figure 6.20 Experimental Set-Up for Test Group 4.

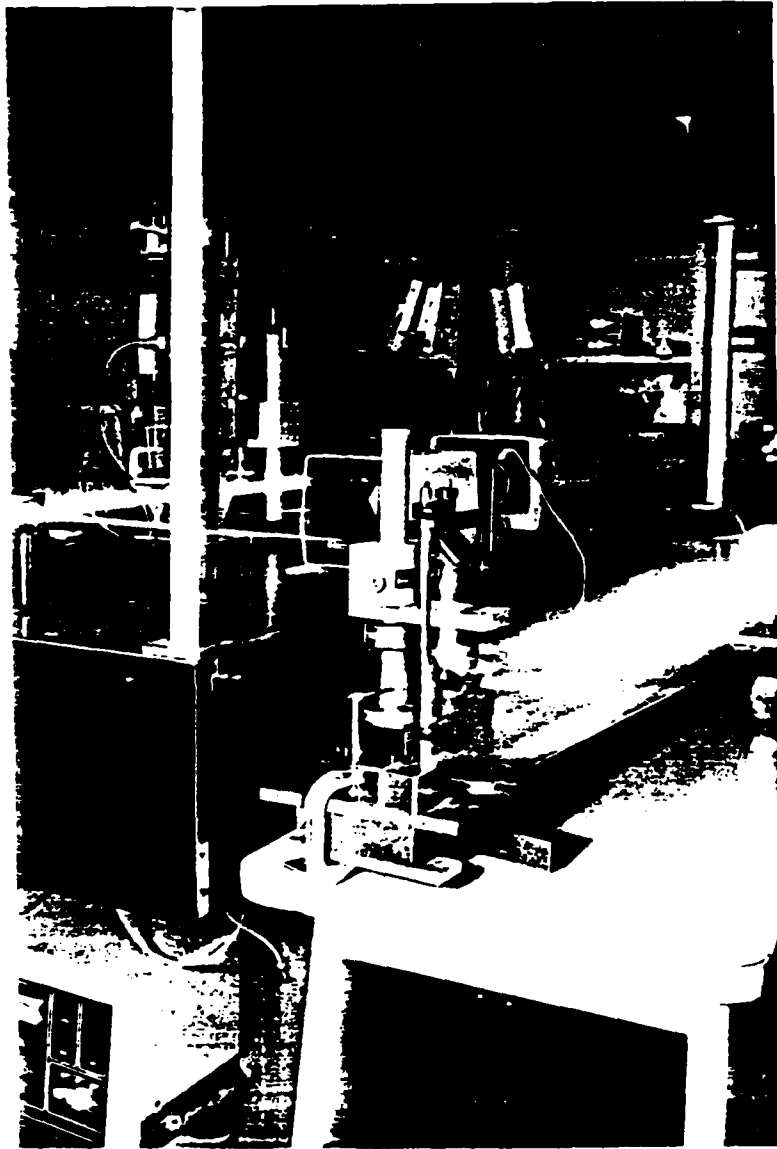


Figure 6.21 Optical Set-Up for Laser Beam

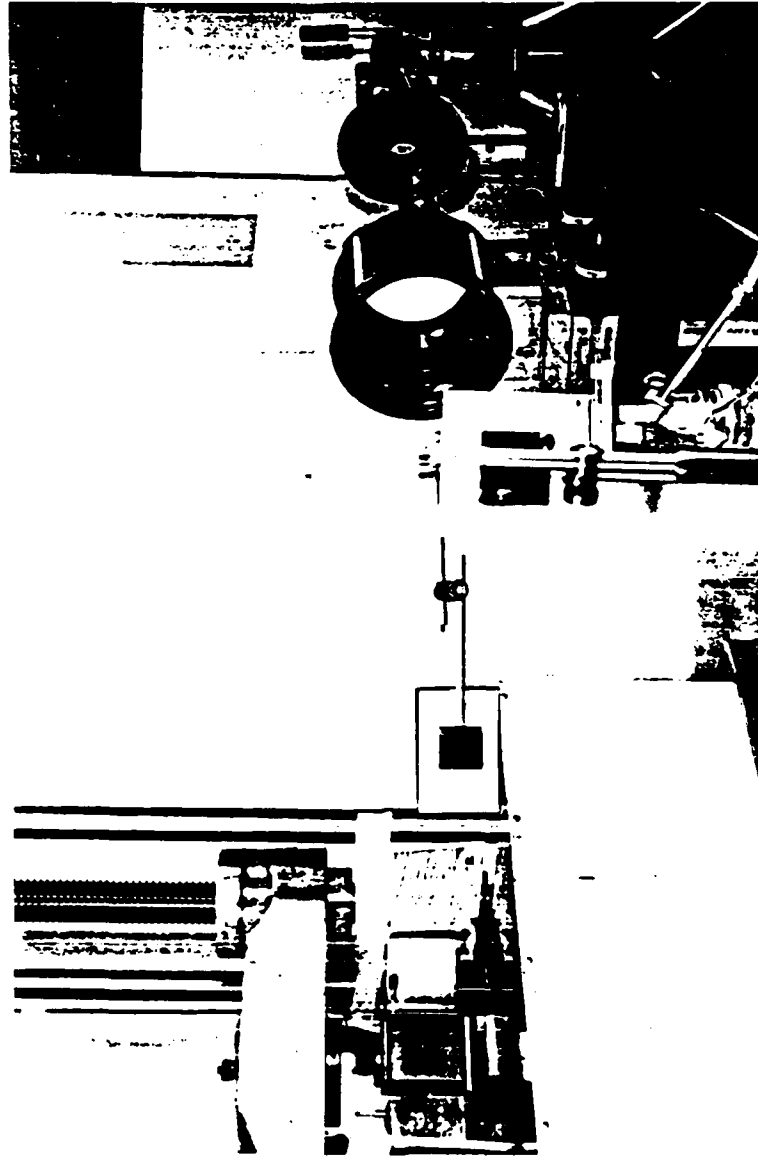


Figure 6.22 Experimental Set-Up for Test Group 5.

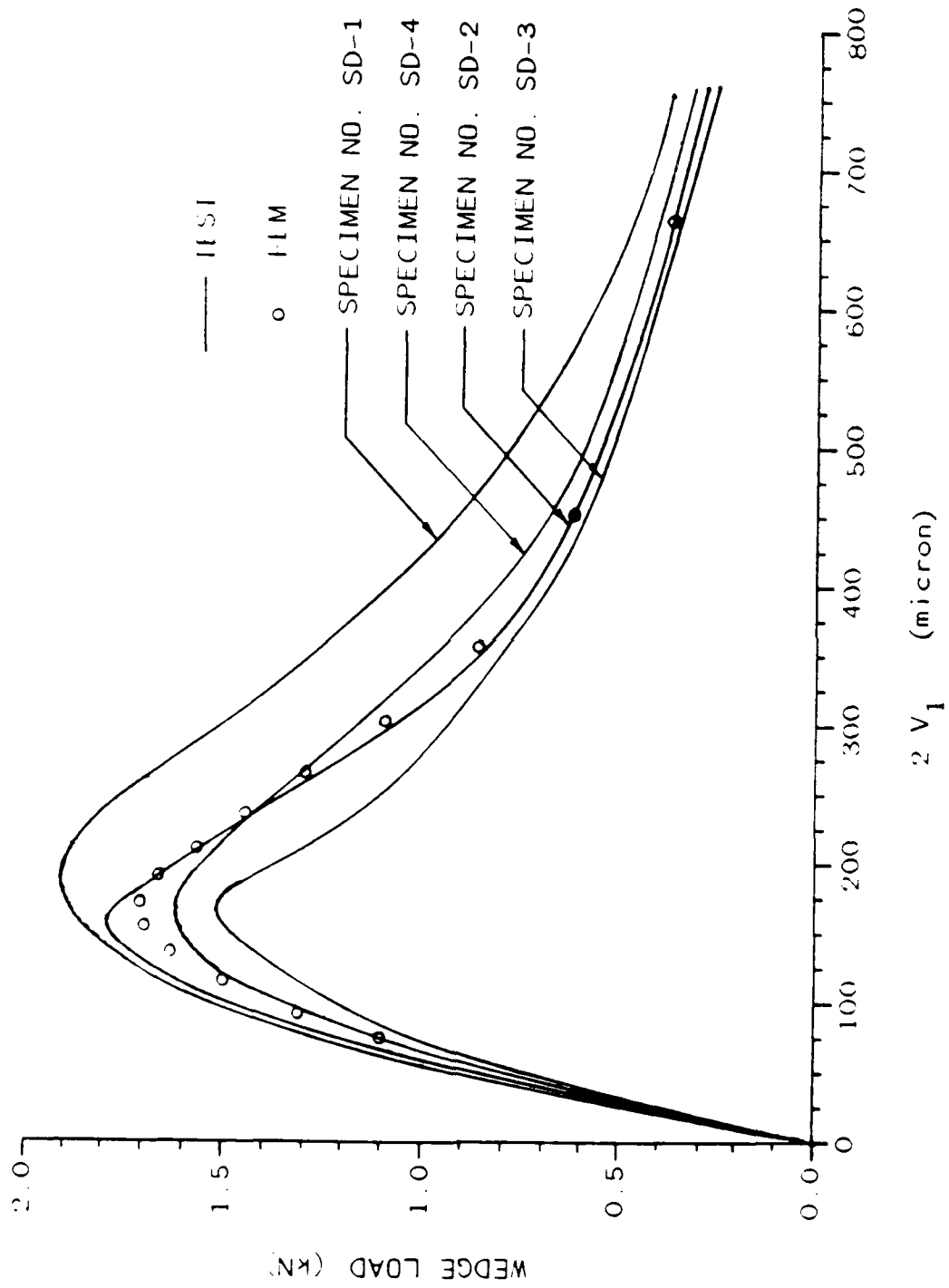


Figure 6.23 Wedge Load Versus $2V_1$ for Small

CLWI DCB Specimens, Group 4.

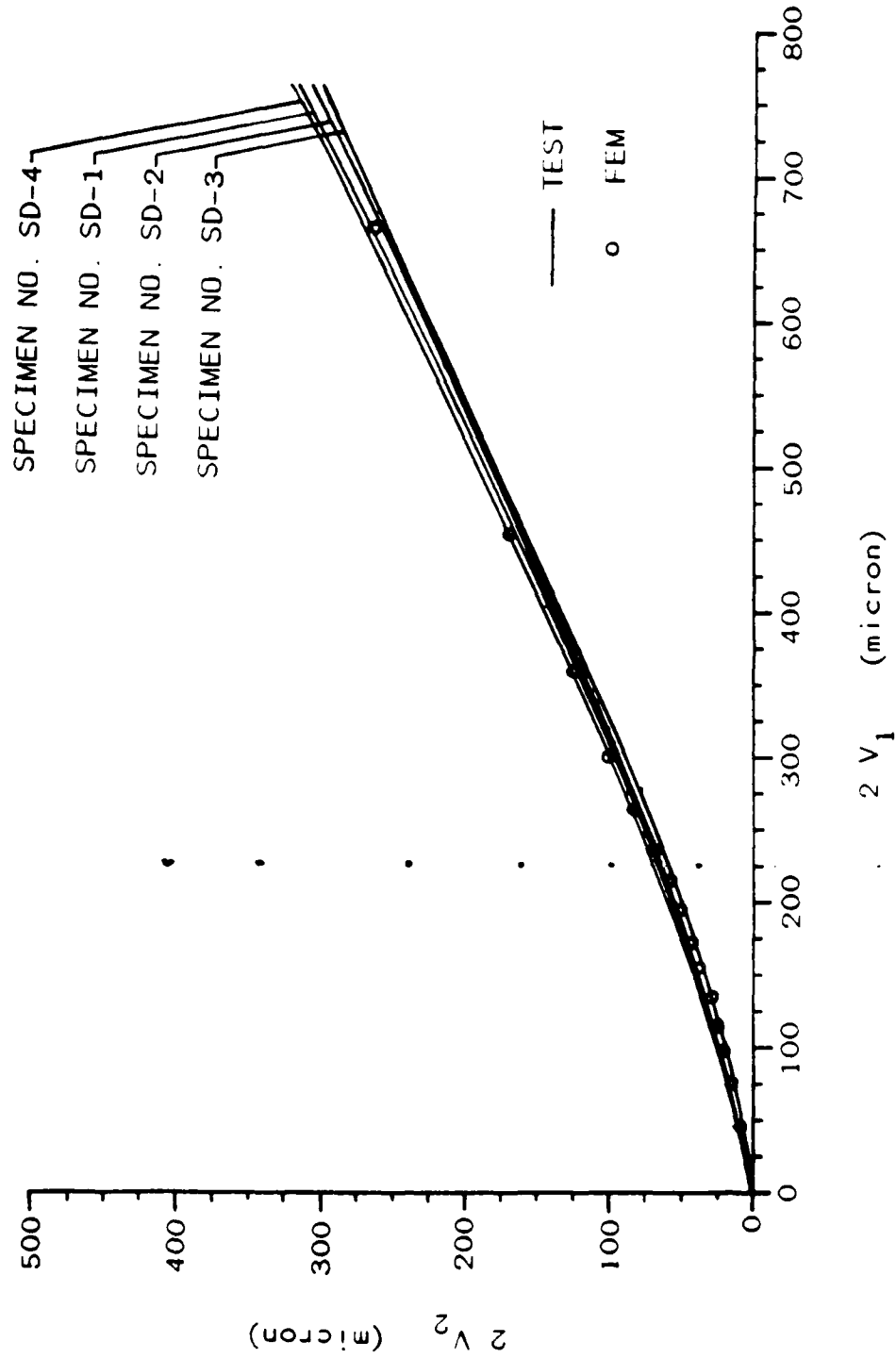


Figure 6.24 $2V_2$ Versus $2V_1$ for Small

CLWL-DCB Specimens, Group 4.

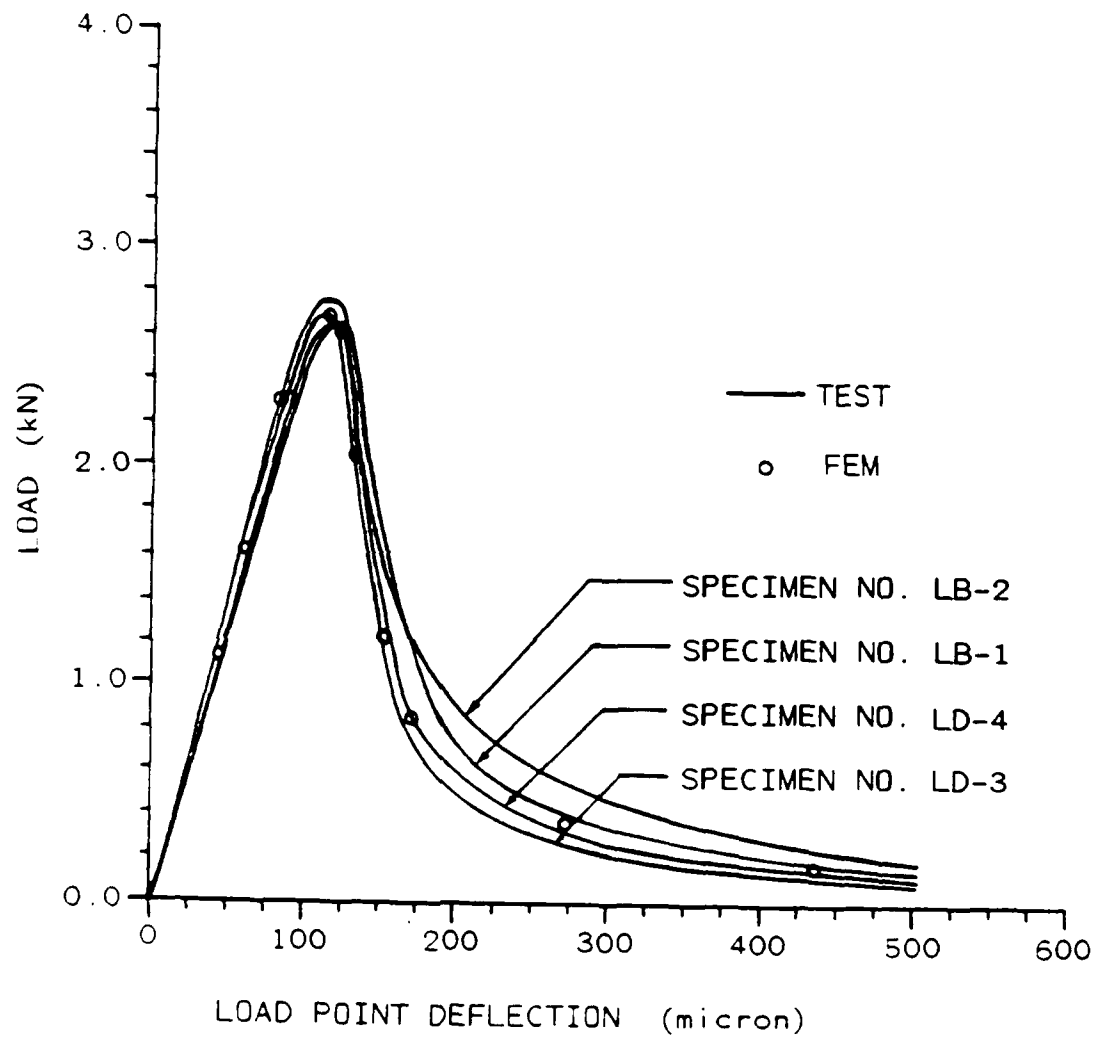


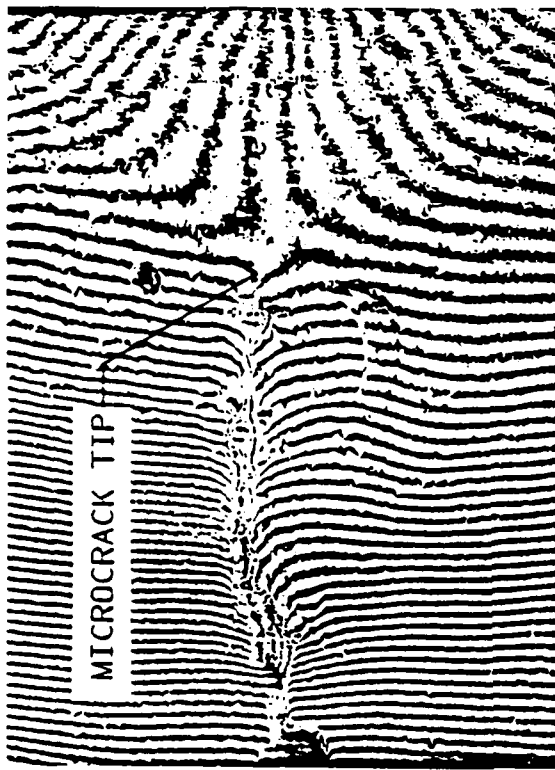
Figure 6.25 Load Versus Deflection Curves
Three Point Bend Specimens, Group 5.

After the peak load, the load decreased while the fracture process zone continued to extend. The moire fringe patterns data showed that a fully developed fracture process zone was achieved when the critical COD of 250 microns was reached.

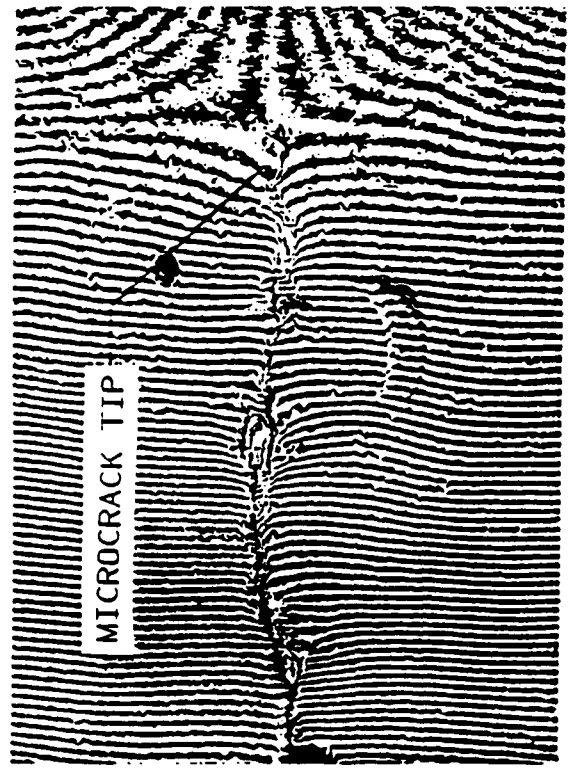
Figures 6.26 and 6.27 show typical sequentially recorded moire interferometry fringe patterns for the CLWL-DCB specimen No. SD-2 and the three-point bend specimen No. LB-1 at different load levels. These fringes are displacement contours of $1/1200$ mm intervals in the direction of perpendicular to the prenotches.

The order of the moire fringes was used to determine the COD's variation along the fracture process zone. The continuous curves in Figures 6.28 and 6.29 represent the COD variations along the fracture process zone at different load levels for the CLWL-DCB specimens No. SD-2 and No. SD-4. The continuous curves in Figures 6.30 and 6.31 represent the COD variations along the fracture process zone at different load levels in the three point bend specimens No. LB-4 and No. LB-1, respectively.

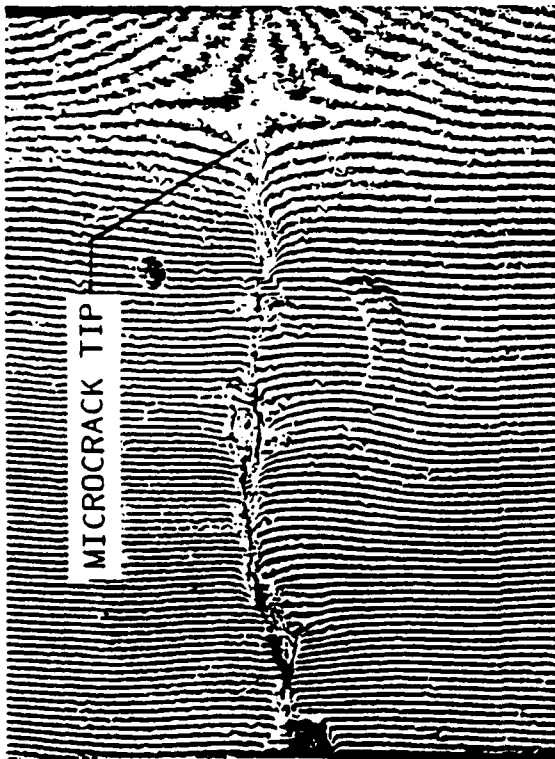
All moire patterns showed that the fracture process zone is not wide as three times aggregate size as postulated by others [60]. Instead, one aggregate size may be a better representation of the fracture process zone width. Similar observation was also obtained in the



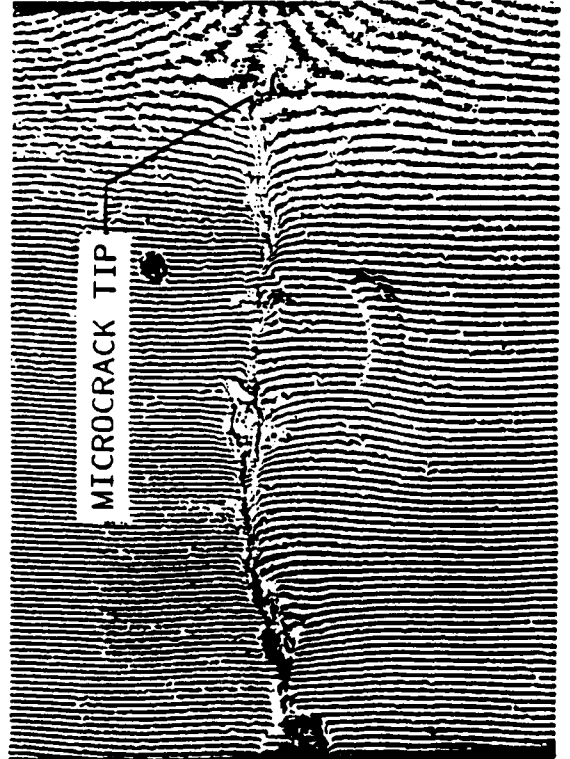
(a) LOAD = 1424 N



(b) LOAD = 979 N



(c) LOAD = 845 N



(d) LOAD = 601 N

Figure 6.26 Sequential Moire Fringe Patterns of
CLWL-DCB Specimen, Specimen No. SD-2

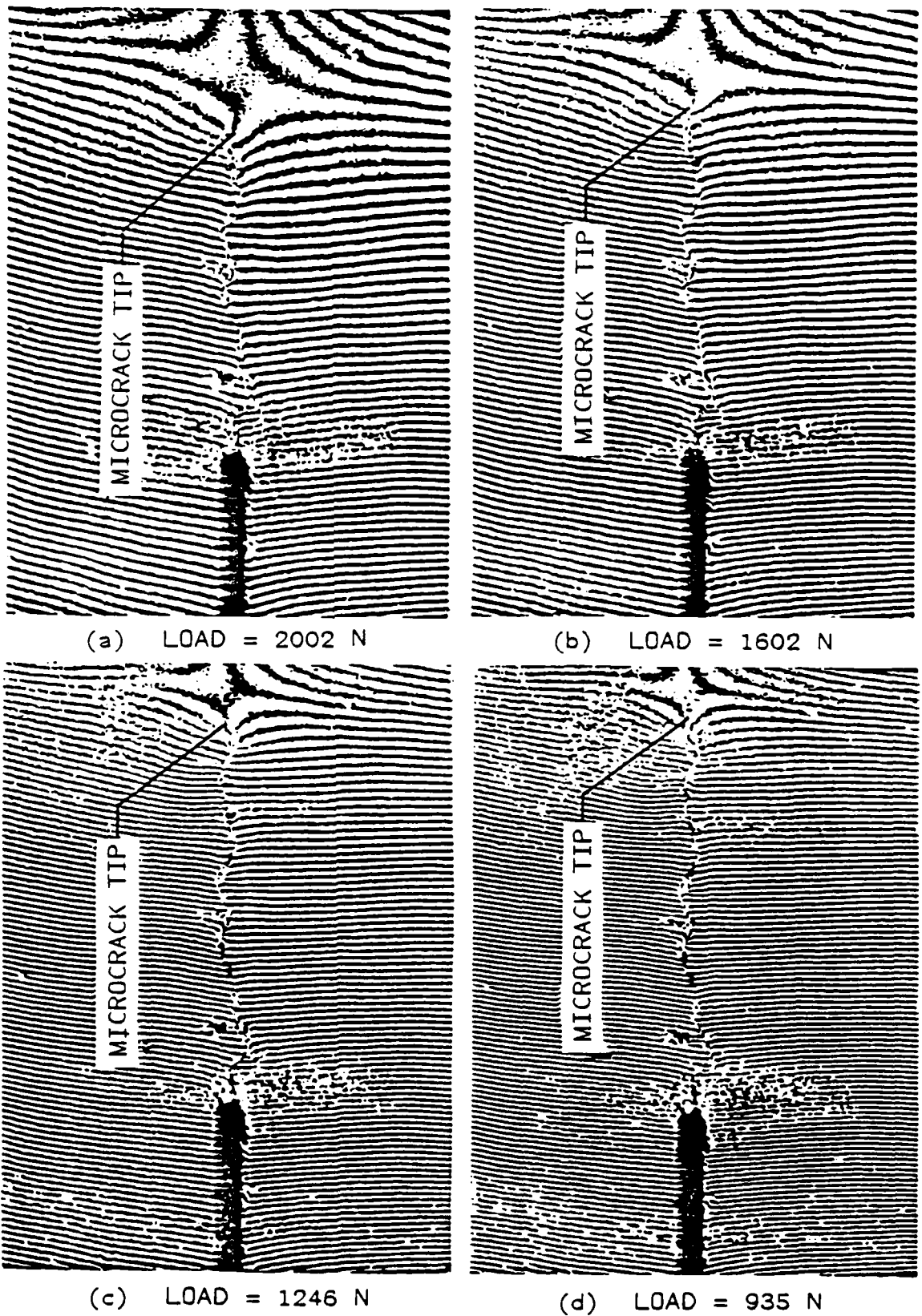


Figure 6.27 Sequential Moiré Fringe Patterns of Three Point Bend Specimen, Specimen No. LB-1

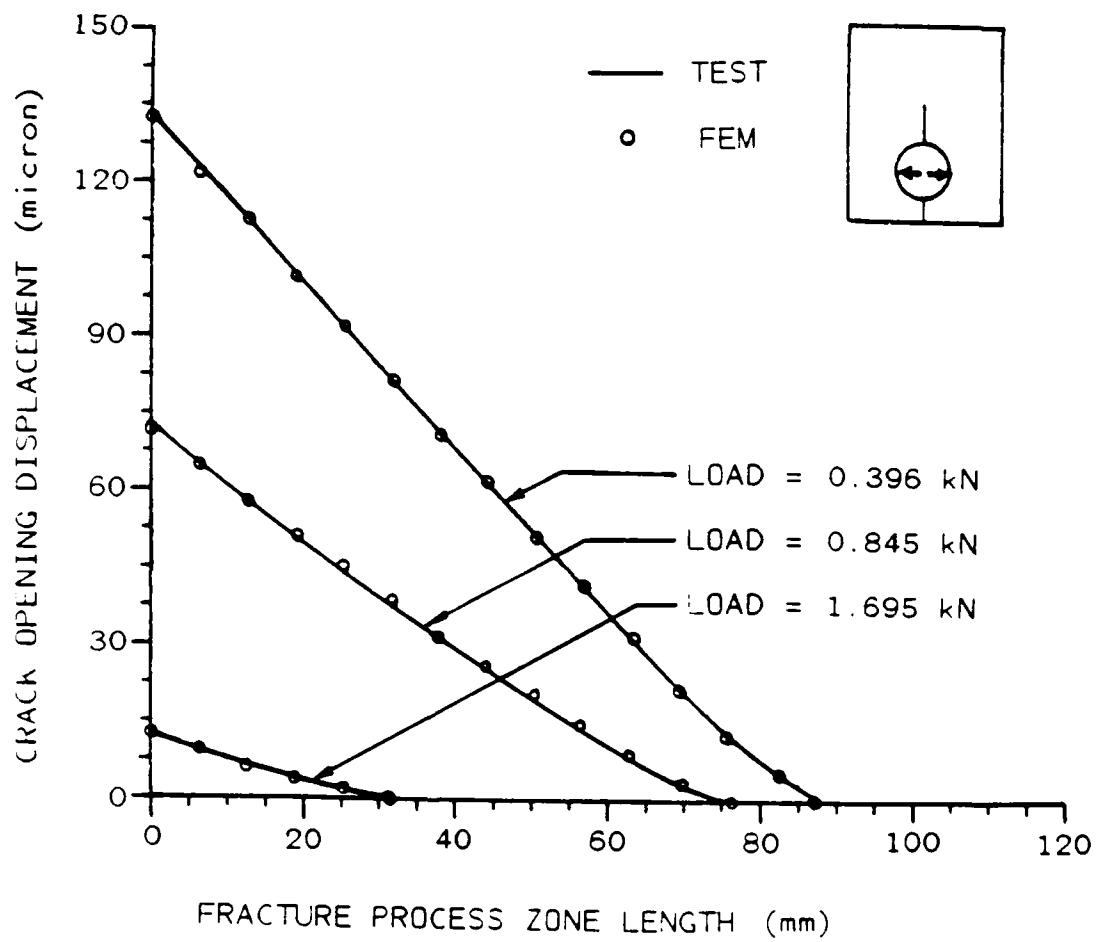


Figure 6.28 COD Variations along Fracture Process Zone
CLWL-DCB Specimen No. SD-2

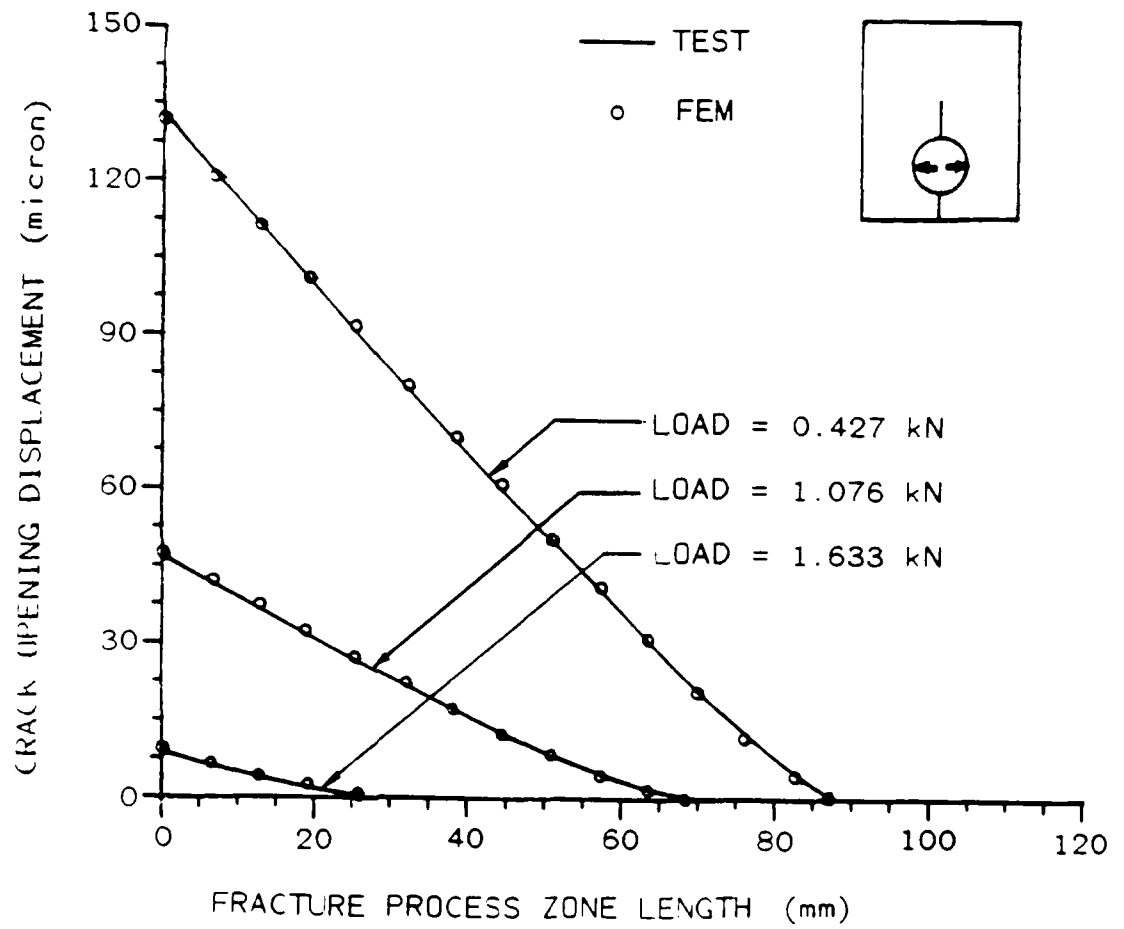


Figure 6.29 COD Variations along Fracture Process Zone
CLWL-DCB Specimen No. SD-4

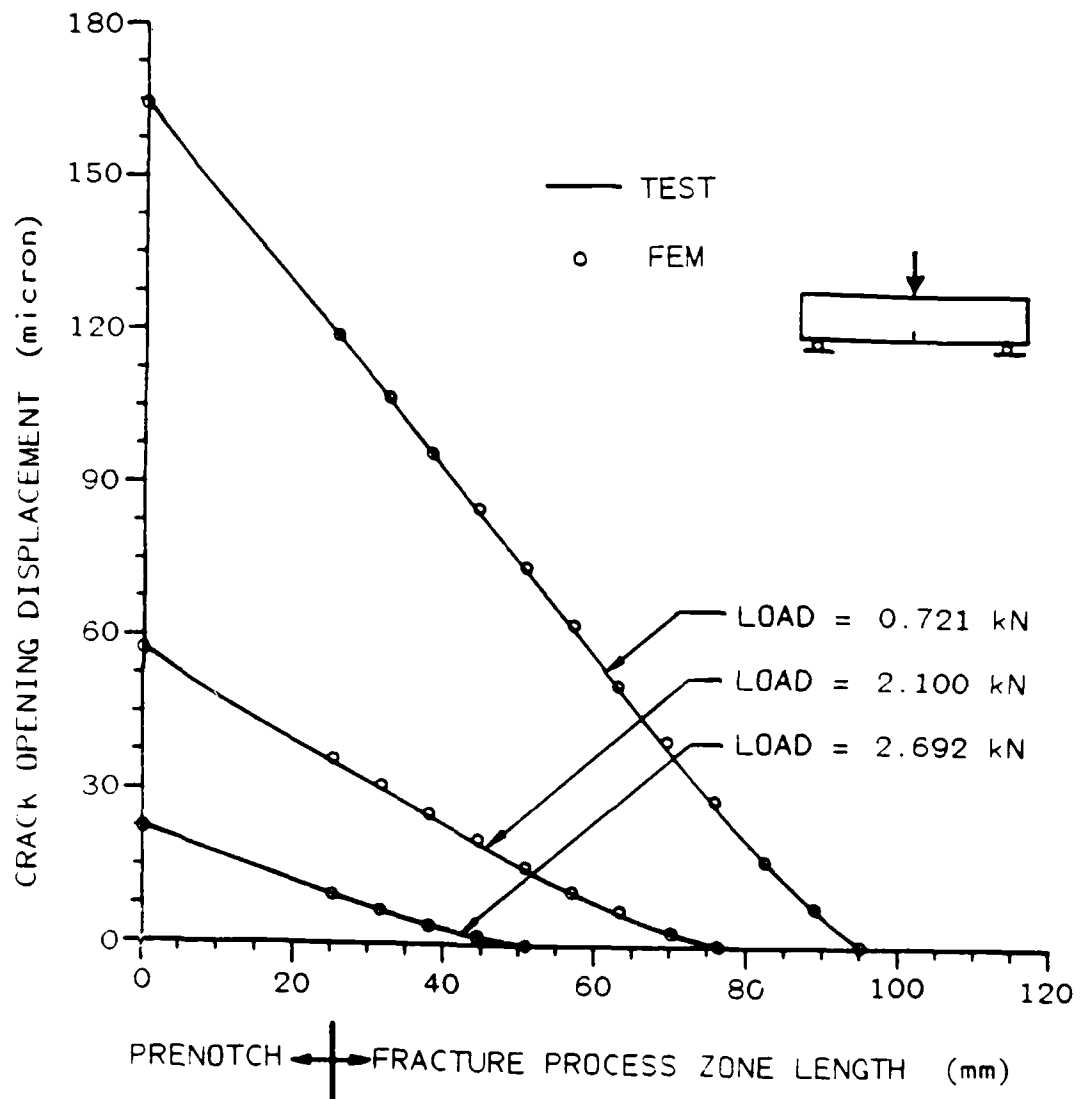


Figure 6.30 COD Variations along Fracture Process Zone
Three Point Bend Specimen No. LB-4

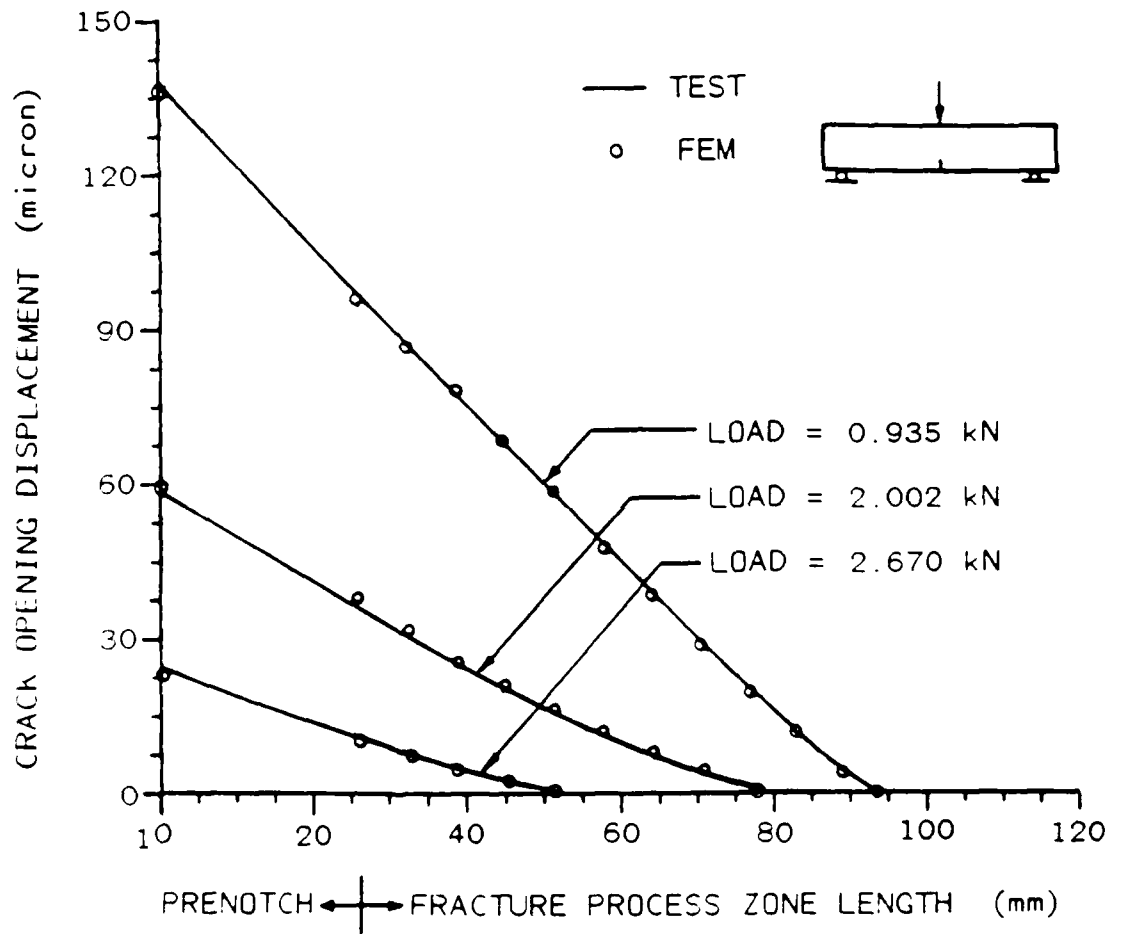


Figure 6.31 COD Variations along Fracture Process Zone
Three Point Bend Specimen No. LB-1

author's early moire interferometry test work on small beam specimens and large CLWL-DCB specimens. Some rough estimations on fracture process zone width are given in Table 6.2.

Table 6.2 Estimated Average Values of Fracture Process Zone Width

| Specimen No. | Specimen Type | Max. Aggr. Size | Frac. Proc Zone Width |
|--------------|---------------|-----------------|-----------------------|
| SD-2 | CLWL-DCB | 6.4 mm | 6.2 mm |
| SD-4 | CLWL-DCB | 6.4 mm | 6.5 mm |
| LD-1 | CLWL-DCB | 9.5 mm | 9.3 mm |
| LB-4 | Beam | 6.4 mm | 5.8 mm |
| SB-1 | Beam | 6.4 mm | 5.0 mm |

6.3.2 Numerical Results

The finite element mesh used for the CLWL-DCB specimens and that for the three point bend specimens are shown in Figures 6.32 and 6.33, respectively. As described in Chapter 5, the fundamental solutions, or the Green functions were first computed by linear elastic finite element analysis. The functional form of Equation (5-9) with three unknown parameters α , β and f_t' was assumed.

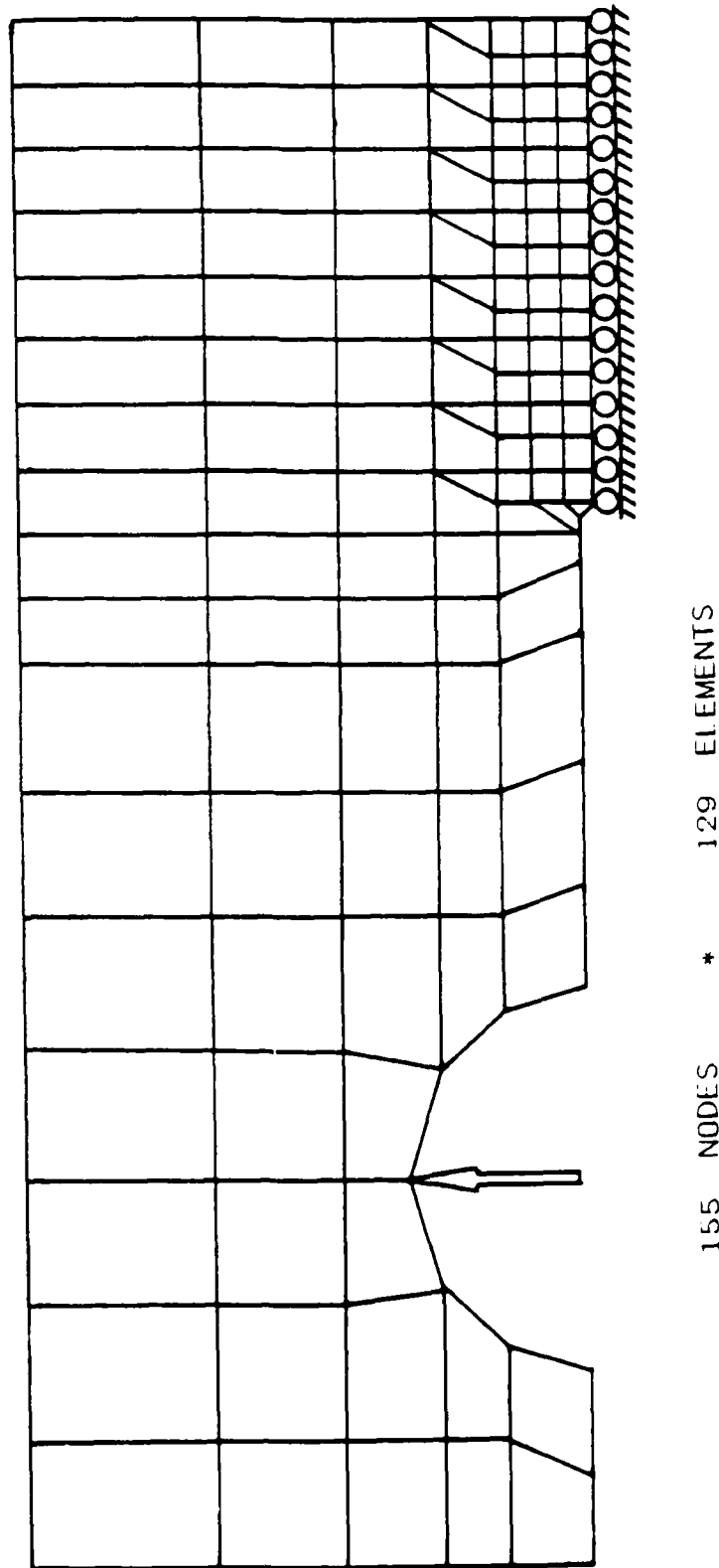
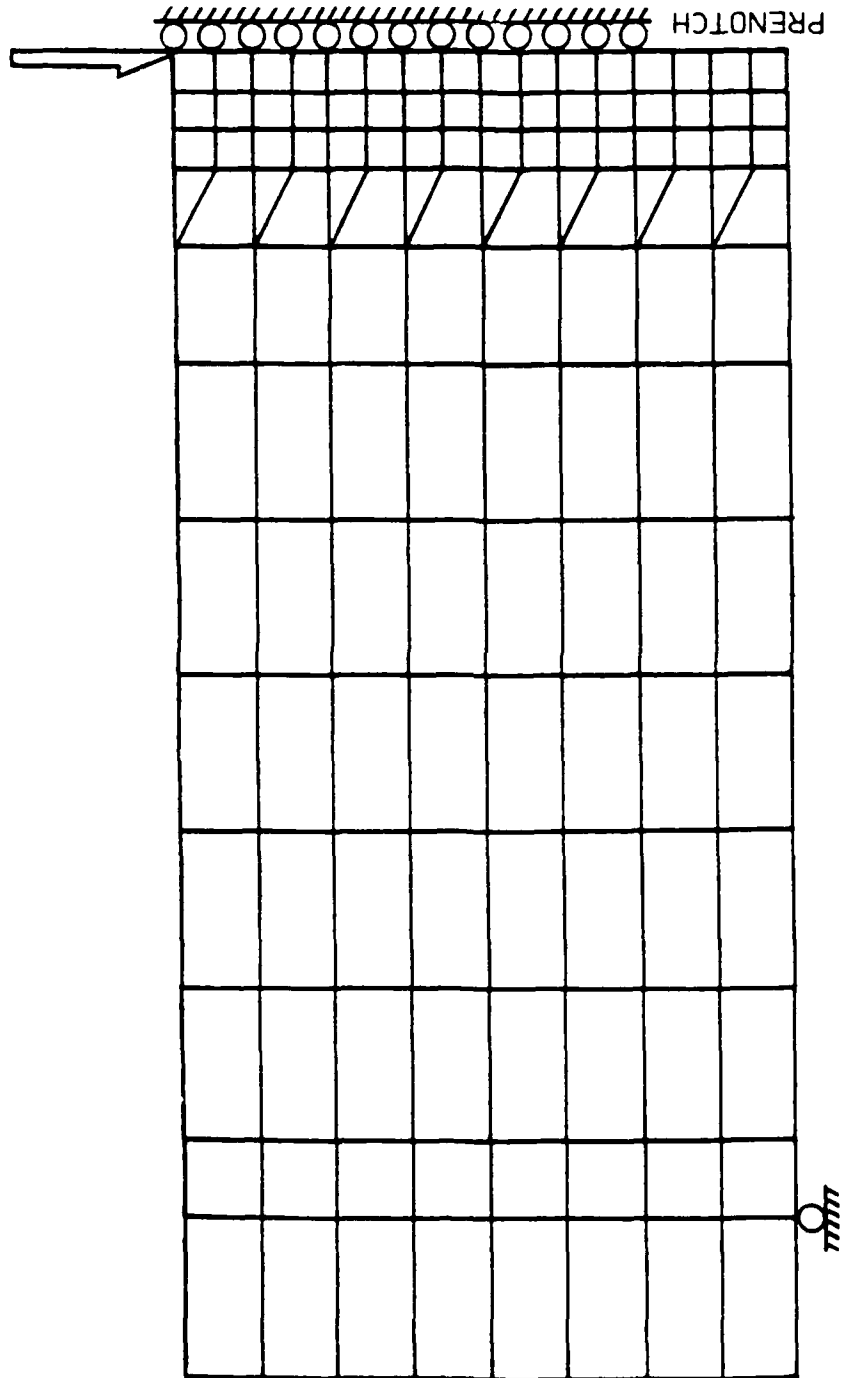


Figure 6.32 Finite Element Mesh for Group 4
Small CLWL-DCB Specimens



149 NODES * 128 ELEMENTS

Figure 6.33 Finite Element Mesh for Group 5 Large Three Point Bend Specimens

The resulting fundamental solutions were stored on a hard disc and later retrieved by another program which is used to determine the three unknown parameters in the crack closure stress versus COD relation which optimally satisfied the input experimental results of COD along the fracture process zone, load, $2V_1$ and $2V_2$ for the CLWL-DCB or load point displacement for the three point bend specimens.

The above generation phase of analysis was carried out twice using the test data of a CLWL-DCB specimen No. SD-2 and a three point bend specimen No. LB-4, respectively. The same resultant crack closure stress versus COD curve, as shown in Figure 6.34, for these two types of specimen was obtained through this hybrid experimental-numerical analyses. This relation also agrees well with the results of direct tension tests [12,42,103,104] as shown in Figure 6.35. The area under this curve is estimated to be 107 N/M, which is reasonably close to the work of fracture reported by others [46]. Also, the previously developed three-line model through the trial and error procedure was used to check the validity of the direct procedure and the function assumed. Good agreements in the general shape and the area, which is shown in Figure 6.36, were obtained.

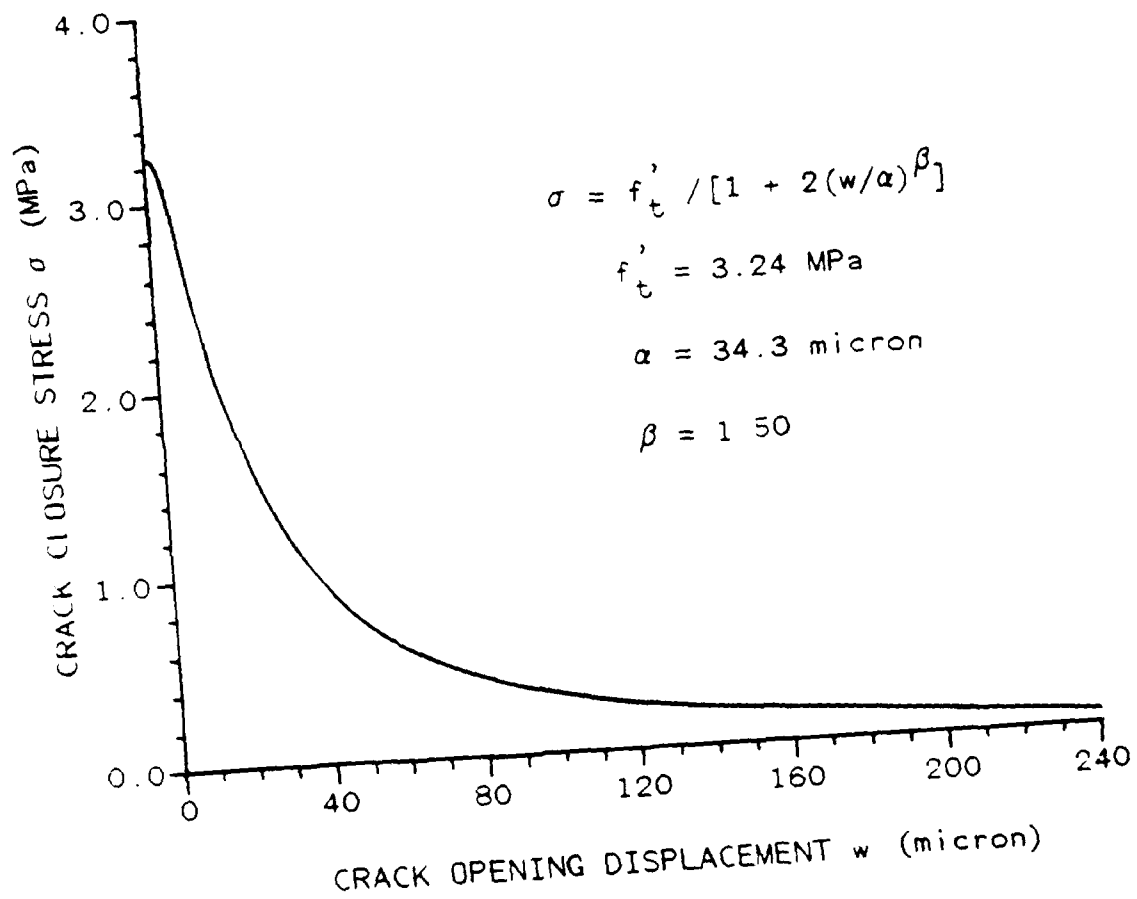
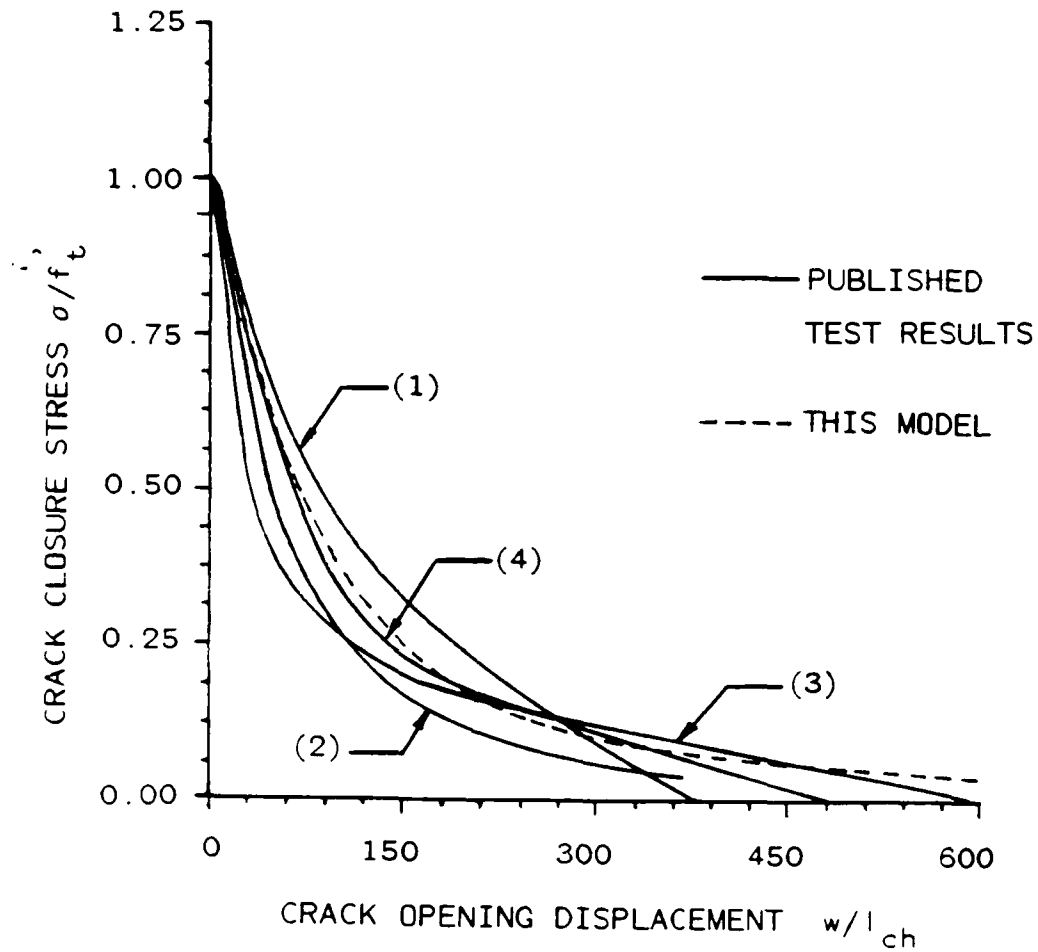


Figure 6.34 Crack Closure Stress Versus COD Relation for One Continuous Curve Model



(1) Evans, R. H. [103]

(2) Petersson, P. E. [42]

(3) Reinhardt, H. W. [12]

(4) Gopalarathan, V. S. and Shah, S. P. [104]

$$l_{ch} = G_F E / f_t'^2 \quad \text{CHARACTERISTIC LENGTH}$$

Figure 6.35 Comparison of Crack Closure Stress Versus COD Relationship with Published Direct Tension Test Results

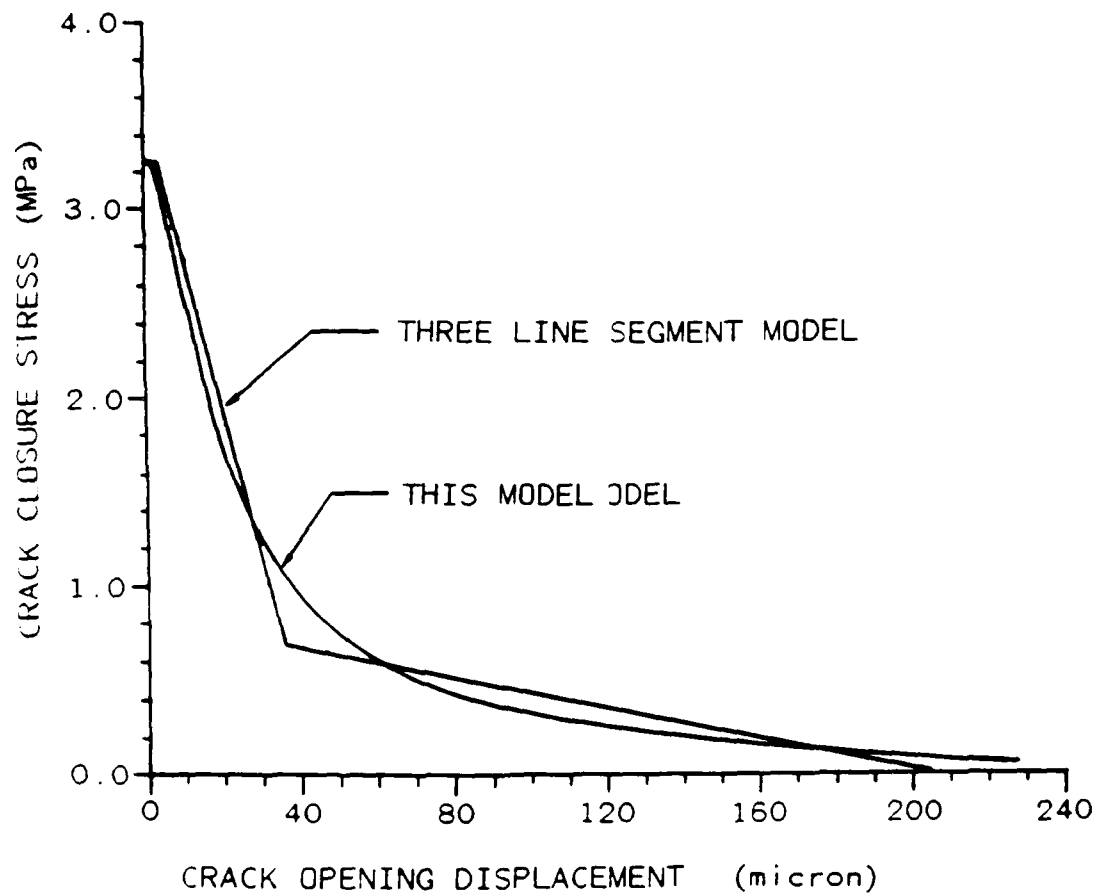
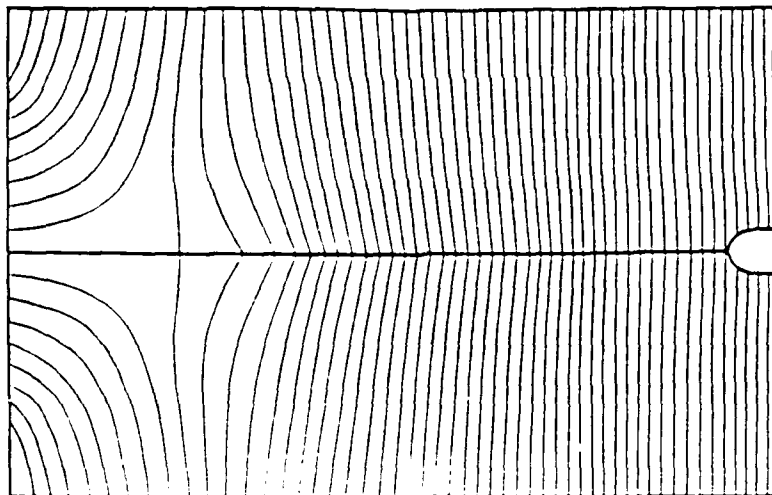


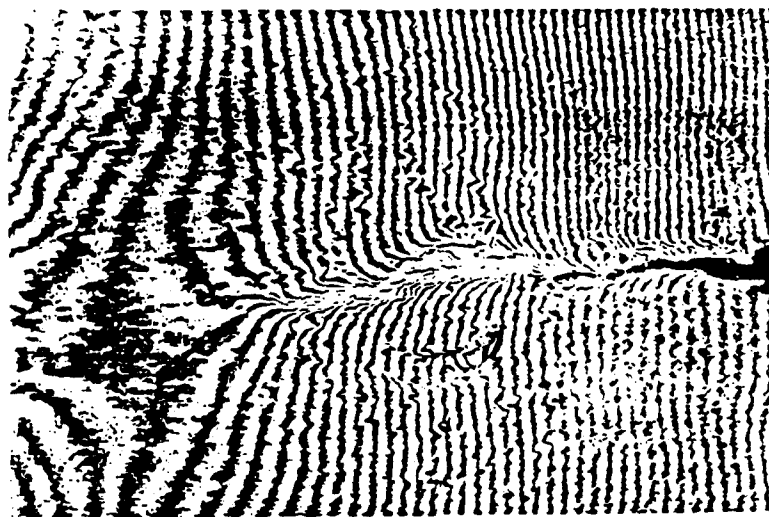
Figure 6.36 Comparison of Three - Line Model with One - Curve Model for Group 4,5 specimens

Once the constitutive relationship is established, other specimen behaviors can be predicted by the use of application phase of this finite element model. A third program, which computes the crack opening displacement, load, $2V_1$ and $2V_2$ for the CLWL-DCB and the load point displacement for the three point bend specimens, was used to compute the behaviors of other specimens. This is the application phase of the analysis.

In the application phase of analysis, the wedge load versus $2V_1$, $2V_2$ versus $2V_1$ relations for the CLWL-DCB specimens and the load versus load-point displacement relation for the three point bend specimens were computed and are represented by the data points in Figures 6.23, 6.24 and 6.25. The COD along the fracture process zone for the CLWL-DCB specimen No. SD-2 and No. SD-4 and for the three point bend specimen No. LB-4 and No. LB-1 were also computed and are shown as data points in Figures 6.28, 6.29, 6.30 and 6.31. The moire fringe patterns were also numerically generated. Figures 6.37 and 6.38 show a comparison of the predicted fringe patterns and the real test results for the CLWL-DCB specimen No. SD-4 and the three point bend specimen No. LB-1, respectively. The excellent agreements between computed and test results vouches for the reliability of the fracture process zone model which was determined directly through test data.

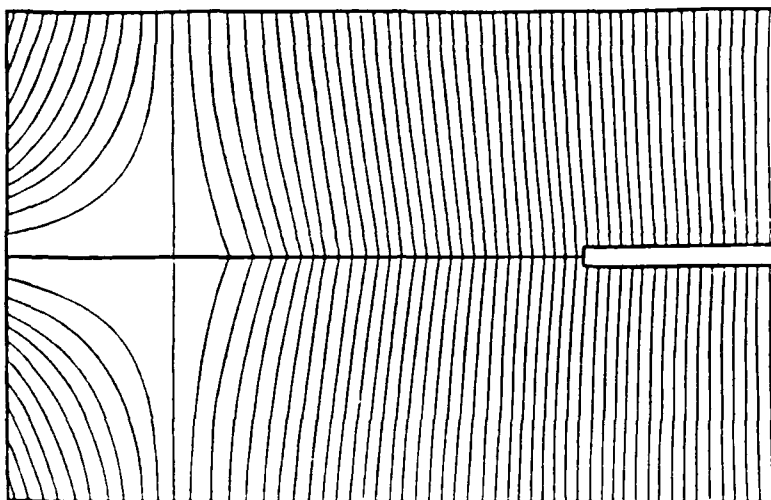


FEM PREDICTION

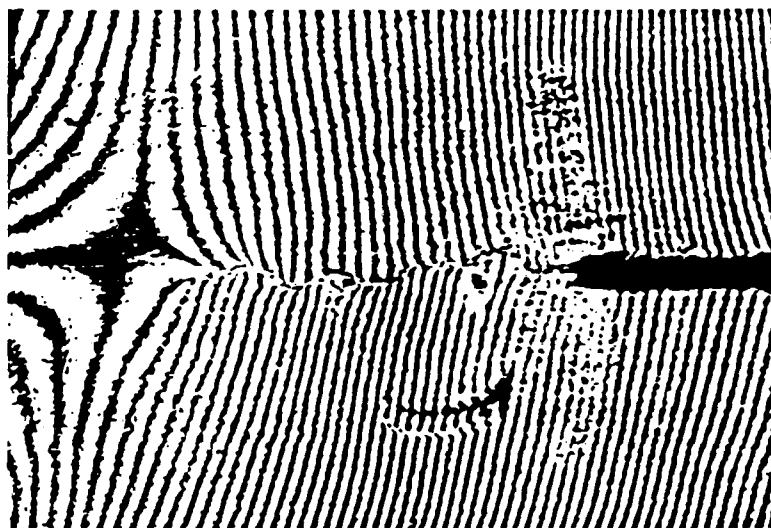


MOIRE TEST

Figure 6.37 Comparison of Test and Numerically
Generated Moire Fringe Patterns.
CLWL-DCB Specimen No. SD-4



FEM PREDICTION



MOIRE TEST

Figure 6.38 Comparison of Test and Numerically
Generated Moire Fringe Patterns.
Three Point Bend Specimen No. LB-1

Besides these comparisons, other numerical results were also obtained which predicted the stress distribution and energy partition. Since these quantities are not directly measurable, only numerical results were obtained. Figure 6.39 and Figure 6.40 show the normal stress distributions along the crack paths of CLWL-DCB and three point bend specimens, respectively. The existence of a considerable crack closure stress explains the increase in the loading capacity by the fracture process zone. Similar stress distributions were obtained for these two types of specimens. This fact suggests that different overall stress state need to be created in order to check the stress state dependency of the fracture model. Figures 6.41 and 6.42 are energy partitions for CLWL-DCB and three point bend specimens, respectively. The strain energies undergo an increase then decrease while the fracture energies monotonically increase at increasing rates with respect to the crack extensions. The total amount of the fracture energy should be equal to the G_F times the fracture area, which can be a double check of the finite element computation.

6.3.3 Discussions

In order to match the test results, a modulus of elasticity, E , was needed for the computations that was

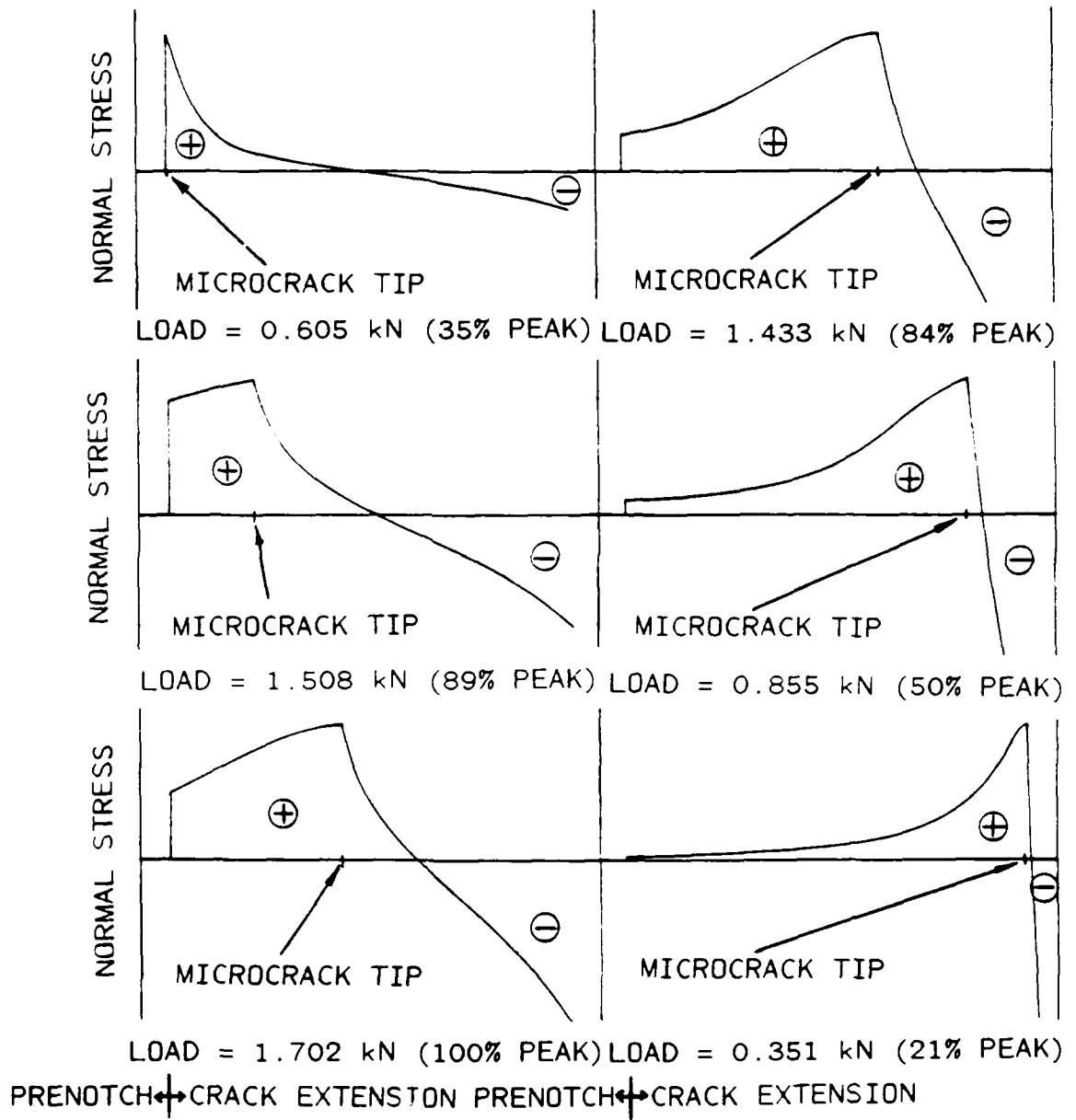


Figure 6.39 Computed Sequential Normal Stress Distributions along the Crack Path in Group 4 CLWL-DCB Specimens

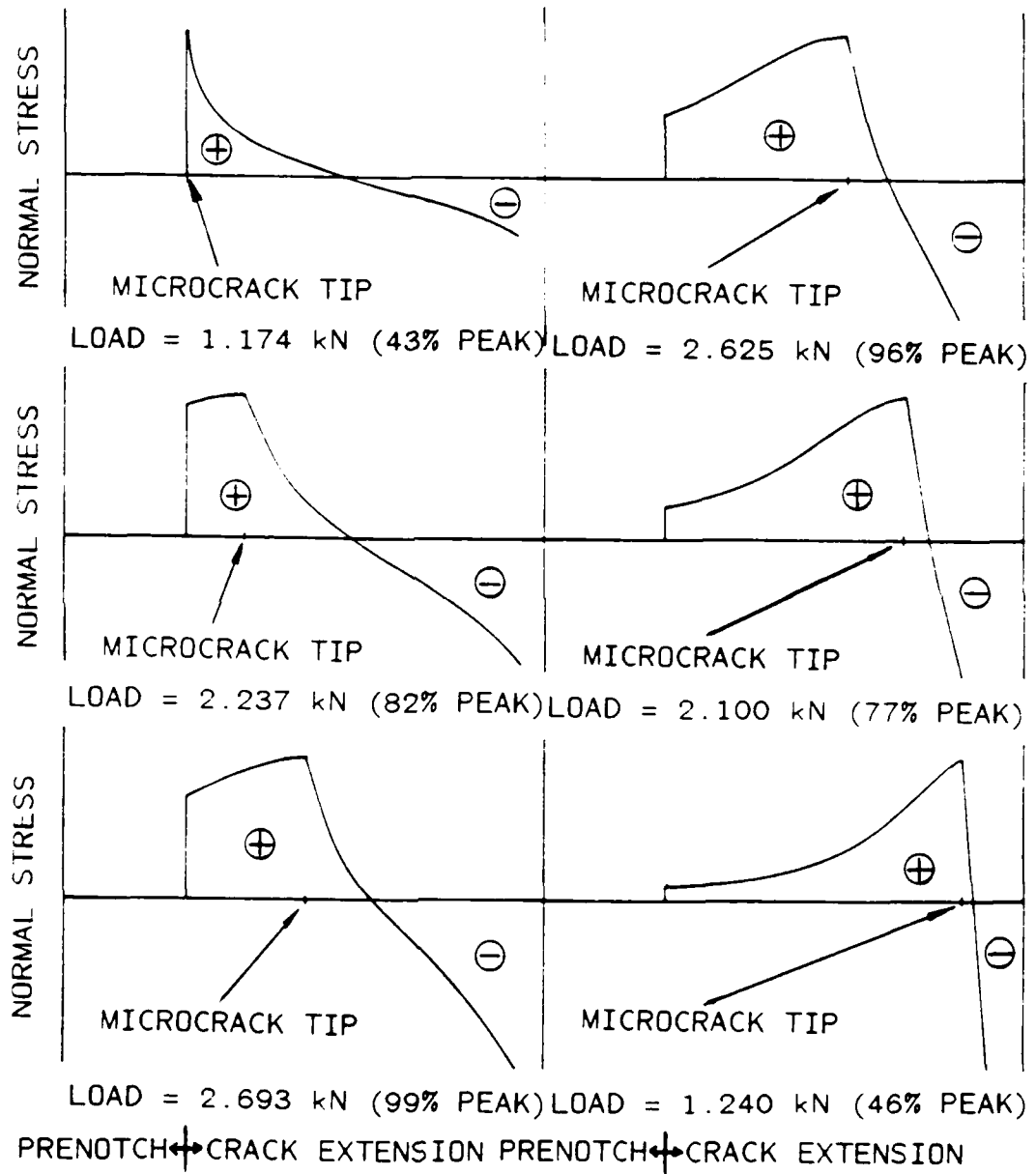


Figure 6.40 Computed Sequential Normal Stress Distributions along the Crack Path in Group 5 Three Point Bend Specimens

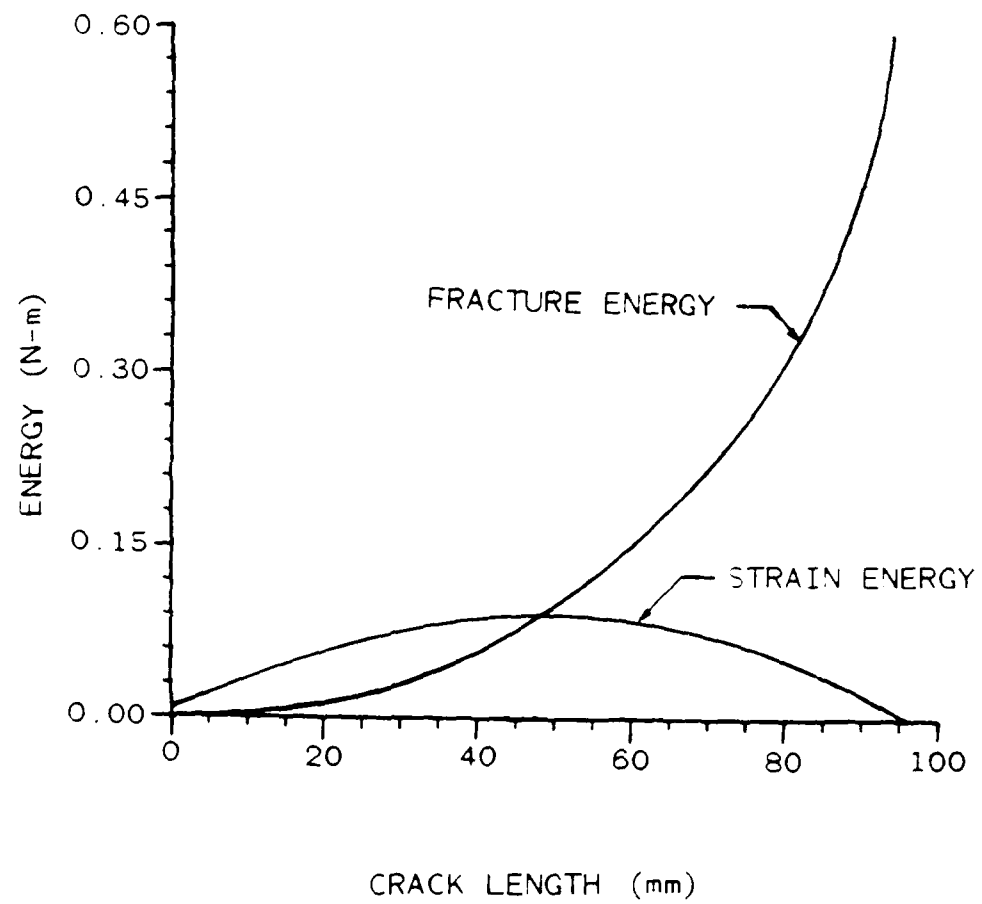


Figure 6.41 Energy Partition for CLWL-DCB Specimen Test, Group 4

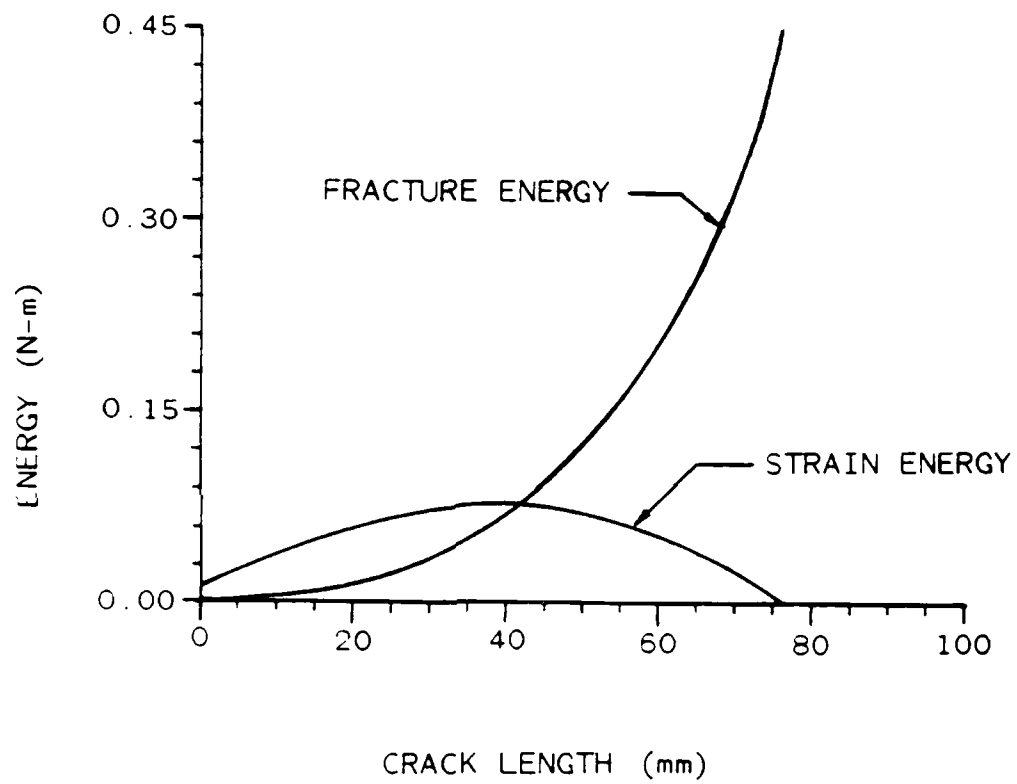


Figure 6.42 Energy Partition for Three Point Bend Specimen Test, Group 5

smaller than the values measured using the small tension specimens. The use of a smaller modulus of elasticity is reasonable since the measured E is the tensile tangential modulus which is smaller than the average slope for the ascending portion of the stress-strain curve. Furthermore, these specimens were subjected to both tensile and compressive loading where the compressive modulus for this concrete could be 20% smaller [9] than the tensile modulus. When only one E is used for computations, a smaller modulus would better represent the average condition than the initial tensile tangential modulus value.

The tensile strength, f'_t , was considered as one of the fracture parameters determined in the optimization procedure. The resulting tensile strength was slightly smaller than that measured by the direct tension test, but is within the range of the variation in material property and experimental error.

The Poisson's Ratio was assumed to be 0.15 [9]. The compressive strength was not needed for numerical analysis because the specimens were designed to fail in tension. All material properties are listed in Table 6.3.

In the finite element computation of three point bend specimen, an elastic support was assumed to compensate the finite stiffness of the loading assembly as well as any other additional reductions in the loading area stiffness.

Through a comparison of the initial slope of the load versus load point deflection curves of the test and numerical results, the stiffness of the support used in the computation was determined to be 53 kN/mm. This may be the cause of the discrepancies between the test and numerical data in Reference [116]. For the CLWL-DCB specimen, there is no such a problem because no deformation is measured at loading point and no need to support the specimen in the loading plane. Wedge load is a self-balanced loading system in the specimen plane.

Table 6.3 Material Properties for Computation
Specimens of Adequate Size

| | Measured | Estimated |
|-----------------------|----------|------------|
| Modulus of Elasticity | 29.6 GPa | 26.5 GPa |
| Poisson's Ratio | 0.15 | 0.15 |
| Compressive Strength | 35.4 MPa | not needed |
| Tensile Strength | 3.4 MPa | 3.2 MPa |

Finally, an explicit illustration is given in Figure 6.43, which shows crack closure stress and crack opening displacement distributions in fracture process zone for a CLWL-DCB specimen, as well as the associated moire fringe pattern.

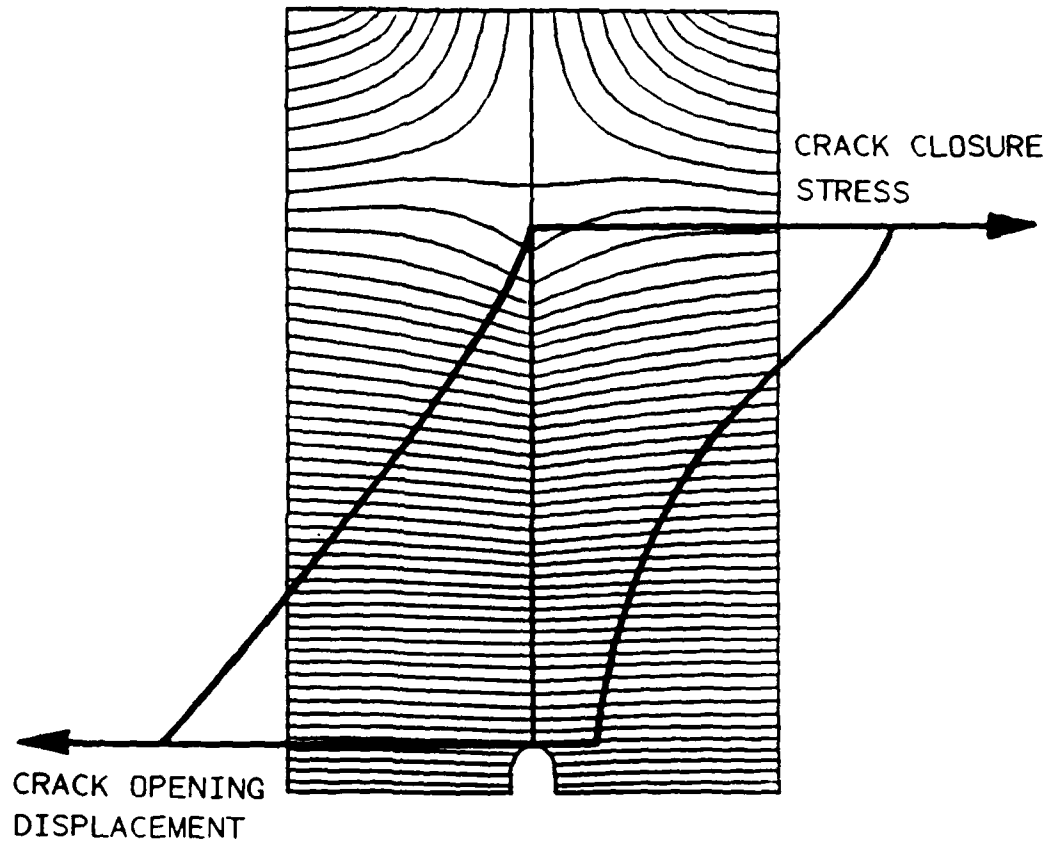


Figure 6.43 Crack Closure Stress, Crack Opening Displacement Distributions along Fracture Process Zone and Associated Computed Moire Fringe Pattern for CLWL-DCB Specimen No. SD-4

CHAPTER SEVEN

DYNAMIC FRACTURE OF CONCRETE SPECIMENS

Dynamic fracture mechanics has not been well developed even for metals. For concrete, results are even fewer. In this research area, two types time dependent phenomena and their combinations are investigated. Dynamic fracture can be the case of dynamic load with static crack or dynamic crack with static load or both of them are dynamic. The subject of this study belongs to the third category.

In this chapter the fracture process zone model developed for stable crack growth in concrete was extended to simulate dynamic crack propagation in concrete members subjected to impact loading conditions. A dynamic linear elastic finite element code with build-in function of the fracture process zone effect was developed and executed to predict specimen behaviors and study the strain rate effects on fracture of concrete.

7.1 Dynamic Fracture Process Zone Model

7.1.1 General

The commonly observed strain softening effect in static fracture of concrete tests has also been observed in concrete dynamic direct tension tests [86], This means that fracture process zone generally exists in cracked concrete

members so that any single parameter model of dynamic fracture mechanics is neither appropriate. The question is that if the Dugdale type fracture process zone model developed for static fracture is still valid for modelling dynamic fracture of concrete, and if the answer is positive, what kind of modifications should be made to represent strain rate effect. In order to answer these questions, specimens of different geometries and materials must be tested and multiple identical specimens should be tested at different loading rates together with dynamic finite element analysis. Since the dynamic test apparatus had not been set up at University of Washington when this work was carried out, test results from Mindess et al. [88,89] at the University of British Columbia and from Shah et al. [91,92] at the Northwestern University were used as data bases for developing a fracture process zone model.

7.1.2 Formulation Considerations

Although the use of the superposition principle and Green functions reduces computing time for the simulation of the static fracture process zone, it does not when the inertial forces are included for dynamic finite element computation. The reason is that inertial forces are applied on every nodal point so that too many fundamental solutions must be computed and saved on the computer.

Hence, the formulation based on the superposition principle, described in Chapter 5, was not used for the dynamic finite element computations. Instead, a direct finite element computation using three-line model was conducted.

For constructing the dynamic fracture process zone model, all the assumptions used for static fracture study in the foregoing chapters are still valid here. The details of the dynamic finite element implementation are given in APPENDIX D and only the essential procedures are presented here.

7.2 Preliminary Results

7.2.1 Simulation of Mindess' Impact Tests

The fracture process zone model used in this analysis was derived, through a hybrid experimental-numerical technique, from the results of laboratory tests of static mode I and mixed mode I and II fracture of concrete CLWL-DCB specimens. As shown in Figure 7.1, the variation in the crack closure stress in fracture process zone can be approximated by three straight lines which intersect at three critical crack widths. Figure 7.2 shows the constitutive model, for the fracture process zone, which relates the crack closure stress and crack opening

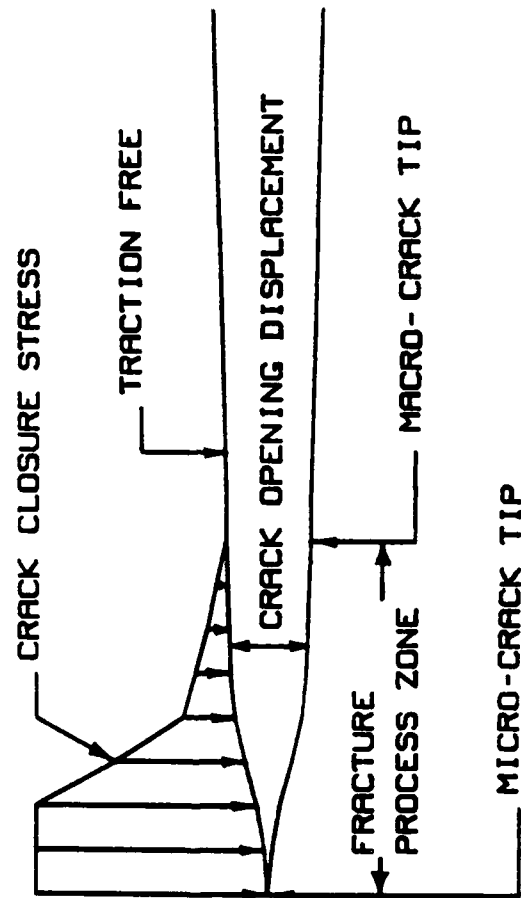


Figure 7.1 Fracture Process Zone of Concrete for Dynamic Fracture Modelling

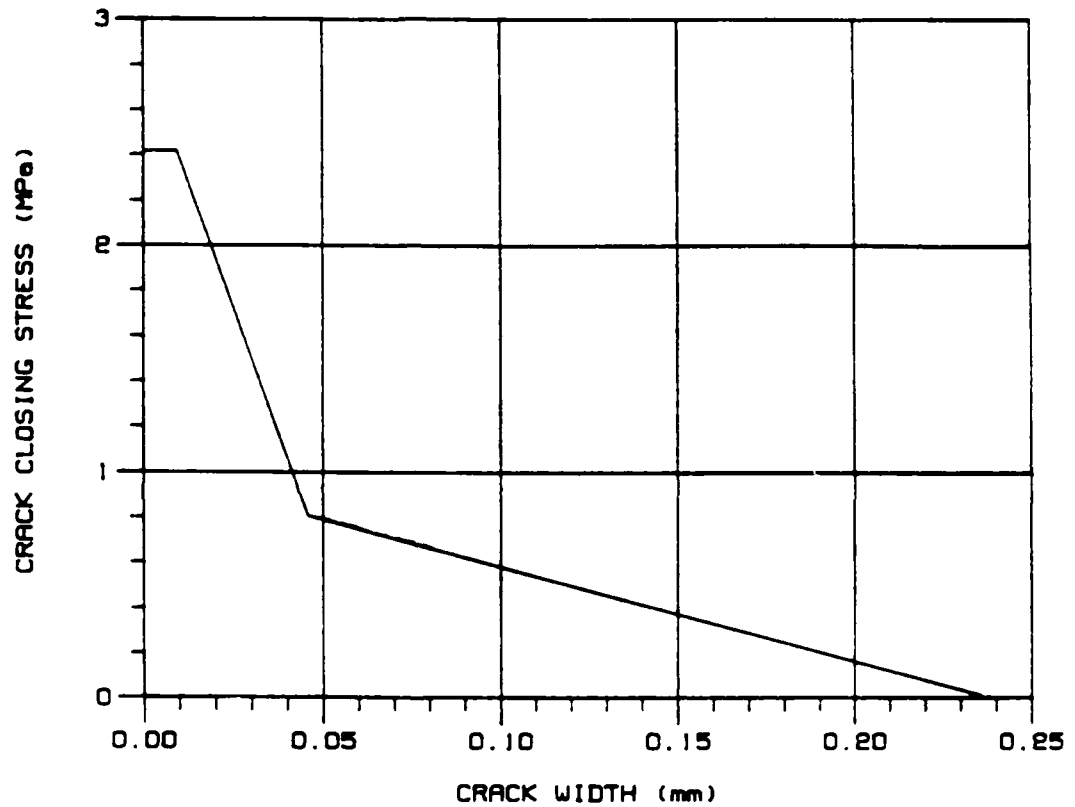


Figure 7.2 Crack Closure Stress Versus COD for Modeling Fracture Process Zone in Impacted Beams. Simulation of Mindess' Impact Tests

displacement in the fracture process zone. This constitutive relation was developed originally for static loading fracture [9]. Also, it was assumed that dynamic linear elasticity theory is still valid in the region outside the fracture process zone.

The fracture process zone model was incorporated into an implicit dynamic finite element code. The three segments of the fracture process zone, which satisfy the crack closure stress versus COD relation shown in Figure 7.2, are determined through numerical iteration. That iterative scheme is similar to the incremental-iterative procedure of elastic-plastic analysis. It consists of matching, through trial and error, an assumed variation in crack width along the postulated fracture process zone with the computed crack width for the prescribed load history and crack closure stress distribution.

The fracture criterion is a simple tensile overload criterion with fracture occurring along the preset crack path for mode I crack propagation when the maximum average tensile stress in the assumed controlled volume, that is the maximum aggregate size, of the crack tip element reaches the prescribed tensile strength. In Figure 7.3, the broken and solid lines indicate the position of the crack prior to and after its advancement, respectively, and

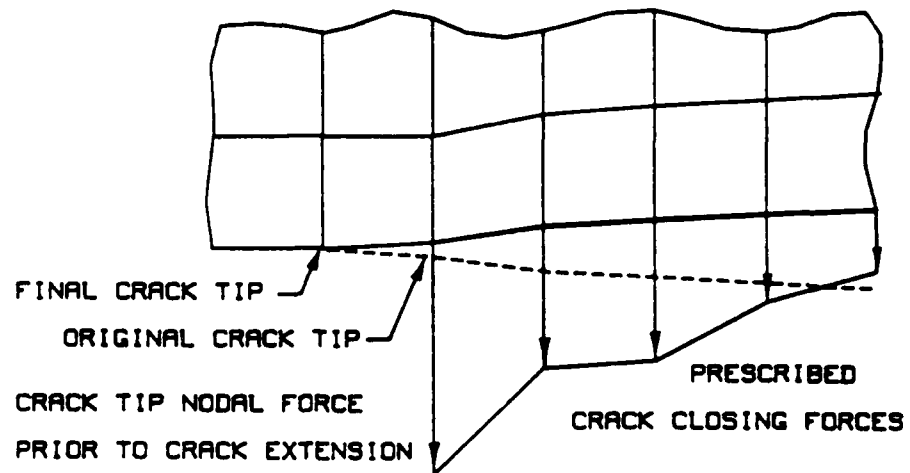


Figure 7.3 Crack Tip Nodal Force Released Mechanism
Dynamic Finite Element Simulation

the crack tip nodal force at D that exists prior to crack propagation. Thus, when the maximum average tensile stress along AD exceeds the tensile strength of the concrete, the crack tip nodal force at D is released at a prescribed rate that is governed by the crack velocity [111]. Lacking any definitive data on measured crack velocity versus driving force relation for concrete, two hypothetical crack velocities were used in this analysis: one was the theoretical terminal velocity for Rayleigh wave propagation, which in this case is 1847 mps; and, the other was ten percent of the dilatational stress wave velocity or 319 mps. The latter velocity is comparable to the velocities observed for brittle materials, such as glass [117], reaction bonded silicon nitride [118,119], and ductile materials, such as polycarbonate [120] and carbon steel [121]. Table 7.1 shows the material properties of the concrete assumed for this analysis.

Table 7.1 Material Properties of Concrete
for Simulation of Mindess' Test

| | |
|----------------------------|------------------------|
| Elastic Modulus | 23.6 GPa |
| Tensile Strength | 2.46 MPa |
| Poisson Ratio | 0.15 |
| Density | 2404 kg/m ³ |
| Dilatational Wave Velocity | 3190 mps |

Impact Test Specimen No. 1

Figure 7.4 shows the proportions, loading, and instrumentation for a plain concrete beam. That beam was impacted by a falling hammer at an impact velocity of about 3 mps [88]. Figure 7.5 shows the load history as measured at the hammer [88]. Figure 7.6 shows the finite element mesh used in the analysis. Figures 7.7 and 7.8 show the computed lengths for crack extension with time, with and without the fracture process zone, for assumed instantaneous crack velocities of 1847 mps and 319 mps, respectively. The computed response is indicated by stepwise broken lines. The computation was terminated at the last element in the crack path, and the elapsed time from initial impact to complete failure of the beam had to be estimated by fitting a curve through those discontinuous run-arrest crack paths. The average crack velocities obtained from the computation with the fracture process zone are in good agreement with that of the test results. On the otherhand, the average crack velocities obtained from the computation without the fracture process zone are too high compared to the test result. These results suggest that energy is dissipated within fracture process zone and in turn retards crack propagation even under dynamic loading. It should also be noted that the computed time to failure is relatively insensitive for the two

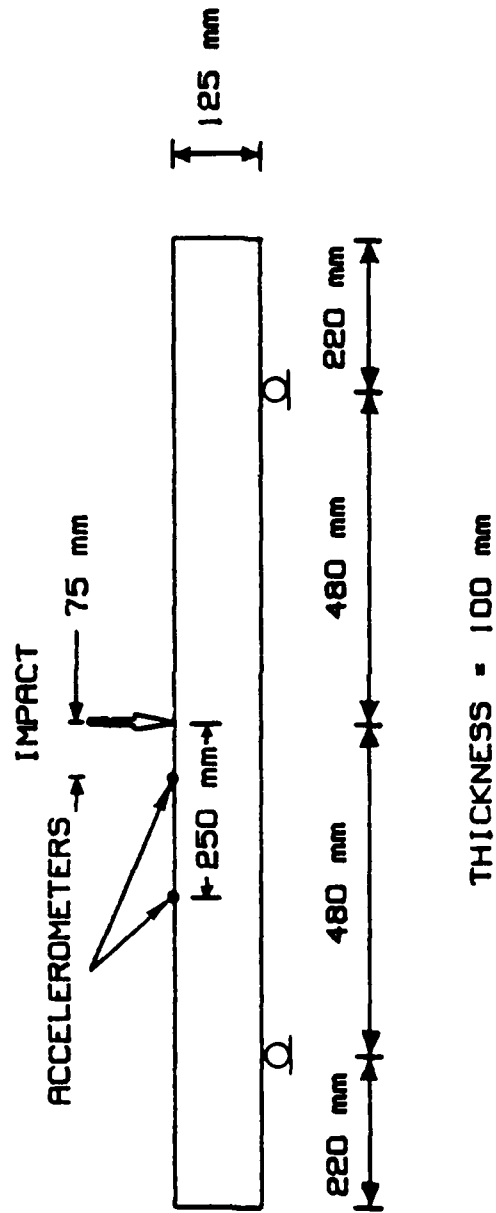


Figure 7.4 Mindess' Impacted Concrete Beam Test Specimen No. 1, Ref. [88]

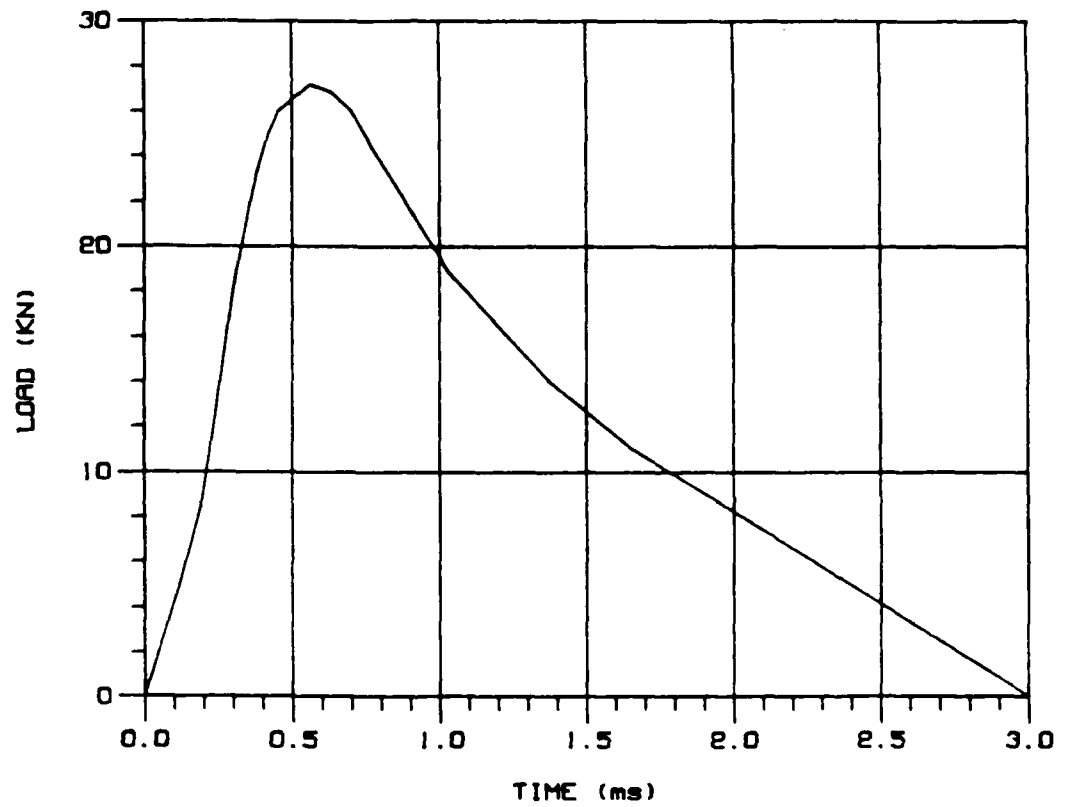
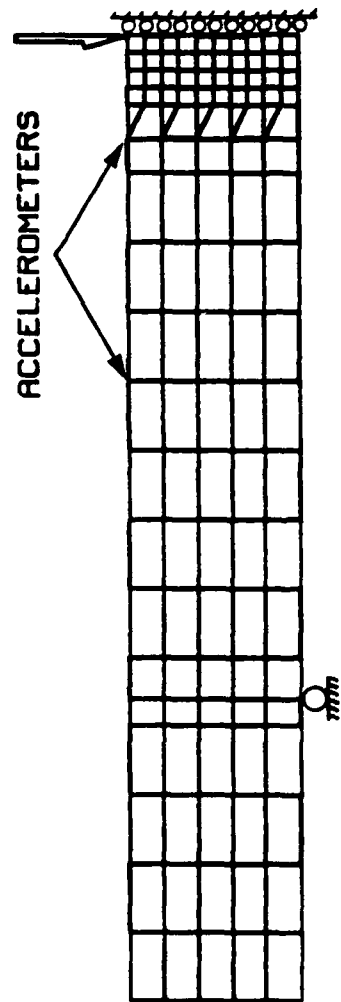


Figure 7.5 Prescribed Load-History for Concrete beam Specimen No.1, 1, Ref. [88]



145 NODES * 180 ELEMENTS

Figure 7.6 Finite Element Model for Impacted Beam Specimen No.1, 1, Ref. [88]

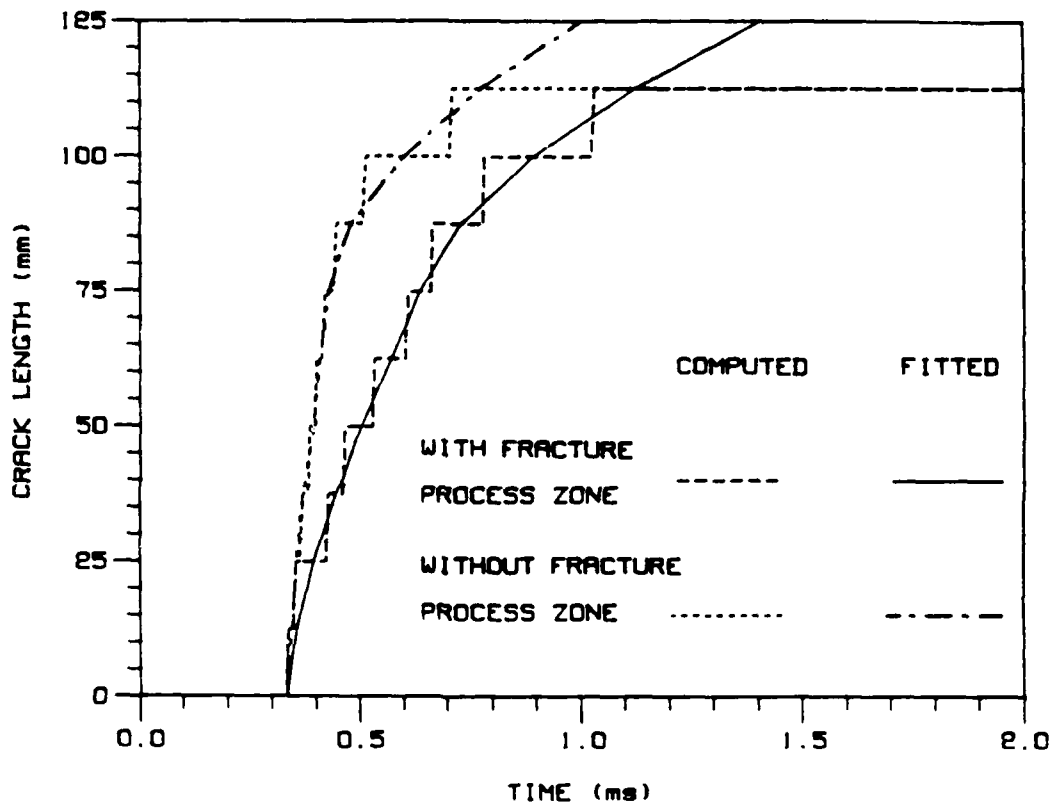


Figure 7.7 Computed Crack Length Versus Time
Specimen No. 1, Ref. [88]
Assumed Crack Velocity 1847 mps

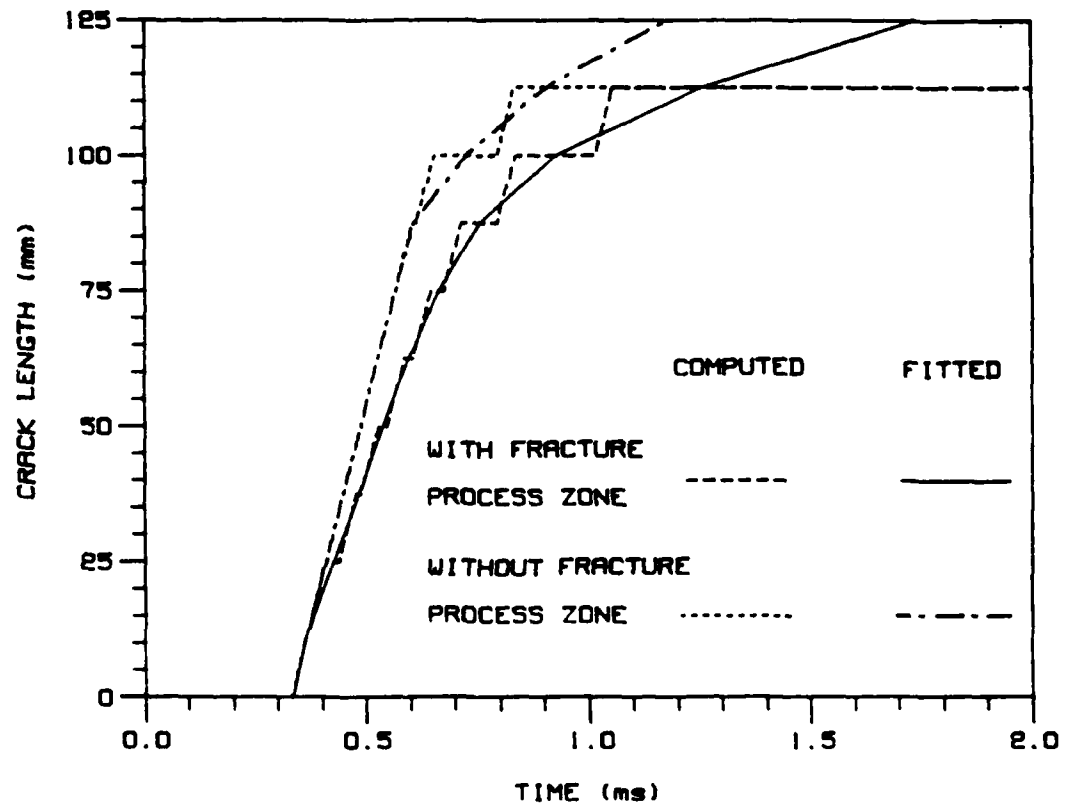


Figure 7.8 Computed Crack Length Versus Time
Specimen No. 1, Ref. [88]
Assumed Crack Velocity 319 mps

widely varying crack velocities used in the analysis. In effect, the shorter propagation time for the higher velocity is offset by the longer arrest time in this numerical test.

Figures 7.9 and 7.10 show the velocity versus time curves at the two accelerometer positions indicated in Figure 7.6. Since the computed velocity curves for the postulated crack velocities are nearly identical, no attempt was made to distinguish between the two different computations. The continuously varying acceleration traces reported in Reference [88] were integrated to provide the experimental velocity traces which were then compared with the numerical results. While the agreement between the measured and computed results is only fair, the better agreement between the computed results with a fracture process zone underscores the effectiveness of the postulated fracture process zone in modeling dynamic fracture of concrete.

Figure 7.11 shows the computed and measured load point deflections. The computed results were obtained by using finite element models with and without the fracture process zone. The close agreement between all three results indicates that the load point deflection is not sensitive to the details of the crack tip state or the assumed crack velocity.

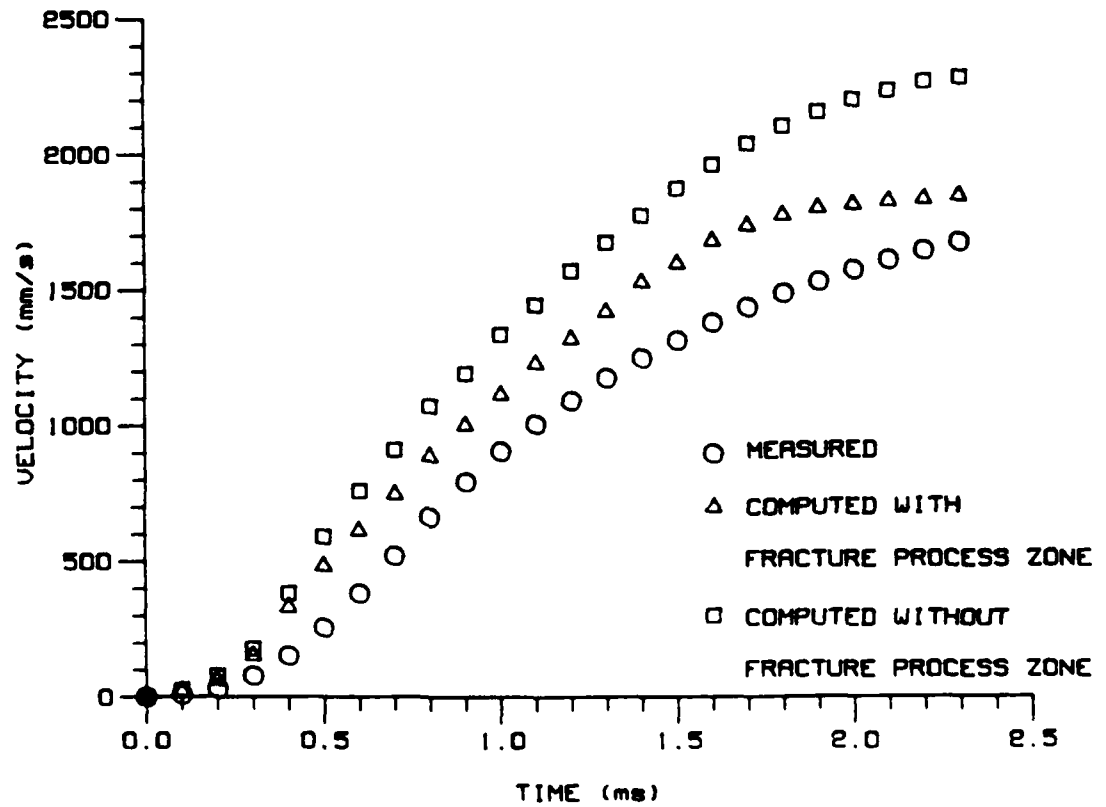


Figure 7.9 Deflection Velocity Versus Time Curves
at 75 mm from Beam Center
Specimen No. 1, Ref. [88]

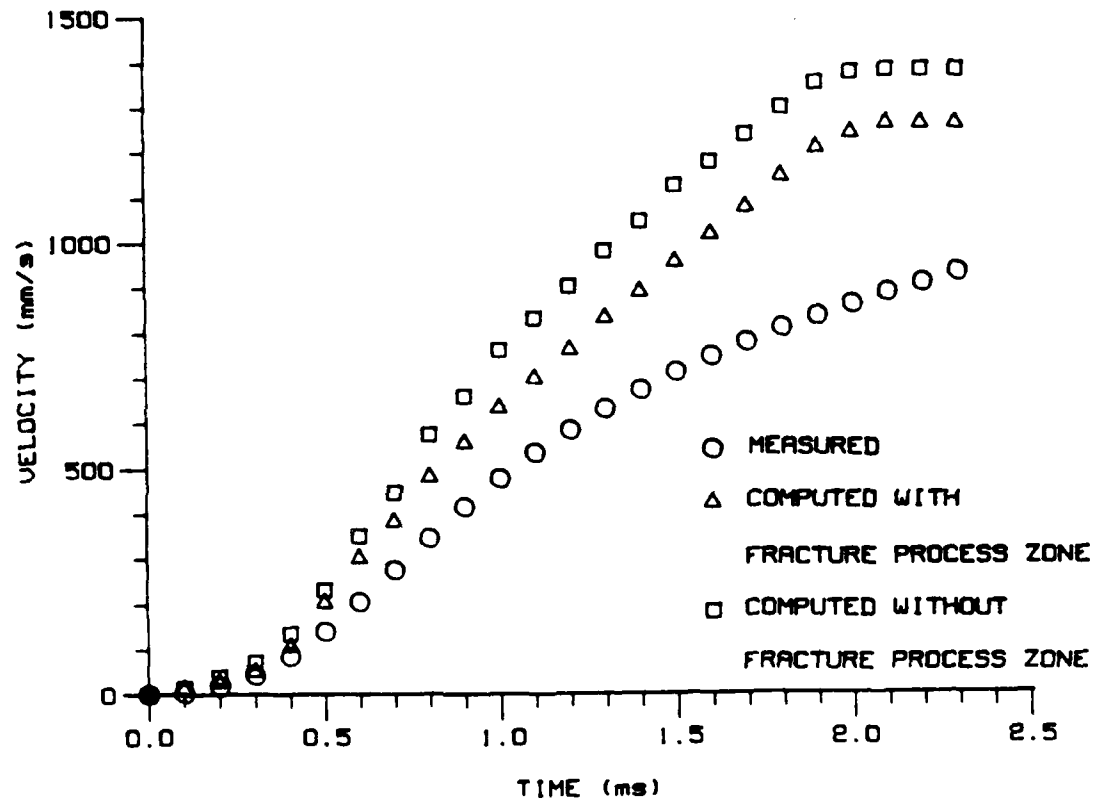


Figure 7.10 Deflection Velocity Versus Time Curves
at 250 mm from Beam Center
Specimen No. 1, Ref. [88]

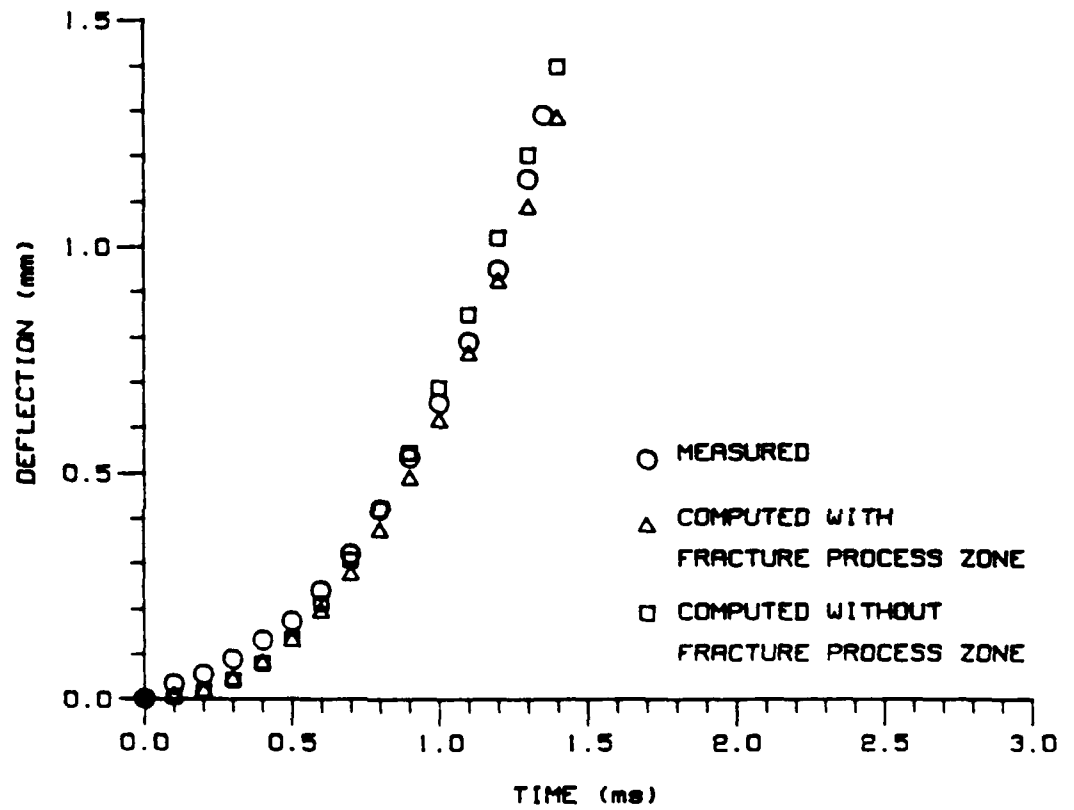


Figure 7.11 Load Point Deflection Versus Time for Specimen No.1, 1, Ref. [88]

Impact Test Specimen No. 2

Figure 7.12 shows the plain concrete beam which is reported in Reference [89]. This beam was impacted by a falling hammer with an impact load history as shown in Figure 7.13. Figure 7.14 shows the finite element mesh used in the analysis.

Figures 7.15 and 7.16 show the computed crack length versus time relation, without and with the fracture process zone, for instantaneous crack velocities of 1847 mps and 319 mps, respectively. The same conclusions as those obtained from test specimen No. 1 can be made from the comparison of the average crack propagation velocities computed with tested. The estimated average crack velocities are shown in Table 7.2.

Table 7.2 Estimated Average Crack Velocities
for Mindess' Impact Test

| | Specimen No. 1 | | Specimen No. 2 | |
|-------------------------------------|----------------|---------|----------------|---------|
| Instantaneous Crack Velocity | 1847 mps | 319 mps | 1847 mps | 319 mps |
| Estimated Average Crack Velocity | | | | |
| Without Fracture Process Zone | 179 mps | 147 mps | 150 mps | 125 mps |
| With Fracture Process Zone | 104 mps | 90 mps | 100 mps | 100 mps |

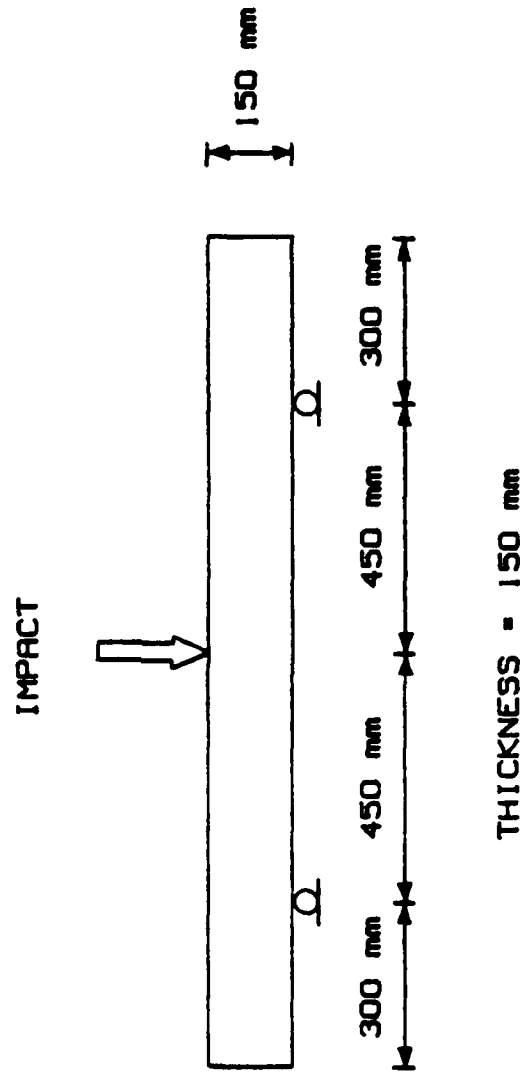


Figure 7.12 Mindess' Impacted Concrete Beam Specimen No. 2, Ref. [89]

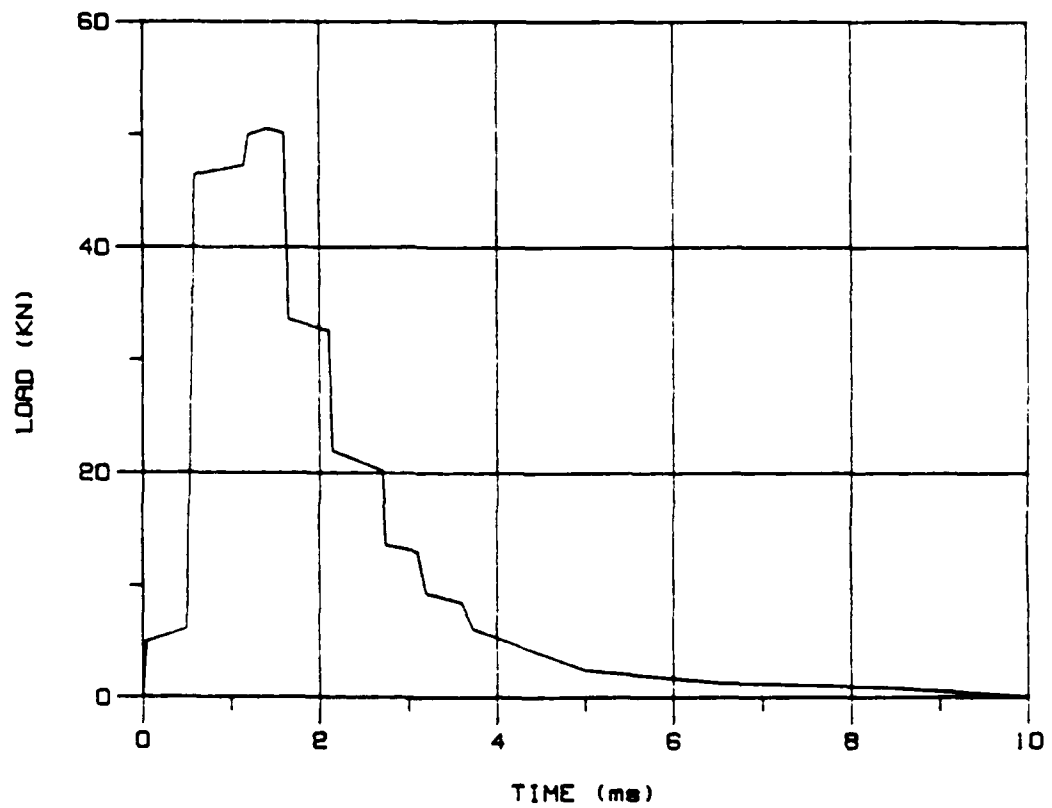
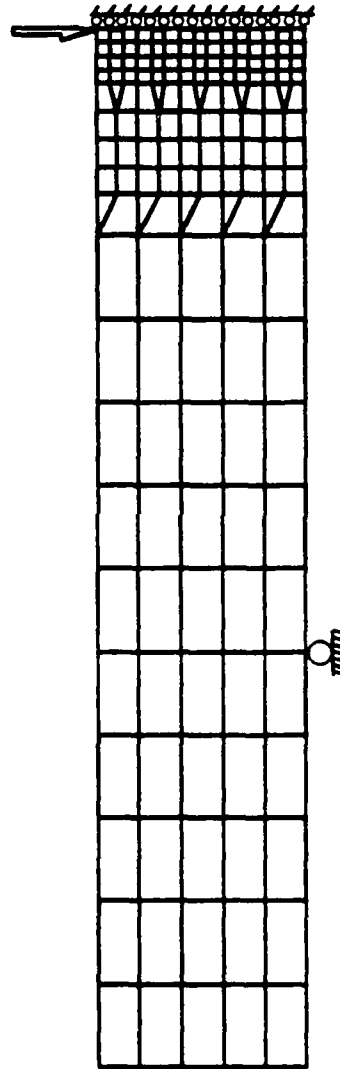


Figure 7.13 Prescribed Load-Histroy for Concrete beam Specimen No. 2, Ref. [89]



190 NODES * 165 ELEMENTS

Figure 7.14 Finite Element Model for Impacted Beam
Specimen No. 2, Ref. [89]

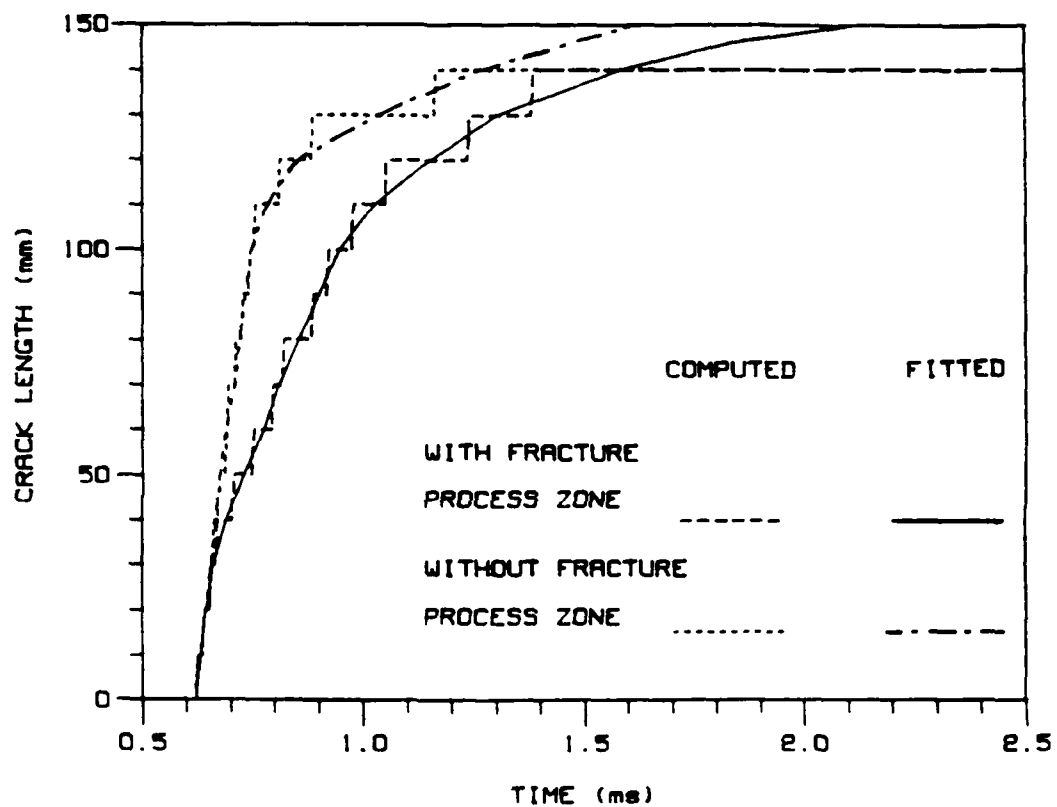


Figure 7.15 Computed Crack Length Versus Time
Specimen No. 2, Ref. [89]
Assumed Crack Velocity 1847 mps

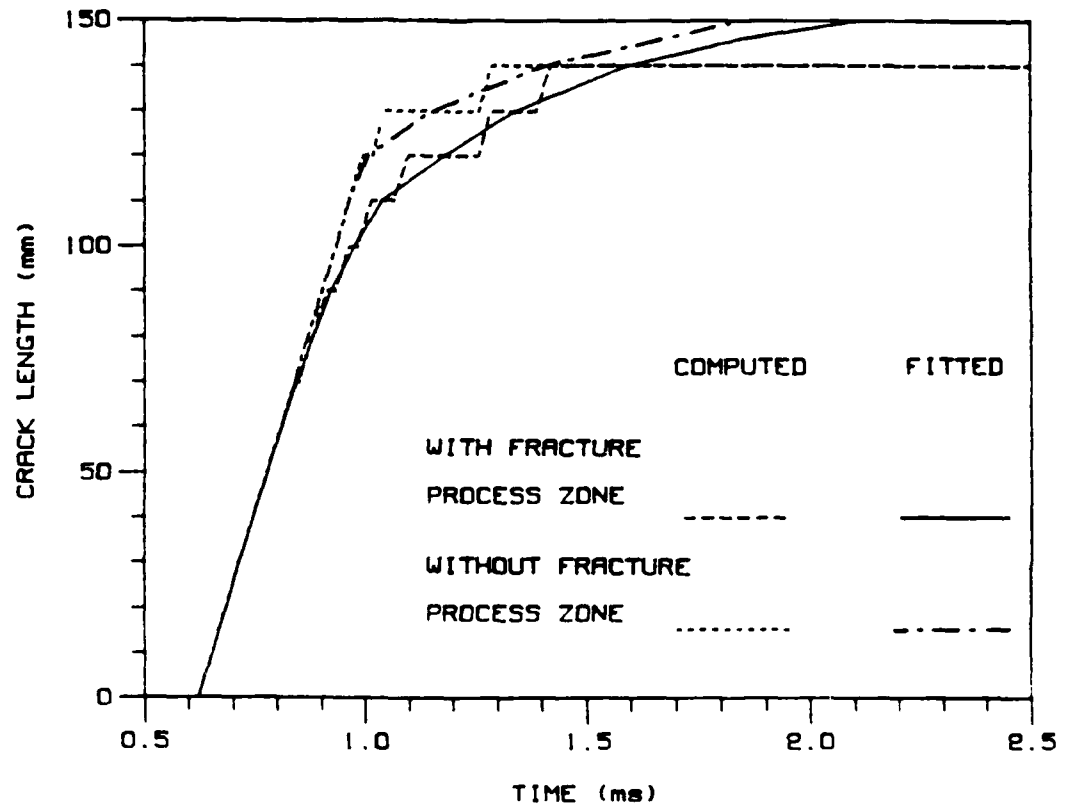


Figure 7.16 Computed Crack Length Versus Time
Specimen No. 2, Ref. [89]
Assumed Crack Velocity 319 mps

An advantage of the finite element analysis is that one numerical experiment will provide a multitude of numerical data. One such data is the energy partition during fracture. Figures 7.17 and 7.18 show the variations in the kinetic, strain and fracture energies, with time. The sum of these three energies, at any instant, was within one percent of the accumulated external work, which was computed independently. This agreement which differs with the results of Reference [88], provided a consistency check on the numerical procedure. Unlike other fracture specimens [122], Figures 7.17 and 7.18 show that the kinetic energy dominates and is the primary energy sink for absorbing the input work for these impacted concrete specimens.

7.3 Refined Results

7.3.1 Simulation of Shah's Impact Tests

This simulation also used three-line model. For dynamic analysis, the three critical crack opening displacements w_1 , w_2 and w_3 in Figure 7.19, were assumed to be strain rate invariant and only the dynamic tensile strength was assumed to be strain rate dependent. That dependency was assumed to vary at the same rate as the observed variations in the total work to fracture in the

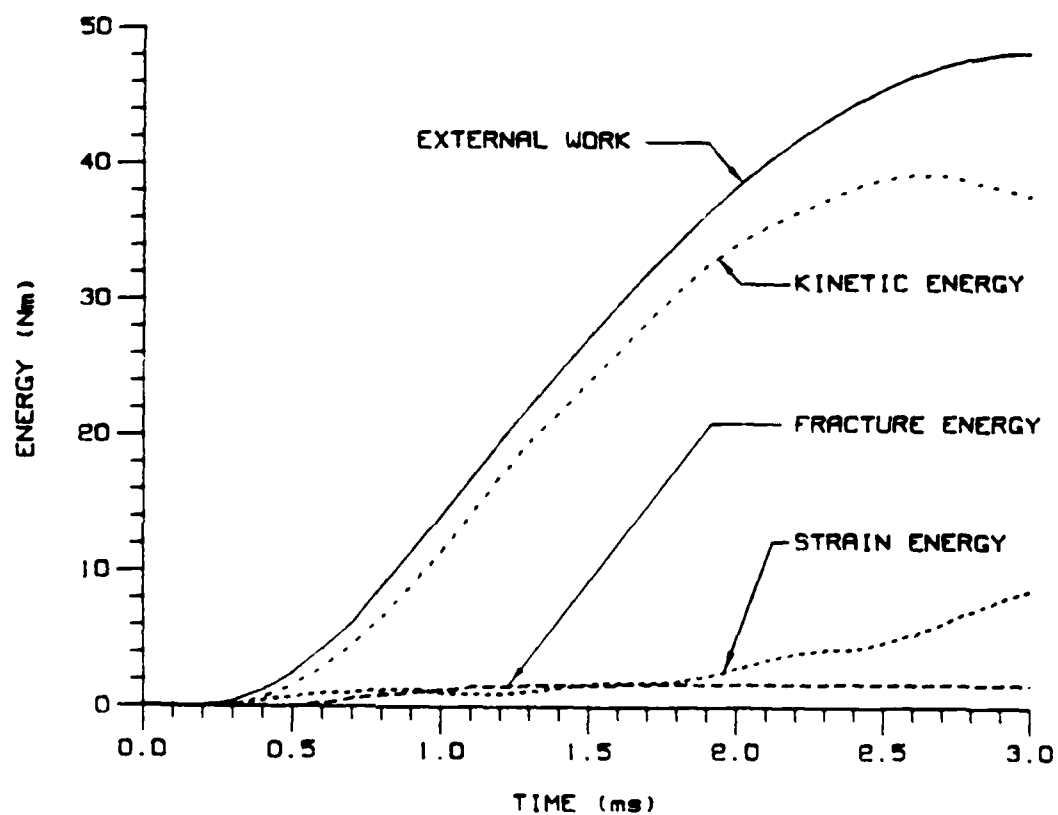


Figure 7.17 Energy Partition for Impacted Beam
Specimen No. 1, Ref. [88]
Assumed Crack Velocity 1847 mps

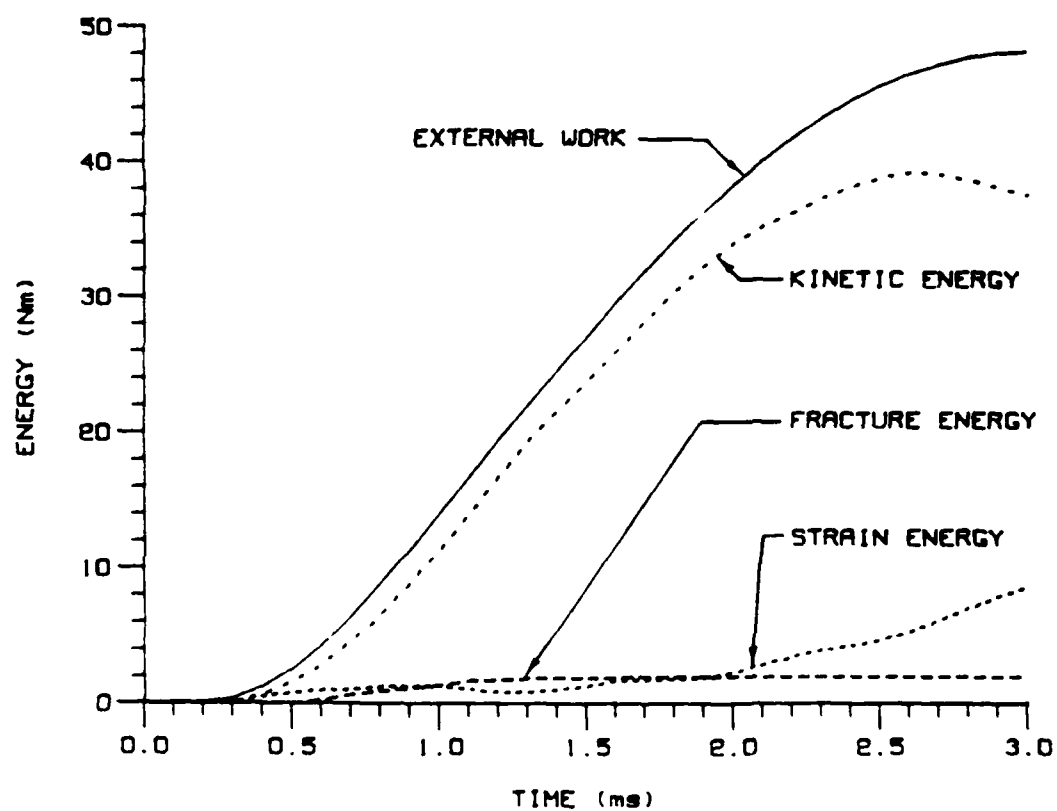


Figure 7.18 Energy Partition for Impacted Beam
Specimen No. 1, Ref. [88]
Assumed Crack Velocity 319 mps

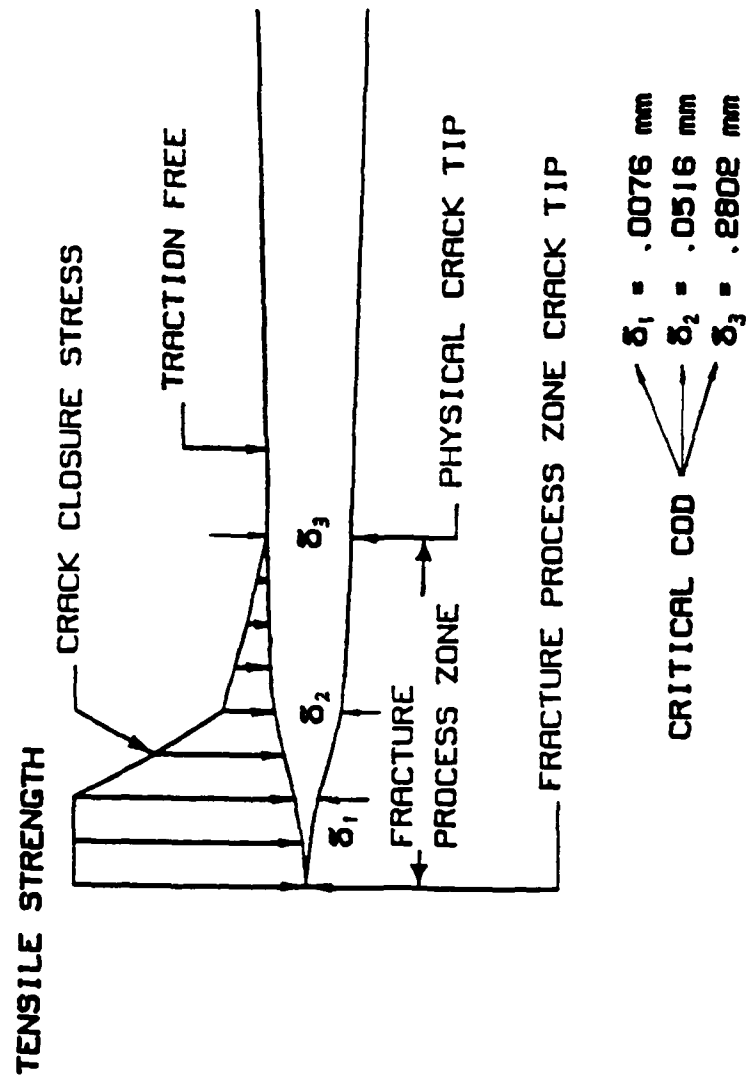


Figure 7.19 Fracture Process Zone Used in Modeling Shah's Charpy Impact Tests

tests (total area to fracture under the load versus load point displacement curve). The unknown dynamic tensile strength for this study was therefore estimated from the static tensile strength of the mortar [92], the static and dynamic work for fracture for a strain rate of 0.3 1/sec and the ratio of the peak loads for the concrete and mortar [91], etc. Detailed derivations for the input data are given in Appendix D and the derived input data are listed in Table 7.3.

The use of the previously derived static fracture process zone model was reasonable because the crack velocities measured in the impacted concrete three point bend tests were less than ten percent of the dilatational stress wave velocity for concrete.

Table 7.3 Material Properties of Shah's Specimens

| Material | Concrete | | | Mortar |
|-----------------------------------|----------|------|------|--------|
| Specimen | 1 | 2 | 3 | |
| Strain Rate (sec^{-1}) | 0.1 | 0.2 | 0.4 | 0.3 |
| Elastic modulus (GPa) | 31.3 | 31.3 | 31.3 | 22.0 |
| Tensile Strength (MPa) | 4.85 | 5.05 | 5.51 | 3.91 |
| Poisson's Ratio | 0.15 | 0.15 | 0.15 | 0.15 |
| Density (kg/m^3) | 2410 | 2410 | 2410 | 2410 |

A dynamic finite element model, as shown in Figure 7.20, was used to simulate the dynamic fracture response of the impacted prenotched concrete beams and unnotched mortar beams of References [91,92]. Since the loading was symmetrical only half the beam is shown in Figure 7.20.

Shown in Figures 7.21 and 7.22 are the measured impact loads and the computed reactions for the two supports of a concrete and a mortar beam, respectively. That impact load history was prescribed at the impact point on the bend specimen and the dynamic finite element code was executed in its application mode to dynamically fracture the beam. The computed reactions are shown in Figure 7.21 and 7.22. Although the "measured" reactions were not quantitatively reported in Reference [91], they were claimed as to be comparable to the applied loads in that reference. That observation was confirmed by the finite element analysis.

Shown in Figure 7.23 are the constitutive relations, i.e., crack closure stress versus crack opening displacement, for the four fracture process zones which were generated after the iterative numerical analysis of the tests on the three concrete and one mortar beam specimen tests. The difference between the constitutive equations for mortar and concrete, is obviously greater than the sensitivity of that relationship for the concrete

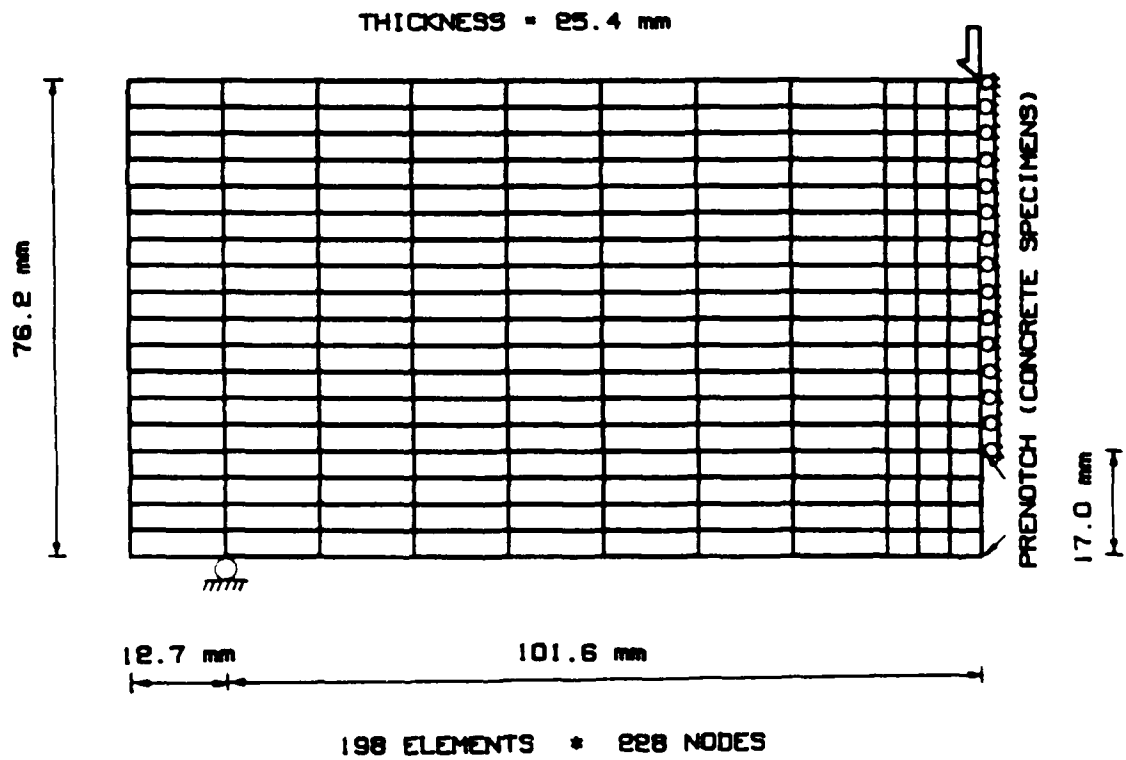


Figure 7.20 Specimen Configuration and Finite Element Model for Concrete and Mortar Beam Impact Tests, Ref. [91]

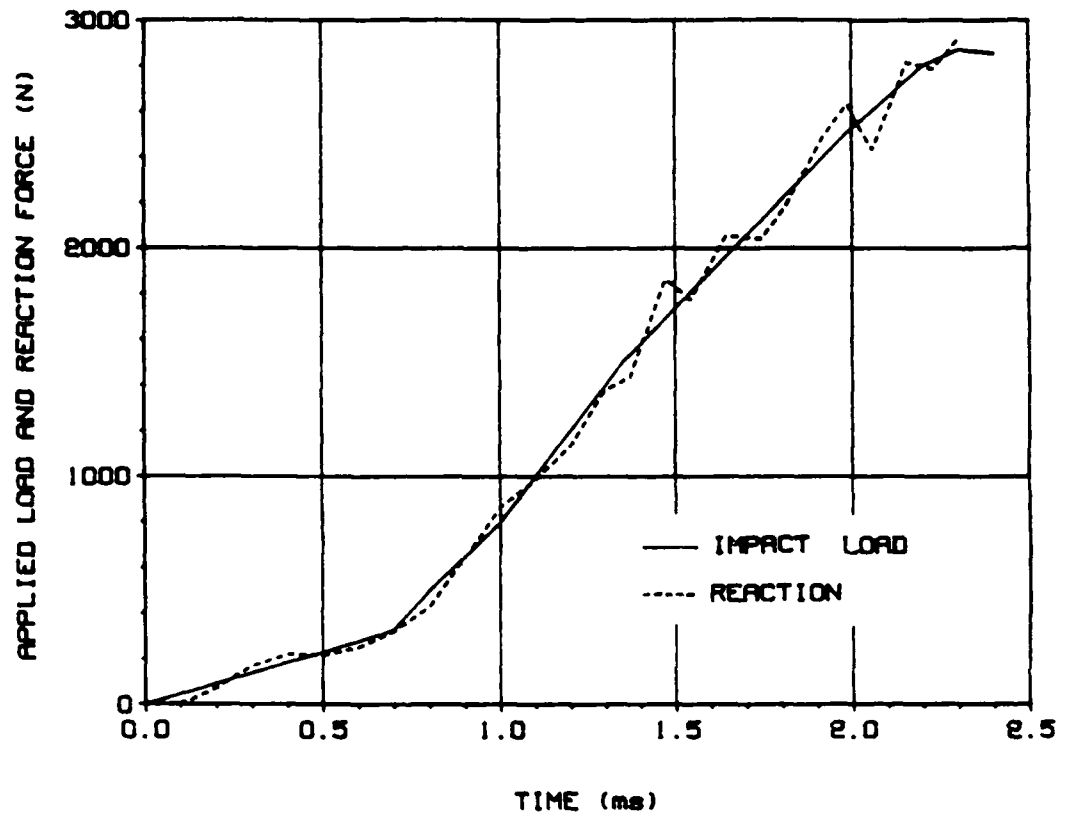


Figure 7.21 Applied Load and Reaction Force History
Concrete Specimen No. 1, Ref. [91]

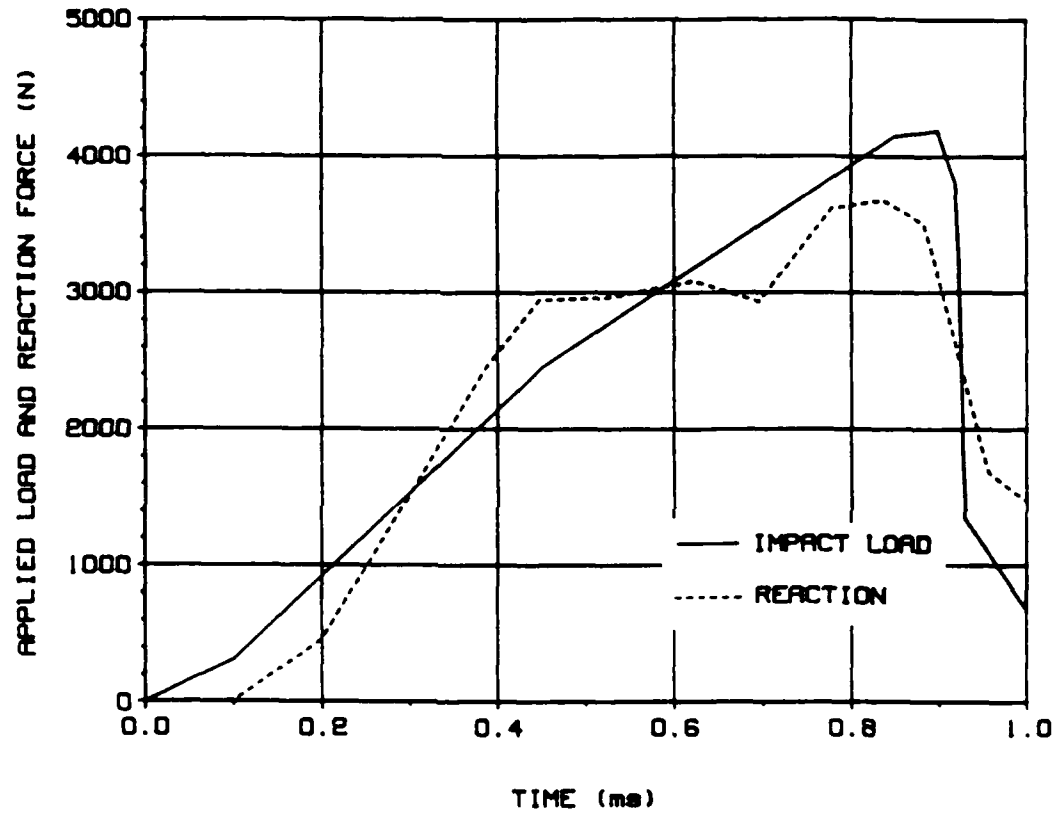


Figure 7.22 Applied Load and Reaction Force History
Mortar Specimen, Ref. [92]

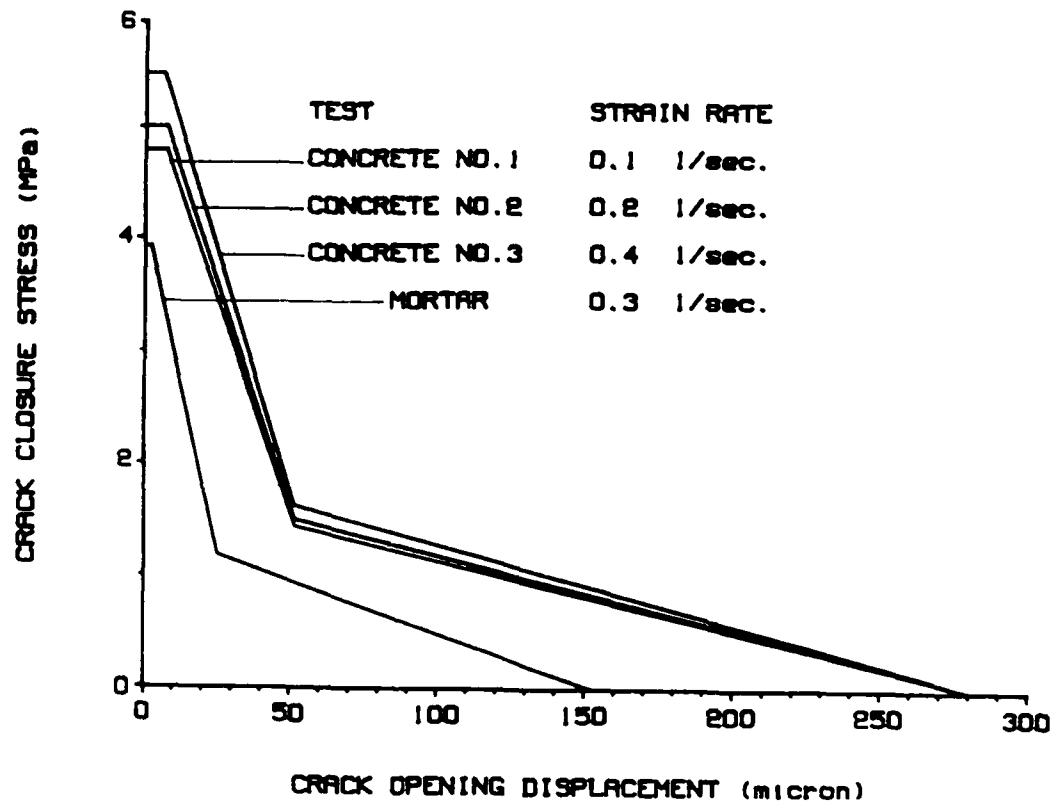


Figure 7.23 Crack Closure Stress Versus COD for Modeling Fracture Process Zone in Impacted Beams. Simulation of Shah's Impact Tests

beam test to strain rate variations between 0.1 and 0.4 1/sec.

Although not apparent from Figure 7.23, the computations also showed that the process zone length decreased with increasing strain rate. A similar trend was observed experimentally by Shah et al. [91]. A higher strain rate increases the dynamic tensile strength. However, the accompanying decrease in the fracture process zone length offsets that increase. the total dissipated fracture energy, were nearly invariant for the strain rate variations examined in this study.

Shown in Figures 7.24 and 7.25 are typical computed and measured crack extension histories for the concrete and mortar beams. Knowing that the stair shape of the computed results is due to the discrepancy of the numerical analysis, only fitted curves are presented in these figures. The crack extension histories were measured, using a KRAK-GAGE.* That gage exhibited some ductility and thus in Figure 7.24 there is a finite time delay of about 1 millisecond between the passage of the crack tip as computed, and the strains as recorded. The slopes of the computed and measured crack extension histories are,

* TTI Division, Hartran Corporation, FL.

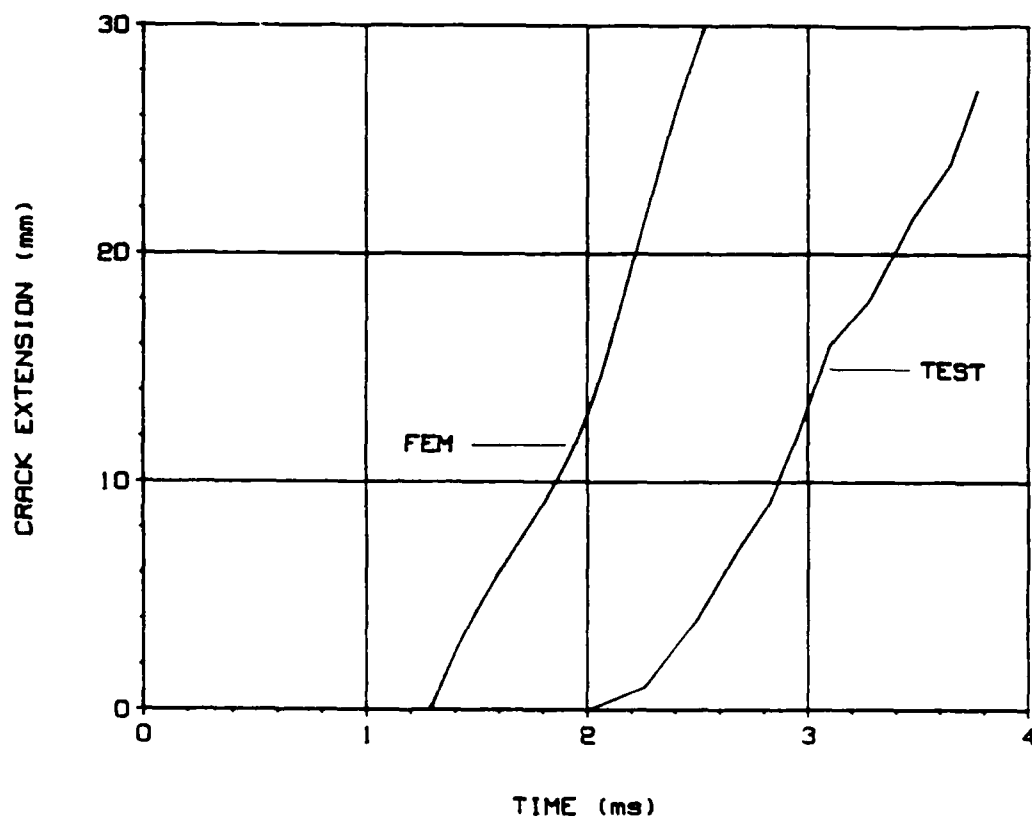


Figure 7.24 Crack Extension History for Concrete Beam Specimen No. 1, Ref. [91]

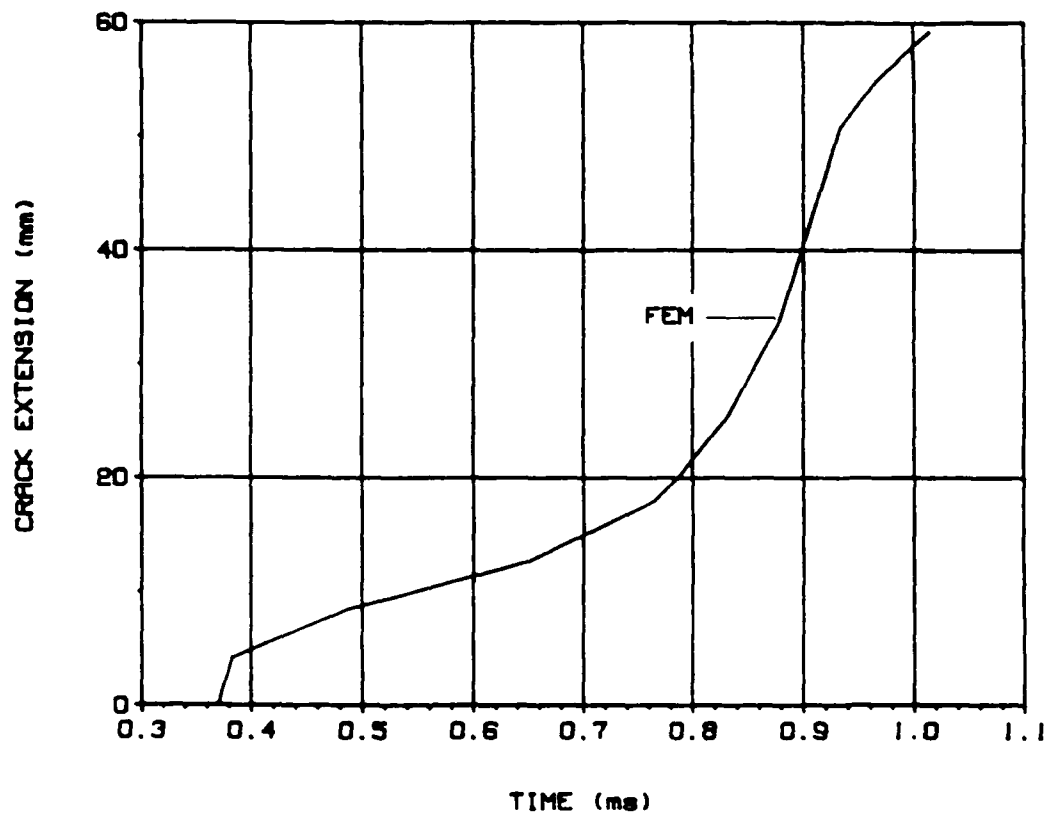


Figure 7.25 Crack Extension History for Mortar Beam
Ref. [92]

however, in good agreement with each other and indicate that computed and measured crack velocities are in agreement despite the time lag in the KRAK-GAGE responses.

Figures 7.26 and 7.27 show the measured and computed strain histories for the concrete and mortar beams, respectively. Strains were measured at the notch tip in the concrete beam and on the extreme tension fiber at the quarter length of the span for the mortar beam. There is reasonable agreement between the computed and measured strains.

Figures 7.28 and 7.29 show the computed deflection histories for the load point of the three concrete beams and the mortar beam, respectively. Also shown in Figure 7.29 is the measured deflection, which is in good agreement with its computed counterpart, for the mortar beam. The slope of that curve represents the specimen's velocity at the impact point. For the mortar beam the measured and computed specimen velocities for that point were the same and both were about 100 mm/s. That value is much less than the measured tip velocity of 2405 mm/s [92] just prior to impact. The inertia of the beam, plus the damping effect of the rubber pad provided at the impact point, were probable causes for this low specimen velocity.

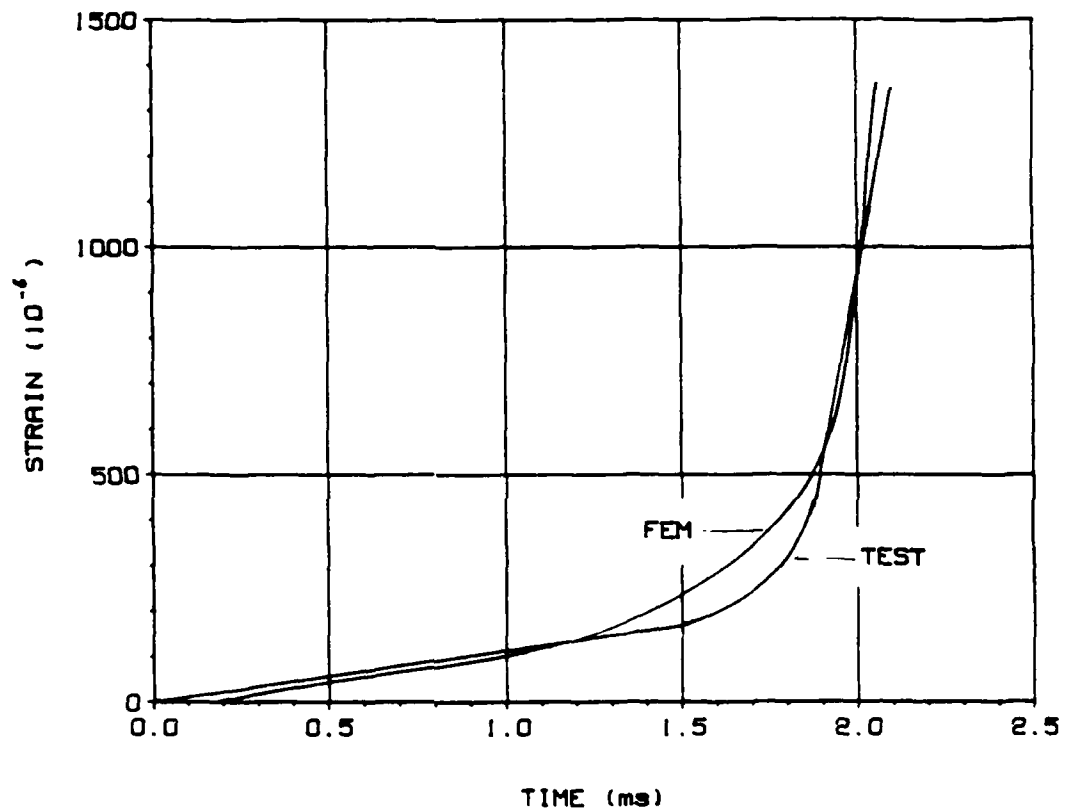


Figure 7.26 Strain History at Prenotch Tip of Impacted Concrete Beam, Specimen No. 1, Ref. [91]

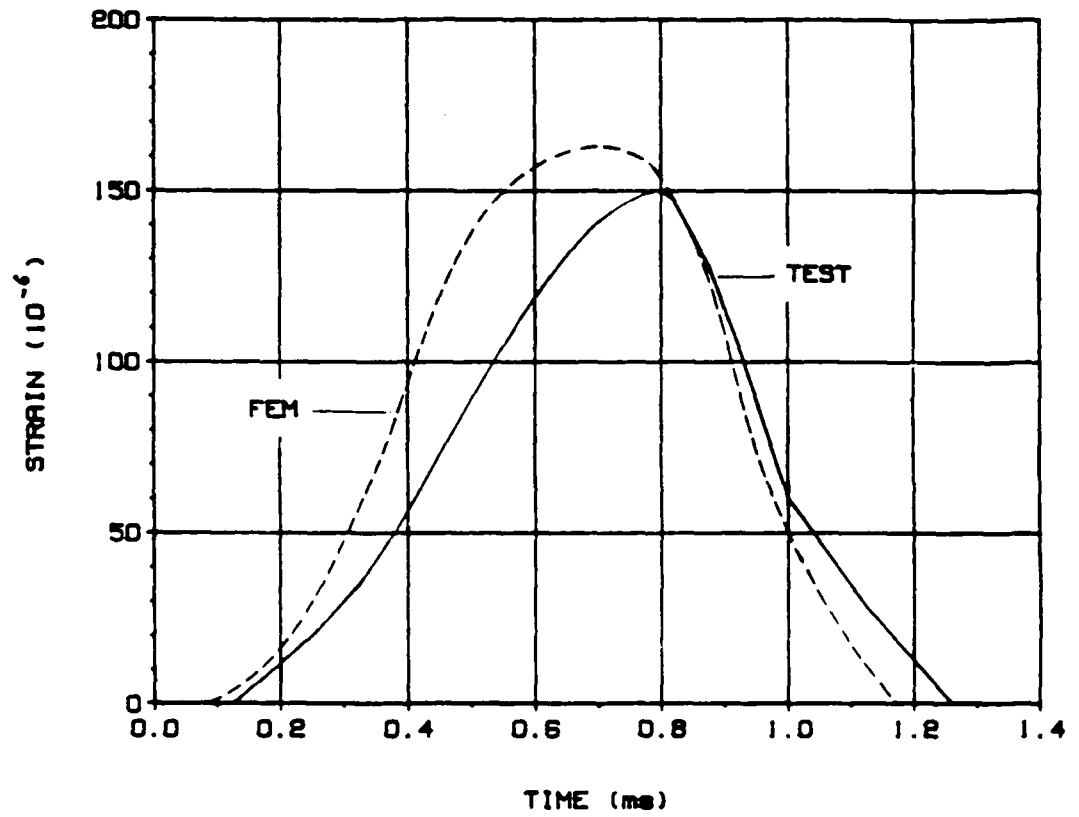


Figure 7.27 Strain History at Quarter-Span of Impacted Mortar Beam, Ref. [92]

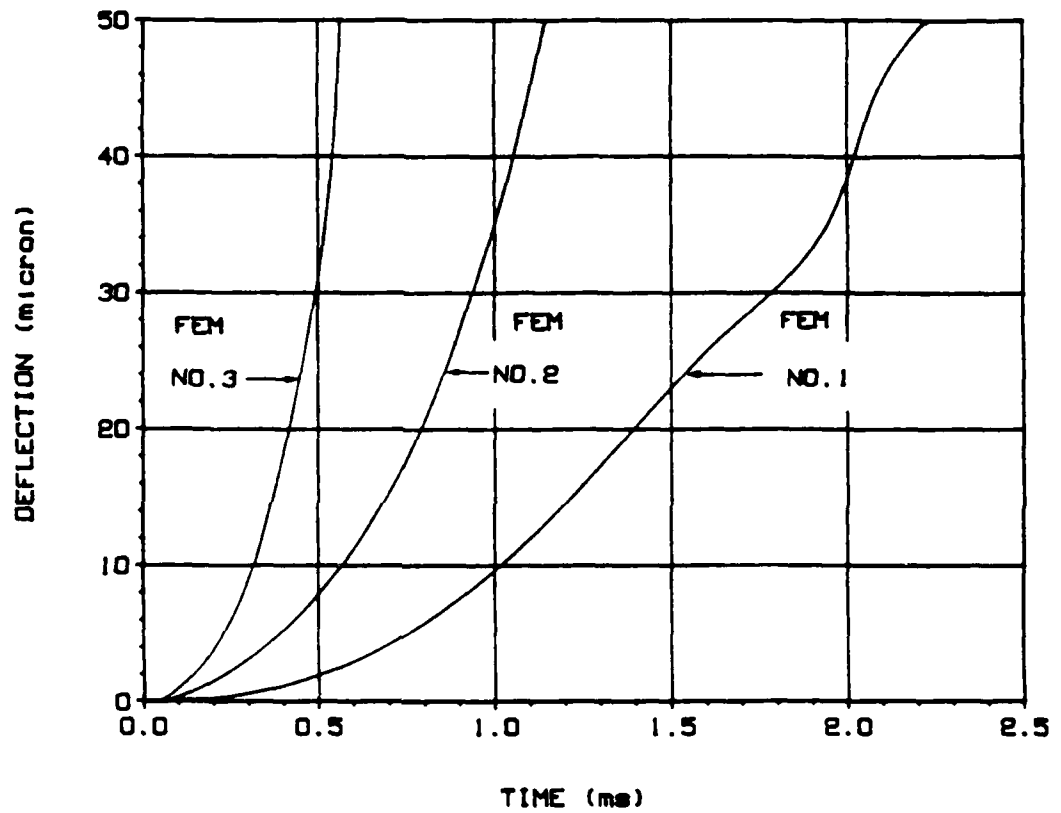


Figure 7.28 Load-Point Deflection History of Concrete Specimens, Ref. [91]

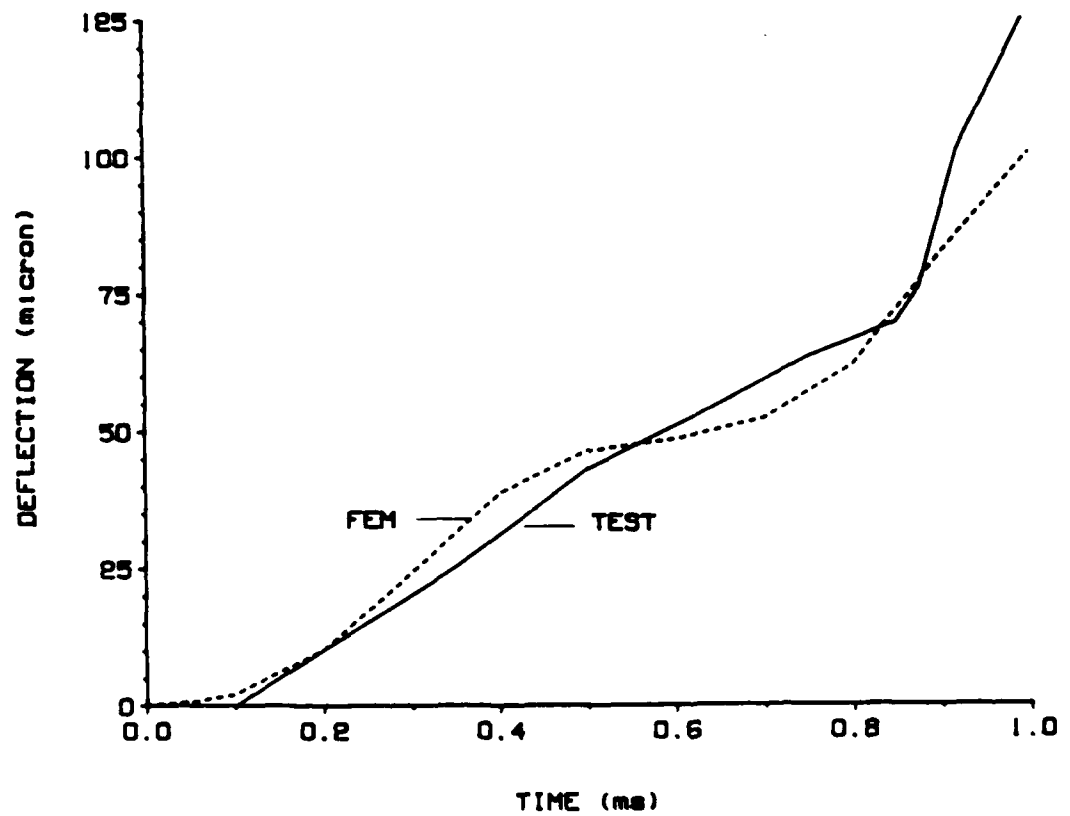


Figure 7.29 Load-Point Deflection History of Mortar Specimen, Ref. [92]

Shown in Figures 7.30 and 7.31 are the energy partitions for the concrete and mortar beams, respectively. The relatively small amount of kinetic energy in both specimens indicates that little of the impact energy was dissipated to overcome inertial resistance.

Figure 7.32 shows the variations in the dynamic fracture energy dissipation rate with crack extension. The rate is shown with respect to unit crack extension. Thus, those curves represent the dynamic counterpart of crack growth resistance curves in terms of fracture energy dissipation rate. The strain rate dependence of these resistance areas is apparent from Figure 7.32. Values increase with both increasing crack extension and increasing strain rate.

Figure 7.33 shows the dynamic fracture energy dissipation rate, with respect to unit crack extension, versus crack velocity for the concrete beams. This figure is equivalent to the dynamic fracture toughness versus crack velocity relationship for metallic and polymeric dynamic fracture specimens [123]. Typically, those relationships exhibit a gamma shape. While the same gamma shape is preserved for the concrete specimens, there is also a pronounced strain rate effect. Thus a unique dynamic fracture energy dissipation rate versus crack velocity relation obviously does not exist for concrete or

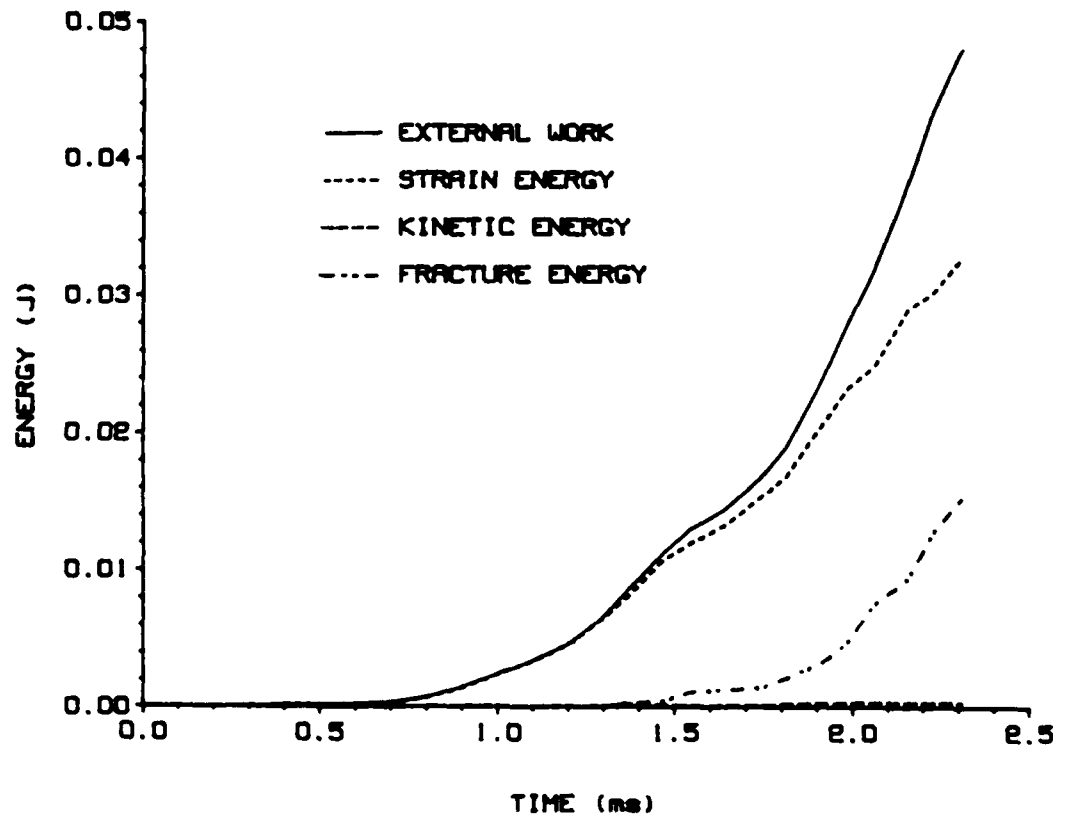


Figure 7.30 Energy Partition for Concrete Impact Test Specimen No. 1, Ref. [91]

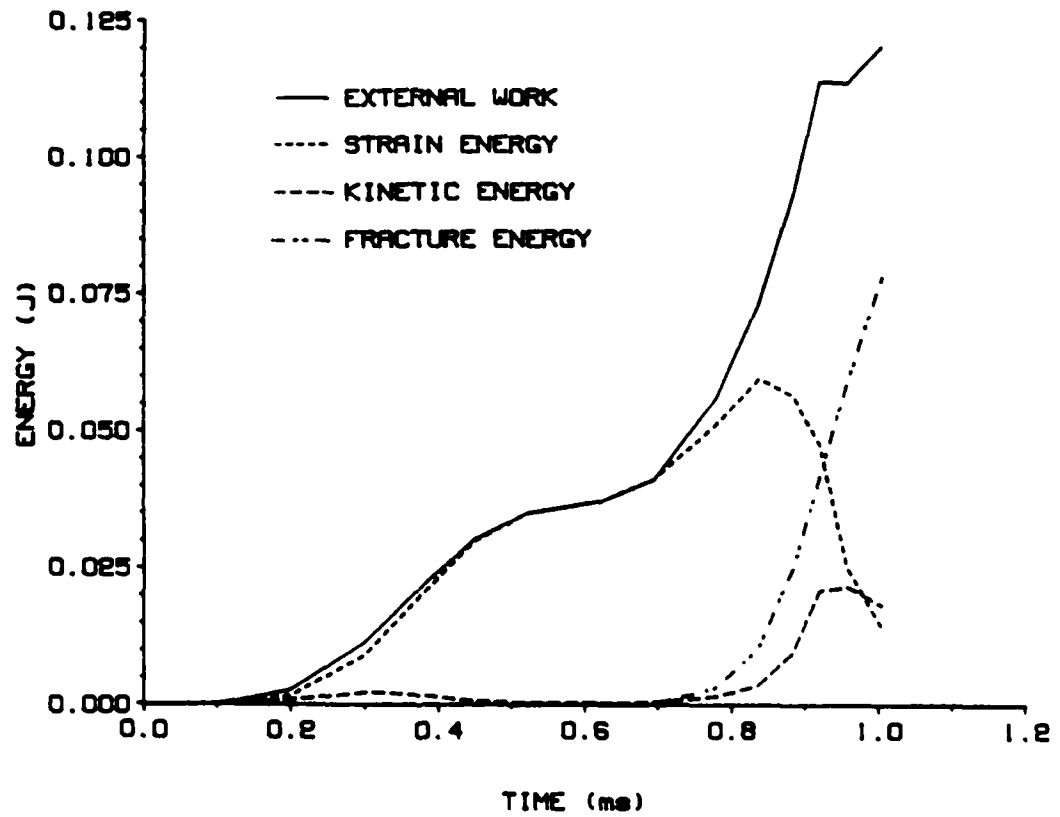


Figure 7.31 Energy Partition for Mortar Impact Test
Ref. [92]

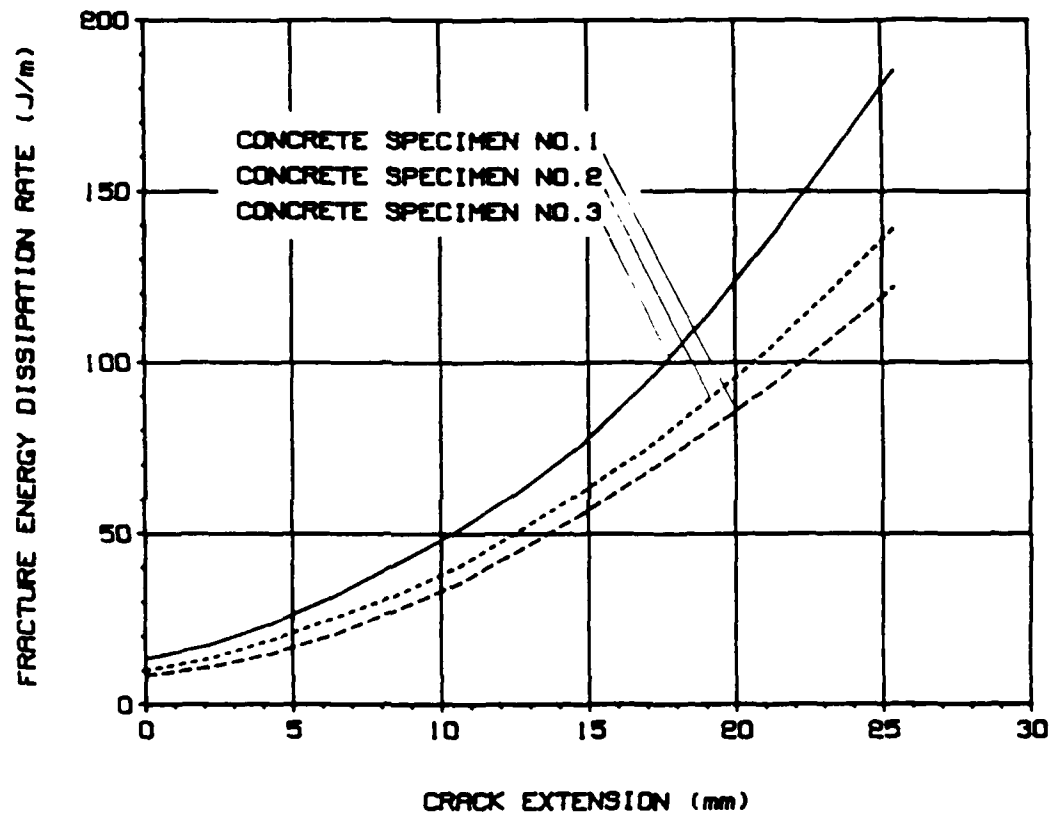


Figure 7.32 Fracture Resistance Curves for Concrete Specimens, Ref. [91]

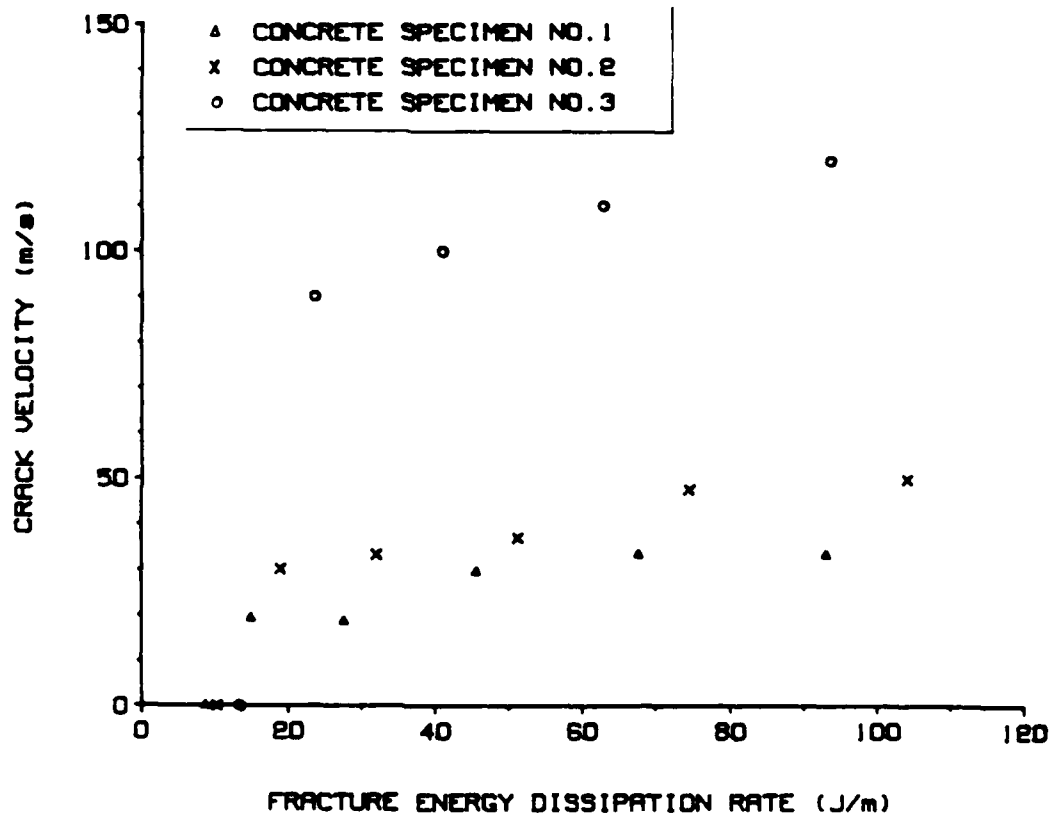


Figure 7.33 Crack Velocity Versus Fracture Energy Dissipation Rate for Concrete Specimens
Ref. [91]

mortar.

Thus, a theoretical dynamic crack propagation model for concrete fracture under impact loading has been constructed. The preliminary results obtained to date show that the combination of the fracture process zone model with elasto-dynamic transient finite element analysis is an appropriate approach for analyzing dynamic fracture of concrete.

CHAPTER EIGHT

SUMMARY

In this dissertation a systematic study of fracture mechanics applied to concrete materials is reported. The prime objective of this study was to define the law governing tensile failure of concrete under either static or dynamic conditions. The developments reported here involve new concepts, new test techniques, and new numerical methods. The significant contributions resulting from this study are summarized in this chapter.

(1) The essential reasons for differences in the mathematical models necessary to describe fracture in concrete and fracture in metallic and polymeric materials have been explained. The large size for the fracture process zone in concrete means single parameter mathematical models can never effectively characterize that zone. Also, due to the large resultant strain softening effects, the implications of the whole fracture process rather than those associated with the fracture point must be considered. In concrete the fracture point is only the starting point for the fracture process. The final point in the fracture process is not reached until there is complete material separation and the remaining strength is zero. This concept explains why traditional fracture

mechanics concepts cannot be used directly for fracture analysis of concrete and has indicated the nature of the model that must be developed for concrete and similar materials.

(2) Experimental procedures have been developed for testing concrete fracture specimens. In addition to conventional experimental techniques, a moire interferometry technique was developed for studying the fracture process zone in concrete CLWL-DCB specimens and three point bend specimens. First, an exploratory white light moire interferometry test on small specimens revealed the potential of that method for detecting and measuring the fracture process zone in a concrete material. Later, a laser moire interferometry test procedure, with a real reference grating, was developed which could be used to observe a fully developed fracture process zone and to evaluate CODs within that zone in an appropriate sized specimen. Custom-made diffraction gratings of 600 line/mm for active or specimen gratings and 1200 line/mm for the real reference grating were used in these tests.

(3) A numerical procedure was developed for extracting multiple fracture parameters, that described the process zone model, and for predicting specimen behavior such as crack extension, COD in fracture process zone, stress and displacement field in the specimen, and so on.

This numerical procedure included a linear elastic finite element computation of Green functions and a nonlinear routine to analyze the fracture process zone based on the superposition principle. The iteration scheme [49], developed previously to describe the fracture process zone behavior, was an indirect nonlinear routine which relied on physical reasoning and trial and error to obtain results. In this dissertation that model has been refined and placed on a mathematical basis. Once that mathematical formulation was available a direct method for extracting fracture parameters was developed. This direct method involved the use of a Newton-Raphson routine, coupled with a Householder transformation, which effectively optimized and stabilized the solution of the fracture parameters in the sense of least squares. A simple smooth curve was used to describe the functional form of the crack closure stress versus COD relation. To characterize that form only three unknown parameters, including the tensile strength of the concrete material, need be determined.

(4) Findings on stable crack growth in concrete specimens can be summarized as the followings:

- (a) The development of a fracture process zone or microcracking zone prior to attainment of the peak load was clearly observed using moire

interferometry. A fully developed fracture process zone was obtained during the course of this study.

- (b) The fracture process zone width observed in these tests was about one times the maximum aggregate size and not three times the maximum aggregate size as postulated by others [60].
- (c) A CLWL-DCB specimen has an inherently rigid nature that provide stable crack growth. A simple shop press without any closed loop control can be used to study the static fracture process in small scale concrete specimens.
- (d) Vibration control is not needed for moire interferometry testing when a real reference grating is used. Thus, the method reported in this thesis can be used to develop portable equipment suitable for field testing.
- (e) Tensile fracture of concrete has been successfully modeled using a fracture process zone characterized by a unique crack closure stress versus COD relationship.
- (f) The crack closure stress versus COD relation has been found to be maximum aggregate size dependent in large specimens. And 25% larger peak load was obtained for a CLWL-DCB specimen with maximum

aggregate size of 6.4 mm than a geometrically identical specimens with maximum aggregate size of 9.5 mm.

- (g) The smooth curve for the crack closure stress versus COD relationship derived from the test data of the CLWL-DCB and three point bend specimens agreed well with available direct tension results as reported in previous investigations [12,42,103,104].
- (h) The three straight line segment model previously developed was used to check the validity of the smooth curve model and the direct method. Very good agreement both in the general shape and in area was obtained.

(5) The fracture process zone model developed from static loading results was also used to predict dynamic fracture of concrete specimens under impact loading conditions. The impacted beam tests conducted by Mindess [88,89] and by Shah [91,92] were used as the data base for extending that model. An existing dynamic finite element program was modified to allow for incorporation of this fracture process zone into it. Then that program was executed in its application phase, and the dynamic responses of the concrete test specimens during the

fracture process were predicted. Good agreement between the measured and computed crack velocities, loading point deflections, strain histories and reactions at supports were obtained.

(6) Some preliminary strain rate effects for dynamic fracture of concrete that have been obtained to date are as follows:

- (a) The three critical CODs which represent the boundaries of the microcracking, transition and aggregate bridging sub-process zone within the overall model were strain rate invariant for the strain rate regime studied.
- (b) The dynamic tensile strength of the fracture process zone is less strain rate dependent than tensile strengths inferred from the results of impacted Modulus of Rupture specimens.
- (c) The unique gamma curve for dynamic fracture energy dissipation rate versus crack velocity that exists for metals and polymers does not exist for concrete. For concrete that curve shows considerable strain rate effect.
- (d) The experimental observation that the fracture process zone length decreased with increasing strain rate was confirmed analytically by dynamic

finite element modeling.

CHAPTER NINE

CONCLUSIONS

The salient conclusions from this investigation are as follows:

- (1) Fracture mechanics method developed for metallic or polymeric materials can not be applied directly to concrete and a method, appropriate for concrete, is developed in this study.
- (2) The form of the fracture process zone for concrete and variations in CODs along that zone can be determined by the moire interferometry procedures developed in this study.
- (3) The fracture process zone for concrete has a length that is dependent of specimen geometry and size and a width is about one times the maximum aggregate size.
- (4) A fracture process zone model that relates crack closure stress to COD is an excellent one for predicting the tensile fracture behavior of concrete.
- (5) An appropriate direct solution for this fracture process zone model can be formulated using Green functions and superposition principles.
- (6) A smooth curve representation of the crack closure stress versus COD relationship is appropriate and a representation can readily be formulated that the same

general shape as the three line segment model developed in prior University of Washington studies.

- (7) When this fracture process zone model derived from test data is used, the behavior for other specimen types and loading conditions can be accurately predicted using finite element analysis.
- (8) The fracture process zone model reported here can be readily extended to predictions of the dynamic responses of concrete fracture specimens subjected to impact load.
- (9) The dynamic tensile strength of concrete is less strain rate sensitive than the results of Modulus of Rupture beam tests.
- (10) Dynamic finite element analysis showed that the length of the fracture process zone decreased as the strain rate increased.
- (11) The CLWL-DCB specimen was found to be an inherently rigid specimen suitable for characterizing stable crack growth in concrete.
- (12) Moire interferometry that utilizes a real reference grating does not require vibration control. The method reported here can be used to develop portable equipment suitable for field testing.

CHAPTER TEN

RECOMMENDATIONS

Further research on the following topics is recommended:

- (1) As noted in Chapter 6, the CLWL-DCB specimen and the three point bend specimen are both essentially bend specimens. As shown in Figures 6-39 and 6-40, the normal stress distributions along the crack path for both specimens are very similar to each other. Therefore, there is a need to develop a specimen in which there is a different overall stress state field in order to check the effect of the overall stress state on the fracture process zone model.
- (2) A direct tension test set-up and test procedure should be developed. Direct tension test results are the best data form which a mathematical model can be derived. Although several results can be found in the literature, one problem remains unsolved. This problem can be called "rotational instability" and it is the result to be expected for non-uniform strain-softening of the material.
- (3) The existence or non-existence of mode II fracture in concrete should be investigated. If this mode exists then how to model that type of fracture, as well as

mixed mode I and II fractures, should be investigated.

- (4) A model for concrete fracture under cyclic loading conditions should be developed. Because a complicated processes that occur during unloading and reloading no such model currently exists. The work on ceramic composites reported here (APPENDIX E), however, provide a rational basis for developing a model for concrete.
- (5) Investigations of the strain rate effects during dynamic fracture of concrete should be continued. Tests at different strain rates should be conducted in order to find strain rate effects. Then, finite element analysis in its application phase should be used to study the appropriate form for fracture process zone model as demonstrated by those results.
- (6) Investigations should be made of the dynamic mixed mode fracture of concrete. A model should be developed for predicting the crack path for dynamic crack propagation. Such modeling is likely to be a very challenging task.
- (7) Portable moire interferometry equipment, with a real reference grating, should be constructed and its suitability for field testing demonstrated.
- (8) An analytical procedure that includes strain hardening or bulk dissipation effects should be developed. For

such analyses the whole region under study becomes nonlinear, The superposition principle can no longer be used so that computations become much more complicated and expensived. However, incorporation of such effects is needed if actual behavior is to be realistically modeled.

- (9) The fracture process zone model developed here should be extended to fiber and conventional reinforced concrete. In the later case, the implications of that model for predicting bond behavior between concrete and an embedded steel reinforcing bar should be examined.
- (10) The implications of the model developed here for failure analysis of real structures should be examined with a view to improving present design requirements associated with shear, bond, cracking and minimum reinforcement ratios. In particular an examination needs to be made of the extent to which traditional empirical formulae can be replaced by fracture mechanics based analyses.

REFERENCES

1. Powers, T. C., "The Nature of Concrete," Significance of Tests and Properties of Concrete and Concrete Making Materials, ASTM STP No. 169-B, Philadelphia, 1978, pp. 59-73.
2. Richart, F. E., Brandtzaeg, A. and Brown, R. L., Bulletin No. 185, Engineering Experiment Station, University of Illinois, 1928, pp. 104.
3. Jones, R., "A Method of Studying the Formation of Cracks in a Material Subjected to Stresses," British Journal of Applied Physics, V. 3, No. 7, July 1952, pp. 229-232.
4. Griffith, A. A., "The Phenomenon of Rupture and Flow in Solids," Philip Transactions Royal Society of London, A-221, 1920, pp. 163-198.
5. Kaplan, M. F., "Crack Propagation and Fracture of Concrete," ACI Journal, V. 58, No. 5, November 1961, pp. 591-610.
6. Barker, D. B., Hawkins, N. M., Jeang, F. L., Cho, K. Z. and Kobayashi, A. S., "Concrete Fracture in a CLWL Specimen," Journal of Engineering Mechanics, ASCE, V. 111, No 5, May 1985, pp. 623-638.
7. Cho, K. Z., Kobayashi, A. S., Howkins, N. M., Barker, D. B., and Jeang, F. L., "Fracture Process Zone of Concrete Cracks," Engineering Mechanics Division Journal, ASCE, V. 110, No. 8, August 1984, pp. 1174-1184.
8. Kobayashi, A. S., Hawkins, N. M., Barker, D. B. and Liaw, B. M., "Fracture Process Zone of Concrete," Application of Fracture Mechanics to Cementitious Composites," ed. by S. P. Shah, Northwestern University, September, 1984, pp. 25-47.
9. Jeang, F. L., "Non-Linear Concrete Fracture in CLWL-DCB Specimens," Ph.D. Thesis, University of Washington, Seattle, Washington, March 1985.
10. Akutagawa, S., "Wedge Configuration and Loading History Considerations for Concrete CLWL-DCB Specimens," MSCE Thesis, University of Washington, Seattle, Washington, August 1984.

11. Wecharatana, M. and Shah, S. P., "Prediction of Non-linear Fracture Process Zone in Concrete," CEE-820311, Northwestern University, 1983.
12. Reinhardt, H. W., "Fracture Mechanics of an Elastic Softening Material Like Concrete," HERON, V. 29, No. 2, 1984.
13. Arrea, M. and Ingraffea, A. R., "Mixed-Mode Crack Propagation in Mortar and Concrete," Dept. of Structural Engineering, Cornell University, Ithaca, NY, 1981.
14. Ingraffea, A. R., and Gerstle, W. H., "Non-Linear Fracture Models for Discrete Crack Propagation," Application of Fracture Mechanics to Cementitious Composites, ed. by S. P. Shah, Northwestern University, September 1984, pp. 171-209.
15. Bazant, Z. P., "Size Effect in Blunt Fracture: Concrete, Rock, Metal," Engineering Mechanics Journal, ASCE, V. 110, No. 4, April 1984, pp. 518-535.
16. Irwin, G. R., "Fracture Dynamics," Fracturing of Metals, ASM publication, 1948, pp. 147-166.
17. Irwin, G. R., "Plastic Zone Near a Crack and Fracture Toughness," Proceedings of 7th Sagamore Conference, 1930, IV-63.
18. Oriwan, E., "Fracture and Strength of Solids," Reports on Progress in Physics, V. XII, 1948, pp. 185.
19. Glucklich, J., "Fracture of Plain Concrete," Engineering Mechanics Division Journal, ASCE, V. 89, No. EM6, December 1963, pp. 127-138.
20. Huang, T. S., "Crack Propagation Studies in Micro-Concrete," M. S. Thesis, Dept. of Civil Engineering, Colorado University, 1966.
21. Naus, D. J. and Lott, J. L., "Fracture Toughness of Portland Cement Concrete," ACI Journal, V. 66, June 1969, pp. 481-489.

22. Imbert, I. D., "The Effect of Holes on Tensile Deformations in Plain Concrete," Highway Research Record, No. 324, Highway Research Board, January 1970, pp.54-65.
23. Shah, S. P. and McGarry, F. J., "Griffith Fracture Criterion and Concrete," Engineering Mechanics Division Journal, ASCE, V. 97, No. EM6, December 1971, pp. 1663-1676
24. Gjorve, O. E., Sorensen, S. I. and Arnesen, A., "Notch Sensitivity and Fracture Toughness of Concrete," Cement and Concrete Research, V. 7, 1977, pp. 333-344.
25. Walsh, G. B., "Fracture of Plain Concrete," Indian Concrete Journal, V. 46, November 1972, pp. 469-470.
26. Waish, G. B., "Discussion of the Paper "Measuring the Fracture Toughness of Cement Paste and Mortar," by J. H. Brown (Magazine of Concrete Research, V. 24, 1972, pp. 185-196), Magazine of Concrete Research, V. 25, 1973, pp. 220-221.
27. Walsh, G. B., "Crack Initiation in Plain Concrete," Magazine of Concrete Research, V. 28, No. 94, March 1976, pp. 37-41.
28. Strange, P. C. and Bryant, A. H., "Experimental Tests on Concrete Fracture," Engineering Mechanics Division Journal, ASCE, V. 105, No. EM2, April 1979, pp. 337-342.
29. Mindess, S., Lawrence, F. V., Jr., and Kesler, C. E., "The J-Integral as a Fracture Criterion for Fiber Reinforced Concrete," Cement and Concrete Research, V. 7, 1977, pp. 731-742.
30. Halvorsen, G. T., "Toughness of Portland Cement Concrete," Ph.D. Thesis, University of Illinois, 1979.
31. Halvorsen, G. T., "J-Integral Study of Steel Fiber Reinforced Concrete," International Journal of Cement Composites, V. 2, 1980, pp. 13-22.

32. Rice, J. R., "A Path Independent Integral and the Approximate Analysis of Strain Concentration by Notches and Cracks," Applied Mechanics Journal, ASME, V. 35, June 1968, pp. 379-386.
33. Carrato, J. L., "Experimental Evaluation of the J-Integral, M.S. Thesis, University of Illinois, 1980.
34. Hillerborg, A., "Analysis of One Single Crack," Fracture Mechanics of Concrete, ed. by F. W. Wittmann.
35. Shah, S. P., "Whither Fracture Mechanics in Concrete Design," Proceedings of the Engineering Foundation Conference on Cement Production and Use, 1979, pp. 187-199.
36. Hutchinson, J. W., "Nonlinear Fracture Mechanics," Dept. of Solid Mechanics, The Technical University of Denmark.
37. Wecharatana, M. and Shah, S. P., "Resistance to Crack Growth in Portland Cement Composites," Fracture in Concrete, ed. by W. F. Chen and E. C. Ting, Proceedings of ASCE Session, Hollywood, Florida, October 27-31, 1980, pp. 82-105.
38. Dugdale, D. S., "Yielding of Steel Sheets Containing Slits," Journal of Mechanics, Physics and Solids, V. 8, 1960, pp. 100-104.
39. Barenblatt, G. J., "The Mathematical Theory of Equilibrium Crack in the Brittle Fracture," Advances in Applied Mechanics, V. 7, 1962, pp. 55-125.
40. Hillerborg, A., "A Model for Fracture Analysis," Lund Institute of Technology, Building Material Division, Report TVBM-3005, Lund, Sweden, 1978.
41. Modeer, M., "A Fracture Mechanics Approach to Failure Analysis of Concrete Materials," Ph. D. Dissertation, Building Material Division, Lund Institute of Technology., Sweden, 1979.
42. Petersson, P. E., "Crack Growth and Development of Fracture Zones in Plain Concrete and Similar Materials," Ph. D. Dissertation, Lund Institute of Technology, Sweden, 1981.

43. Visalvanich, K. and Naaman, A. E., "Fracture Model for Fiber Reinforced Concrete," HERON, V. 29, No. 2, 1984.
44. "Determination of the Fracture Energy of Mortar and Concrete by Means of Three-Point Bend Tests on Notched Beams," Draft RILEM Recommendation, Materials and Structures, V. 18, No. 106, 1985, pp. 285-290.
45. Hillerborg, A., "The Theoretical Basis of a Method to Determine the Fracture Energy G_F of Concrete," Materials and Structure, V. 18, No. 106, 1985, pp. 291-296.
46. Hillerborg, A., "Results of Three Comparative Test Series for Determining the Fracture Energy G_F of Concrete," Materials and Structure, V. 18, No. 107, 1985, pp. 406-413.
47. Mindess S., "The Effects of Specimen Size on the Fracture Energy of Concrete," Cement and Concrete Research, V. 14, 1984, pp. 431-436.
48. Gustafsson, P. J. and Hillerborg, A., "Improvements in Concrete Design Achieved Through the Application of Fracture Mechanics," Application of Fracture Mechanics to Cementitious Composites, ed. by S. P. Shah, Northwestern University, September 1984, pp. 487-500.
49. Liaw, B. M., Jeang, F. L., Hawkins, N. M. and Kobayashi, A. S., "A Non-linear Model for Concrete Fracture," Submitted to ASCE Journal of Engineering Mechanics, 1987.
50. Carpinteri A., Di Tommaso, A. and Fanelli, M., "Influence of Material Parameters and Geometry on Cohesive Crack Propagation," Fracture Toughness and Fracture Energy of Concrete, ed. by F. Wittmann, 1985, pp. 117-135.
51. Carpinteri A., Colombo, G. and Giuseppetti, G., "Accuracy of the Numerical Description of Cohesive Crack Propagation," Fracture Toughness and Fracture Energy of Concrete, ed. by F. Wittmann, 1985, pp. 189-195.

52. Li, V. C., "Fracture Resistance Parameters for Cementitious Materials and Their Experimental Determination," Application of Fracture Mechanics to Cementitious Composites, ed. by S. P. Shah. 1985, pp. 431-449.
53. Li, V. C. and Liang, E., "Fracture Process in Concrete and Fiber Reinforced Cementitious Composites," ASCE Journal of Engineering Mechanics, V. 112, 1986, pp. 566-586.
54. Li, V. C. Chan, C. M. and Leung K. Y., "Experimental Determination of the Tension-Softening Relations for Cementitious Composites," Cement and Concrete Research, V. 17, 1987, pp. 441-452.
55. Bazant, Z. P. and Cedolin, L., "Blunt Crack Band Propagation in Finite Element Analysis," Engineering Mechanics Division Journal, ASCE, V. 105, No. EM2, April 1979, pp. 297-315.
56. Bazant, Z. P. and Cedolin, L., "Fracture Mechanics of Reinforced Concrete," Engineering Mechanics Division Journal, ASCE, V. 106, 1980, pp. 1287-1306.
57. Bazant, Z. P. and Cedolin, L., "Propagation of Crack Bands in Heterogeneous Materials," Advanced in Fracture Research, Proceedings of 5th International Conference on Fracture, V. 4, Cannes, 1981, pp. 1523-1529.
58. Bazant, Z. P., "Crack Band Model for Fracture of Geomaterials," Proceedings of 4th International Conference on Numerical Methods in Geomechanics, Held in Edmonton, Alberta, Canada, June 1982, V. 3, pp. 1137-1152.
59. Bazant, Z. P. and Cedolin, L., "Finite Element Modeling of Crack Band Propagation," Journal of Structural Engineering, V. 109, No. 1, January 1983, pp. 69-92.
60. Bazant, Z. P. and Oh, B. H., "Crack Band Theory For Fracture of Concrete," Materials and Structures (RILEM), V. 16, 1983, pp. 155-177.

61. Bazant, Z. P., Kim, J. K. and Pfeiffer, P., "Determination of Nonlinear Fracture Parameters from Size Effect Tests," Application of Fracture Mechanics to Cementitious Composites, ed. by S. P. Shah, Northwestern University, September 1984, pp. 143-169.
62. Hawkins, N. M., Wyss, A. N. and Mattock, A. H., "Fracture Analysis of Cracking in Concrete Beams," Structural Division Journal, ASCE, V. 103, No. ST5, May 1977, pp. 1015-1030.
63. Bazant, Z. P., "Size Effect in Blunt Fracture: Concrete, Rock, Metal," ASCE Journal of Engineering Mechanics, V. 110, 1984, pp. 518-535.
64. Rots, J., Nauta, P., Kusters, G. and Blaauwendraad, J., "Smeared Crack Approach and Fracture Localization in Concrete," Heron, V. 30, No. 1, 1985.
65. Rots, J., Kusters, G. and Blaauwendraad, J., "Strain-Softening Simulations of Mixed-Mode Concrete Fracture," Fracture of Concrete and Rock, ed by S. P. Shah and S. E. Swartz, June 1987.
66. Borst, R. de, "Computational Aspects of Smeared Crack Analysis," Constitutive Modeling of Concrete Structures, Prineridge Press, Swansea, 1986.
67. Jenq, Y. S. and Shah, S. P., "A Fracture Toughness Criterion for Concrete," Engineering Fracture Mechanics, V. 21, No. 5, 1985, pp. 1055-1069.
68. Jenq, Y. S. and Shah, S. P., "A Two Parameter Fracture Model for Concrete," ASCE Journal of Engineering Mechanics, V. 111, No. 10, 1985, pp. 1227-1241.
69. Diederichs, U., Schneider, U. and Terrien, M., "Formation and Propagation of Cracks and Acoustic Emission," Fracture Mechanics of Concrete, ed. by F. W. Wittmann, 1983, pp. 157-205.
70. Maji, A. K. and Shah, S. P., "Application of Acoustic Emission and Laser Holography to Study Microfracture in Concrete," Presented at ACI Annual Convention, San Antonio, Texas, March 22-27 1987.

71. Maji, A. K. and Shah, S. P., "A Study of Fracture Process of Concrete Using Acoustic Emission," Proceeding of Society of Experimental Mechanics, Spring Conference, New Orleans, June 8-13, 1986.
72. Izumi, M., Mihashi, H. and Nomura, N., "Acoustic Emission Technique to Evaluate Fracture Mechanics Parameters of Concrete," Fracture Toughness and Fracture Energy of Concrete, ed. by F. W. Wittmann, 1986, pp. 259-268.
73. Chhuy, S., Baron, J. and Francois D., "Mecanique de la Rupture Applique au Beton Hydraulique," Cement and Concrete Research, V. 9, No. 5, 1979, pp. 641-648.
74. Berthelot, J. M. and Robert, J. L., "Damage Process Characterization in Concrete by Acoustic Emission," Lake Tahoe, Nevada, October, 1985.
75. Chhuy, S., Cannard, G., Robert, J. L. and Acker, P., "Experimental Investigations on the Damage of Concrete with Natural Aggregates," Submitted to RILEM (Materials and structures).
76. Iori, I., Lu, H., Marozzi, C. A. and Pizzinato, E., "Method per la Determinazione dei Campi Spostamento nei Materiali Eterogenei (Conglomerati Naturali ed Artificiali) a Bassa Resistenza Specifica a Trazione, L' Industria Italiano Del Cemento, No. 4, 1982, pp. 275-280.
77. Cedolin, L., Dei Poli, S. and Iori, I., "Experimental Determination of the Fracture Process Zone in Concrete," Cement and Concrete Research, V. 13, 1983, pp. 557-567.
78. Cedolin, L., Dei Poli, S. and Iori, I., "Tensile Behavior of Concrete," ASCE Journal of Engineering Mechanics, V. 113, No. 3, 1987, pp. 431-449.
79. Mindess, S., "Rate Effects on the Fracture of Cementitious Materials," Application of Fracture Mechanics to Cementitious Composites, Northwestern University, September 1984, pp. 465-484.

80. Wittmann, F. H., "Influence of Time on Crack Formation and Failure of Concrete," Application of Fracture Mechanics to Cementitious Composites, Northwestern University, September 1984, pp. 443-464.
81. Suaris, W. and Shah, S. P., "Mechanical Properties of Materials Under Impact and Impulsive Loading," Concrete Structure Under Impact and Impulsive Loading, Interassociation (RILEM, CEB, IABSE, IASS) Symposium, West Berlin, June 1982, pp. 33-62.
82. Reinhardt, H. W., "Strain Rate Effects on the Tensile Strength of Concrete as Predicted by Thermodynamic and Fracture Mechanics Models," Cement-Based Composite: Strain Rate Effects on Fracture, ed by S. Mindess and S. P. Shah, MRS Symposia proceedings, V. 64, 1986, pp. 1-20.
83. Mellinger, F. M. and Birkimer, D. L., "Measurements of Stress on Cylindrical Test Specimens of Rock and Concrete Under Impact Loading," Tech. Rep. 4-46, Dept of Army, Ohio River Div. Lab., April 1966.
84. Takeda, J. and Tachikawa, H., "Deformation and Fracture of Concrete Subjected to Dynamic Load," Proceedings of International Conference on Mechanical Behavior of Materials, V. IV, Concrete and Cement Paste, Glass and Ceramics, Kyoto, August 1971, pp. 267-277.
85. Cowell, W., "Dynamic Properties of Plain Portland Cement Concrete," Technical Report No. R447, US Naval Engineering Laboratory, Port Hueneme, CA, June 1966.
86. Kormeling, H. A., Zielinski, A. J. and Reinhardt, H. W., "Experiments on Concrete Under Single and Impacted Loading," Report No. 5-80-3, Delft University of Technology, Stevin Laboratory, May 1980.
87. Tinic, C. and Bruhwiler, E., "Effects of Compressive Loads on the Tensile Strength of Concrete at High Strain Rates," International Journal of Cement, Composite and Lightweight Concrete, V. 7, No. 2, 1985, pp. 103-108.

88. Bentur, A., Mindess, S. and Banthia, N., "The Behaviour of Concrete Under Impact Loading: Experimental Procedures and Methods of Analysis," RILEM Materials and Structures, V. 19, N. 113, September-October, 1986, pp. 317-378.
89. Mindess, S and Bentur, A., "A Preliminary Study of the Fracture of Concrete Beams Under Impact Loading, Using High Speed Photography," Cement and Concrete Research, V. 15, No. 3, 1985, pp. 474-484.
90. Gopalaratnam, V. S., Shah, S. P. and John, R., "A Modified Instrumented Charpy Test for Cement-Based Composites," SEM Experimental Mechanics, V. 24, No. 2, pp. 102-111, June 1984.
91. John, R. and Shah, S. P., "Fracture of Concrete Subject to Impact Loading," Cement, Concrete and Aggregates, CCAG DP, ASTM, V. 8, 1986, pp. 24-32.
92. Gopalaratnam, V. S. and Shah, S. P., "Properties of Steel Fiber Reinforced Concrete Subjected to Impact Loading," ACI Journal, V. 83, 1986, pp. 117-126.
93. Suaris, W. and Shah, S. P., "Rate-Sensitive Damage Theory for Brittle Solids," Journal of Engineering Mechanics, ASCE, V. 110, No. 6, June 1984, pp. 985-997.
94. Suaris, W. and Shah, S. P., "Constitutive Model for Dynamic Loading of Concrete," Journal of Structural Engineering, ASCE, V. 111, No. 3, March 1985, pp. 563-576.
95. Suaris, W. and Shah, S. P., "Inertial Effects in Instrumented Impact Testing of Cementitious Composites," ASTM, Journal of Cement, Concrete and Aggregate, March 1982, pp. 78-83.
96. John, R., Shah, S. P. and Jenq, Y. S., "A Fracture Mechanics Model to Predict the Rate Sensitivity of Mode I Fracture of Concrete," Cement and Concrete Research, V. 17, No. 2, April 1987, pp. 249-262.
97. Kachanov, L. M., "Introduction to Continuum Damage Mechanics," Martinus Nijhoff Publishers, 1986.

98. Kachanov, L. M., "On Creep Rupture Time, Izv, Acad, Nauk SSSR, Otd. Techn. Nauk, No. 8, 1985, pp. 26-31.
99. Mazars, J., "Mechanical Damage and Fracture of Concrete Structures," Advances in Fracture Research, ed. by Francois D., V. 4, 1981, pp. 1499-1506.
100. Chen, E. P., "Continuous Damage Mechanics Studies on the Dynamic Fracture of Concrete," Cement Based Composites: Strain Rate Effects on Fracture, ed. by S. Mindess and S. P. Shah, Material Research Society Symposia Proceedings, V. 64, 1986, pp. 63-77.
101. Mihashi, H. and Izumi, M., "A Stochastic Theory for Concrete Fracture," Cement and Concrete Research, V. 7, No. 4, July 1977, pp. 411-421.
102. Zech, B. and Wittmann, F. H., "Variability and Mean Value of Strength of Concrete as Function of Load," ACI Journal, V. 77 September-October 1980, pp. 358-362.
103. Evans, R. H. and Marathe, M. S., "Microcracking and Stress-Strain Curves for Concrete in Tension," RILEM Material and Structure, V. 1, 1968, pp. 61-64.
104. Golaparatnam, V. S. and Shah, S. P., "Softening Response of Plain Concrete in Direct Tension," ACI Journal, V. 82, No. 3, June 1985, pp. 310-323.
105. Reinhardt, H. W., "Crack Softening Zone in Plain Concrete Under Static Loading," Cement and Concrete Research, V. 15, 1985, pp. 42-52.
106. Guo, Z. H. and Zhang, X. Q., "Investigation of Complete Stress-Deformation Curves for Concrete in Tension," ACI Material Journal, V. 84, July-August 1987, pp. 279-285.
107. Heilmann, H. G., Hilsdorf, H. H. and Finsterwalder, K., "Festigkeit und Verformung von Beton unter Zugspannungen, Deutscher Ausschuss fur Stahlbeton, Heft 203, W. Ernst & Sohn, Berlin (in German), 1969.

108. Diamond, S. and Bentur, A., "On the Cracking in Concrete and Fibre-Reinforced Cements," Application of Fracture Mechanics to Cementitious Composites, ed. by S. P. Shah, Martinus Nijhoff Publishers, 1985, pp. 87-140.
109. Tait, R. B. and Garrett, G. G., "In Situ Double Torsion Fracture Studies of Cement Mortar and Cement Paste Inside a Scanning Electron Microscope," Cement and Concrete Research, V. 16, No. 2, 1986, pp. 143-155.
110. Wittmann, F. H., "Structure of Concrete with Respect to Crack Formation," Fracture Mechanics of Concrete, ed. by F. H. Wittmann, Elsevier Science Publishers, 1983.
111. Kobayashi, A. S., "Dynamic Fracture Analysis by Dynamic Finite Element Method - Generation and Propagation Analysis," Nonlinear and Dynamic Fracture Mechanics, ed. by N. Perrone and S. N. Atluri, ASME, AMD-35, 1979, pp. 19-36.
112. Kobayashi, A. S., "Hybrid Experimental-Numerical Stress Analysis," Experimental Mechanics, V. 23, September 1983, pp.338-347.
113. Post, D., "Developments in Moire Interferometry," Optical Engineering, V. 21, 1987, pp. 458-467.
114. Kang, B. S., "Experimental Investigation of Ductile Fracture by White Light Moire Interferometry," Ph.D Dissertation, University of Washington, Seattle, WA, 1987.
115. ASTM 561-81, "Standard Practice for R-Curve Determination," American Society of Testing and Materials, Philadelphia, PA, 1981.
116. Ratanalert, S. and Wecharatana, M., "Evaluation of Existing Fracture Models in Concrete," Presented at ACI Fall Convention, Seattle, November, 1987.
117. Kobayashi, A. S., Emery, A. F. and Liaw, B. M., "Dynamic Fracture Toughness of Glass," Fracture Mechanics of Ceramics, V. 6, ed. by R. C. Bradt, A. G. Evans, D. P. H. Hasselman and F. F. Lange, 1983, pp. 47-62.

118. Kobayashi, A. S., Emery, A. F. and Liaw, B. M., "Dynamic Fracture Toughness of Reaction Bonded Silicon Nitride," Journal of American Ceramic Society, V. 66, No. 2, February 1983, pp. 151-155.
119. Liaw, B. M., Kobayashi, A. S. and Emery, A. F., "Effect of Loading Rate on Dynamic Fracture of Reaction Bonded Silicon Nitrided," to be published in American Society for Testing Materials, Special Technical Publication.
120. Lee, O. S., Kobayashi, A. S. and Komine, A., "Further Studies on Crack Tip Plasticity of a Tearing Crack," Experimental Mechanics, V. 25, No. 1, March 1985, pp. 66-74.
121. Kobayashi, A. S., Emery, A. F., Love, W. J., Lee, C.-H., Chao, Y.-H and Place, B. M., "Rapidly Propagating Ductile Crack in a 2-in. Pressurized Pipe," Fracture, Fatigue and Advanced Mechanics, ed. by W.E. Short and S. Y. Zamrik, ASME, PVP, V. 98-8, 1985, pp. 119-124.
122. Kobayashi, A. S., Emery, A. F. and Liaw, B. M., "Dynamic Fracture of Three Specimens," Fracture Mechanics: Fourteenth Symposium - V. II, Testing and applications, ASTM, STP 791, ed. by J. C. Lewis and G. Sines, 1983, pp. II-251-II-265.
123. Kobayashi, A. S., Ramulu, M., Dadkhah, M. S., Yang, K. H. and Kang, B. S., "Dynamic Fracture Toughness," International Journal of Fracture, V. 30, 1986, pp. 275-285.
124. Sambell, R. A., Bowen, D. H. and Phillips, D. C., "Carbon Fibre Composites With Ceramic and Glass Matrices, Part 1, Discontinuous Fibres," Journal of Material Science, V. 7, 1972, pp. 663-675.
125. Lewis, D., III, "Cyclic Mechanical Fatigue in Ceramic-Ceramic Composites -An Update," Ceramic Engineering and Science Proceedings, July-August 1981, pp. 661-701.

APPENDIX A

SPECIMEN PREPARATION DETAILS

The materials for each cast were weighed and placed in a horizontal pan mixer. The required amount of water was then added slowly as the mixer rotated. One batch of concrete was sufficient to produce five 457.2 mm (18 in.) square CLWL-DCB specimens and five companion 152.4 x 304.8 mm (6 x 12 in.) cylinders or five small CLWL-DCB specimens and five large beam specimens with five cylinders.

The specimens were cast in a horizontal position in oil lubricated steel forms and steel cylinders and plates screwed to those forms to create holes for the split pins and starter cracks. Each specimen was compacted with a mechanical form vibrator that moved across the top of the specimen. Particular care was taken to avoid segregation of the ingredient materials. Each control cylinder was fabricated in three layers and compacted with a one-inch diameter electric immersion vibrator.

All specimens and their companion cylinders were cured in the same manner. Immediately after casting, the specimens and cylinders were covered with polyethelene sheets and stored at room temperature. The forms were stripped at an age of two days, the specimens and cylinders

removed from the forms, the steel inserts carefully knocked off from the specimens, and then both specimens and cylinders immediately placed in plastic bags. Except during surface polishing operations, they were kept in the plastic bags at room temperature until the age of 28 days.

Prior to transferring the optical diffraction grating onto the specimen surface, the upper surfaces of the CLWL-DCB and the three point bend specimen must be carefully ground and polished according to the following steps:

- (1) After one week of curing, the concrete specimens are removed from the plastic bags and placed horizontally on wooden blocks. The specimen must be laid flat so that the surface is not subject to any bending stress during this surface treatment.

- (2) With a carborundum stone the specimen is manually ground to a flat surface where the optical diffraction grating is being transferred. Wash the ground area occasionally with fresh water.

- (3) The overall flatness was checked by a used holographic plate (glass) of 102 mm x 102 mm (4 in. x 4 in.) size and the local flatness was checked by a metal flatness gage.

(4) The specimens are then washed and placed back into the plastic bags. They must be kept wet for 28 days after casting.

(5) The specimens are then checked for ground area flatness again and if necessary ground and polished again following the steps of (1) through (4).

APPENDIX B

DIFFRACTION GRATING MAKING AND TRANSFER

The 600 line/mm specimen active grating, and the 1200 line/mm real reference grating, were all made by holographically recording the interference patterns of two collimated coherent laser beams. The recording medium was a 102 mm x 102 mm Kodak holographic film plate with precision flatness. The light source was a 5 watt argon laser made by Spectrum Physics and operated at 300 mw output. The laser beam was firstly equally split by a beam splitter into two beams. Then these two beams were expanded and cleaned by spatial filters and collimated by two parabolic mirrors. These two collimated beams were projected onto the film plate at a symetric incident angle which was determined from the beam interference equation given in Chapter 4 of the text. All the optical devices were mounted on a vibration isolation bench. The exposure time was 0.5 second determined by experience.

The exposed film plate was then processed through the following steps:

- (1) Develop for 5 minutes in D-19 developer.

- (2) Stop developing by red stopper.
- (3) Fix for 2 minutes in Kodak rapid fixer.
- (4) Bleach for 0.5 minutes in a special bleach given below.
- (5) Coat for 0.5 minutes in photoflow.

The special bleach consisted of equal proportion of solutions A and B. Solution A was $(\text{NH}_4)_2\text{C}_{20}\text{O}_{14}$ 20 g with 500 ml water. Solution B was NaCl 45 g plus H_2SO_4 14 ml with 500 ml water.

The film was dried at room temperature and the result was a phase type diffraction grating. Then, the 600 line/mm frequency of the grating was transferred to a specimen's surface by a replication procedure that involved three steps, as follows:

- (1) Coat the mold grating by vacuum deposition with aluminum of 0.1 micron thickness.
- (2) Glue the coated mold to the finished specimen's surface using epoxy, Type PC-10.
- (3) After one day, pull the mold off from the specimen surface leaving the aluminum coating behind.

The aluminum layer left on the specimen surface has the same grating frequency as the mold grating but changes slightly with the deformation of the specimen. The difficulties in making and transferring these gratings to the specimen arise primarily from the large grating size.

This technique was developed previously for testing much smaller specimens [113]. For making a large grating, precision in the optical alignment is important because the highest fringe order of the null pattern increases quadratically increased with grating size. Effective transfer of a grating frequency requires experience in driving out air bubbles from the bonding layer. The detailed grating transfer procedure is given below.

The grating transfer procedure is as follows:

- (1) The grating area is precoated with epoxy Type AE-10. A small knife is used to spread the epoxy and fill the small holes on concrete surface. This epoxy layer should be as thin as possible.

- (2) The epoxy is cured overnight and sanded for remaining of the epoxy layer thus leaving the small holes filled. A gauze sponge is used to clean dust and polishing powder without chemical cleaning agent.

- (3) 10 g epoxy PC-10 (clear type) is mixed for gluing a 102 mm x 102 mm (4 in, x 4 in.) grating. The epoxy is poured onto the center of the transfer area.

- (4) The grating is pushed at the corners on the epoxy puddle immediately, smoothly and uniformly in order to drive out the excess epoxy. Then, a weight of 25 pounds is placed on top of the grating through a half inch thick rubber pad and watch the alignment for one hour.

(5) The cured epoxy is cleaned after overnight curing. The master grating plate is removed by wedging a single edge blade, where the sputtered aluminum layer of the grating is left behind on the specimen. Clean air is used to blow away any dust and the grating is covered with lens paper for protection.

APPENDIX C

SOLUTION OF OVERDETERMINISTIC CONTRADICTIONARY EQUATIONS

The multiple sets of contradictory equations, (5-12) through (5-15) for CLWL-DCB specimen and the other multiple sets of contradictory equations, (5-12), (5-13), (5-16) for three point bend specimen can be solved by a Newton-Raphson routine through the following steps.

(1) These equations should be normalized in order to give an equal level of relative error allowance for different variables. Weight can also be added to the normalized equations in any future refinement.

(2) These normalized equations are nonlinear with respect to their unknowns which are fracture parameters. Thus, they can then be incrementally linearized using a standard Newton-Raphson iterative solution routine.

(3) At each iteration step, Householder transformation was used to solve these linear but contradictory equations for increments of unknowns. Householder transformation is an orthogonal linear transformation. It can be used to obtain least square results without forming normal equations. Since normal equations are always more ill-conditioned than the original equations, use of the Householder transformation is helpful

for improving the solution stability which is an inherent problem existing in the least square procedure.

APPENDIX D

SOME DYNAMIC FINITE ELEMENT COMPUTATION DETAILS

Dynamic Finite Element Implementation and Procedure.

Once the dynamic model is formulated, it can be incorporated into a dynamic finite element code. Due to its nonlinear nature, iteration is necessary as explained in Chapter 5. The implemented code should include the following computation steps.

(1) Execute the dynamic finite element program until the maximum tensile stress at the crack tip element reaches the tensile strength of the concrete.

(2) Release the first node along the expected crack path and prescribe a crack closure force equivalent to f'_t on this node.

(3) Iterate without advancing the time step to match the $\sigma - w$ relation of the fracture process zone model.

(4) Advance time steps and keep iteration until the next node along the crack path needs to be released according to the tensile strength criterion.

(5) Release this second node and apply crack closure forces on these released nodes in accordance with the $\sigma - w$ relation.

(6) Return to (4) until the last element along the expected crack path is reached by the running crack tip.

The choice of element size lies in the availability of the computational resources. As usual, the smaller the elements, the more accurate the results.

The time step size should be determined by the element size and the minimum stress wave propagation speed so that the stress wave can only pass through at most one element in one time step. The smaller the time step size, the better the results.

Determination of CODs, f'_t , E , ν , ρ for Concrete and Mortar for Dynamic Analysis on Shah's Impact Tests.

(1) Concrete:

The three critical crack opening displacements w_1 , w_2 and w_3 were determined using the formula given in Reference [9]. For $f'_c > 5010$ psi.

$$w_1 = 0.75 - (0.07 f'_c / 1000);$$

$$w_2 = 1.25 (f'_c / 1000 - 1) w_1;$$

$$w_3 = w_2 + 9,$$

where f'_c is the concrete compressive strength in psi and CODs units are 10^{-3} inch. The f'_c given in Reference [91] is 6452 psi, so that the calculated CODs are:

$$w_1 = 0.298 \times 10^{-3} \text{ inch,}$$

$$w_2 = 2.033 \times 10^{-3} \text{ inch,}$$

$$w_3 = 11.03 \times 10^{-3} \text{ inch.}$$

The Modulus of Elasticity E was taken from Reference [91] as 4.55×10^6 psi. The Poisson's ratio ν was assumed to be 0.15. The density ρ was estimated as 150 lb/ft^3 , i.e., $2.25 \times 10^{-4} \text{ lbm/inch}^3$ and then checked against the stress wave velocity of about 12,000 ft/s given in Reference [91].

The static tensile strength of the concrete was not reported in Reference [91]. Therefore dynamic tensile strength values were estimated as follows.

a) The dynamic tensile strength for mortar at a strain rate of 0.3 1/s was estimated, using the information given in Reference [92] (see (2)), as 566.6 psi. Then the peak load values for the concrete and mortar specimens for the strain rate of $0.2 \times 10^{-4} \text{ 1/s}$ were taken from the curves in Figures. 5 and 8 of Reference [91] as 2.27 kN and 1.67kN, respectively. The dynamic tensile strength for the concrete for $\dot{\epsilon} = 0.3 \text{ 1/s}$ was determined by multiplying the ratio for those peak loads by the dynamic tensile strength for the mortar.

$$f'_t = 566.5 \text{ psi } (2.27/1.67) = 770 \text{ psi.}$$

b) The peak load values of 28 kN, 32 kN and 38 kN shown in Figures. 9-11 of Reference [91] were used, in conjunction with the foregoing tensile strength data for $\dot{\epsilon} = 0.3$ 1/s to roughly estimate the dynamic tensile strength of the concrete at strain rates of 0.1, 0.2 and 0.4 1/s. Since the value for the peak load for $\dot{\epsilon} = 0.3$ 1/s was not available, it was estimated from interpolation of the data for $\dot{\epsilon} = 0.2$ 1/s and $\dot{\epsilon} = 0.4$ 1/s as 35 kN. Then, the desired strength values were obtained by proportionality.

A. For $\dot{\epsilon} = 0.1$ 1/s,

$$f'_t = 770 \text{ psi } (2.8/3.5) = 616 \text{ psi} = 4.25 \text{ MPa.}$$

B. For $\dot{\epsilon} = 0.2$ 1/s,

$$f'_t = 770 \text{ psi } (3.2/3.5) = 704 \text{ psi} = 4.85 \text{ MPa.}$$

C. For $\dot{\epsilon} = 0.4$ 1/s,

$$f'_t = 770 \text{ psi } (3.8/3.5) = 836 \text{ psi} = 5.76 \text{ MPa.}$$

Since peak loads are proportional to moduli of rupture (MOR), those values A, B, and C are consistent with an assumption that tensile strength has the same strain rate sensitivity as MOR values.

c) For the assumption used in the main text of this thesis, namely that the tensile strength of the concrete has the same strain rate sensitivity as the fracture energy G_F , values increased only 30%. Ratio for those two percentages was therefore used to modify the strengths

calculated in b). Thus:

For $\dot{\epsilon} = 0.1$ 1/s,

$$f'_t = 770 + (616 - 770) (30/70) = 704 \text{ psi} = 4.85 \text{ MPa.}$$

For $\dot{\epsilon} = 0.2$ 1/s,

$$f'_t = 770 + (704 - 770) (30/70) = 733 \text{ psi} = 5.05 \text{ MPa.}$$

For $\dot{\epsilon} = 0.4$ 1/s,

$$f'_t = 770 + (836 - 770) (30/70) = 799 \text{ psi} = 5.51 \text{ MPa.}$$

(2) Mortar

The three critical crack opening displacements w_1 , w_2 , and w_3 were obtained by local and error analysis of the load versus deflection curve for static loading given in Figure 5 of Reference [92]. The results are:

$$w_1 = 0.1 \times 10^{-3} \text{ inch,}$$

$$w_2 = 1.0 \times 10^{-3} \text{ inch,}$$

$$w_3 = 6.0 \times 10^{-3} \text{ inch.}$$

The Modulus of Elasticity E was first taken from Reference [92] as 3.97×10^6 psi, then modified to 3.20×10^6 psi in order to fit the tangent to the slope of the $P - \delta$ curves in Figure. 5 of Reference [92]. The Poisson's Ratio ν was assumed to be 0.15. The density ρ was estimated in the same way as for concrete (see (1)).

The static tensile strength of mortar, given as 405 psi in Reference [92], was modified to 420 psi to fit the $P - \delta$ curve for the static test in Figure 5 of

Reference [92], and the G_F values of 0.58 lb/inch for $\dot{\epsilon} = 0.3$ 1/s and 0.43 lb/inch for $\dot{\epsilon} = 10^{-6}$ 1/s taken from Table 3 of Reference [92] were used to obtain the dynamic tensile strength for $\dot{\epsilon} = 0.3$ 1/s. Following the assumption used in Chapter 7 of this dissertation, the tensile strength is

$$f'_t = 420 \text{ psi} (0.58/0.43) = 566.5 \text{ psi} = 3.91 \text{ MPa}$$

Values for elastic modulus, tensile strength, Poisson's Ratio and density for the different strain rates used in the analysis are shown in metric units in Table 7.3.

APPENDIX E

A MODEL FOR FATIGUE OF A SIMILAR MATERIAL

An analogy between concrete and ceramic-ceramic composite fracture was established by relating the aggregate bridging forces in concrete with the crack bridging of randomly oriented SiC fibers in glass matrix composites. A model that mimics the failure process of fiber reinforced ceramic composite under cyclic loading, characterized by a discrete crack extension, has been developed.

In tensile tests [124] and low-cycle fatigue under bending tests [125] ceramic composites exhibit strain softening effects. This nonlinear response is due to the existence of a fracture process zone in which there is crack bridging by the ceramic fibers in the wake of the crack extension and possible fiber-end induced micro-cracking ahead of the crack tip. These crack bridging results in crack closure pressures, which elevate the apparent fracture toughness and induce stable crack growth under displacement controlled loading conditions, along the fracture process zone. Functionally, the aggregates in concrete are similar to the chopped ceramic fiber in the ceramic matrix since both systems share small particulate to matrix modulus ratios. This similarity in

turn, suggests that the fracture process zone developed for concrete fracture may be used with modification in modelling the fracture process of ceramic-ceramic composites.

Figure E.1 shows schematically the fracture process zone which is a simplified version of that of concrete, with the crack bridging force, or the crack closure stress as it is referred to the figure, decreasing monotonically with increasing crack widths. The variation in the crack closure force, which generally is a fracture specimen dependent function of the crack opening displacement (COD), along the fracture process zone is determined by trial and error by matching numerical and experimental gross responses of concrete specimens subjected to a variety of loading conditions. Lacking such studies, a linear relation between the crack closure stress and the COD, as shown in Figure E.2, was assumed for this study of ceramic-ceramic composites.

The flexural test conducted by Lewis [125] provided experimental evidence for developing a model. Figures E.3 and E.4 show the specimen configuration and the mesh for finite element computation, respectively. The fracture criterion used in this study was a limiting tensile stress criterion at the fracture process zone crack tip and a control volume of 0.1 mm was used in the finite element

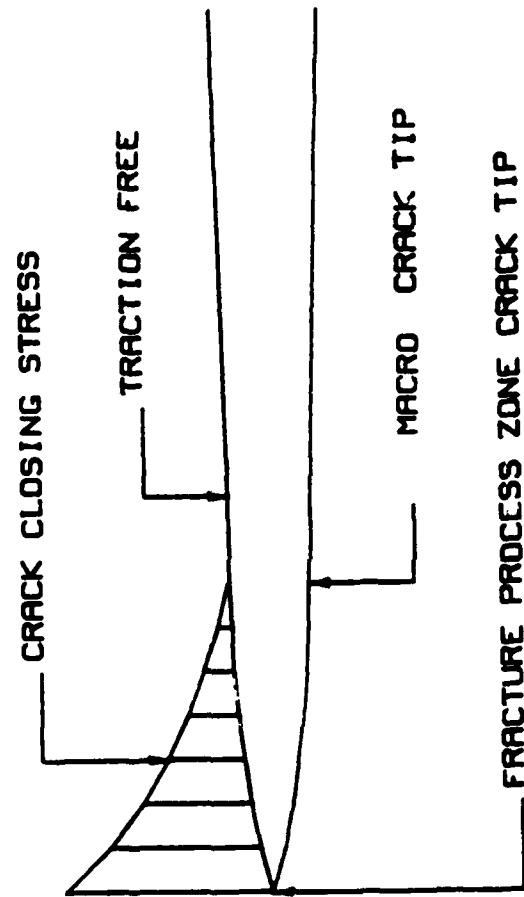


Figure E.1 Fracture Process Zone in Ceramic Composite

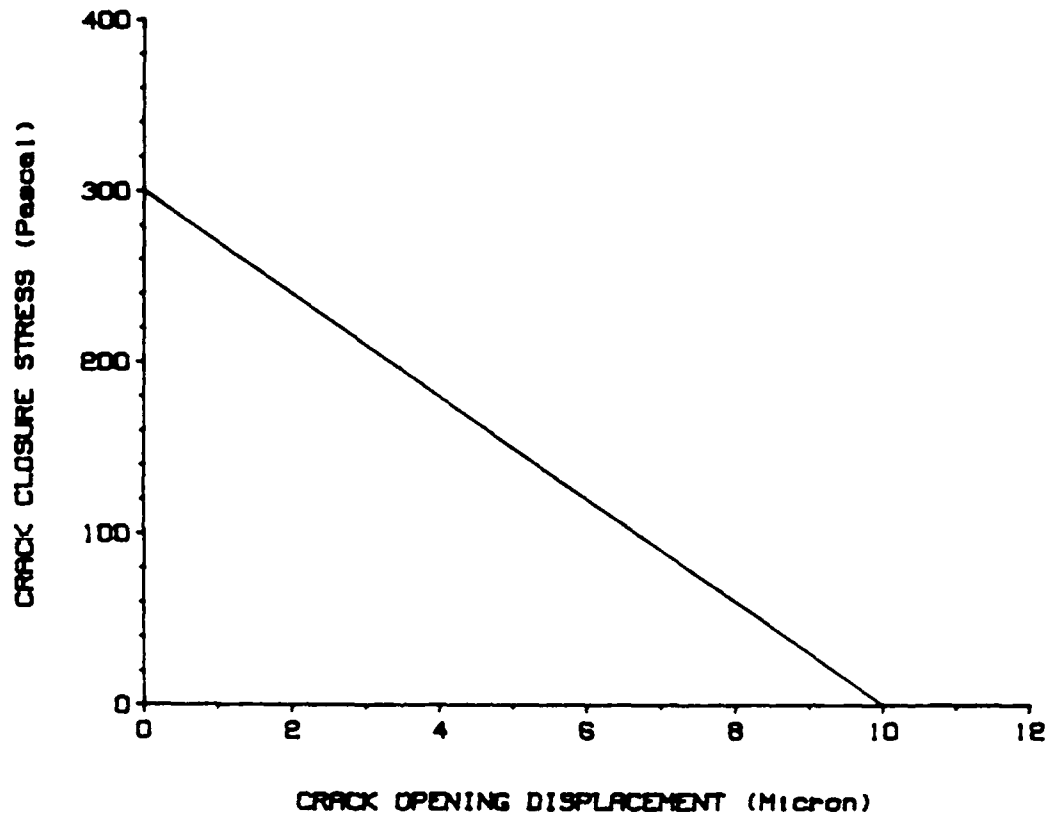


Figure E.2 Crack Closure Stress Versus COD Relation
SiC/Mullite Composite Flexural Specimen

| | |
|-----------------------|---------|
| TENSILE STRENGTH | 300 MPa |
| MODULUS OF ELASTICITY | 400 GPa |
| POISSON'S RATIO | 0.15 |

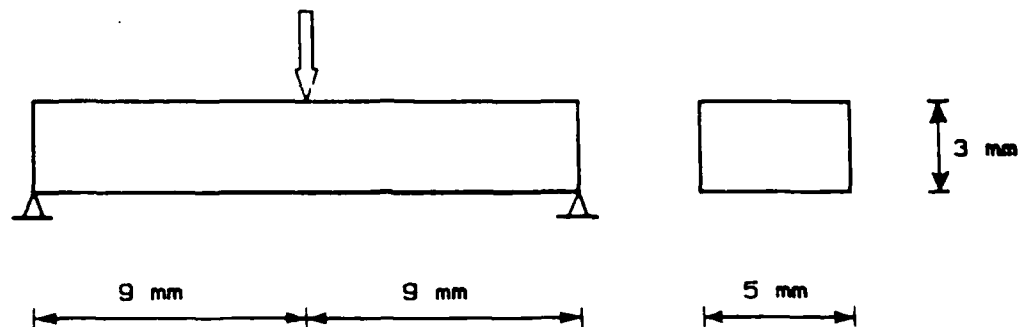


Figure E.3 SiC/Mullite Composite Flexural Specimen

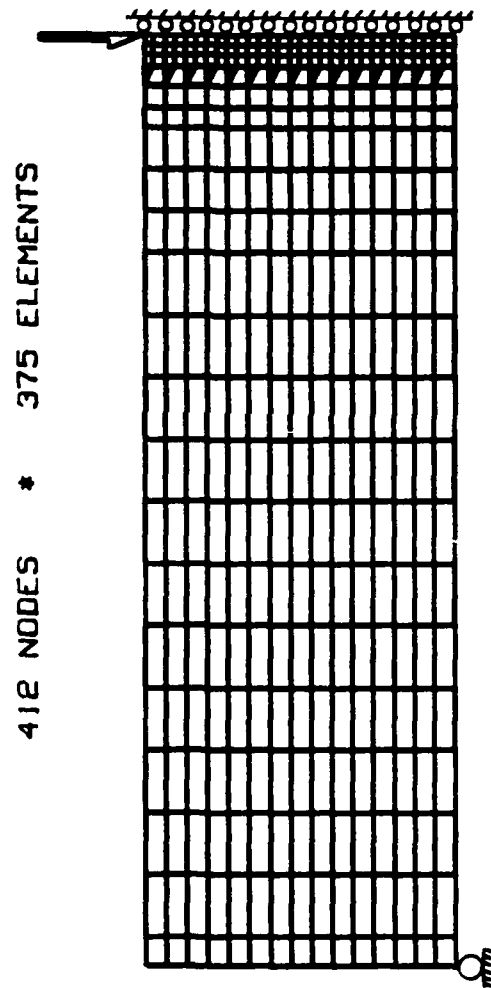


Figure E.4 Finite Element Model for Ceramic Composite
Flexural Specimen

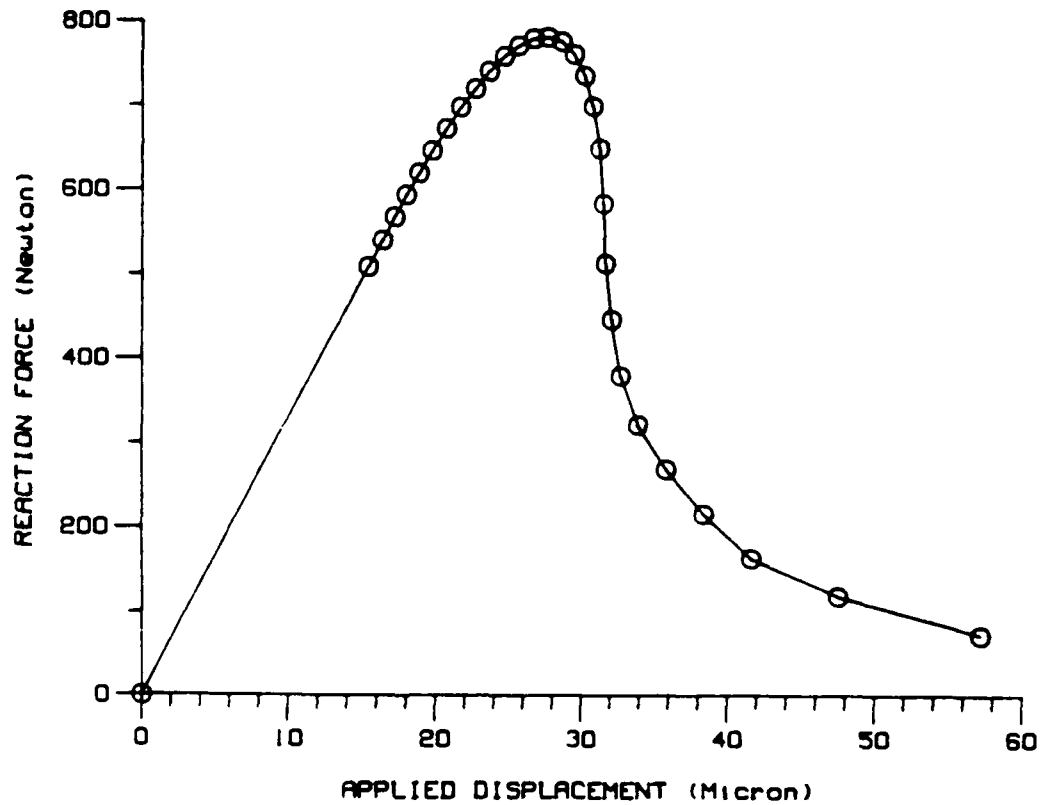


Figure E.5 Reaction Force Versus Applied Displacement
SiC/Mullite Composite Flexural Specimen

computation. Shown in Figure E.5 is the load-displacement curve for the flexural specimen under monotonic displacement controlled loading. This curve, which is commonly observed in concrete testing, exhibits a pre-peak stiffness softening and a post-peak strength toughness. The same specimen was tested under force controlled cyclic loading to its maximum load-capacities. While the monotonic loading response can be computed using finite element methods incorporating a fracture process zone, prediction of the unloading and reloading process requires the development of a theoretical model additional to the fracture process zone model discussed previously. The assumptions used in developing such model were as follows:

- 1) In the unloading process, the material inside the fracture process zone behaves linearly.
- 2) There is a stage in the middle of both unloading and subsequent reloading phases at which the crack closure stress in the fracture process zone vanishes and the permanent deformation of the material in the fracture process zone is evaluated at the corresponding load level.
- 3) The incremental extension of the macro-crack tip after each loading cycle is determined by a crack opening displacement criterion which, in this study, was assumed to be 3 microns.

Figure E.6 provides an explanation of the failure process of ceramic composites under cyclic loading. According to assumption 1), the unloading curve should be a straight line as shown by AC in Figure E.6 (a). Due to the existence of permanent deformation, the material in the process zone undergoes tension and then compression. Point B, in the figure, represents the neutral state which is assumed in assumption 2. Figure E.6 (b) shows the pre-B reloading curve which is the same as the unloading curve because crack extension during the previous cycle has no effect on the compressive load capacity. Figure E.6 (c) shows the incremental advance of the macro-crack tip in accordance with the second assumption. The post-B reloading curve which deviates from CA starting at B following the second and third assumptions. The only problem left is to find the position of B. As shown in Figure E.6 (d), the curve OE is the load-deflection relation for the case in which there is no crack closure stress in the fracture process zone. Obviously, the point B should be on both curves OE and CA. Hence, point B is the intersection of these two curves.

Figure E.7 shows how the cyclic load-deflection curves were generated. The computation steps can be summarized as the followings:

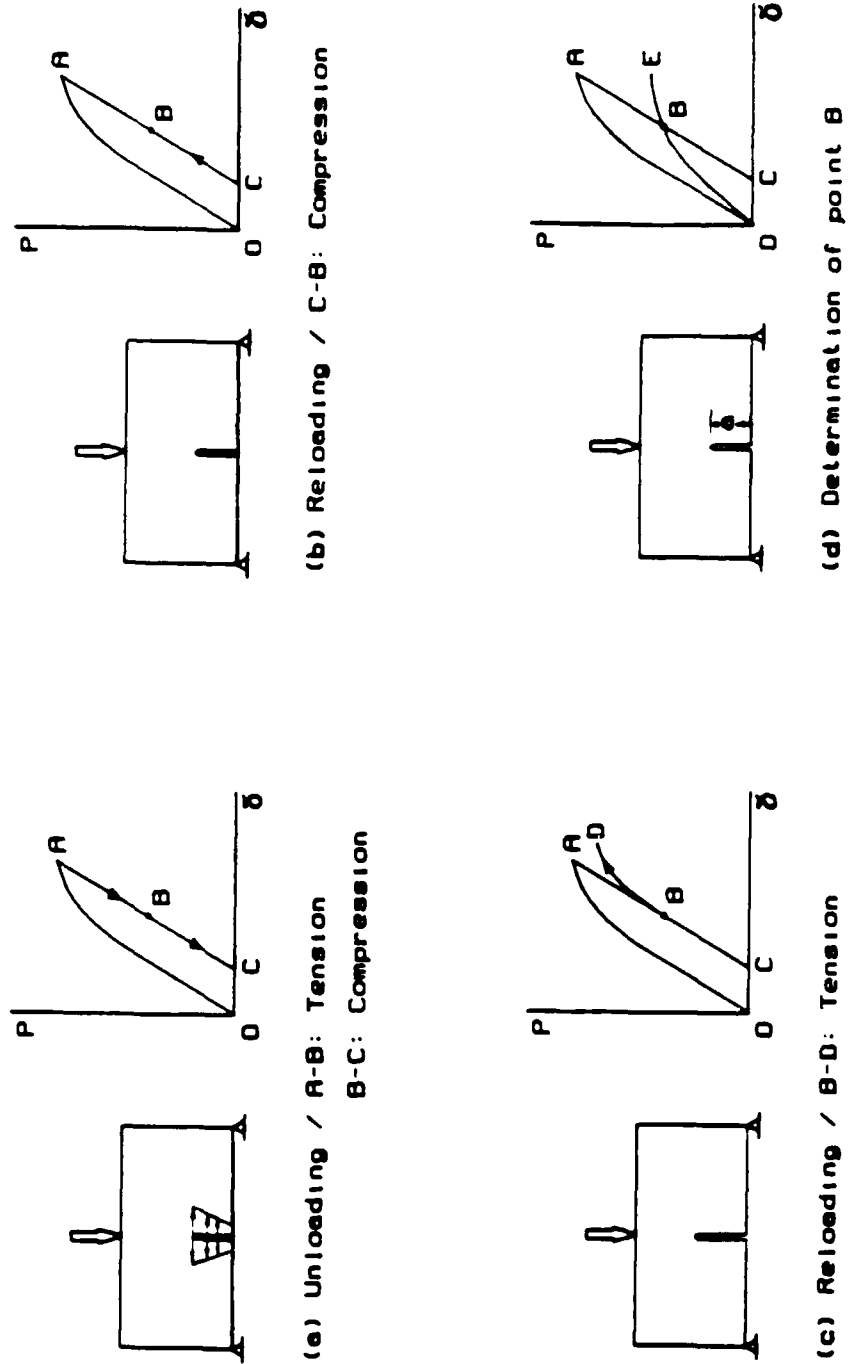
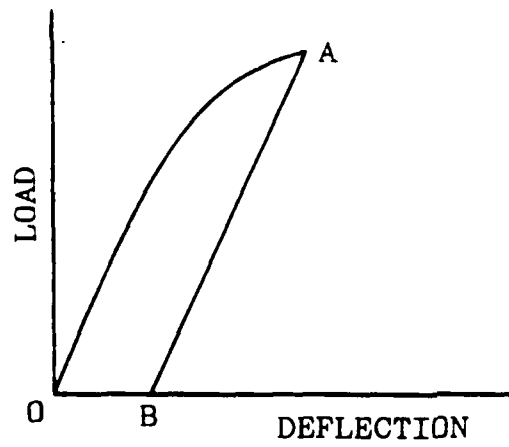
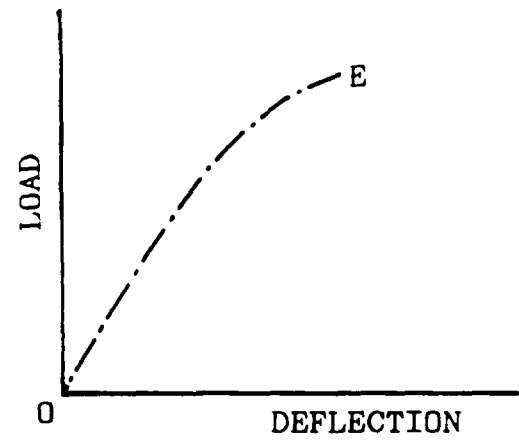


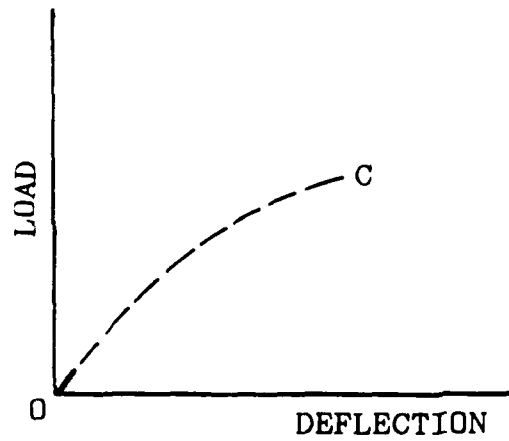
Figure E.6 Failure Process Under Cyclic Loading
A Model for Ceramic Composite



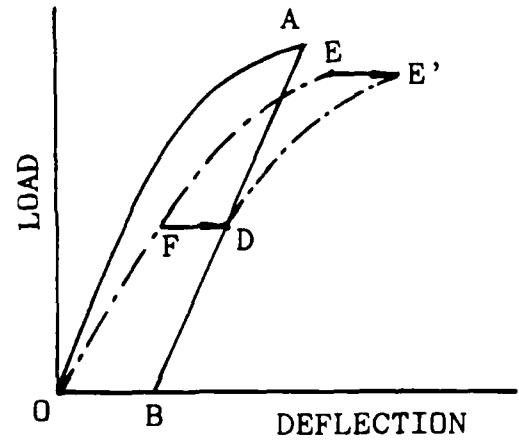
(a)



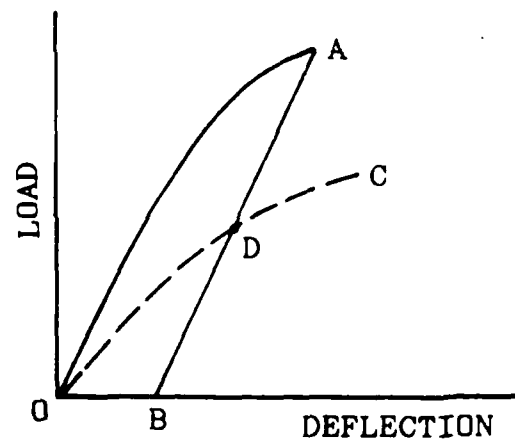
(d)



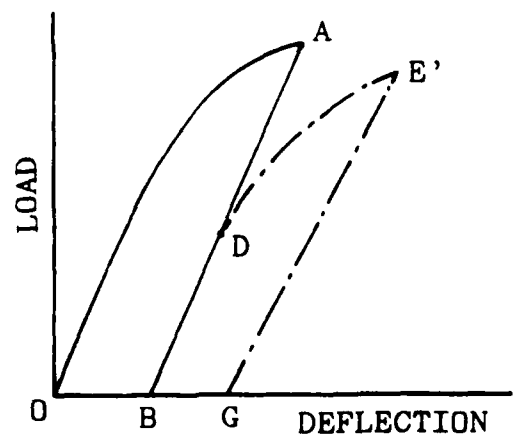
(b)



(e)



(c)



(f)

Figure E.7 Generation of Cyclic Loading Curves
A Model for Ceramic Composite

(a) The first cycle of load versus deflection curve was computed using the fracture process zone model for loading process and assumption 1) for unloading process. The result is shown in Figure E.7 (a) as OAB.

(b) Without prescribing any crack closure stress on the microcrack surfaces load versus deflection curve was re-computed and shown in Figure E.7 (b) as OC.

(c) The "neutral point", thus, was determined as to be the intersection of AB and OC shown in Figure E.7 (c) as D.

(d) The second cycle of load versus deflection curve was then computed with an advancement of traction free crack according to assumption 3). The result is shown in Figure E.7 (d).

(e) Curve EF was translated Horizontally to E'D as shown in Figure E.7 (e). The length of EE' is the same as that of FD.

(f) The second cycle of load versus deflection curve was completed by drawing a straight line E'G whose slope is the same as that of curve OF at point O as shown in Figure E.7 (f).

Figure E.8 presents the final result which is in good agreement with the test result [125]. Since the actual test result was reproduced by numerical computation based on a postulated model, the model was verified.

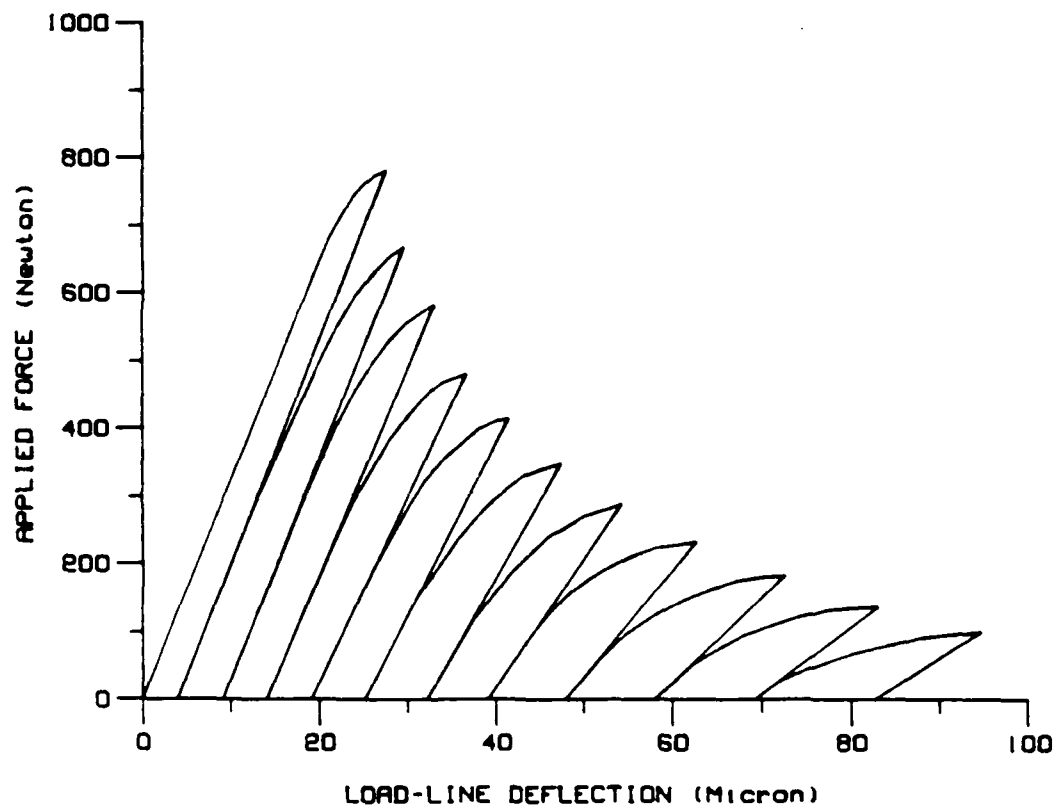


Figure E.8 Cyclic Flexural Load - Deflection Curves
SiC/Mullite Composite Flexural Specimen

Shown in Figure E.9 are computed load versus deflection relationship for specimens with differing prenotched lengths and in Figure E.10 are computed crack profiles for a propagating crack in a specimen without a prenotch. These theoretical predictions can be used later to verify this model whenever test results become available for such comparisons.

Obviously, similar modeling analysis can be carried out for concrete and a more detailed treatment developed for studying the failure mechanism of a material during the unloading and reloading phases of low cycle fatigue testing.

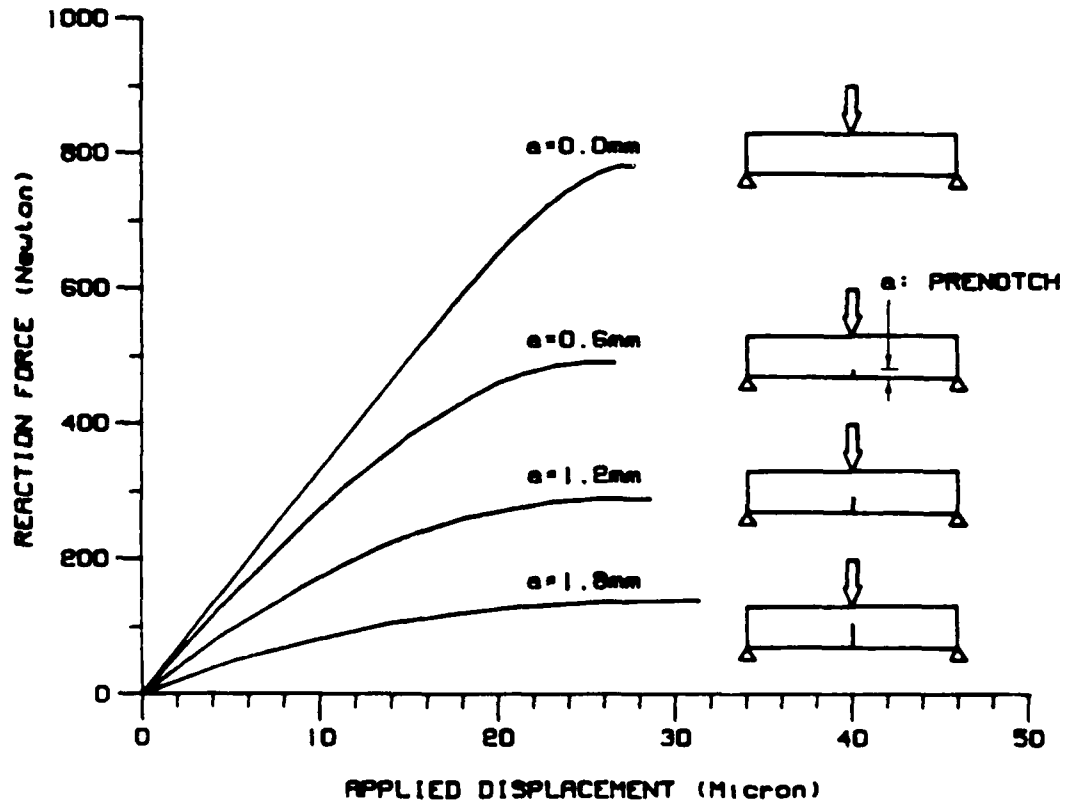


Figure E.9 Reaction Force Versus Applied Displacement for Cracked Beams of Ceramic Composite

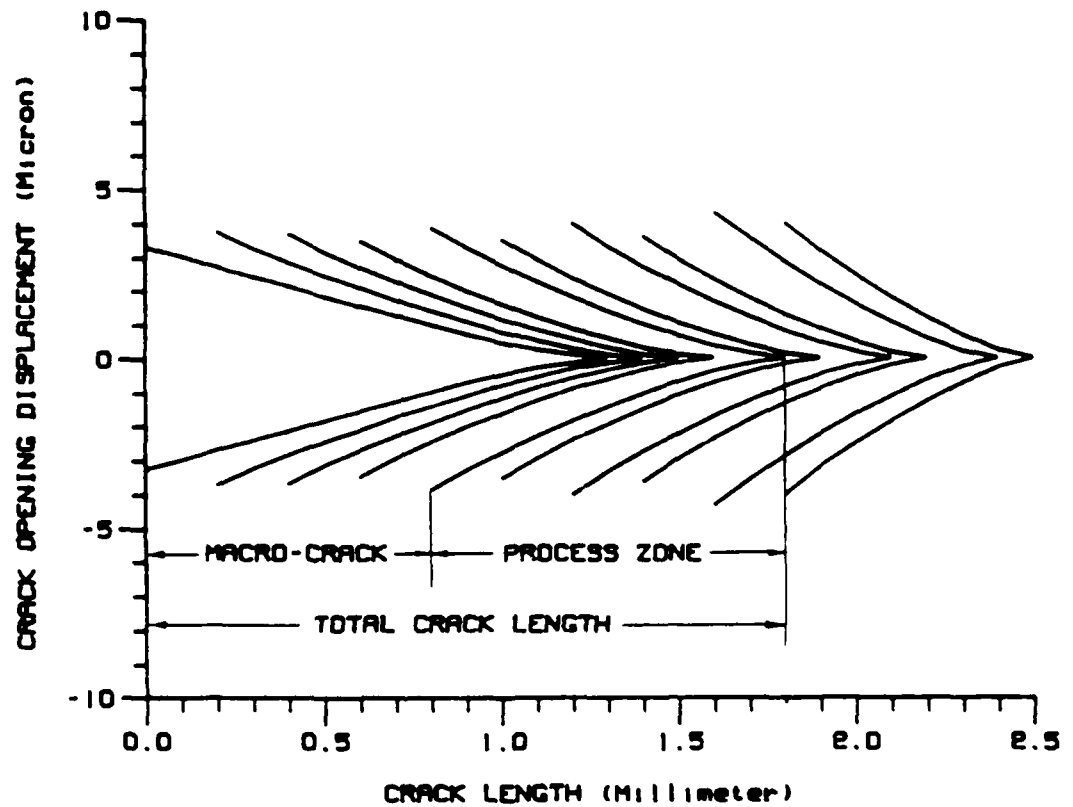


Figure E.10 Crack Profile at Maximum Load for Each Loading Cycle in Flexural Specimens of Ceramic Composite, Finite Element Results

APPENDIX F

K_R CURVE RE-EVALUATION BASED ON TEST RESULTS

The method of evaluation of K_R values for Crack-Line Wedge-Loaded Double-Cantilever Beam (CLWL-DCB) specimens of metals is given in ASTM Standard 561-81 [115]. This method was applied to the CLWL-DCB concrete specimens by Jeang [9] in 1985 at the University of Washington. Recently, Jeang's results have been re-evaluated, and based on the fracture process zone model reported here, new values for K_R were derived.

In ASTM Standard 561-81, crack opening displacements at 2 specific locations on the crack line, termed $2V_1$ and $2V_2$, are to be measured. Then, the ratio of $2V_1$ to $2V_2$ is used to obtain the effective crack length by consulting a table in the Standard. Finally, the K_R value, is computed using a formula of LEFM, for which the measured wedge load value and the effective crack length value are input data. Jeang conducted 5 groups of concrete CLWL-DCB tests with different concrete compressive strengths, aggregate sizes and specimen sizes. He substituted his measured $2V_1/2V_2$ and wedge load values into the table and the formula in the Standard and obtained values for K_R . Data points on a K_R versus effective crack length diagram showed con. Through regression processing, the curves which were appropriate

second degree polynomials of best fit to the data points were obtained. These results were presented in Jeang's [9] dissertation as Figure 4.20. Since K_R values were not measured, Jeang's results are only partial-test results.

Standard 561-81 is intended for metals only, not concrete. In order to determine if the ASTM Standard applies to concrete and can be used to obtain K_R values for CLWL-DCB specimens of concrete, a finite element analysis was conducted on the computer. The fracture process zone model was incorporated into that finite element program and along with the experimental data reported in Jeang's dissertation. Analyses were carried out in two ways. First, Jeang's procedure was followed except that computed $2V_1$, $2V_2$ and wedge load values were used for input rather than the measured data. The computation results are shown in Figures F.1 through F.5 by the dashed lines. Second, an energy analysis was performed by evaluating the fracture energy (work of fracture) dissipation rate within the fracture process zone as the microcrack tip advanced. Then, the fracture energy rate was converted to K_R through the following relationship:

$$K_R = (E \cdot G / (1 - \nu)) \quad (\text{for plane strain})$$

in which E , ν , and G are Young's modulus, Poisson's Ratio and fracture energy rate, respectively. The results

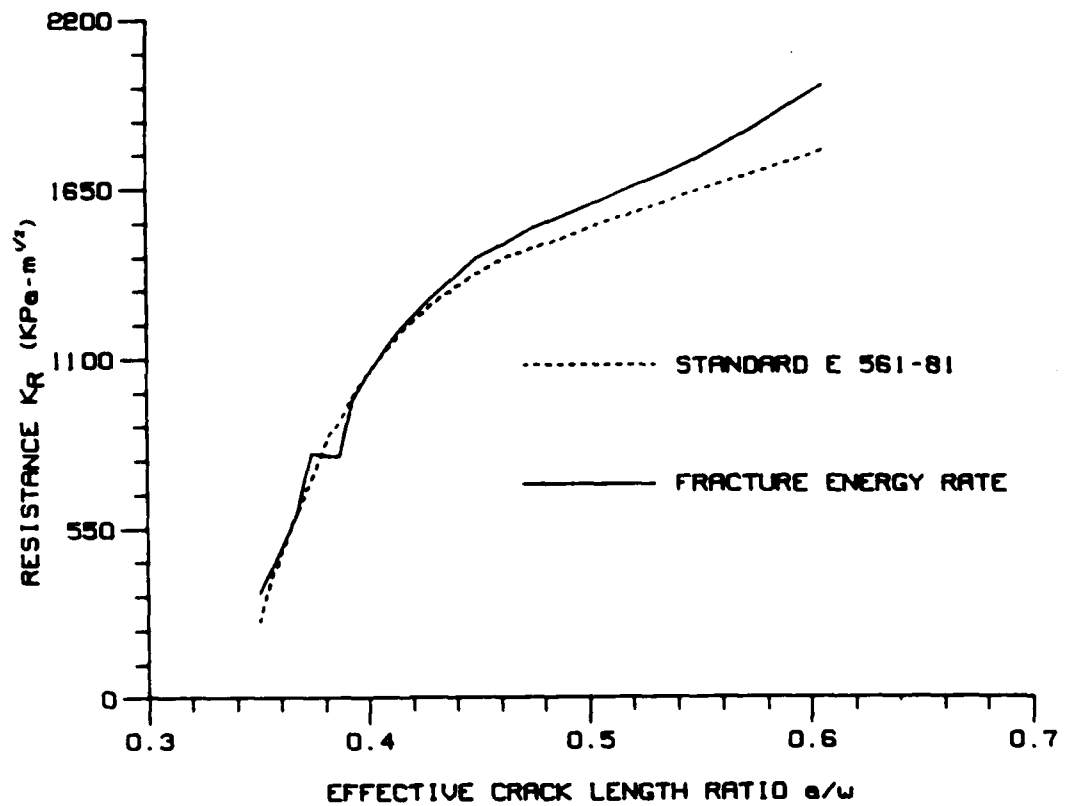


Figure F.1 Crack Growth Resistance Curve For CLWL-DCB Specimen, Group 1, Ref. [9]

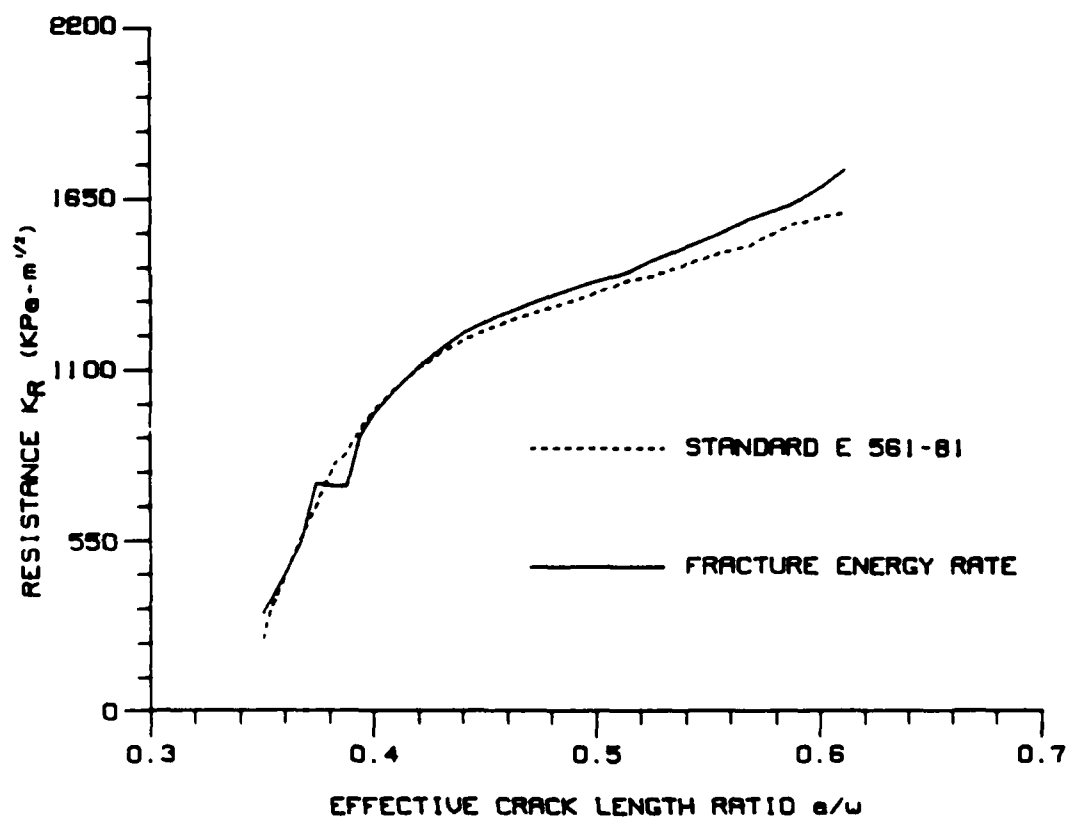


Figure F.2 Crack Growth Resistance Curve For
CLWL-DCB Specimen, Group 2, Ref. [9]

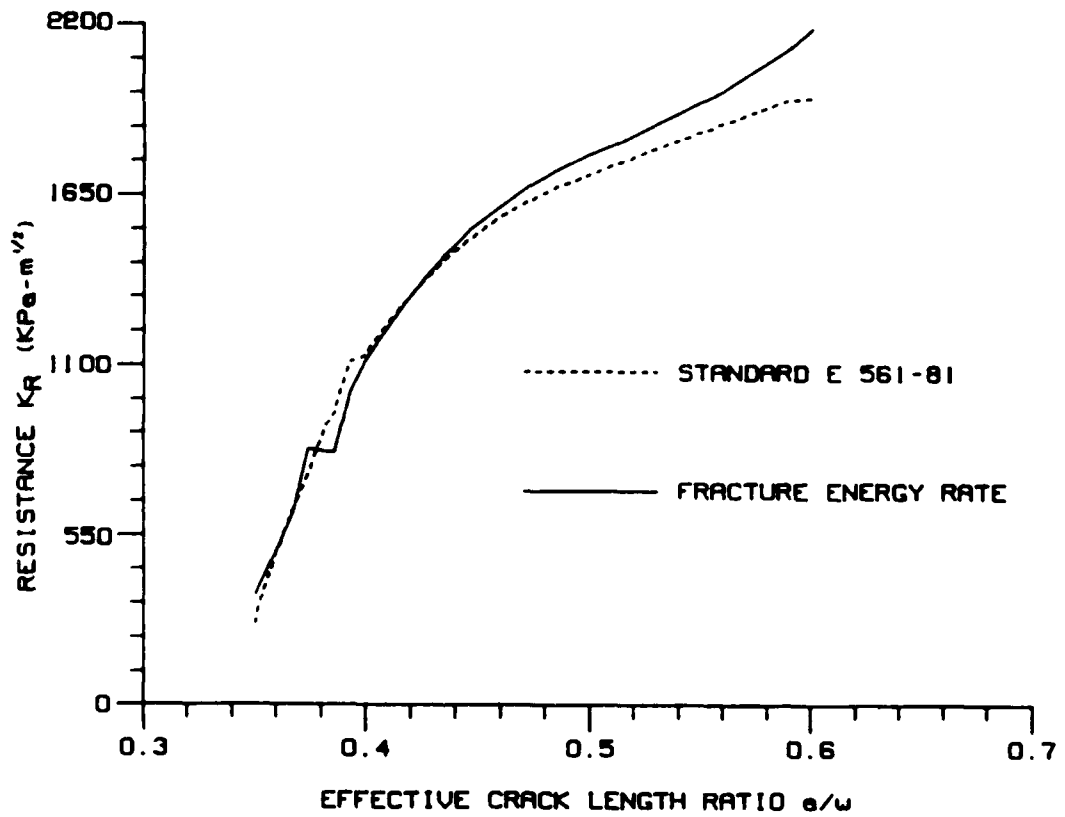


Figure F.3 Crack Growth Resistance Curve For
CLWL-DCB Specimen, Group 3, Ref. [9]

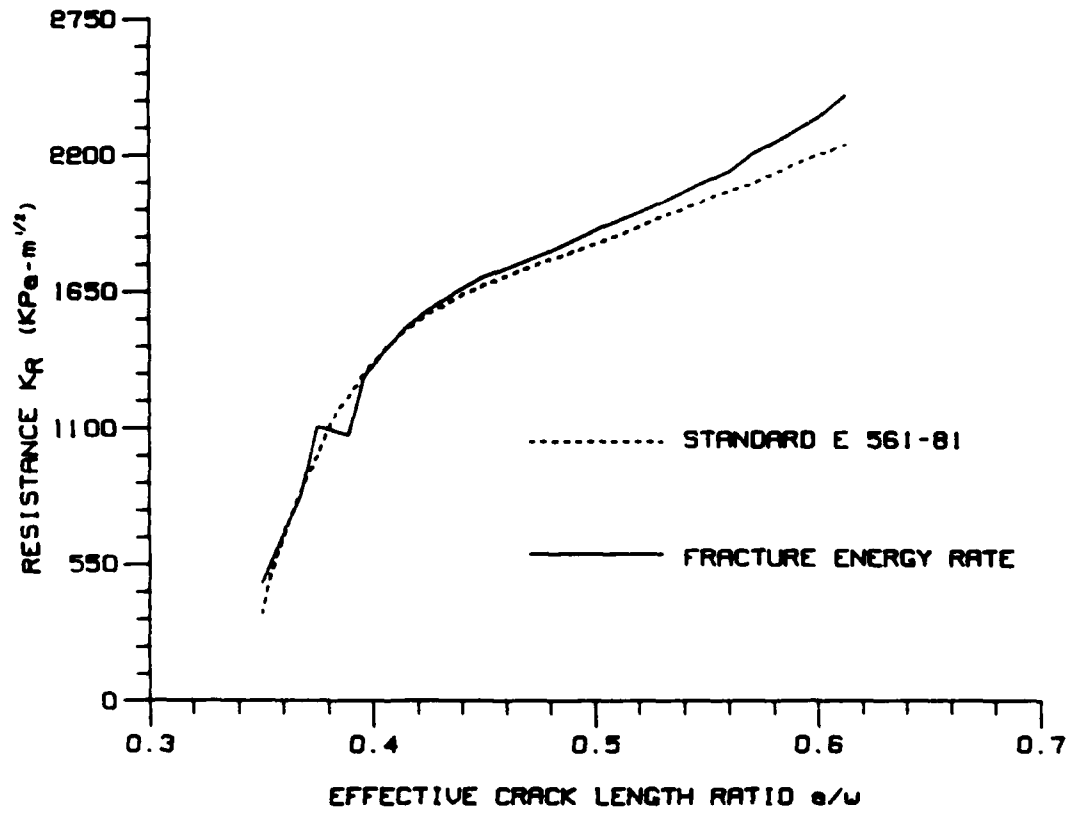


Figure F.4 Crack Growth Resistance Curve For CLWL-DCB Specimen, Group 4, Ref. [9]

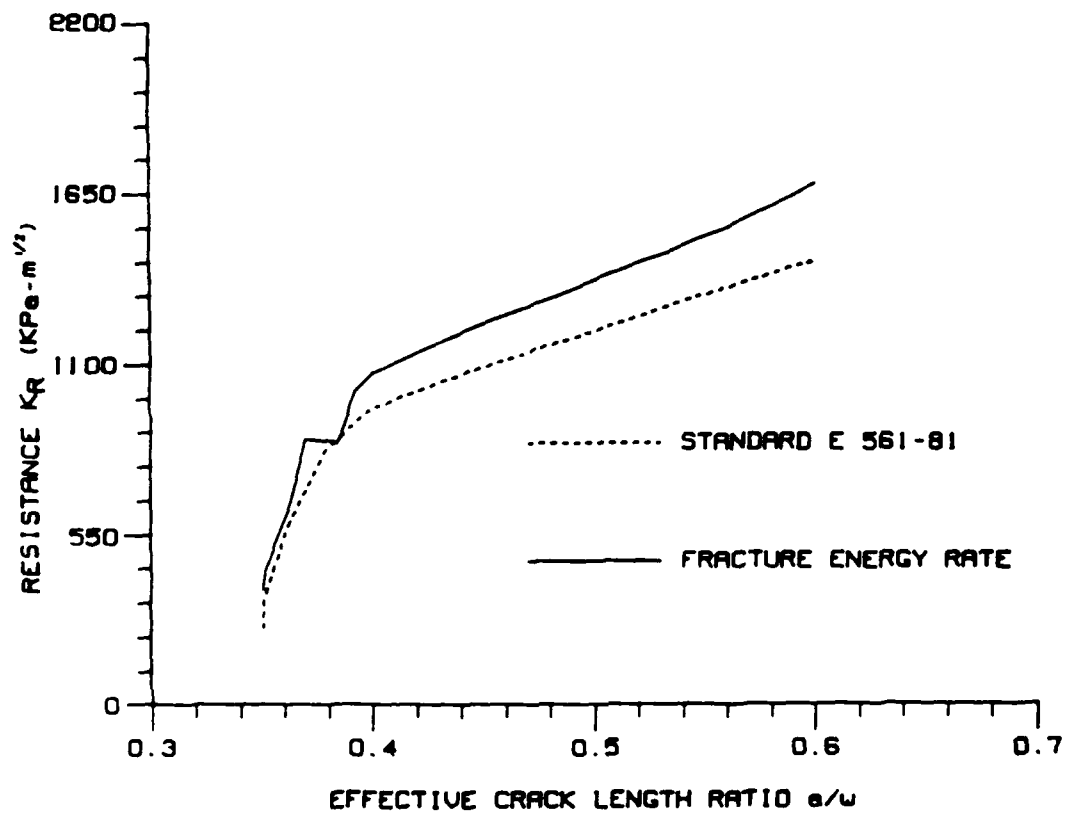


Figure F.5 Crack Growth Resistance Curve For CLWL-DCB Specimen, Group 5, Ref. [9]

obtained with that procedure are shown in Figures F-1 through F.5 by solid lines.

It should be pointed out here that there is no well defined crack tip for concrete and the evaluation of the fracture energy rate is crucially influenced by the location of the crack tip. Two crack tips, described as the micro-crack tip and the macro-crack tip, respectively, in the literature. Since the crack bridging stress is zero at the macro-crack tip and reaches its maximum value at the micro-crack tip, the locations of the micro-crack tip must be much more important than those of the macro-crack tip. Therefore, the location of the micro-crack tip was chosen to define the fracture energy rate and, in turn, to define K_R .

Examination of Figures F-1 through F-5 shows that there is a step change at some location within every K_R curve evaluated from energy considerations. That step is due to a sudden drop in the crack bridging stress when the crack opening displacement reaches a value such that the fracture energy rate ceases to increase with increasing displacements. This kind of discontinuity in behavior is possible for a heterogeneous material.

It is apparent that the K_R values for concrete specimens can be evaluated by fracture energy analysis and that Standard 561-81 applies to concrete although it is a

little conservative.